Electroanalytical studies of diamond electrodes



A thesis submitted for the degree of

Doctor of Philosophy in Physical & Theoretical Chemistry

Ella Bentin

St Catherine's College, University of Oxford

EPSRC CDT in Diamond Science and Technology, University of Warwick

Michaelmas term 2021

Abstract

The experimental work presented in this thesis explores the suitability of boron-doped diamond (BDD) electrodes for the electrochemical sensing of compounds important to health. Various forms of BDD electrode have found increased application to electroanalysis in the past two decades, but there is still room to explore more complex molecules with synthetic BDD. The aim of this thesis is to examine whether the known chemical and material advantages—wide potential window, low background capacitance, chemical inertness, and physical robustness—can be realised.

Although BDD electrodes generally have higher resistance to fouling by analyte media than other carbon and metallic electrode materials, electrode poisoning can still be very problematic. The first study investigates ways to restore or improve the electrode response reliably and quickly after it has been fouled. The fouling analyte was dopamine (DA), known to form a wide variety of polymers and is one of the most fouling chemicals that exists. After 3 cyclic scans, a thick adsorbed layer was observed by scanning electron microscopy (SEM), which negatively impacted the accuracy of further measurements. In a solution of 1 mM DA, the heavily fouled BDD can be efficiently returned to high activity by using 20 pulses of alternating ± 10 mA cm^{-2} current density with 100 ms duration. If only anodic pulses are used, then this is not observed. This treatment *in situ* increased the quality of the signal to beyond the initial value for an acid-cleaned electrode. This finding provides confidence for exploring other heavily fouling analytes.

The second study examined the voltammetric behaviour of the genotoxic pollutant 2-amino-9-fluorenone (2-AFN) and its interaction with double-stranded DNA (dsDNA). Cyclic voltammetry revealed complex adsorptive behaviour of 2-AFN onto the BDD. Applying 60 pulses of alternating ± 10 mA cm^{-2} current density with 100 ms duration *in situ* gave consistent and reproducible voltammetry. With the aid of SEM and X-ray photoelectron spectroscopy to study the nature of the adsorption, it was shown that 2-AFN diffuses to the electrode and undergoes proton-dependent (below pH 10.0) irreversible oxidation in the anodic region to form dimers or longer polymer chains. These and other monomers can then also take part in the reversible reduction of the carbonyl group. By optimising the parameters of differential pulse voltammetry, the limit of detection of 2-AFN was found to be 10 nM—an order of magnitude lower than previously reported.

After exposing dsDNA to 2-AFN, preferential damage to the guanosine moiety was observed, suggesting the intercalation of 2-AFN into the planar aromatic structure of dsDNA. Extensive square wave voltammetry showed that 2-AFN causes a disproportionate amount of damage to dsDNA, observed as significant deviations from the expected peak currents and potentials.

In the third study, bare BDD electrodes were used in the pulsed voltammetric and amperometric quantification of five pesticides in buffered solutions and in river water: namely, the four carbamates carbaryl (CB), carbofuran (CF), fenobucarb (FC), and aldicarb (AC), along with malathion (MT). After exposure to 1 mM MT, a reduction feature was observed on subsequent scans that is highly sensitive to pH. This is attributed to a complex carbon–oxygen adsorbate that is robust to aggressive cleaning methods and only removable by hydrogen-plasma etching. For the carbamates, detection limits of 1 µM for FC, CB, CF (better than other undecorated planar electrodes), and 2.5 µM for AC were obtained. The same limits and calibration ranges were achieved via amperometric batch-injection in spiked river water for CB, and CF. The detection limit in river water for FC was 5 µM. The oxidised BDD electrode demonstrated linear sensitivity up to 100 µM. Alkaline hydrolysis applied prior to analyte mixing allowed for the simultaneous detection of CF, CB, and FC.

The fourth study turns to a group of compounds that has recently come back into public interest: antibiotics. Amoxicillin (AMX), cefadroxil (CFX), ofloxacin (OFX), and tetracycline (TC) have all been used for growth promotion in industrial farming. These molecules are rarely investigated via electrochemistry, and here BDD electrodes were applied to the analysis of OFX for the first time, achieving a competitive detection limit of 1 µM. Because of peak-definition and sensitivity problems of AMX, this work focused on the other three analytes. Square-wave voltammetry was used to achieve a detection limit of 500 nM for CFX and 1 nM for TC, which is an order of magnitude lower than previously reported. All three exhibited a wide dynamic range, up to 200 µM. A major advantage of using a BDD electrode was realised for this project. Because of the inertness of the diamond surface, adsorption which dominates the electrochemistry of these compounds on non-diamond electrodes did not take place.

The thesis concludes with a summary of key results and suggestions for future research topics.

Dedicated to my parents and grandparents, whose love and support never wavered.

Acknowledgements

First, thank you Prof. John S. Foord, for taking me on as a student, and for helping and guiding me through this work. This thesis would not have been possible without your scientific insight, patience, and good humour.

I am grateful to Dr Robert Jacobs for his help in the Surface Analysis Facility, particularly with SEM and UV-vis. I would like to thank Dr Jennifer Holt from the Materials Department for her help with access and operation of the SEM, and Dr Philip Holdway for collecting the XPS data and for discussions about how things used to be.

The diamond CDT has not only introduced me to experts in all things diamond-related, but also made me proud to be a part of a cohort of students who added laughter to science. They readily shared theoretical knowledge, practical tips, great conference times, and generated the most incredible diamond ideas. The Foord Group members (Emina, Mailis, Martin, Chenbo, Xiaosheng, Yifan, and Scarlett) have helped me in my work and kept the basement sun shining. I appreciated the support and friendship of several Part II students over the years (Melissa, David, Amy, Jovanna, Alice-Joy, Jessica). The Kukura, Vallance, Robinson, and Krishnan Groups have contributed to an enjoyable working environment in the CRL. I would like to thank Dr Johanna Svanberg Larsson, for showing me the ropes when I first started working in the lab and for our interesting discussions about chemical matters, books, and travel. I would also like to thank Dr Hiu-ming Lau and Sushanta Mahanta, for the thought-provoking debates, fitness sessions, and friendship.

My thanks also go to Dr Martin Christlieb from the Green Building, for being the first to show me the world of academia and research. I am indebted to Dr Danny O'Hare and Professor Darryl Overby from Imperial College London for the engaging summers spent in the laboratory. I am thankful to Professors Mark Newton and Julie Macpherson from the University of Warwick for their encouragement and advice. Their enthusiasm inspired me to stay the course.

This research was made possible by the Engineering and Physical Sciences Research Council, the University of Oxford, and St Catherine's College, I am thankful for their generous support in scholarships and grants.

Lastly, I am immensely grateful to my family for their love, encouragement, support, and patience through all these years.

Abbreviations

The following table contains the most common abbreviations used in this thesis.

2-AFN	2-amino-9-fluorononone
AC	aldicarb
AcB	sodium acetate buffer
AChE	acetylcholinesterase
AMX	amoxicillin
BDD	boron-doped diamond
CA	carbaryl
CF	carbofuran
CFX	cefadroxil
CV	cyclic voltammetry or voltammogram
DA	dopamine
DI	deionised
dsDNA	double-stranded DNA
DNA	deoxyribonucleic acid
DPV	differential pulse voltammetry
FC	fenobucarb
GC	glassy carbon
LoD	limit of detection
MT	malathion
NP	nanoparticle
OFX	ofloxacin
PBS	phosphate buffer solution
PTFE	poly(tetrafluoroethylene)
RSF	relative sensitivity factor
SEM	scanning electron microscopy
ssDNA	single-stranded DNA
SWV	square-wave voltammetry
TC	tetracycline
UHV	ultra-high vacuum
XPS	x-ray photoelectron spectroscopy

Contents

1 Introduction 1

1.1 Synthetic diamond 1

1.1.1 Chemical vapour deposition 3

1.1.2 Chemical structure 5

1.1.3 Electronic structure 6

1.1.4 Surface properties of BDD 8

1.2 Role of BDDs in electrochemistry 12

1.2.1 Benefits of chemical inertness 12

1.2.2 Scientific and commercial applications 14

1.3 Scope of this thesis 16

2 Theory and techniques 24

2.1 Electrochemical theory 24

2.1.1 Electrode potentials at equilibrium 24

2.1.2 Practical measurement of potential 26

2.1.3 Non-equilibrium processes 28

2.1.4 Measurement of current at non-equilibrium 29

2.1.5 Electrode kinetics 31

2.1.6 Mass transport 33

2.1.7 Supporting electrolyte 36

2.1.8 Dynamic electrochemical methods 37

2.1.9 Set-up for the present work 44

2.2 X-ray photoelectron spectroscopy 44

2.2.1 Photoelectron production 44

2.2.2 Electron detection 46

2.2.3 General spectral features 47

2.2.4 Fitting photoelectron spectra 50

2.2.5 Operational parameters 53

2.3 Scanning electron microscopy 53

3 Investigation of the *in situ* activation of BDD for dopamine detection 58

3.1 Introduction 58

3.2 Experimental details 63

3.2.1 BDD cleaning 63
3.2.2 Surface analysis 64
3.3 Results and discussions 65
3.3.1 Pristine oxygen-terminated BDD 65
3.3.2 Dopamine redox 67
3.3.3 Reactivation with the patented method 68
3.3.4 Separation of polarisation 72
3.3.5 Stability 76
3.3.6 Importance of pulses 78
3.3.7 Reproducibility 82
3.3.8 Scanning electron microscopy 83
3.3.9 Photoelectron X-ray spectroscopy 85
3.4 Conclusions 95

4 Electrochemical characterisation of 2-AFN and its interaction with DNA 104
4.1 Introduction 104
4.2 Experimental details 108
4.2.1 Reagents and solutions 108
4.2.2 Voltammetry parameters 109
4.3 Results and discussions 109
4.3.1 Cyclic voltammetry 109
4.3.2 Surface restoration 111
4.3.3 Successive scans 113
4.3.4 Scan-rate dependence 114
4.3.5 pH dependence 117
4.3.6 Scanning electron microscopy 121
4.3.7 X-ray photoelectron spectroscopy 124
4.3.8 Differential pulse voltammetry 127
4.3.9 Sensing of nucleosides 129
4.3.10 Sensing of DNA strands 133
4.3.11 dsDNA interactions with 2-AFN 135
4.4 Conclusions 145

5 Detection of carbamate and organophosphate pesticides with bare BDD 152
5.1 Introduction 152

5.2 Experimental details 156
5.2.1 Solutions 157
5.2.2 Alkaline hydrolysis 157
5.2.3 Voltammetry parameters 157
5.3 Malathion results and discussions 158
5.3.1 Cyclic voltammetry 158
5.3.2 XPS of electrodes after malathion exposure 162
5.4 Carbamates results and discussions 165
5.4.1 Cyclic voltammetry at pH 7.0 165
5.4.2 Alkaline hydrolysis 167
5.4.3 pH-dependence of the carbamates 171
5.4.4 Scan-rate dependence 172
5.4.5 Square-wave voltammetry 176
5.4.6 Batch injection analysis 185
5.5 Conclusions 188

6 Electroanalysis of β-lactam, quinolone, and tetracycline antibiotics 196
6.1 Introduction 196
6.2 Experimental details 200
6.2.1 Solutions 200
6.3 Results and discussions 201
6.3.1 Cyclic voltammetry 201
6.3.2 pH dependence 204
6.3.3 Square-wave voltammetry 208
6.4 Conclusions 212

7 Summary and outlook 217
7.1 Summary 217
7.2 Outlook 219

Chapter 1

Introduction

The purpose of this work is to explore the electrochemical properties and applications of electrically conductive diamond for sensing molecules of importance in health. Natural pure diamonds are not conductive; but during the growth of synthetic diamond, boron can be incorporated to increase its conductivity. In recent decades, synthetic diamonds have enjoyed growing popularity in the gem market, and diamond has been gaining recognition for its potential applications in science and technology [1–3].

1.1 Synthetic diamond

Diamonds are expensive and prestigious because of their rarity and beauty, enhanced by an excellent advertising campaign [4]. For millennia, diamonds were exclusively obtained by mining, until 1954, when they were first synthesised by "Project Superpressure" at General Electric [5]. The original press was designed by H. Tracy Hall et al. [6].

The discovery of artificial diamond growth was not immediately relevant to the natural gem price, which is still orders of magnitudes higher even when laboratory-grown stones are of gem quality [7]. From 1870 to 2019, the world production of diamond increased from ~1 to ~130 million carats (1 ct = 0.2 grams) [8–9], reaching a peak output of 175 million ct in 2006, accompanied by a steadily increasing price [10]. The kind of diamonds embedded in rotary saws or in knives for cutting glass would on average be 0.02–0.03 ct, with a price of around £0.05 per ct. The 1 ct boron-doped diamond (BDD) electrodes used in this thesis

cost £75 each [11]. A 1 ct engagement ring could cost anywhere upwards of £5000 [12].

In 1772, Antoine Lavoisier discovered that diamond is a crystalline form of carbon; by burning diamonds with a lens in closed glass vessels, bubbling the combustion products through lime-water, and identifying the precipitates as “afforded by calcareous substances” [13,14]. After that, synthesising diamond became an area of research. One of the earliest records of attempts to synthesise artificial diamond was published by J. B. Hannay in 1879 [15]. In an 11-page communication to the Royal Society, he described trying to convert bone oil and paraffin spirit mixtures into diamond using heat and pressure, reporting that no diamonds were found when nitrogen compounds were absent. Eight of those pages were descriptions of how the reaction tubes exploded [15]. His ideas were scientifically sound, though hampered by the limitations of 19th-century engineering.

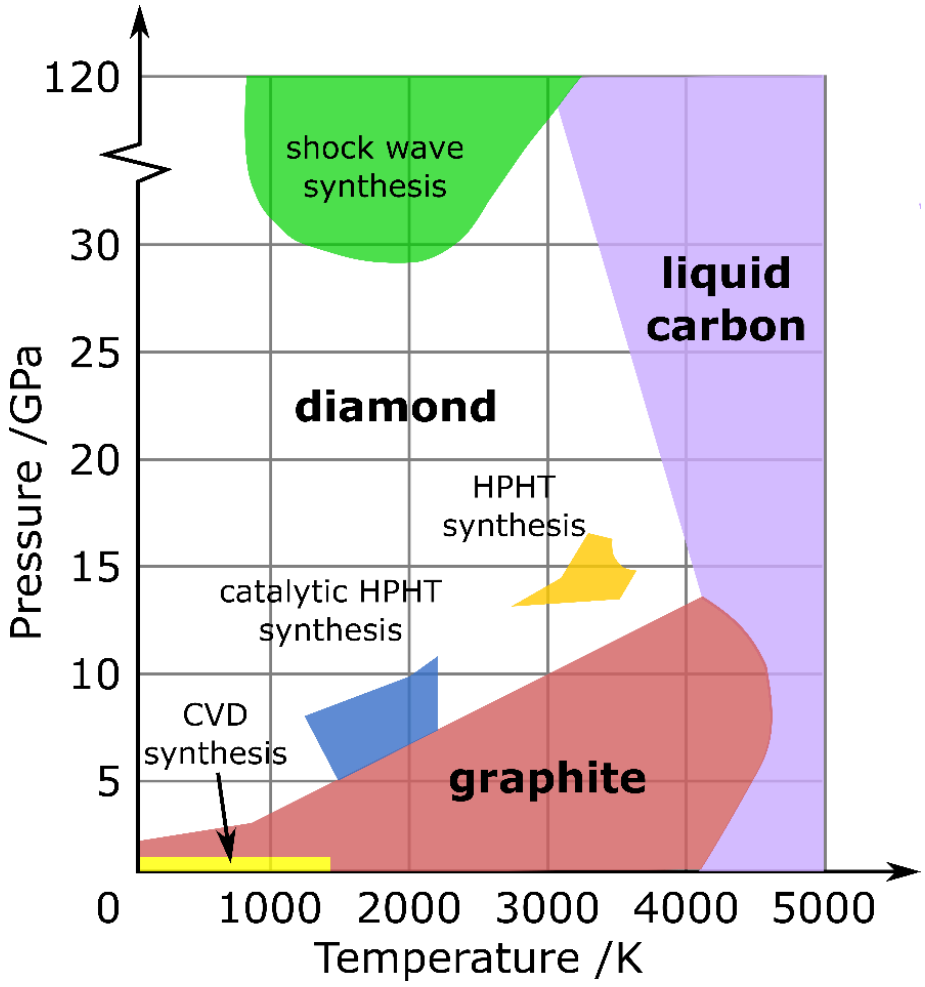


Figure 1.1 Phase diagram of carbon [6,16,17].

Nowadays, powders and crystals for mechanical applications are made in high-pressure high-temperature (HPHT) presses, which replicate growth conditions within the Earth. The press must be able to sustain at least 5 GPa at 3000 K [6], which was the engineering challenge the team at General Electric was tasked to solve. At those conditions (Figure 1.1), high-purity carbon powder dissolves in a molten transition metal (iron, cobalt, or nickel) that serves as both solvent and catalyst. As the pressed material undergoes controlled cooling, diamond crystals precipitate out, and their final size is determined by the length of time they are left to grow.

Originally, HPHT synthesis was carried out in a doughnut-shaped die belted by shrink-fit steel sleeves which confined the sample chamber, and two curved and tapered pistons applied pressure [6]. In the 1960s, H. Tracy Hall invented the tetrahedral and cubic press systems [18], which now produce the majority of the world's synthetic diamond powder, in China [9]. The HPHT growth technique is, however, not the only one used to produce high-quality diamond for industrial applications. The other method, which is growing in popularity, is chemical vapour deposition.

1.1.1 Chemical vapour deposition

Graphite has a more negative free energy than diamond, though only by 2.9 kJ mol^{-1} at standard conditions, so graphite is thermodynamically more stable than diamond under these conditions [19]. There is, however, a large activation barrier between them, so interconversion is slow. The CVD method relies on this barrier since diamond is formed at low pressure where it is thermodynamically unstable.

Chemical vapour deposition (CVD) grows the diamond lattice ‘Lego-style’, by adding carbon atoms onto the nanodiamond (ND) crystals ‘seeded’ on a substrate, typically silicon. This happens at high temperatures and low pressures (under plasma) in the reaction chamber [20]. Three gaseous ingredients are required for BDD formation: carbon (e.g. in

methane), boron (e.g. as trimethylborane), and hydrogen. It is essential that hydrogen is present in the largest proportion (> 95%). In plasma, the molecular-bound hydrogen dissociates into a 'sea' of hydrogen atoms which bond to the diamond surface, to maintain sp^3 bond configuration, and etches away any bonded sp^2 species. The hydrocarbon molecules undergo hydrogen abstraction [21], producing highly reactive carbon-containing radical species, such as methyl ($\bullet CH_3$) which diffuses to the ND surface to form the C–C bond necessary to propagate the diamond lattice [22].

Thus, the diamond produced is metastable: it is kinetically but not thermodynamically stable. Once it is formed, it cannot reconvert to graphite without an energetic push. So, even as atomic hydrogen etches both diamond and graphite, the growth rate of diamond exceeds the etch rate. The excess hydrogen also acts as the carrier gas to remove volatile by-products from the reaction chamber.

The substrate is typically uniformly seeded with ND, and as they increase in size the growing diamond 'islands' merge to form a film. The density of the seeds and the growth time dictate the porosity and size of the crystallites at the surface [23]. Polycrystalline diamond films are classified by their grain size: microcrystalline (MC), nanocrystalline (NC), and ultra-nanocrystalline (UNC). Monocrystalline diamonds are also grown by CVD, to study crystallographic influences, though they are mostly produced by HPHT and for gem purposes.

Electrodes made from BDD are often found in two states: as-grown and polished. For the as-grown surface, MC BDD is inherently rougher than NC and UNC BDD which contain greater proportions of non-diamond carbon (NDC). The amount of NDC present in the BDD matrix affects the electro-catalytic activity of the electrode—the less, the better—and is one of the markers of quality [24]. Boron-doped diamonds used in the present study are as-grown microcrystalline standalone plates produced by CVD (Figure 1.2).

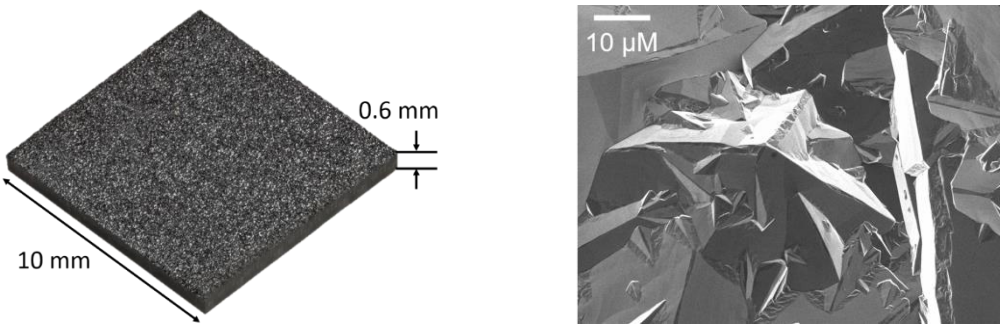


Figure 1.2 A BDD plate as used in this study, and an electron micrograph of it.

There are many kinds of CVD method, named after the way the plasma is produced: hot-filament [25], arc-jet [26], microwave-assisted [27], etc. The BDD electrodes in this study were grown via microwave-assisted CVD, and a similar set-up is used to terminate electrodes with hydrogen. The atomic purity of CVD diamonds can be controlled by the elemental content in the gas phase, resulting in doped diamonds which have a range of mechanical, optical, and electronic properties.

1.1.2 Chemical structure

Pure diamond is one of the hardest materials on Earth. This characteristic has long been exploited by engravers and, since 1976, synthetic polycrystalline diamond cutters have been used by exploration geologists [28]. Its hardness derives from its chemical structure, where each carbon atom is bonded to four others by sp^3 hybridisation, in which four covalent bonds are directed towards the corners of a regular tetrahedron [29]. This crystal structure (Figure 1.3) provides not only mechanical hardness but also high thermal conductivity. However, diamond has a chemical bonding structure in which all the electrons are considered to be localised in sp^3 bonds; therefore electron transport is not readily achieved, and the material is an electrical insulator.

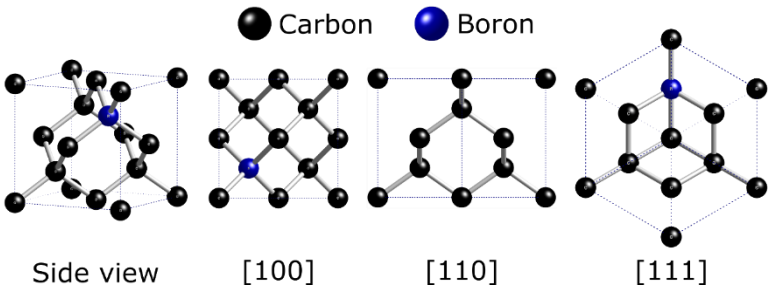


Figure 1.3 The face-centred cubic structure of BDD; boron substitution is shown.

Due to the lattice rigidity and the small lattice parameter, only boron and nitrogen can be readily substituted for carbon. Interstitial dopants such as silicon, phosphorus, and sulphur are possible, but difficult, because the strain energy is large. Where a carbon atom is not replaced by other elements, a vacancy is created. The most well-known defect is the nitrogen vacancy, as the vacancies tend to come to rest next to a substituted nitrogen [30]. Under high temperature, vacancies move within the lattice and onto to the crystal surface and escape and make the crystal more defect-free. This phenomenon can be exploited by the gem industry to increase the value of brownish stones by increasing their clarity. The next section explains why the greater boon comes with boron-doping.

1.1.3 Electronic structure

Pure diamond has a bandgap of 5.47 eV [31] and is an insulator. Intentional introduction of impurities creates energy states in the bandgap (Figure 1.4) and increases conductivity.

An acceptor dopant forms a shallow energy state for electrons near the valence-band (VB) edge. These states act as traps, capturing thermally excited electrons from the VB and leaving behind holes in their place. Since the equilibrium hole concentration exceeds the electron carrier concentration, the material is p-type. Donor dopants form shallow levels below the conduction-band (CB) edge and increase the free-electron carrier concentration in the CB. Electrons are readily promoted from the shallow impurity levels to the CB through thermal processes. Thus the material has an excess concentration of free electrons in the CB and is called n-type [32].

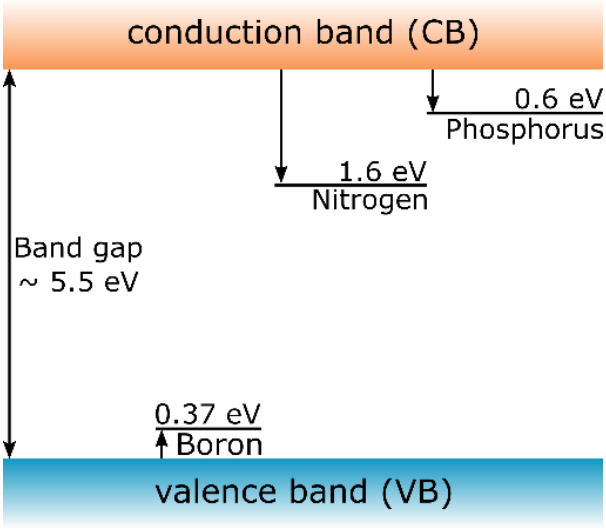


Figure 1.4 Energy band diagram showing energy states from common dopants [33].

With boron (acceptor) or nitrogen (donor) doping one might expect the creation of p-type or n-type semiconductors, respectively. This is true for boron, but not so for nitrogen. Nitrogen forms levels nearer the middle of the bandgap, which do not readily ionise. These states are typically referred to as deep-level traps, capturing and later re-emitting electrons and holes [32]. Electrons and holes can recombine at deep-level traps, thereby decreasing the free-carrier concentrations.

Boron forms an acceptor level around 0.37 eV [34], and increasing its concentration reduces the resistivity of the BDD [35]. Visser et al. initially proposed the now-accepted model that describes the two main components of conduction in diamond: valence-band conduction and hopping transport [36]. Valence-band conduction dominates at low boron atom concentrations ($< 10^{19}$ cm^{-3}), and is dependent on high temperatures; hopping transport between acceptor states occurs at higher doping levels (10^{19}–10^{20} cm^{-3}) and is less restricted by temperature [37]. Of the roughly 2×10^{23} carbon atoms per cm^3 of diamond, around 1 in 1000 must be replaced by boron ($\sim 2.5 \times 10^{20}$ cm^{-3}) to demonstrate metallic conduction [35] without thermal activation.

1.1.4 Surface properties of BDD

There are two common types of surface termination on diamond: hydrogen (H) and oxygen (O). Diamond grown by CVD leaves the reaction chamber H-terminated. Such diamond has negative electron affinity and surface conductivity. These characteristics are favourable to the reversible electrochemical behaviour of redox couples in aqueous solutions, which have been well studied [38]. However, it is worthy of note that the investigation of these properties in non-aqueous solutions is relatively limited [39].

The H-terminated surface is hydrophobic, and stable in air for several months if left undisturbed. The H-terminated surface will slowly oxidise over time [40] becoming more O-terminated and hydrophilic [41], but can be restored by exposure to hydrogen plasma [42]. The hydrophobicity of the fresh surface may be explained by the interaction of sp^3 carbon with hydrogen atoms, and the polar nature of water. During growth or subsequent hydrogen treatment, reconstruction of surface carbon occurs, giving rise to $C^{\delta-}$–$H^{\delta+}$ bonds. This hydrogenated surface is relatively non-polar, because of the low difference in electronegativity between the two atoms, and so it is analogous to a paraffin-type chemical structure which is hydrophobic. When C–H bonds are replaced with $C^{\delta+}$–$O^{\delta-}$ bonds, which have a stronger dipole moment [43], they are more polar and show a larger interaction with water, and therefore the C–O surface is hydrophilic. The types of oxygen and hydrogen termination are briefly discussed in more detail at the end of this section.

The wide band gap in diamond puts the vacuum level very close to the CB, and the electron affinity is positive. However, if the surface is H-terminated, a photoelectron threshold energy of 4.4 eV is detected [44], so the work function (WF) of H-terminated diamond is reduced. This reduction can be attributed to $C^{\delta-}$–$H^{\delta+}$ surface dipoles, which act as an accelerating potential for electrons leaving the surface. This is shown graphically in Figure 1.5. The band gap does not change, the Fermi level (E_F) within the band gap does

not change, and against the vacuum level as reference, the reduced WF means that the CB is raised above the vacuum level by 1.1 eV [44], and electron affinity becomes negative [45], meaning that electrons thermalised in the CB can readily escape into vacuum.

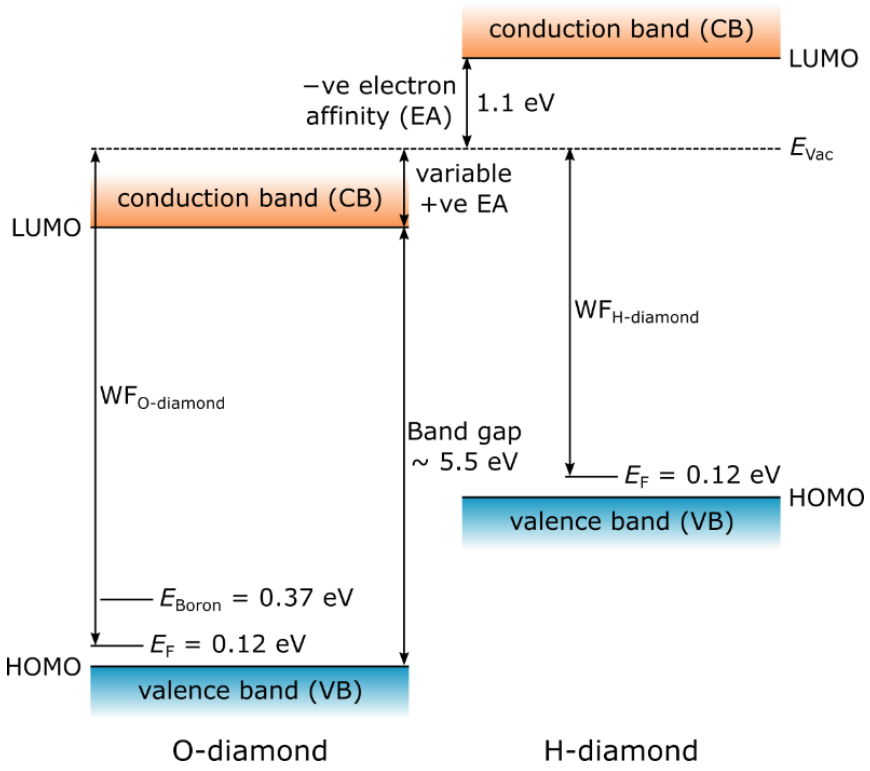


Figure 1.5 The energy band diagram for H- and O-terminated diamond.

For electrochemical purposes, the VB of all semiconductors (including O-terminated diamond) lies more than 0.7 eV below the VB maximum [46], so only the strong reduction of the electron affinity by hydrogen termination shifts the VB up above the chemical potential of typical wetting layers [47]. This allows greater mobility of holes within the material, where the hole charge can be compensated by anions in the wetting layer, thus establishing surface conductivity.

Surprisingly, un-doped CVD diamonds were found to be conductive in 1989, with resistivity of the order of 10^{-3} to 10^{-2} Ω m at room temperature [48]. Although the mechanism of this conductivity is still up to debate, the identification of a conductive layer where the carriers are holes in a surface accumulation layer gives rise to the term *surface conductivity* [49].

Maier et al. proposed the now-accepted *electrochemical model* to explain the surface conductivity of diamonds [50]. By probing diamond resistivities before and after exposure to air, they showed that H-termination alone is not sufficient to induce surface conductivity [50]. Rather, the diamond must also be exposed to air. If the electron affinity of atmospheric species exceeds the lower ionisation value of H-terminated diamond (4.2 eV) [51], they can adsorb onto the diamond surface, but electron affinities of those species typically lie below 2.5 eV [50]. However, a thin water layer, as naturally formed on all surfaces upon exposure to the atmosphere, provides an electron system which can act as a surface acceptor for diamond [52]. Figure 1.6 shows that if normal (water-containing) atmosphere is in contact with a solid phase, electrons will transfer between the adsorbed water film and the solid, to bring the Fermi energy of the solid equal to that of the ambient film [53].

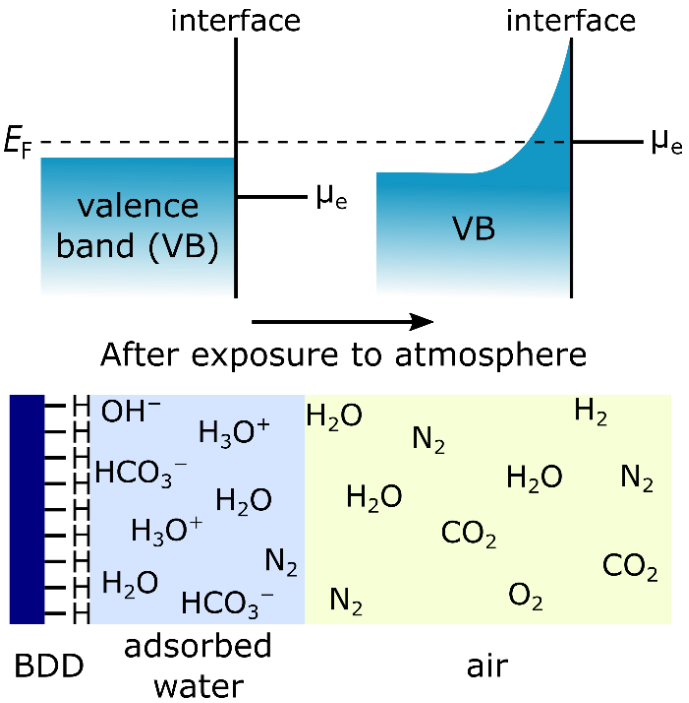


Figure 1.6 Band bending during electron transfer at the diamond–water interface.

This reaction is driven by the difference between the chemical potential of electrons in the liquid phase (μ) and in the diamond E_F. From left to right in Figure 1.6, initially μ is below E_F, then electrons are being transferred from diamond to the water layer ($H_3O_{(aq)}^+$). The compensating holes in the diamond form the accumulation layer, and the associated

space charge induces a potential (surface band bending) that raises μ, until they are equal at the interface [54]. Electron exchange from diamond to the water layer is governed by the redox reaction (1.1) and also proceeds left to right:

$$2H_3O^+ + 2e^- \rightarrow H_2 + 2H_2O. \quad (1.1)$$

Such Fermi-level shifts require defect-free sub-surface diamond layers with perfect H-termination of the surface [47], and this surface conductivity vanishes after anodic oxidation [54].

Oxygen-terminated diamond differs from H-terminated diamond in several key aspects. First, induced surface conductivity is not observed with O-termination. In this situation, the dipole is reversed ($C^{\delta+}$–$O^{\delta-}$), which gives rise to a positive electron affinity [55]. Second, O-terminated diamond is hydrophilic, with a negative surface charge [1]. Finally, under normal storage conditions, an H-terminated surface gradually oxidises, meaning that O-termination is the more stable state.

A range of carbon–oxygen functionalities naturally exist on the surface, and some grain orientations preferentially host certain groups. For example, C–OH groups are the most abundant on the [111] face on O-terminated single crystal diamond. However, C–O–C, C=O, and more highly oxidised groups dominate on the [100] face [56]. The ratios of various groups, and thus degree of oxidation, can be determined by different treatments. A non-exhaustive list includes chemical–mechanical polishing [57], anodic polarisation [58], laser ablation [59], and exposure to atomic hydrogen or oxygen [60].

Overall, the surface termination of BDD can significantly affect electrochemical interactions at the solid-electrolyte interface, surface wettability, and electron-transfer kinetics. Exploiting these effects for electrochemical performance, the research described in this thesis uses the stable nature of oxygen-terminated diamonds for sensing applications.

1.2 Role of BDDs in electrochemistry

By the second paragraph of almost all articles concerning the use of BDD, its extraordinary material qualities will have been stated. Among the myriad of BDD materials in a wide range of electrochemical studies, this section will focus on those that use unmodified oxygen-terminated diamond. The first three rows in Table 1.1 lists the material properties of BDD electrodes used in the present work [11]. Information on the hardness and thermal conductivity is also important for developing future applications.

There are excellent reviews of BDD electrochemistry by veterans in the field, covering topics ranging from diamond synthesis and material properties to electrochemical applications [2,3,23]. The subsections below only provide a brief overview of some literature selected to be of particular relevance to the present research, making specific references as to how the properties in Table 1.1 have been employed.

Table 1.1 Properties of microcrystalline BDD, boron-doped to metallic conductivity

Material property	**Value**
Boron-atom concentration	2 to 6 × 10^{20} cm^{-3}, averaged over 0.16 mm^2
Bulk resistivity	2 to 1.8 (± 0.25) × 10^{-3} Ω m
Operating current density	> 20,000 A m^{-2}
Vickers hardness [61]	~ 100 GPa
Thermal conductivity [62]	650750 W m^{-1} K^{-1}

1.2.1 Benefits of chemical inertness

Boron-doped diamond electrodes have a low density of ionisable or redox-active groups on the surface, which creates three main benefits for the electrochemist. First, they exhibit smaller double-layer capacitance (~10 μF cm^{-2}) relative to other materials, observed as a significant decrease both of undesirable distinct background peaks and capacitive background current which improves the limit of detection of analytes [63]. Figure 1.7

shows that the central regions in the BDD response is much wider than those collected with gold, platinum, or glassy-carbon electrodes. Second, this chemical inertness increases the onset potentials of hydrogen evolution (rise of current at negative potentials) and oxygen evolution (rise of current at positive potentials). The difference between those potentials is known as the potential window or solvent window. When a cut-off current density of 1.0 mA cm^{-2} is selected to define the potential window, a potential window of over 3 V in aqueous solution, 4.6 V in organic solutions, and 4.9 V in room-temperature ionic liquids has been obtained for single crystal BDD [3,64]. Figure 1.7 shows cyclic voltammograms obtained in 0.1 M $H_2SO_{4(aq)}$ solution—a common background electrolyte. The plots are separated by vertical shifting for better visual comparison. In relation to other electrodes, the electrochemical potential window of diamond electrode is the biggest, and its background current is the smallest. The boron-doping and non-diamond-carbon levels can also change the potential-window range [23].

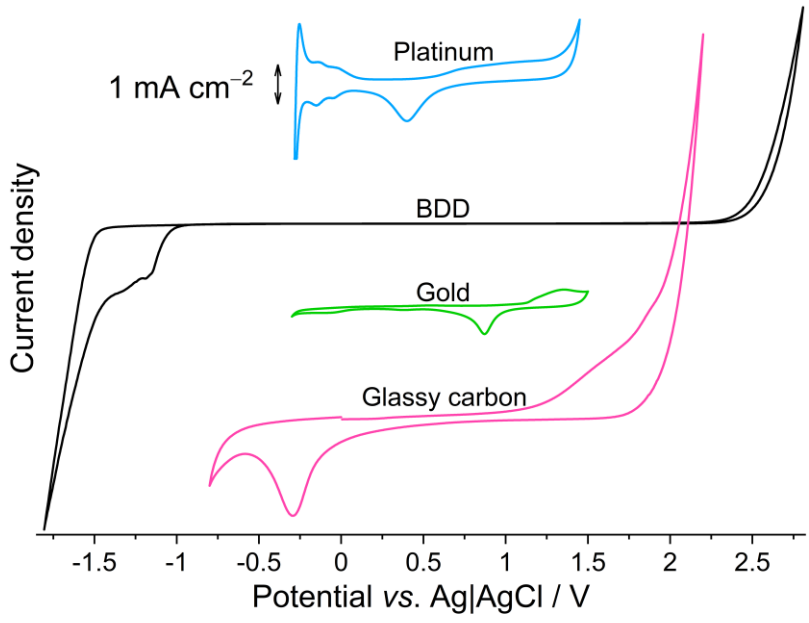


Figure 1.7 Cyclic voltammograms of common electrode materials in 0.1 M H_2SO_4, showing the variation in their potential windows. The scan rate was 100 mV s^{-1}.

The low concentration of active surface groups on diamond brings the third benefit of improved resistance to fouling (either from the products of electrolysis or from the sample

environment itself [65]), and possibly related to that is the remarkable degree of reproducibility of electrochemical response with BDDs. Also due to its structural integrity, in the event of fouling, electrochemical cleaning procedures involving potentiostatic and potentiodynamic treatments, cathodic or anodic, can be successfully employed [66]. Chapter 3 looks at this aspect of BDDs in greater detail.

1.2.2 Scientific and commercial applications

There are five main areas for which BDD electrodes have been particularly applied: electroanalysis, electrochemical degradation, electrosynthesis, electrochemical energy storage, and electrocatalysis. From this list, the first two are the founding motivation for the present work, and most of the literature reviewed relates to them.

Depending on their size, typically diameter, BDD electrodes can be classified as macro (> 1 mm), micro (25–100 μm), ultramicro (100 nm to 25 μm), nano (< 100 nm). To analyse the response of macro electrodes, planar diffusion is assumed—although mixed in is radial diffusion from edge effects. However, for micro-electrodes, radial effects dominate, which can enhance mass-transport rates. Macro-electrodes are suitable for a wide range of situations but can also suffer from non-uniformity in the incorporation of boron and non-diamond carbon species. By choosing the starting material carefully, the ohmic resistance of micro-electrodes can be finely controlled; in general, they record decreased charging currents, are less sensitive to solution resistance, and are more suitable for fast voltammetric measurements. However, the engineering challenges in their manufacture are not trivial, and success rate is highly dependent on craftsmanship.

The structure of the electrode surface can also affect its interaction with analytes. Macro-electrodes made with BDD deposited on nanostructured silicon, to produce a spiky surface covered with ~15 μm-high needles, have been found to be highly bactericidal for both Gram-negative and Gram-positive bacteria, and at the same time able to analyse

dopamine and uric acid [67]. Chemical functionalisation routes can also tether receptors to nanoparticles (NPs) decorated atop BDD electrodes, for the detection of cancer biomarkers [68] or to monitor DNA binding and denaturation events [69]. Additionally, the orientation of the electrode can dictate the dominant mode of mass transport. In particular, at a vertical electrode, if the detection event produces heavy products or involves the possible desorption of adsorbed NPs, then gravity may play a greater role than diffusion in moving the products away from the surface and may thus interfere with initial assumptions about the active surface.

While we have considered the three intrinsic material characteristics and shown the benefits of the chemical inertness of BDD, sometimes, the as-prepared material is not electrocatalytically active enough towards the analyte of interest. Regardless of surface structure, there are generally two approaches to boost BDD activity, either by increasing the NDC content in the material (by altering purity during growth, laser ablation [70], ion implantation after growth [71]), or introducing nanoparticle deposits onto an as-grown diamond surface (by drop-casting [72], electrodeposition [73], or sputtering [74]). Although questions regarding the long-term stability of metal-nanoparticle–BDD electrodes are not insignificant, there are many examples where these electrodes have made powerful progress in the field of electroanalysis [75–77].

The microstructural stability of BDD gives it high resistance to oxidative damage, and it excels in the detection of analytes that require positive potentials for detection [3]. This has led to its incorporation into various forms of flow-injection analysis (FIA) and liquid chromatography [78]. The first report of its use in this regard was for azide detection [79]. Although untreated BDD is often used, pre-treatment has been shown to improve the linear dynamic range, reproducibility and stability, and limit of detection for some redox reactions [80]. In many amperometric FIA studies, the researchers made use of cathodic pre-

treatments to increase H-termination of the surface, because it reduces fouling compared to glassy carbon, due to the absence of an extended π-electron system [81].

BDD's excellent thermal and mechanical properties commend it for operation in physically extreme conditions, such as in detecting hydrogen sulfide (H_2S) down oil-well boreholes at 700–1400 bar and 125–150°C [82,83]. Hydrogen sulfide, H_2S, is a potentially lethal gas, posing a constant hazard for drill workers. At low concentrations, it smells of rotten eggs, but at higher, lethal, concentrations it is odourless.

BDD has proven to be a material that efficiently generates high yields of hydroxyl radicals. The production of hydroxyl radicals under anodic conditions plays a significant role in advanced oxidation processes, which can be used to eliminate a broad range of organic contaminants in wastewater [84,85]. Here the toughness of polycrystalline BDD lengthens the lifetime of the electrodes, and this plays a role in making electrochemical treatments cost effective. Polycrystalline BDD for advanced oxidation processes are among the first to be commercially available, such as by Diamox (UK) and ProAqua (Austria).

For electro-degradation, lowering the cost of production of large-area BDD electrodes is foremost on the agenda. For electroanalysis, the challenge is to increase electrode responsiveness towards the target analyte without compromising the inherent mechanical benefits of using BDD.

1.3 Scope of this thesis

The purpose of the present study is to explore the advantages, and test the limitations, of commercially available, bare, unpolished BDD electrodes. The fouling-resistant properties of BDD were tested thoroughly in performing electroanalysis of biomolecules that are consequential for health, and of chemicals that cause adverse effects to the body and to the environment. The work can be roughly divided into four parts, respectively relating to:

- The neurotransmitter dopamine (Chapter 3)

- The carcinogenic poly-aromatic hydrocarbon derivative 2-amino-9-fluorenone and DNA nucleosides and strands (Chapter 4)
- Pesticides: carbaryl, fenobucarb, carbofuran, and aldicarb (Chapter 5)
- Antibiotics: amoxicillin, ofloxacin, tetracycline, and cefadroxil (Chapter 6).

The investigations in Chapters 4, 5, and 6 detail redox behaviour in buffered solutions of pH 2–12. A feature of all these chemical systems is that they tend to produce strong fouling of the electrode, where adsorbed films tend to poison the electrode surface. One important aspect of this work is the study of how fouling can be overcome by using *in situ* methods. The literature was searched for information on the suitability of BDD electrodes for these sensing situations in terms of detection limit, reproducibility, and linear range. The extent to which simultaneous and real-world environment detection was also looked into.

An in-depth discussion of literature will be given in each chapter. The thesis concludes with a summary of the results and posits some ideas for future work.

References

[1] R. L. Mccreery, "Advanced carbon electrode materials for molecular electrochemistry," *Chemistry Review*, vol. 108, pp. 2646–2687, 2008, doi: 10.1021/cr068076m.

[2] R. G. Compton, J. S. Foord, and F. Marken, "Electroanalysis at diamond-like and doped-diamond electrodes," *Electroanalysis*, vol. 15, no. 17, pp. 1349–1363, 2003, doi: 10.1002/elan.200302830.

[3] N. Yang *et al.*, "Conductive diamond: synthesis, properties, and electrochemical applications," *Chemical Society Reviews*, 2018, doi: 10.1039/C7CS00757D.

[4] D. J. Bergenstock and J. M. Maskulka, "Diamonds are forever," *Business Horizons*, vol. 44, no. 3. pp. 37–44, 2001. doi: 10.1016/S0007-6813(01)80033-1.

[5] W. G. Schulz, "First diamond synthesis: 50 years later, a murky picture of who deserves credit," *Chemical & Engineering News*, vol. 82, no. 5, pp. 30–31, 2004.

[6] F. P. Bundy, H. T. Hall, H. M. Strong, and R. H. Wentorf, "Man-made diamonds," *Nature*, vol. 176, p. 51, 1955.

[7] D. W. Olson, "Industrial diamond statistics and information," *Mineral commodity summaries*, 2020.

[8] A. J. A. (Bram) Janse, "Global rough diamond production since 1870," *Gems and Gemology*, vol. 43, no. 2, pp. 98–119, 2007, doi: 10.5741/GEMS.43.2.98.

[9] O. Linde and A. Epstein, "The Global Diamond Industry 2019," 2019. doi: 10.1057/9781137537614.

[10] "Diamond's guide historical price graph," *A Star Diamonds*, 2016. https://astardiamonds.com/en/diamond-s-education/information/diamond-s-price-history.html.

[11] "Electrochemistry products E6 eShop." https://e6cvd.com/us/application/electrochemistry/pe-10x10-mm-0-6-mm-thick.html.

[12] "How much does an engagement ring cost?" https://taylorandhart.com/ring-guidance/engagement-ring-cost.

[13] A.-L. de Lavoisier, "Sur la destruction du diamant par le feu," in *Histoire de l'Académie Royale des Sciences. Seconde Partie.*, 1772, pp. 564–616. doi: 10.1484/m.dda-eb.4.2017005.

[14] S. Tennant, *On The Nature of the Diamond*, vol. I. London, 1797.

[15] J. B. Hannay, "On the artificial formation of the diamond," *Proceedings of the Royal Society of London*, vol. 30, pp. 450–461, 1879.

[16] F. P. Bundy, "The P, T phase and reaction diagram for elemental carbon, 1979," *Journal of Geophysical Research*, vol. 85, no. B12, pp. 6930–6936, 1980.

[17] L. F. Dobrzhinetskaya, "Microdiamonds—Frontier of ultrahigh-pressure metamorphism: A review," *Gondwana Research*, vol. 21, no. 1, pp. 207–223, 2012, doi: 10.1016/j.gr.2011.07.014.

[18] H. T. Hall, "Diamond synthesis," US2947608A, 1960

[19] I. V. Popov, A. L. Görne, A. L. Tchougréeff, and R. Dronskowski, "Relative stability of diamond and graphite as seen through bonds and hybridizations," *Physical Chemistry Chemical Physics*, no. 21, pp. 10961–10969, 2019, doi:

10.1039/c8cp07592a.

[20] K. V. Ravi, "Low pressure diamond synthesis for electronic applications," *Materials Science and Engineering B*, vol. 19, no. 3, pp. 203–227, 1993, doi: 10.1016/0921-5107(93)90190-X.

[21] A. E. Fischer, Y. Show, and G. M. Swain, "Electrochemical performance of diamond thin-film electrodes from different commercial sources," *Analytical Chemistry*, vol. 76, no. 9, pp. 2553–2560, 2004, doi: 10.1021/ac035214o.

[22] J. E. Butler and R. L. Woodin, "Thin film diamond growth mechanisms," *Thin Film Diamond*, vol. 342, no. 1664, pp. 15–30, 1994, doi: 10.1007/978-94-011-0725-9_2.

[23] J. V. Macpherson, "A practical guide to using boron doped diamond in electrochemical research," *Physical Chemistry Chemical Physics*, vol. 17, no. 5, pp. 2935–2949, 2015, doi: 10.1039/c4cp04022h.

[24] J. A. Bennett, J. Wang, Y. Show, and G. M. Swain, "Effect of sp[sup 2]-bonded nondiamond carbon impurity on the response of boron-doped polycrystalline diamond thin-film electrodes," *Journal of The Electrochemical Society*, vol. 151, no. 9, p. E306, 2004, doi: 10.1149/1.1780111.

[25] S. Matsumoto, Y. Sato, M. Kamo, and N. Setaka, "Vapor deposition of diamond particles from methane," *Japanese Journal of Applied Physics*, vol. 21, no. 4, pp. L183–L185, 1982.

[26] K. Kurihara, K. Sasaki, M. Kawarada, and N. Koshino, "High-rate synthesis of diamond by DC plasma jet chemical vapor deposition," *Applied Physics Letters*, vol. 52, no. 6, pp. 437–438, 1988, doi: 10.1063/1.99435.

[27] M. Kamo, Y. Sato, S. Matsumoto, and N. Setaka, "Diamond synthesis from gas phase in microwave plasma," *Journal of Crystal Growth*, vol. 62, no. 3, pp. 642–644, 1983, doi: 10.1016/0022-0248(83)90411-6.

[28] D. Scott, "The history and impact of synthetic diamond cutters and diamond enhanced inserts on the oil and gas industry," *Industrial Diamond Review*, vol. 66, no. 1, pp. 48–55, 2006.

[29] W. H. Bragg and W. L. Bragg, "The structure of the diamond," *Nature*, vol. 91, p. 557, 1913.

[30] M. W. Doherty, N. B. Manson, P. Delaney, F. Jelezko, J. Wrachtrup, and L. C. L. Hollenberg, "The nitrogen-vacancy colour centre in diamond," *Physics Reports*, vol. 528, no. 1, pp. 1–45, 2013, doi: 10.1016/j.physrep.2013.02.001.

[31] C. D. Clark, P. J. Dean, and P. V. Harris, "Intrinsic edge absorption in diamond," *Proceedings of the Royal Society of London. Series A, Mathematical and Physical Sciences*, vol. 277, no. 1370, pp. 312–329, 1963.

[32] K. F. Brennan, *The Physics of Semiconductors—with Applications to Optoelectric Devices*. Cambridge: Cambridge University Press, 1999.

[33] J. C. Angus, Y. V. Pleskov, and S. C. Eaton, "Chapter 3 Electrochemistry of diamond," *Semiconductors and Semimetals*, vol. 77, no. C, pp. 97–119, 2004, doi: 10.1016/S0080-8784(04)80015-2.

[34] A. T. Collins and A. W. S. Williams, "The nature of the acceptor centre in semiconducting diamond," *Journal of Physics C: Solid State Physics*, vol. 4, pp. 1789–1800, 1971, doi: 10.1088/0022-3719/1/6/137.

[35] J. P. Lagrange, A. Deneuville, and E. Gheeraert, "Activation energy in low compensated homoepitaxial boron-doped diamond films," *Diamond and Related Materials*, vol. 7, no. 9, pp. 1390–1393, 1998, doi: 10.1016/S0925-9635(98)00225-8.

[36] E. P. Visser, G. J. Bauhuis, G. Janssen, W. Vollenberg, J. P. Van Enckevort, and L. J. Giling, "Electrical conduction in homoepitaxial, boron-doped diamond films," *Journal of Physics: Condensed Matter*, vol. 4, no. 36, pp. 7365–7376, 1992, doi: 10.1088/0953-8984/4/36/011.

[37] W. Gajewski *et al.*, "Electronic and optical properties of boron-doped nanocrystalline diamond films," *Physical Review B—Condensed Matter and Materials Physics*, vol. 79, no. 4, 2009, doi: 10.1103/PhysRevB.79.045206.

[38] S. C. B. Oliveira and A. M. Oliveira-Brett, "Voltammetric and electrochemical impedance spectroscopy characterization of a cathodic and anodic pre-treated boron doped diamond electrode," *Electrochimica Acta*, vol. 55, no. 15, pp. 4599–4605, 2010, doi: 10.1016/j.electacta.2010.03.016.

[39] K. Muzyka, J. Sun, T. H. Fereja, Y. Lan, W. Zhang, and G. Xu, "Boron doped diamond: Current progress and challenges in view of electroanalytical applications," *Analytical Methods*, no. 11, p. 397, 2019, doi: 10.1039/c8ay02197j

[40] E. Vanhove *et al.*, "Stability of H-terminated BDD electrodes: An insight into the influence of the surface preparation," *Physica Status Solidi (A) Applications and Materials Science*, vol. 204, no. 9, pp. 2931–2939, 2007, doi: 10.1002/pssa.200776340.

[41] R. Boukherroub, X. Wallart, S. Szunerits, B. Marcus, P. Bouvier, and M. Mermoux, "Photochemical oxidation of hydrogenated boron-doped diamond surfaces," *Electrochemistry Communications*, vol. 7, no. 9, pp. 937–940, 2005, doi: 10.1016/j.elecom.2005.05.010.

[42] S. A. Grot *et al.*, "The effect of surface treatment on the electrical properties of metal contacts to boron-doped homoepitaxial diamond film," *IEEE Electron Device Letters*, vol. 11, no. 2, pp. 100–102, 1990, doi: 10.1109/55.46942.

[43] A. Louis Allred, "Electronegativity values from thermochemical data," *Journal of Inorganic and Nuclear Chemistry*, vol. 17, no. 1949, pp. 215–221, 1961, doi: 10.1021/jp020500+.

[44] D. Takeuchi *et al.*, "Direct observation of negative electron affinity in hydrogen-terminated diamond surfaces," *Applied Physics Letters*, vol. 86, no. 15, pp. 1–3, 2005, doi: 10.1063/1.1900925.

[45] I. L. Krainsky and V. M. Asnin, "Negative electron affinity mechanism for diamond surfaces," *Applied Physics Letters*, vol. 72, no. 20, pp. 2574–2576, 1998, doi: 10.1063/1.121422.

[46] S. Torrengo, "Surface functionalization and characterization of diamond thin films for sensing applications," PhD Thesis, University of Trento, 2010.

[47] C. E. Nebel, B. Rezek, and A. Zrenner, "Electronic properties of the 2D-hole accumulation layer on hydrogen terminated diamond," *Diamond and Related Materials*, vol. 13, no. 11–12, pp. 2031–2036, 2004, doi: 10.1016/j.diamond.2004.06.028.

[48] M. I. Landstrass and K. V. Ravi, "Resistivity of chemical vapor deposited diamond films," *Applied Physics Letters*, vol. 55, no. 10, pp. 975–977, 1989, doi: 10.1063/1.101694.

[49] C. E. Nebel, "Surface-conducting diamond," *Science*, vol. 318, no. 5855, pp. 1391–1392, 2007, doi: 10.1126/science.1151314.

[50] F. Maier, M. Riedel, B. Mantel, J. Ristein, and L. Ley, "Origin of surface conductivity in diamond," *Physical Review Letters*, vol. 85, no. 16, pp. 3472–3475, 2000, doi: 10.1103/PhysRevLett.85.3472.

[51] J. Ristein, M. Riedel, and L. Ley, "Electrochemical surface transfer doping," *Journal of The Electrochemical Society*, vol. 151, no. 10, p. E315, 2004, doi: 10.1149/1.1785797.

[52] K. Larsson, "Surface chemistry of diamond," in *Novel Aspects of Diamond*, 1st edn, N. Yang, Ed., Springer International Publishing, 2015, pp. 53–83. doi: http://dx.doi.org/10.5772/57353.

[53] V. Chakrapani, J. C. Angus, A. B. Anderson, S. D. Wolter, B. R. Stoner, and G. U. Sumanasekera, "Charge transfer equilibria between diamond and an aqueous oxygen electrochemical redox couple," *Science*, vol. 318, no. 5855, pp. 1424–1430, 2007, doi: 10.1126/science.1148841.

[54] D. Shin, H. Watanabe, and C. E. Nebel, "Redox-couple interactions with undoped single crystalline CVD diamond," *Diamond and Related Materials*, vol. 15, no. 1, pp. 121–128, 2006, doi: 10.1016/j.diamond.2005.08.026.

[55] J. B. Cui, J. Ristein, and L. Ley, "Electron affinity of the bare and hydrogen covered single crystal diamond (111) Surface," *Physical Review Letters*, vol. 81, no. 2, pp. 429–432, 1998, doi: 10.1103/PhysRevLett.81.429.

[56] L. Ostrovskaya, V. Perevertailo, V. Ralchenko, A. Dementjev, and O. Loginova, "Wettability and surface energy of oxidized and hydrogen plasma-treated diamond films," *Diamond and Related Materials*, vol. 11, no. 3–6, pp. 845–850, 2002, doi: 10.1016/S0925-9635(01)00636-7.

[57] E. L. H. Thomas, G. W. Nelson, S. Mandal, J. S. Foord, and O. A. Williams, "Chemical mechanical polishing of thin film diamond," *Carbon*, vol. 68, pp. 473–479, 2014, doi: 10.1016/j.carbon.2013.11.023.

[58] D. Gandini *et al.*, "Electrochemical behaviour of synthetic boron-doped diamond thin films anodes," *New Diamond and Frontier Carbon Technology*, vol. 9, no. 5, pp. 303–316, 1999.

[59] A. F. Sartori *et al.*, "Laser-Induced Periodic Surface Structures (LIPSS) on heavily boron-doped diamond for electrode applications," *ACS Applied Materials and Interfaces*, vol. 10, no. 49, pp. 43236–43251, 2018, doi: 10.1021/acsami.8b15951.

[60] Z. Shpilman, I. Gouzman, E. Grossman, R. Akhvlediani, and A. Hoffman, "Hydrogen plasma and atomic oxygen treatments of diamond: Chemical versus morphological effects," *Applied Physics Letters*, vol. 92, no. 23, 2008, doi: 10.1063/1.2939561.

[61] X. Liu, Y. Y. Chang, S. N. Tkachev, C. R. Bina, and S. D. Jacobsen, "Elastic and mechanical softening in boron-doped diamond," *Scientific Reports*, vol. 7, no. 42921, 2017, doi: 10.1038/srep42921.

[62] G. Williams, J. A. Calvo, F. Faili, J. Dodson, T. Obeloer, and D. J. Twitchen, "Thermal conductivity of electricaly conductive highly boron doped diamond and its applications at high frequencies," in *2018 17th IEEE Intersociety Conference on Thermal and Thermomechanical Phenomena in Electronic Systems (ITherm)*, 2018, pp. 235–239.

[63] P. Zuman, V. Kapetanovic, and M. Aleksic, "Recent developments in electroanalytical chemistry of cephalosporins and cefamycins," *Analytical Letters*, vol. 33, no. 14, pp. 2821–2857, 2000, doi: 10.1080/00032710008543225.

[64] M. Panizza and G. Cerisola, "Application of diamond electrodes to electrochemical processes," *Electrochimica Acta*, vol. 51, no. 2, pp. 191–199, 2005, doi: 10.1016/j.electacta.2005.04.023.

[65] R. Trouillon and D. O'Hare, "Comparison of glassy carbon and boron doped diamond electrodes: Resistance to biofouling," *Electrochimica Acta*, vol. 55, no. 22, pp. 6586–6595, 2010, doi: 10.1016/j.electacta.2010.06.016.

[66] B. C. Lourencao, R. F. Brocenschi, R. A. Medeiros, O. Fatibello-Filho, and R. C. Rocha-Filho, "Analytical applications of electrochemically pretreated boron-doped diamond electrodes," *ChemElectroChem*, vol. 7, no. 6, pp. 1291–1311, 2020, doi: 10.1002/celc.202000050.

[67] G. Hazeill, P. W. May, P. Taylor, A. H. Nobbs, C. C. Welch, and B. Su, "Studies of black silicon and black diamonds as materials for antibacterial surfaces," *Biomaterials Science*, 2018, doi: 10.1039/c8bm00107c.

[68] A. Erdem, "Nanomaterial-based electrochemical DNA sensing strategies," *Talanta*, vol. 74, no. 3, pp. 318–325, 2007, doi: 10.1016/j.talanta.2007.10.012.

[69] A.-M. M. Chiorcea-Paquim, S. C. B. Oliveira, V. C. Diculescu, and A. M. Oliveira-Brett, "Applications of DNA-electrochemical biosensors in cancer research," *Comprehensive Analytical Chemistry*, vol. 77, pp. 237–286, 2017, doi: 10.1016/bs.coac.2017.06.003.

[70] Z. J. Ayres, S. J. Cobb, M. E. Newton, and J. V. Macpherson, "Quinone electrochemistry for the comparative assessment of sp2 surface content of boron doped diamond electrodes," *Electrochemical Communications*, vol. 72, pp. 59–63, 2016, doi: 10.1016/j.elecom.2016.08.024.

[71] F. Picollo *et al.*, "Development and characterization of a diamond-insulated graphitic multi electrode array realized with ion beam lithography," *Sensors*, vol. 15, no. 1, pp. 515–528, 2015, doi: 10.3390/s150100515.

[72] X. Cai, E. E. L. Tanner, C. Lin, K. Ngamchuea, J. S. Foord, and R. G. Compton, "The mechanism of electrochemical reduction of hydrogen peroxide on silver nanoparticles," *Physical Chemistry Chemical Physics*, vol. 20, no. 3, pp. 1608–1614, 2018, doi: 10.1039/c7cp07492a.

[73] L. Hutton, M. E. Newton, P. R. Unwin, and J. V. Macpherson, "Amperometric oxygen sensor based on a platinum nanoparticle-modified polycrystalline boron doped diamond disk electrode," *Analytical Chemistry*, vol. 81, no. 3, pp. 1023–1032, 2009, doi: 10.1021/ac8020906.

[74] M. Behúl *et al.*, "Nanostructured boron doped diamond enhancing the photoelectrochemical performance of TiO_2/BDD heterojunction anodes," *Vacuum*,

vol. 171, no. 109006, 2020, doi: 10.1016/j.vacuum.2019.109006.

[75] J. Svanberg-Larsson *et al.*, "A comparison of explicitly-terminated diamond electrodes decorated with gold nanoparticles," *Electroanalysis*, vol. 28, no. 1, pp. 88–95, 2016, doi: 10.1002/elan.201500442.

[76] J. Svítková, T. Ignat, Ľ. Švorc, J. Labuda, and J. Barek, "Chemical modification of boron-doped diamond electrodes for applications to biosensors and biosensing," *Critical Reviews in Analytical Chemistry*, vol. 46, no. 3, pp. 248–256, 2016, doi: 10.1080/10408347.2015.1082125.

[77] J. E. Kellon, S. L. Young, and J. E. Hutchison, "Engineering the nanoparticle–electrode interface," *Chemistry of Materials*, vol. 31, no. 8, pp. 2685–2701, 2019, doi: 10.1021/acs.chemmater.8b04977.

[78] J. M. Freitas, T. da C. Oliveira, R. A. A. Munoz, and E. M. Richter, "Boron doped diamond electrodes in flow-based systems," *Frontiers in Chemistry*, vol. 7, no. April, 2019, doi: 10.3389/fchem.2019.00190.

[79] J. Xu and G. M. Swain, "Oxidation of azide anion at boron-doped diamond thin-film electrodes," *Analytical Chemistry*, vol. 70, no. 8, pp. 1502–1510, 1998, doi: 10.1021/ac970959d.

[80] Y. Einaga, J. S. Foord, and G. M. Swain, "Diamond electrodes: diversity and maturity," *MRS Bulletin*, vol. 39, no. 06, pp. 525–532, 2014, doi: 10.1557/mrs.2014.94.

[81] G. W. Muna, N. Tasheva, and G. M. Swain, "Electro-oxidation and amperometric detection of chlorinated phenols at boron-doped diamond electrodes: A comparison of microcrystalline and nanocrystalline thin films," *Environmental Science and Technology*, vol. 38, no. 13, pp. 3674–3682, 2004, doi: 10.1021/es034656e.

[82] C. E. Banks, A. S. Yashina, G. J. Tustin, V. G. H. Lafitte, T. G. J. Jones, and N. S. Lawrence, "Exploring alkylated ferrocene sulfonates as electrocatalysts for sulfide detection," *Electroanalysis*, vol. 19, no. 24, pp. 2518–2522, 2007, doi: 10.1002/elan.200704009.

[83] L. Jiang, T. G. J. Jones, O. C. Mullins, and X. Wu, "Hydrogen sulfide detection method and apparatus," US 2003/0134426A1, 2003

[84] K. Mielech-Łukasiewicz and B. Starczewska, "The use of boron-doped diamond electrode for the determination of selected biocides in water samples," *Water*, vol. 11, no. 8, p. 1595, 2019, doi: 10.3390/w11081595.

[85] P. V. Nidheesh, G. Divyapriya, N. Oturan, C. Trellu, and M. A. Oturan, "Environmental applications of boron-doped diamond electrodes: 1. Applications in water and wastewater treatment," *ChemElectroChem*, vol. 6, no. 8, pp. 2124–2142, 2019, doi: 10.1002/celc.201801876.

Chapter 2

Theory and techniques

The work described in this thesis relies on the application of experimental techniques that are well established in the literature. This chapter provides an overview of the fundamental principles of electrochemical theory and discusses nuances in the electrochemical techniques employed. The bulk of the work was electrochemistry; two physical techniques for probing the surface were also used—X-ray photoelectron spectroscopy and scanning electron microscopy—and their theories and functions are also introduced.

2.1 Electrochemical theory

Electrochemistry is concerned with the study of charge-transfer processes, normally at solid–liquid interfaces. Electrochemical methods allow observations to be made on the conditions and rates of occurrence of these perturbations to the species of interest, both qualitatively and quantitatively. There are several principles which regulate this charge-transfer process, such as chemical equilibrium, mass transfer of analyte species, and applied potential differences. Each of these factors is governed by fundamental theory, which is explained below to the level relevant to its application in this work.

2.1.1 Electrode potentials at equilibrium

A metal, or similarly conductive material, if placed in a solution of ions, such as Fe^{2+} and Fe^{3+}, can act as a source or sink of a tiny number of electrons. The movement of electrons qualifies the material as an electrode, such that an equilibrium may exist at its surface:

$$\mathrm{Fe}^{3+}_{(aq)} + \mathrm{e}^{-}_{(s)} \rightleftharpoons \mathrm{Fe}^{2+}_{(aq)} . \qquad (2.1)$$

The transfer of electrons between the electrode and the solution of ions is governed by the physical processes of maintaining energy continuity across an interface. The electrons in a metal are free to move throughout the metal in an 'electron sea'. Energetically, this can be described as 'bands' in which an effective continuum of energy levels is available. These are filled up to an energy maximum known as the Fermi level, E_F, which depends on the material. The electrons in the Fe ions, on the other hand, are localised and restricted to discrete energy levels. Electrons move from a higher to a lower energy state (Figure 2.1). As electron transfer proceeds, the ionic energy levels and E_F move towards each other and annul the driving force for further transfer but leaving a charged solution and electrode [1].

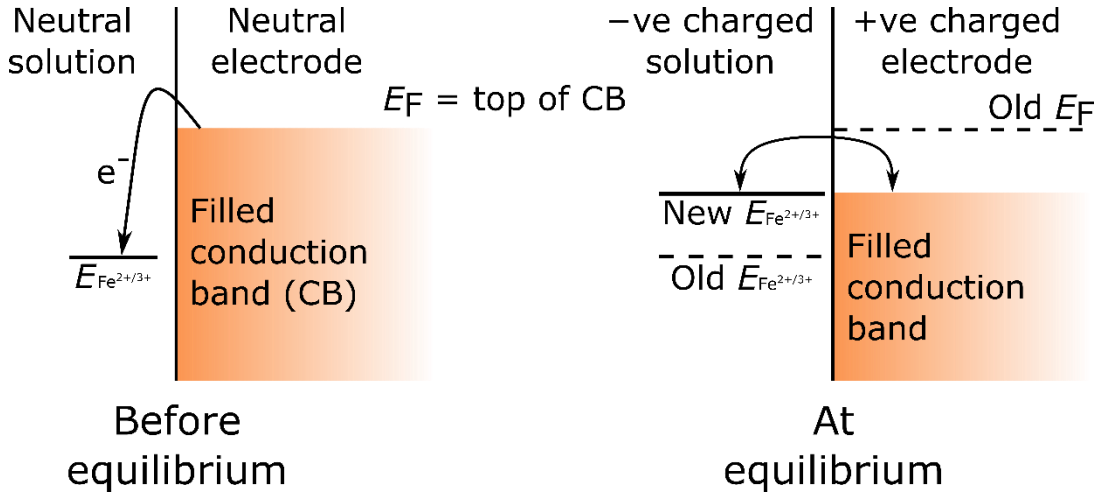


Figure 2.1 The energy of electrons in ions in solution and in a conductive material.

The rate at which this oxidation process occurs depends on the potential at the electrode, when the system is at equilibrium, namely when no net current is flowing. This equilibrium potential is described by the Nernst equation:

$$E_{eq} = E^0 + \frac{RT}{nF} \ln \frac{a_A}{a_B}, \tag{2.2}$$

where E_{eq} is the equilibrium potential, E^0 is the standard electrode potential of the electrochemical reaction, a_A and a_B are the activities of the reactant and product species respectively, R is the gas constant (8.314 J K^{-1} mol^{-1}), T is the absolute temperature, n is the number electrons transferred, and F is the Faraday constant (96,485.3 C mol^{-1}). The

concept of activity is introduced because, strictly speaking, the solutions are generally non-ideal. Activity is the effective concentration that an electrode samples. Activity and concentration are related via the activity coefficient, such that $a_A = \gamma_A \times [A]$. For solutions below approximately 0.01 M, one can assume the electrolyte to be fully dissociated, and concentrations can approximately represent activities [2]. So, regardless of the favoured direction of reaction 2.1, at equilibrium there will exist a potential difference between the electrode and the solution:

$$\Delta\phi_{e/s} = \phi_e - \phi_s = \text{constant} + \frac{RT}{nF}\ln\frac{[\text{reactant}]}{[\text{product}]} = \text{constant} + \frac{RT}{F}\ln\frac{[Fe^{3+}]}{[Fe^{2+}]}, \qquad (2.3)$$

where ϕ denotes electrical potential, ϕ_e is the potential of the electrode, ϕ_s is the potential of the solution phase.

2.1.2 Practical measurement of potential

Practically, a minimum of two electrodes is required to measure a potential difference in a complete circuit. However, in a two-electrode cell, the only measurable quantity is the potential difference between the two electrodes, not the changes which may happen at one alone. Figure 2.2 shows how the potential difference between two metals A and B can be referred against the solution potential, ϕ_s. The solution contains equal concentrations of oxidised and reduced forms of an analyte, to demonstrate chemical equilibrium.

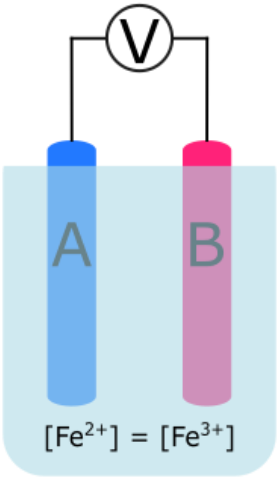


Figure 2.2 Two-electrode set-up, where measured potential = $(\phi_{\text{metal A}} - \phi_s) - (\phi_{\text{metal B}} - \phi_s)$.

Suppose that the potential at one of the electrodes can be 'fixed' ($\phi_{reference}$); then the changes which happen at the other (ϕ_{test}) can always be referred to that level, such that

$$\text{measured potential} = (\phi_{test} - \phi_s) - (\phi_{reference} - \phi_s). \quad (2.4)$$

Suppose again that this reference electrode (REF) operates in such a way that $\phi_{reference} - \phi_s$ is constant; then any changes in $\phi_{test} - \phi_s$ will appear directly as changes in the measured potential. To do this, a third electrode is added, shown in Figure 2.3.

In this three-electrode configuration, the potentiostat works to set up a high impedance across the working electrode (WE) and the REF to measure the potential difference between the two and minimises the current drawn through the latter. To measure the current flow through the WE, a counter electrode (CE) is added to complete the circuit. Now, if a potential more positive than E_{eq} (equation 2.2) is applied to the electrode, species A oxidise to B, and electrons will flow into the WE, and it is measured as a positive current.

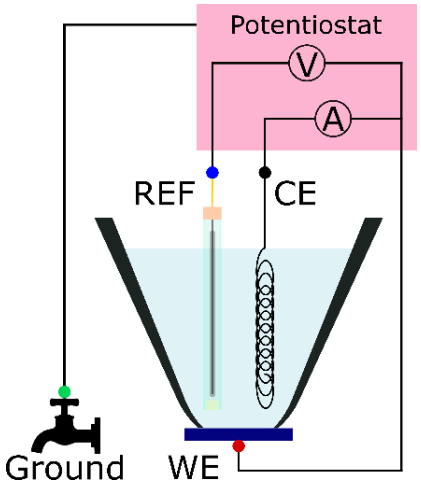


Figure 2.3 A three-electrode set-up similar to that used in the present work.

A variety of materials may be used for the REF depending on experimental requirements. The standard hydrogen electrode (SHE)[1] is the one against which all other electrode potentials are compared. One common REF is a silver wire coated in silver

[1] Practically, the SHE comprises 1 atm of hydrogen gas flowing over a platinised platinum electrode, submerged in an HCl solution of unit activity (1.18 M) at 25 °C, which results in an absolute electrode potential of 4.44 ± 0.02 V.

chloride (Ag|AgCl) submerged in a potassium chloride solution that is highly concentrated. At the wire surface, an equilibrium exists:

$$AgCl_{(s)} + e^-_{(metal)} \rightleftharpoons Ag_{(metal)} + Cl^-_{(aq)}, \quad (2.5)$$

where the rate of dissolution of Ag metal and combining with Cl^- to make AgCl is matched with that of the deposition of the Ag^+ ions as Ag metal. This means that the electrode potential is only dependent on the chloride concentration, which can be relatively stable:

$$\phi_{\text{reference}} - \phi_s = \Delta\phi + \frac{RT}{F}\ln\frac{1}{[Cl^-]}. \quad (2.6)$$

This potential-determining equilibrium is stable as long as the current passing through the REF is below the threshold which would change its internal composition. This could happen when significant amounts of AgCl no longer remain in contact with the silver wire, or if the chloride concentration deviates significantly through poor frit-fitting, as the concentration of chloride ions has a logarithmic effect on the REF potential. Also, temperature affects the Nernst potential linearly, where RT/F is 25.3 mV at 22℃, and 25.7 mV at 25℃, so temperature fluctuations during measurement should be avoided.

2.1.3 Non-equilibrium processes

The previous sections were concerned with equilibrium electrochemistry, and the following sections deal with dynamic electrochemistry, where electrochemical cells operate at non-equilibrium and current is flowing. The net flow of charge is classified as either galvanic or electrolytic; the former is spontaneous ($\Delta G < 0$), while the latter requires an externally applied potential ($\Delta G > 0$), where ΔG is the change in Gibbs energy for the reaction. The first known battery, with layers of zinc and copper, relied on their natural differences in reactivity and generated galvanic current flow. Analytical electrochemistry is concerned with electrolytic electron flow.

For an electron-transfer reaction to occur, it is necessary for the electroactive species to be within molecular distances (1–3 nm) of the electrode surface. As high conductivity is

usually a prerequisite for a material to be made into an electrode, the movement of electrons to and from the interface within the electrode seldom limits the rate of reaction. Thus, a simple electrode reaction (Figure 2.4) must involve at least three steps:

(1) The arrival of reactants to the electrode surface

(2) The transfer of charge across the electrode–solution interface

(3) The removal of products from the surface.

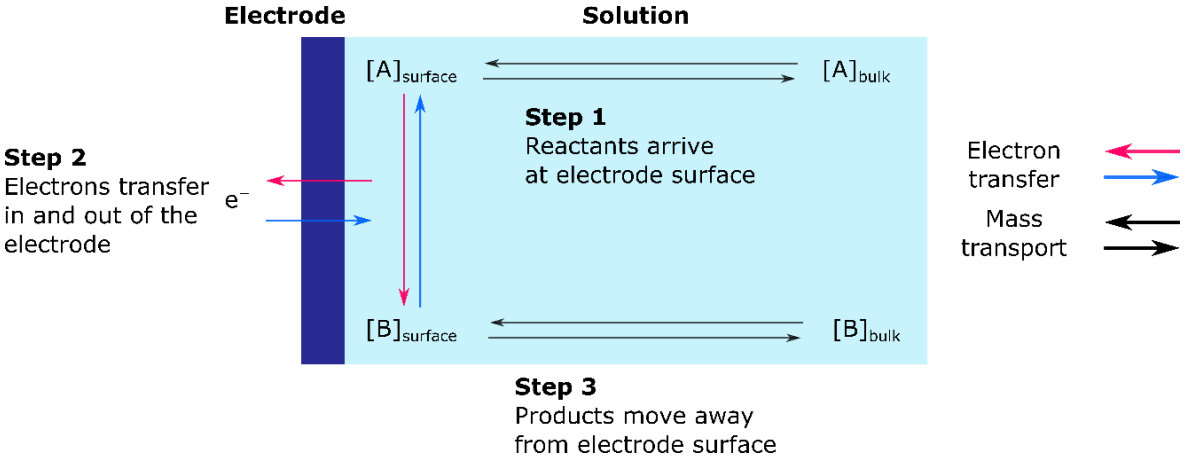


Figure 2.4 At least three steps are required for electron transfer at an electrode.

The overall rate of electrode reaction will be determined by the slowest of these steps. A particular reaction might therefore be limited either by the electron-transfer kinetics (step 2) or by the rate at which material is carried to and from the electrode (steps 1 and 3). In addition to this, more-complex electrode reactions or chemical processes can occur at the surface both preceding and following the main electron-transfer event (such as the post-electrolysis adsorption which Chapter 3 details).

2.1.4 Measurement of current at non-equilibrium

Current flow is the exchange of electrons between the electrode surface and the analyte in solution. However, practically, the recorded current arises from sources other than the reaction of interest. All sources of current are split into faradaic and non-faradaic processes; the latter describes where electrons do not cross the solid–electrolyte interface; the distinction between the two becomes relevant when an external potential is applied.

For all materials in solution, a separation of charge occurs over time naturally, or quickly if a voltage is applied, resulting in the formation of a double layer, as in Figure 2.5. When ions lose their solvation at the inner Helmholtz plane (IHP), they adsorb onto the electrode surface, and solvated molecules 'close' to the electrode surface define the outer Helmholtz plane (OHP). The diffuse layer beyond the OHP is also referred to as 'bulk'. The separated planes comprise different amounts of ions, and thus different amounts of charge, and behave similarly to a capacitor. For dynamic electrochemistry, charging of this 'capacitor' is a non-faradaic process and is a component of the total current.

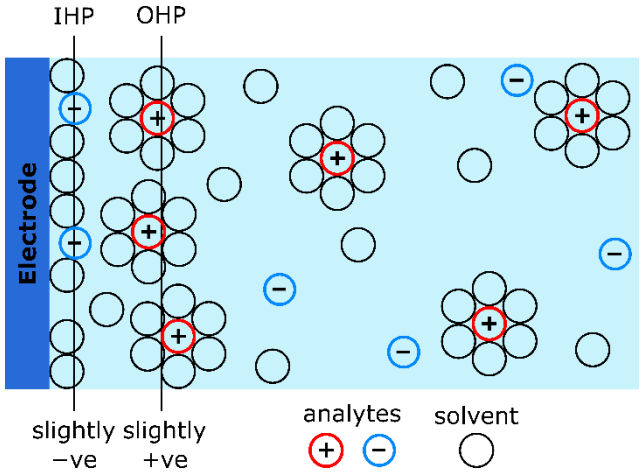


Figure 2.5 The arrangement of solvated and partially solvated ions at the electrode.

The structure of the electric double layer can also affect the electrode kinetics, relevant for when electroactive species are described as 'inner-sphere' or 'outer-sphere'. Ruthenium hexamine chloride is an example of an often used outer-sphere redox couple, as it can exchange electrons even when it only approaches the electrode surface as far as the OHP, so relatively is less affected by the surface structure. The electric double-layer structure can also be significantly affected by adsorption.

Measured background currents comprise non-faradaic currents related to capacitive charging and from interfering electrochemical couples that are active at that potential. The background electrolytes are heavily involved: in particular the movement of electrolyte ions, reorientation of the solvent dipoles, and electrostatic double-layer charging. During

electrochemical measurements, these currents tend to be short-lived and vary hugely depending on the electrode material and surface characteristics (Section 1.1.4).

Faradaic currents mark the passage of electrons that cause oxidation or reduction, where the number of chemical reactions is proportional to the amount of electricity passed:

$$Q = nFm, \tag{2.7}$$

where Q is the total charge exchanged, n is the number of electrons involved in the reaction, F is the Faraday constant, and m is the number of moles of reactants consumed. Taking the derivative with respect to time gives the current i:

$$i = \frac{\mathrm{d}Q}{\mathrm{d}t} = nF\frac{\mathrm{d}m}{\mathrm{d}t}. \tag{2.8}$$

Electron transfer consumes or generates an electroactive species at the surface and creates a concentration gradient perpendicular to the surface. As a result, a flux of electroactive species is set up via diffusion between the solution near the electrode and in the bulk. The current generated is directly proportional to the flux (j, Section 2.1.6), the number of electrons transferred (n), and the area of the electrode (A):

$$i = nFAj. \tag{2.9}$$

2.1.5 Electrode kinetics

Two main factors affect the electrolytic current: electrode kinetics and mass transport. The Butler–Volmer (B–V) model is a simple interpretation of electrode kinetics, where it is often described as ‘fast’ or ‘slow’ in relation to the rate of mass transport to the electrode. To induce current flow, the applied potential E must be larger than the equilibrium potential E_{eq}. The difference $\eta = E - E_{\mathrm{eq}}$ between these potentials is called the overpotential and is a measure of the reversibility of the redox process [3]. Figure 2.6 shows the basic reaction profile according to transition-state theory.

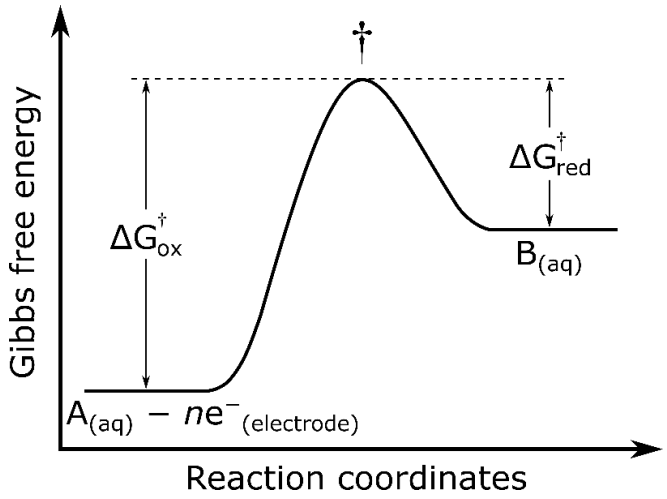


Figure 2.6 Reaction profile for oxidation at equilibrium, where † is the transition state.

The activation barrier height $\Delta G^{\dagger}$ depends on two things: the first is the difference in potential between A and B, while the second is the energy required to rearrange the reactants to get the transition state, and this energy is potential dependent. The transfer coefficient α describes the extent to which the barrier is modified by the potential.

When the reaction in equation 2.3 is driven by η, the flux j of molecules to the electrode surface will be proportional to the heterogeneous rate constant k of electron transfer:

$$j_{\mathrm{ox}} = k_{\mathrm{ox}}[\mathrm{A}]_0, \qquad j_{\mathrm{red}} = k_{\mathrm{red}}[\mathrm{B}]_0, \tag{2.10}$$

where k_{ox} (k_{red}) is the heterogeneous rate constant of electron transfer for the oxidation (reduction) and $[\mathrm{A}]_0$ ($[\mathrm{B}]_0$) is the concentration of the reagent at the surface of the electrode. At equilibrium, reduction also happens, and an analogous equation is incorporated into the expression for the net current:

$$i_{\mathrm{net}} = i_{\mathrm{ox}} - i_{\mathrm{red}} = FAk_{\mathrm{ox}}[\mathrm{A}]_0 - FAk_{\mathrm{red}}[\mathrm{B}]_0. \tag{2.11}$$

To a good approximation, electrochemical electron transfers can be treated as chemical electron transfers, and therefore be described by the Arrhenius equation:

$$k_{\mathrm{ox}} = P_{\mathrm{ox}}\exp\frac{-\Delta G_{\mathrm{ox}}^{\dagger}}{RT}, \qquad k_{\mathrm{red}} = P_{\mathrm{red}}\exp\frac{-\Delta G_{\mathrm{red}}^{\dagger}}{RT}, \tag{2.12}$$

where $\Delta G_{\mathrm{ox}}^{\dagger}$ is the Gibbs free energy of activation, and P is the 'frequency factor' that accounts for the rate of collision between the reagent molecules and the electrode, which

has the same dimensions as k (measured in cm s^{-1}). Since $\Delta G_{ox}^{\dagger}$ depends on the potential difference between the electrode and the electrolyte, equation 2.13 can be rewritten for the oxidation and reduction reactions in terms of η and to include α:

$$k_{ox} = k^0 \exp\frac{-\alpha F\eta}{RT}, \qquad k_{red} = k^0 \exp\frac{(1-\alpha)F\eta}{RT}, \tag{2.13}$$

where k^0 is the standard electrochemical rate constant, and α is a dimensionless transfer coefficient that reflects the sensitivity of the transition state to the change of η, which is typically close to 0.5 while always satisfying $0 < \alpha < 1$. The expression for the net current can thus be written

$$i_{net} = i_0 \left(\frac{[A]_0}{[A]_{bulk}} \exp\frac{-\alpha F\eta}{RT} - \frac{[B]_0}{[B]_{bulk}} \exp\frac{(1-\alpha)F\eta}{RT} \right), \tag{2.14}$$

where $i_0 = nFAk^0[A]_{bulk}^{\alpha}[B]_{bulk}^{1-\alpha}$ is the *standard exchange current*. Equation 2.14 is the extended B–V equation. Written in this form, several inferences can be easily seen. First, when the overpotential η is zero, then $[A]_0/[A]_{bulk} = [B]_0/[B]_{bulk}$ and no current will flow. Second, the net current is proportional to the standard exchange current. Remembering equations 2.10 to 2.13, if the value of k^0 is large, there will be greater flux of species diffusing towards the surface, such that even a small η will produce a large current. This is the mark of reversible electrochemistry, where the consumption of the reagent happens much faster than the rate at which diffusion is supplying it; hence we say that the electrode kinetics are 'fast' [3]. Practically, we are often dealing with quasi-reversible redox reactions, where the current responses are similar to that of the reversible reactions, but the overpotentials required are significantly larger.

2.1.6 Mass transport

Referring to Figure 2.5, when the electrode kinetics are sufficiently fast (step 2), the reaction rate will be largely controlled by the transport of material to and from the electrode surface (steps 1 and 3). There are three modes of mass transfer: diffusion, convection, and

migration. These movements are driven by differentials in concentration, temperature, and electric potential, respectively. Experimentally we try to control all three modes by having a constant bulk concentration and solution temperature, and sufficient background electrolyte to set up shielding around the electrode to prevent ionic migration.

Diffusion

A concentration gradient always drives the movement of the analyte to minimise the difference. For the case of linear diffusion to an infinite planar surface, Fick showed that the number of moles of material diffusing through a unit area in one second—the diffusional flux *j*—for a species A is given by [4]

$$j_{\mathrm{A}} = -D_{\mathrm{A}} \frac{\partial [\mathrm{A}]}{\partial x}, \tag{2.15}$$

where [A] is the concentration of species A, D_{A} is a constant of proportionality known as the diffusion coefficient which is characteristic of the diffusing species, and *x* is a measure of distance in the direction of diffusion. The variation of concentration at a point as a function of time is given by

$$\frac{\partial [\mathrm{A}]}{\partial t} = D_{\mathrm{A}} \left(\frac{\partial^2 [\mathrm{A}]}{\partial x^2} + \frac{\partial^2 [\mathrm{A}]}{\partial y^2} + \frac{\partial^2 [\mathrm{A}]}{\partial z^2} \right) \tag{2.16}$$

in three dimensions. By considering the arrival of a particle at an infinitely large plane, so that we need only be concerned with the *x* component and ignore edge effects, this equation can be simplified into only one dimension. Solutions to the above two equations (2.15, 2.16), Fick's first and second law, with appropriate boundary conditions, provide much of the analytical basis for diffusion-limited electrochemistry.

The diffusion coefficient provides a measure of the mobility of a molecule in a solvent over a certain time. The root-mean-squared displacement in the direction of the *x*-axis, in time *t*, is related to *D* via a simple yet significant equation in voltammetry [5]:

$$\lambda_x = \sqrt{\langle x^2 \rangle} = \sqrt{2Dt}. \tag{2.17}$$

A rule of thumb is: the bigger the molecule the smaller the diffusion coefficient, and the less distance it moves [3]. The value of D is important in electrochemistry, as the accuracy of concentration measurements depends on it. It is strongly temperature-sensitive which means that experiments should ideally be thermostatically controlled.

Here, it is also useful to introduce the Nernst diffusion layer, of thickness δ. Within this distance, diffusional transport is operative, and beyond it, the solution is well mixed and the concentration is maintained at a constant bulk value by natural convection. Of course, there is some gradation between the diffusion layer and bulk; but the Nernst model provides satisfactorily accurate results. The diffusion coefficient is also related to δ by the mass-transport coefficient m_T:

$$m_T = \frac{D}{\delta}. \tag{2.18}$$

Another way to think of the reversibility of voltammetry is via m_T (k^0 and m_T have the same unit, conventionally cm/s): reversible cases correspond to $k^0 \gg m_T$, irreversible cases to $k^0 \ll m_T$, and quasi-reversible cases to $k^0 \approx m_T$.

Convection

Convection is the concerted movement of a fluid as a result of external forces arising naturally from variation in density (typically resulting from heat) and gravity or applied externally by actions such as stirring. Natural convection arises when the electrode or the solution are at different temperatures, or some chemical reaction causes a local environment to gain or lose energy. Natural convection is generally irreproducible and thus undesirable in experiments. Its effects can be minimised by reducing the time of the procedure, or by including a thermostat to an enclosed set-up.

Generally, methods that rely on forced convection use it to provide a fresh supply of reactants to the electrode surface, so that it becomes the dominant mode of mass transport in that situation. The most common method uses rotating disk electrodes.

Migration

The potential drop across the electrode/electrolyte interface exerts an electrostatic force on ions in the region, an effect that becomes more pronounced at applied potentials further away from the equilibrium. This electric field forces ions to migrate in addition to the diffusion-related movements, which complicates the interpretation of experimental data.

To mitigate the effects from migration, a chemically and electrochemically inert 'background electrolyte' is usually added to the solution at high concentrations, commonly around or in excess of 0.1 M (Section 2.1.7). This provides several important advantages. First, the large number of ions provides solution conductivity. Second, the high levels of this supporting electrolyte significantly decrease the distance over which the electric potential drops from its value in the electrode (ϕ_e) to that in bulk solution (ϕ_s). The absence of potential gradients outside the narrow interfacial region prevents ion migration. Third, the activity coefficients of the reactants and products, which are influenced by ionic strength, stay constant, because the high concentration of background electrolyte maintains the ionic strength of the solution during electrolysis.

The combination of the three mass-transfer modes introduces complexity in the interpretation of experimental data owing to some undesirable effects. In the experimental work described by this thesis, the effects of convection are minimised by conducting experiments under still conditions (no stirring), with appropriately concentrated supporting electrolytes. This means that the mass-transport effects arise predominantly from diffusion.

2.1.7 Supporting electrolyte

To prevent migration, the number of ions in the supporting electrolyte should be able to provide sufficient electrostatic shielding as well as improve solution conductivity. As pH can also play an important role in redox reactions, buffers are often used as the supporting electrolyte. Three types of buffer were used in the present work: 0.1 M sodium phosphate

(Chapter 3), 0.1 M sodium acetate (Chapter 4), and 0.2 M universal Carmody (Chapters 4, 5, and 6). The choice of buffer in each project was informed by literature review and experimentation. Especially in Chapter 4 regarding Carmody buffer, at first the pH was set at 4.00, and then it was gradually expanded to a wider range. Very often, the protocols of published research are closely followed to allow faithful reproduction and building up of the work, and the right buffer tends to play an invisible role. But by experimenting with different buffers, we can widen the scope of the research.

Carmody buffer is a wide-range buffer that is prepared with boric acid, citric acid, and trisodium phosphate in only two stock solutions, to a precision of ± 0.05 pH units. Using this universal buffer meant the chemical constituents of the background electrolyte could be constant across all pHs, so if interfering reactions between the background and analyte should happen, they would form a consistent 'noise'.

Milli-Q water (Millipore Corp.) with a resistivity of 18.2 MΩ cm was used for all aqueous solutions and preparations. The pH was measured using a glass-bulb pH meter (SevenEasy, Mettler Toledo), which was calibrated by a three-point calibration (pH 4.00, 7.00, 10.00) before each measurement.

2.1.8 Dynamic electrochemical methods

Numerous electrochemical methods have been designed to measure quantitatively the parameters affected by, or in control of, the electron-transfer process. This section provides a brief overview of the electrochemistry relevant to the methods used in this thesis.

Chronoamperometry

Measuring current over time is the basis of chronoamperometry. The starting potential is chosen to be at some value (E_1) where no faradaic processes occur, to one (E_2) which can oxidise the analyte species at near the electrode. Figure 2.7A gives the applied potential profile, and the Cottrell equation describes the subsequent current decay behaviour:

$$i = nFA[\mathrm{A}]_{\mathrm{bulk}}\sqrt{\frac{D}{\pi t}}, \tag{2.19}$$

where n, F, A, and D have their usual meanings, $[\mathrm{A}]_{\mathrm{bulk}}$ is the concentration of the analyte in the bulk solution, and t is the time passed from the moment the potential is stepped. As in Figure 2.7B, before the step, i_1 is zero (or very low, akin to background) current; then as the potential is stepped, the current spikes to i_2 due to the initial electrolysis of species at the electrode surface, followed by the time-dependent decay due to diffusion.

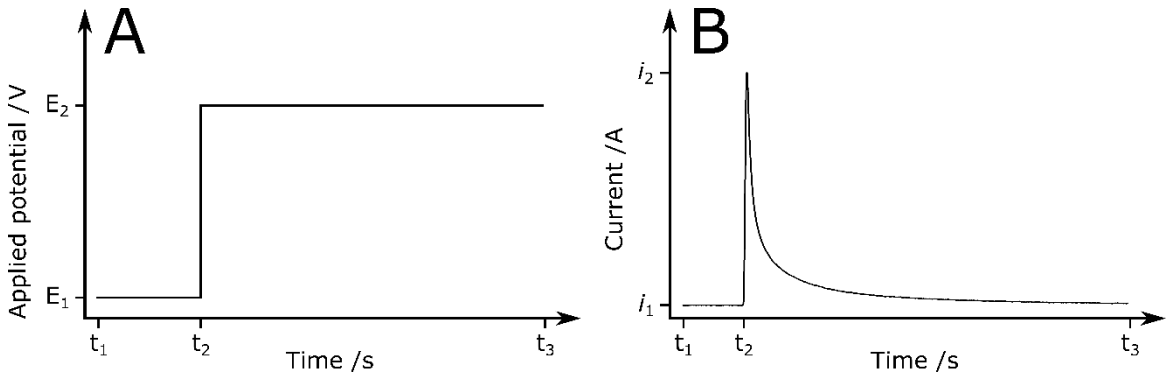


Figure 2.7 (A) The applied potential in chronoamperometry and (B) the response.

The rate at which current decays for stationary electrodes and for quiescent solutions is limited by the rate of diffusion of the reagent to the electrode. The correlation between i and $\sqrt{t}$ tends to deviate from the Cottrell equation after ~100 s due to convection effects. It can be seen from Figure 2.8 that the diffusion layer, the zone near the electrode where concentrations differ from those of the bulk, has no definite thickness.

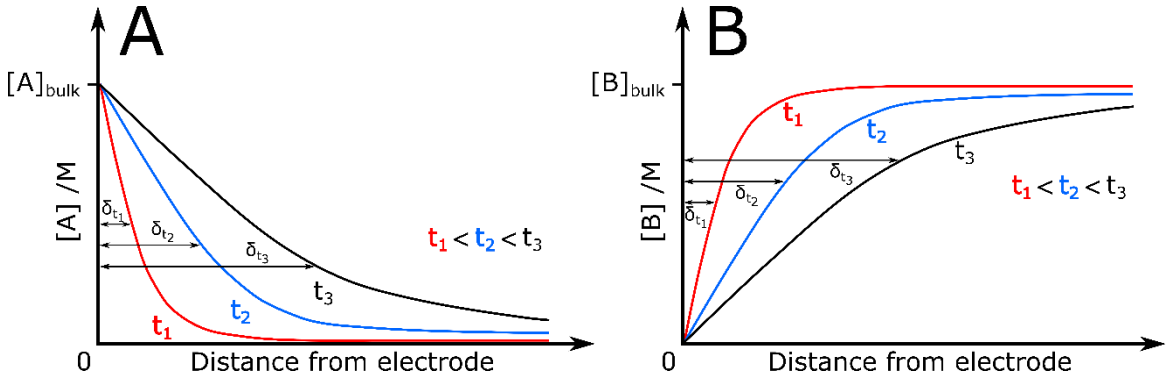


Figure 2.8 Concentration profiles of A and B after the oxidation potential is stepped.

The concentration profiles approach their bulk values asymptotically, until sufficient time has passed and the gradient within δ of the electrode surface becomes linear. As shown in Figure 2.8A,B, the layer thickness δ increases as time of experiment increases. It is useful to think about this thickness in terms of $\sqrt{Dt}$, a unit of length which characterises the distance that a species can diffuse in time *t*, according to equation 2.8. The diffusion layer is completely contained within a distance of $6\sqrt{Dt}$ from the electrode; at distances much greater than this diffusion-layer thickness, the electrode has no appreciable effect on concentration, and the reactant molecules there have no access to the electrode [6]. For example, for a species with a diffusion coefficient of 1×10^{-5} cm^2 s^{-1}, the distance $\sqrt{Dt}$ is about 30 μm for an experimental time of 1 s, but only 1 μm at 1 ms.

Cyclic voltammetry

As the name suggests, in this technique the voltage is swept back and forth cyclically. The rate at which the potential is scanned affects the magnitude of the currents collected. An illustrative potential profile over time and the current response, with respect to the potential—a cyclic voltammogram (CV)—are shown in Figure 2.9.

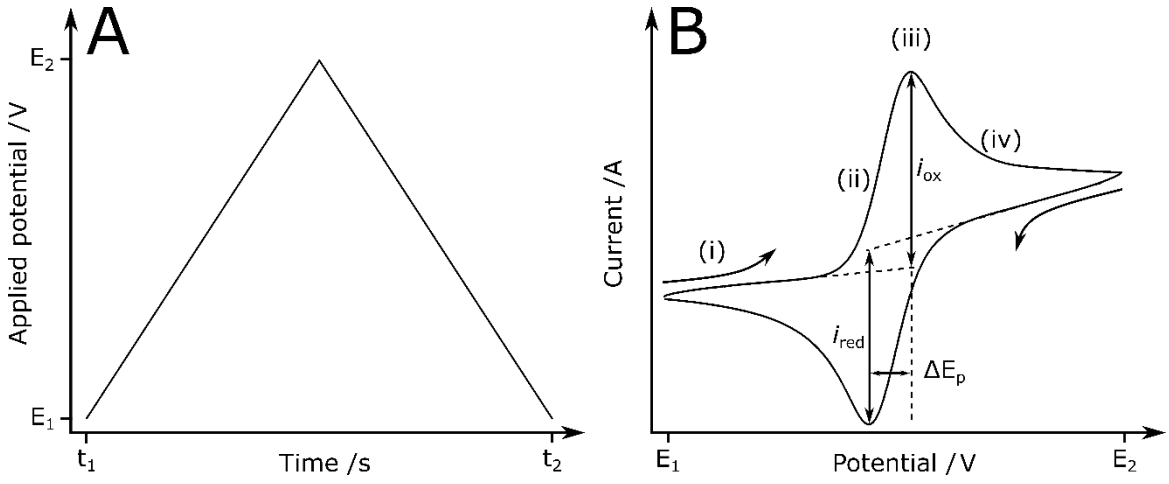


Figure 2.9 Examples of (A) the applied potential for (B) a cyclic voltammogram.

Let us consider the Reaction 2.3 where a species A loses $n = 1$ electron and gets oxidised to species B. Just taking the forward sweep, where the potential moves from E_1 to E_2, a

cyclic voltammogram (CV) goes through four distinct phases:

(i) At E_1, no current flows, since the electrode is insufficiently positive to oxidise A.

(ii) The current increases in proportion to the increasing potential, first exponentially and then linearly.

(iii) As the potential continues to increase, the diffusion layer also constantly expands, so that, once the electrode potential has reached a value at which the surface concentration of A is close to zero, the current reaches a maximum.

(iv) The current decays approximately in proportion to $1/\sqrt{t}$, as in the Cottrell equation.

In a solution where $[A]_{bulk} = [B]_{bulk}$, if the anodic sweep is stopped and the current is allowed to decay to zero, the backward cathodic sweep of the voltammogram would be similar in shape to the anodic one, just reflected in the *x*-axis. Herein lies the experience of the experimenter in choosing E_2 to allow sufficient depletion of A at the surface, so that in the backward scan the solution should appear to the electrode to consist only of B.

As the voltammogram is swept from E_1 to E_2, the thickness of the diffusion layer increases and, the longer the time taken to scan the voltammogram, the thicker the diffusion layer. Fick's first law tells us that, the thinner the diffusion layer, the greater the flux for a fixed concentration drop. This means that, at faster scan rates, the diffusion layer is thinner, causing greater flux and higher currents. However, if the voltammetry is undertaken at sufficiently fast scan rates, all reactions tend towards the irreversible, as the rate of mass transport outcompetes electrode kinetics. For a reversible process at 25°C, the change in peak current, i_p, with respect to scan rate is governed by the Randles–Sevčik (R–S) equation

$$i_p = 0.446nFA[A]_{bulk}\sqrt{\frac{nFDv}{RT}} = 2.69 \times 10^5 nA[A]_{bulk}\sqrt{nDv}, \qquad (2.20)$$

where *n*, *F*, *D*, *R*, *T*, and *A* have their usual meanings, *v* is the scan rate, and α is the transfer coefficient in Butler–Volmer kinetics. The peak currents are determined by the number of

electrons transferred per reaction event and is proportional to the concentration of the analyte. Common causes for weak or invisible peaks on the reverse scan could be slow electron-transfer rates or the presence of a subsequent chemical step that consumes the products of the electrochemical reaction. The peak separation of the CV is dependent on the electron-transfer kinetics between the electrode and the analyte, the placement of E_2, the temperature, and the scan rate.

In real CVs, the faradaic response is superimposed on an approximately constant, non-faradaic, charging current. The measurement of peak currents in CV is imprecise because the correction for charging current is typically uncertain, and even more so for the peak in the back scan. Consequently, CV is not an ideal method for quantitative evaluation of system properties that must be derived from peak heights, such as the concentration of an electroactive species, or the rate constant of a coupled homogeneous reaction [7]. For those, other methods are often better suited, such as pulsed voltammetry.

Differential pulse and square-wave voltammetry

Pulsed techniques rely on the subtraction of the background currents from each potential step to reduce noise. Because of this, pulsed methods are among the most sensitive means for the direct evaluation of concentrations [7].

Differential-pulse voltammetry (DPV) was developed for dropping mercury electrodes, roughly a decade before square-wave voltammetry (SWV). Both use pulses where the base potential of each pulse is changed steadily in small steps (staircase). For DPV, the preelectrolysis (before the pulse application) period τ' is typically 20 to 100 times longer than the pulse duration τ, and it is in the same direction as the staircase. The SWV technique can be considered as a special case of DPV, in which $\tau = \tau'$ and the second half of the pulse traverses the staircase. The typical waveforms for a scan from high to low potential are shown in Figure 2.10A,B.

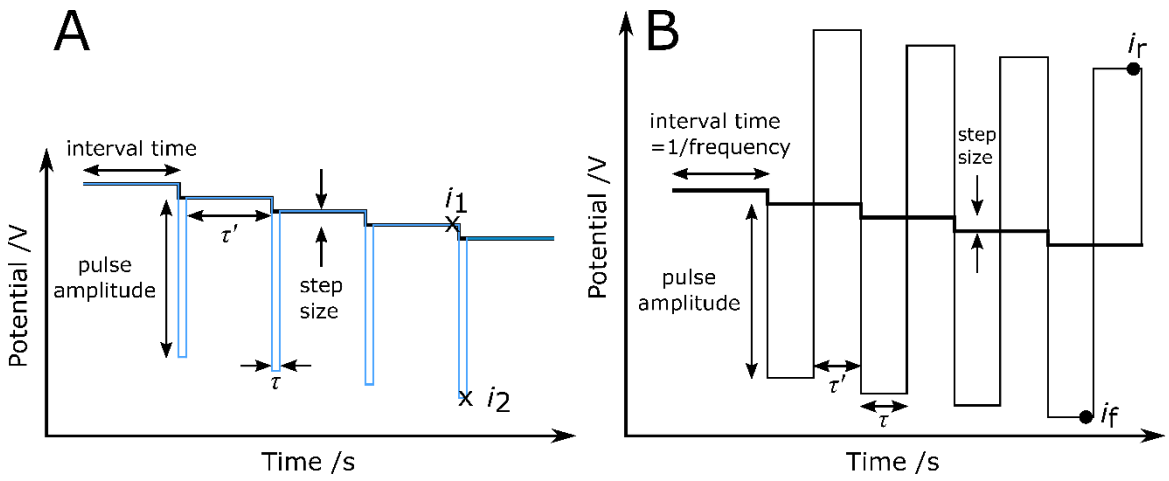


Figure 2.10 (A) differential-pulse and (B) square-wave voltammetry waveforms.

Current samples are taken twice per cycle. For DPV a current sample i_1 is collected once at the end of the pre-electrolysis period, a sample i_2 is collected at the end of the pulse; the difference is $\Delta i_{DPV} = i_2 - i_1$. For SWV, from the current i_f at the end of the forward pulse is subtracted the current i_r at the end of the reverse pulse, to produce $\Delta i_{SWV} = i_f - i_r$. Voltammograms for both techniques are the difference currents plotted against the staircase potential, as in Figure 2.11.

Still taking the one-electron oxidation of A into B (equation 2.3) as the example, during pulsed voltammetry, at potentials before the oxidation potential of A (or reduction potential of B), no faradaic current flows for the initial period of length τ', and the change in potential manifested in the pulse is too small to stimulate the faradaic process; thus $i(\tau) - i(\tau')$ is virtually zero. Then, late in the experiment, when the base potential is in the diffusion-limited-current region, A is oxidised even during the initial period at the maximum possible rate, so again the pulse makes little difference to the current output. However, in the oxidative region of A, the application of the pulse can drive [A] at the surface to a much lower value, increasing the flux of A to the surface from bulk, and enhancing the faradaic current. Only in that region where a small potential difference can make a sizable difference in current flow, where the base potential is such that A is oxidised during τ' at some rate less than the maximum, are there appreciable differences in faradaic current.

Figure 2.11 shows the SWV and DPV peaks of the reduction of 1 mM ruthenium (III) hexaamine chloride (RuHex) in 0.1 M sodium phosphate buffer. The scans went from + 0.4 to – 0.8 V. To demonstrate the difference in sensitivity and background-exclusion ability of both methods, similar parameters were chosen as much as possible: step length of 45.5 ms or 22 Hz, step height of 0.5 mV, and pulse amplitude is 5 mV, resulting in a scan rate of 10 mVs^{-1}. The pulse length for DPV is 4.5 ms, and for SWV it is half the step length.

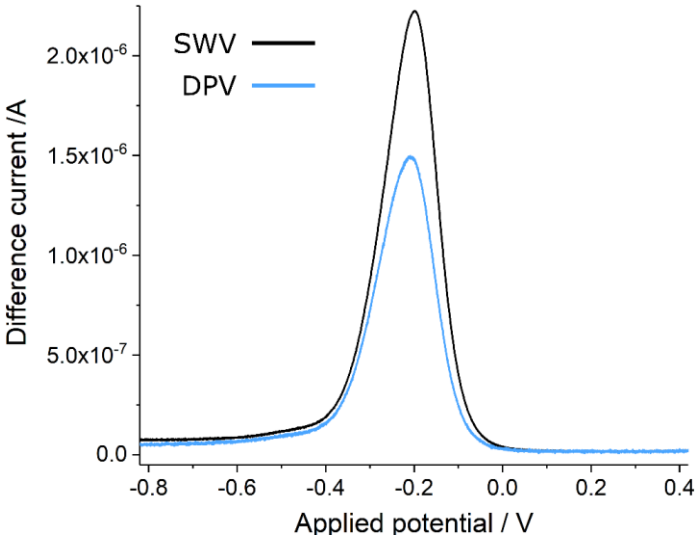


Figure 2.11 Reduction SWV and DPV of 1 mM RuHex, with similar parameters.

Since the diffusion layer is not renewed at the beginning of each measurement cycle, it is not possible to treat each cycle in isolation. The initial condition for each cycle is the complex diffusion layer that has evolved from all prior pulses, and it is a function, not only of the details of the waveform, but also of the kinetics and mechanisms of the chemistry linked to the electrode process. Therefore, theoretical treatments of DPV and SWV are intrinsically much more complex than for CVs.

2.1.9 Set-up for the present work

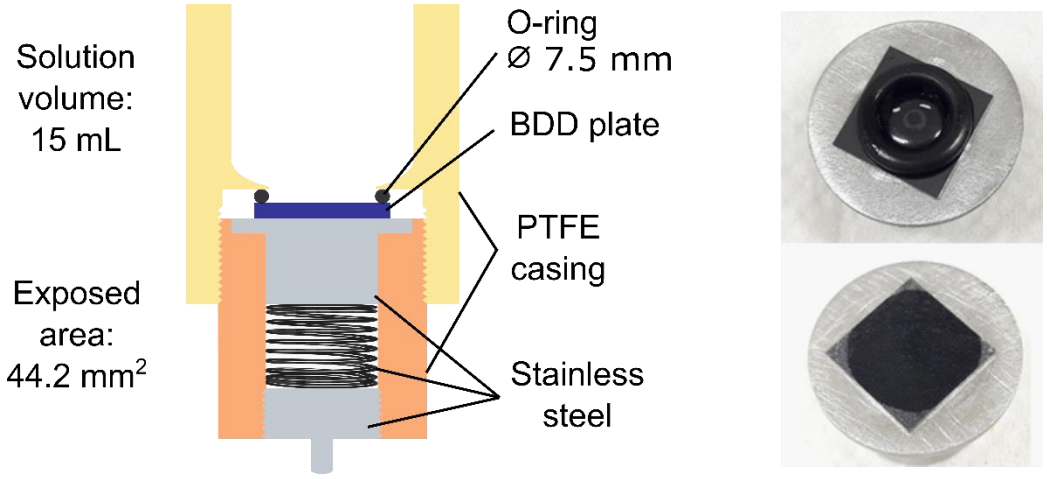


Figure 2.12 Schematic of the in-house-built cell, and the O-ring-limited WE area [8].

The electrochemical cell (15 mL) consisted of a standard three-electrode set-up, where an Ag|AgCl (1 M, CH Instruments, Austin, USA) was the REF and a platinum coil (20 cm, ⌀ 0.5 mm, Goodfellow Metals, Cambridge, UK) acted as the CE. The working electrode (Element Six, Oxford, UK) was clamped in a custom built PTFE cell (Figure 2.12), with a geometric area of 44.2 mm^2 bound by an O-ring [9]. The cell was controlled by the Autolab PGSTAT128N potentiostat (ECO Chemie, The Netherlands) via NOVA 2.1.4. To prevent data loss, it was important to build a real-time data export function into the experimental procedures, as the software was prone to crashing. All experiments were done at 22 ± 1°C.

2.2 X-ray photoelectron spectroscopy

X-ray photoelectron spectroscopy (XPS) is a surface-sensitive analytical technique which provides direct information on the elemental composition and oxidation states of solid materials. The following section gives a brief overview of XPS theory and practice, as well as the main considerations related to analysing spectra.

2.2.1 Photoelectron production

When the sample is irradiated with monochromatic X-rays, electrons in the sample atoms are excited. Only those electrons that have escaped from the sample into the vacuum of the

instrument reach the detector. These electrons originate from the valence and core energy levels, and XPS can provide information on both. In this thesis, the focus is on the more frequently studied core levels; for carbon this is the 1s orbital. In studies involving metals, the valence-level electrons are generally also studied. The ejection mechanism of a core electron is shown in Figure 2.13.

As the atoms are hit with the same excitation energy, the energy of the ejected photoelectrons reflects their orbitals of origin and is specific to the element and surrounding atoms. As a photoelectron travels through the sample, it may undergo inelastic collisions or recombination, cause excitation of other electrons, or be recaptured or trapped in various excited states within the material, all of which can reduce the number of those that manage to escape. These effects appear as an exponential attenuation function as the depth increases, making the signals detected from analytes at the surface much stronger than the signals detected from analytes deeper below the sample surface. Although the X-ray can penetrate up to 1 μm into the surface, only photoelectrons from the top ~5 nm would reach the detector. In comparison, highly penetrative medical X-rays are 50 to 100 keV—around 50 times more energetic.

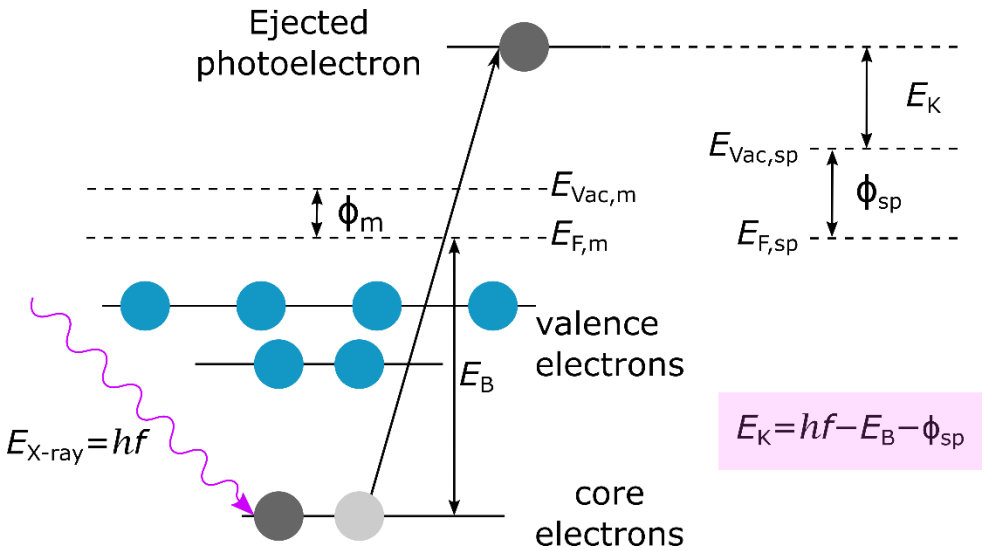


Figure 2.13 Schematic illustration of the XPS process, where photoionization of an atom by the emission of 1s electron from the K shell occurs.

The blue circles in Figure 2.13 represent electrons that do not directly participate in the XPS process, while the grey circle depicts a core electron that is photoionized by the X-rays. The Fermi level is E_F, kinetic energy of the photoelectron is E_k, binding energy is E_b, and ϕ_{sp} is the work function of the spectrometer.

2.2.2 Electron detection

An XPS apparatus contains an X-ray monochromator within an ultrahigh-vacuum (10^{-8} to 10^{-10} mbar) stainless-steel chamber, an electron collection lens, an electron energy analyser, and an electron detector system, as shown in Figure 2.14A.

After the photoelectrons have been ejected from the sample, they are focused into the hemispherical analyser by an electrostatic lens system and are dispersed inside the analyser. Between the two electrically isolated concentric hemispheres (Figure 2.14B), a radial electrostatic field exists which decays proportionately to r^{-2}, where r is the distance from the geometrical centre of the hemispheres. The dimensions and potentials between the hemispheres define the energy between them. Only electrons of a specific kinetic energy (E_{r_2} in Figure 2.14B) can pass through the analyser without hitting either the inner or outer hemispheres to reach the detector. It is called the pass energy, set by the analyser potential.

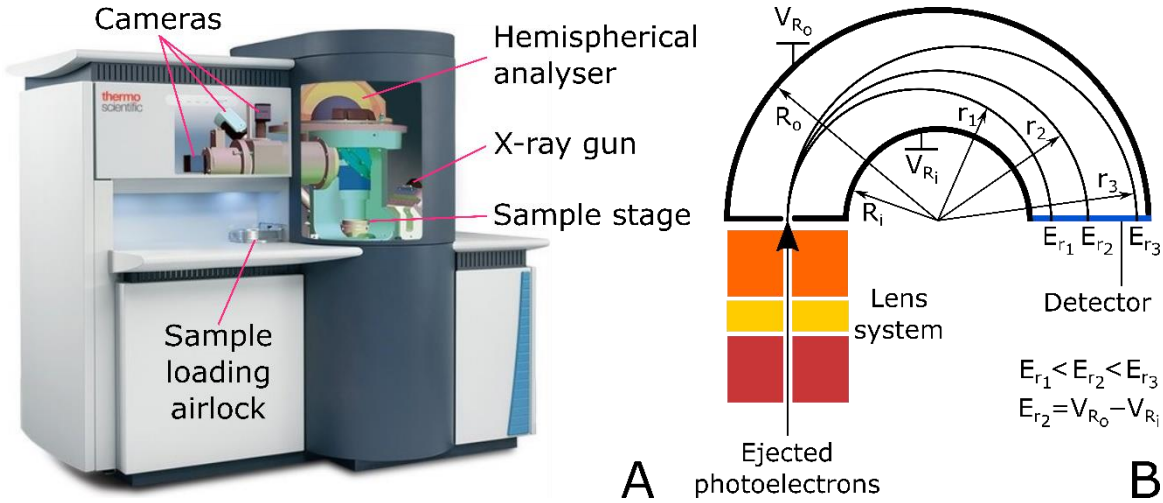


Figure 2.14 (A) XPS spectrometer used. (B) Schematic of hemispherical analyser.

Provided that the excitation energy is high enough, core-level spectra can be obtained for all elements of the periodic table except H and He (since both have no core level). The binding energies of these core levels are sufficiently distinctive for their unambiguous assignment. The spectra are acquired in fixed analyser transmission mode. In this mode, the pass energy of the analyser is held at a constant value and it is entirely the job of the transfer lens system to retard the given kinetic energy channel to the range accepted by the analyser. In this research, XPS was used to detect the chemical termination of diamond electrodes with either oxygen or hydrogen functionalities on the surface.

2.2.3 General spectral features

Main photoelectron lines

The main photoelectron lines as shown in Figure 2.15 are intense and well defined because the electrons are emitted from core orbitals (as discussed in Section 2.2.1) without additional interactions. Such interactions include initial chemical bonding before the photo-electron ejection, post-photoemission core-hole screening, relaxation of photoionisation, and polarisation of surrounding ions, which all contribute to extra energy losses [10]. From each survey peak, chemical information that is more subtle can be extracted.

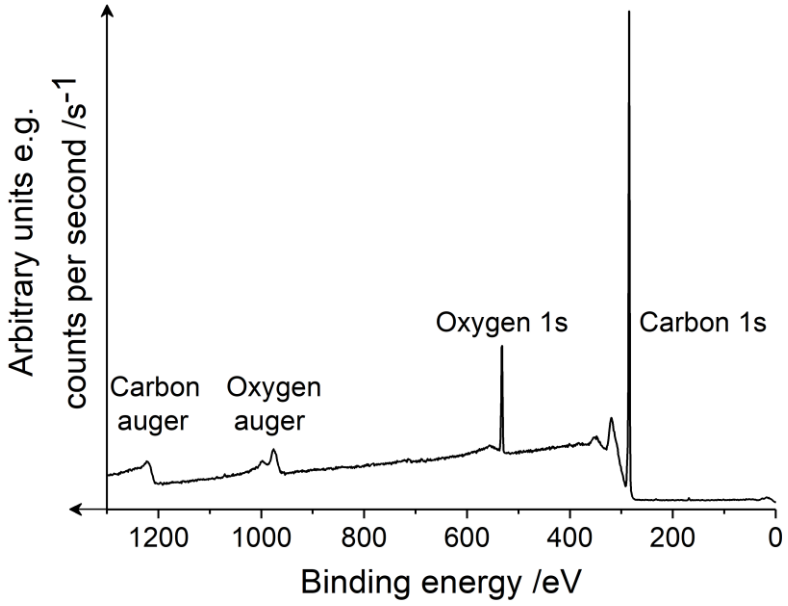


Figure 2.15 The survey scan of a clean oxygen-terminated BDD electrode.

Chemical shifts

The XPS spectrum gives elemental and chemical-state information from the top 10–20 atomic layers (~5–10 nm) of the sample surface, corresponding to the local bonding environment of the species in question. For example, for an oxidised carbon surface, this means the electrons from the different types of C–O bond (Figure 2.16). The latter is affected by its oxidation state. In particular, while the binding energy of the C 1s electron is accepted to be 285.0 eV [11, 12], subtle but reproducible shifts in the actual binding energy can provide information on the precise chemical state of the atom. Photoelectrons from the same element may have different binding energies if some come from the neutral atom while others come from an oxidised atom (Figure 2.16) or from atoms bound in complex aromatic configurations. These chemical shifts are relatively small, and they broaden the main peak of the element, which makes accurate interpretations of real chemical environments complicated. This subtle shift in energy is called the chemical shift, measured in eV.

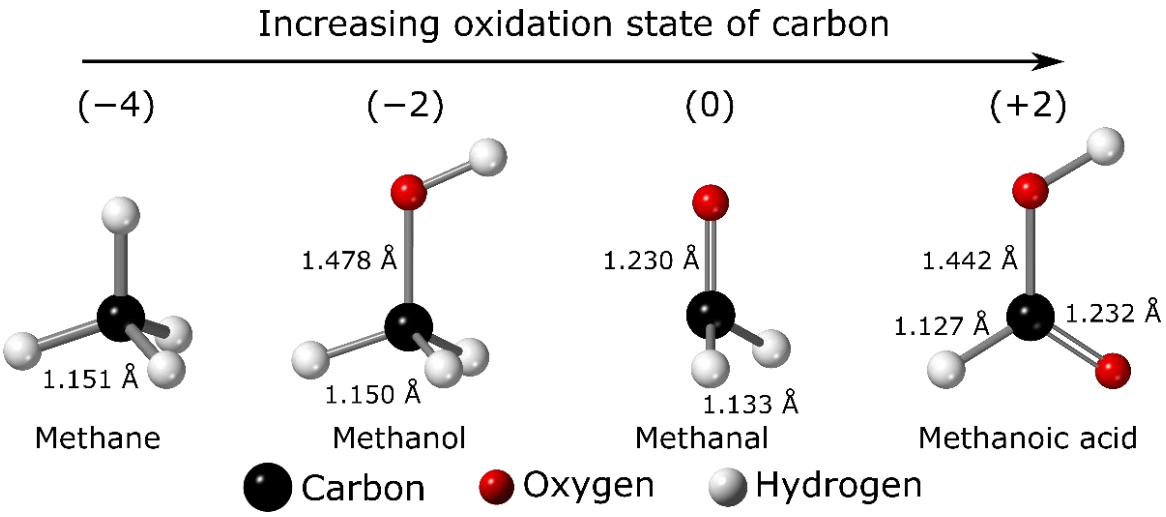


Figure 2.16 Oxidation states for carbon, and bond lengths for each carbon bond.

Shake-up satellites

Peaks from shake-up satellites are a few eV higher in binding energy (BE) than the main peak. They form when an ejected photoelectron interacts or collides with a valence electron

and imparts some energy, leaving the kinetic energy (KE) of the photoelectron slightly reduced (Figure 2.17). Such features are not very common. When seen, they often appear as a peak-broadening shoulder structure [13], or the satellite's peaks are separated from the main peak by a sizable shift, from a few eV up to 15 eV. The most notable example is the bonding–anti-bonding transition of the π molecular orbital (π→π* transition) brought about by C 1s electrons in aromatic organics.

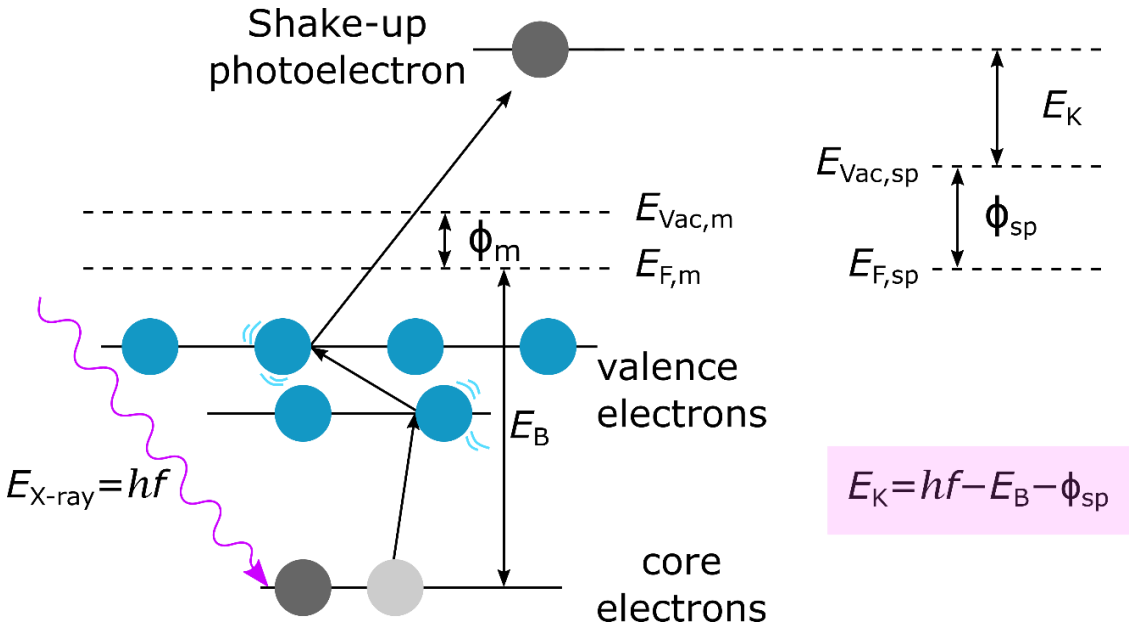


Figure 2.17 Production mechanism of shake-up satellites.

As with the normal XPS process, the Fermi level of the material and of the spectrometer are aligned, $E_{F,m} = E_{F,sp}$, and the measured kinetic energy of the photoelectron is E_k, which is dependent only on, ϕ_{sp}, the work function of the spectrometer.

Another notable feature, aside from shake-ups, are Auger peaks. The incident X-ray ejects a core electron; this leaves a hole in which a higher-energy electron drops down to fill; the remaining energy (characteristic of the difference between the states involved in the process) is the kinetic energy of a second emitted electron. As such, the kinetic energy of the Auger lines is independent of the X-ray source energy. Auger lines are easily distinguishable from the primary spectral lines, and their analysis can provide better spatial resolution [14].

2.2.4 Fitting photoelectron spectra

To fit the components of the chemical shifts, all spectra were analysed with CasaXPS peak-fitting software (version 2.3.17PR1.1).

Baseline subtraction

Electrons in the analyser that undergo inelastic scattering have their kinetic energy changed from the original. Baseline subtraction allows the peak area to be calculated and the subtle chemical shifts identified.

Having a realistic baseline fit is important for the accurate determination of the relative percentage of elements and their chemical states in the sample. There are three common background functions used in XPS analysis: linear, Shirley, and Tougaard. The work presented in this thesis uses the Shirley background [15]. It is more accurate than the linear background, while the Tougaard background requires a large energy range (approximately 50 eV on the higher binding energy side) to give a reasonable fit [16].

Gaussian–Lorentzian mix

The shape of the photoelectron line is represented by a convolution of core-level line shape and instrumental broadening [17]. The diameter of analyser, the pass energy, and the spread of energies in the X-ray source play a major role in determining the full-width half maximum (FWHM) of a given photoelectric line [18]. Localised charging may broaden lines regardless of the precision built into the instrument.

Line broadening arises from a distribution of primary radiation energy convolved by analyser broadening [19]. The Lorentzian (L) function describes the distribution of the energies of characteristic primary radiation from the X-ray tube and the loss of small portions of energy by the ejected photoelectrons (especially in metal samples) interacting with the conduction electrons. The emitted photoelectrons will have a distribution of velocities arriving at the analyser, due to the resolution of the spectrometer. This

broadening effect is described by a Gaussian profile. For carbon nanotube forests, only a Gaussian (G) profile is required [20]. For polymeric carbon samples or those that have metallic characteristics, the C 1s line is asymmetric and the convolution of a Lorentzian profile provides a more accurate fit.

The XPS spectra of the individual chemical states were fitted with asymmetric mixed Gaussian–Lorentzian (G–L) sum functions. This mixing ratio was based upon a variety of literature from the fields of diamond-growth and carbon-material science, and experience with CasaXPS. A 90:10 G–L mix was found to fit well and was kept constant for all samples.

Full-width half maximum

In complicated spectra, it is somewhat uncertain how many peaks are enveloped and how wide each peak should be. The full-width half maximum (FWHM) for a given photoelectric line is affected by features of the instrument, such as the analyser diameter, the pass energy, and the spread of energies from the X-ray source, and by the sample, such as localised charging. In our case of conductive BDD, variations in FWHM can be assumed to arise from the instrument, so if that is fixed during fitting, the errors in the energy resolution can be reduced.

In CasaXPS, peak positions were linked to each other and constrained to ± 0.3 eV of the reported relative shifts, so the software has reasonable starting points and boundaries in which to find good mathematical fits that also correspond with actual structural differences. On each iteration, a direction-set method was used to adjust parameters and minimise the chi-squared value, and the residual plots were closely checked to make sure no correlation exists within the residuals. When all peaks are appropriately offset, and the FWHMs are forced to have the same value, the model becomes less sensitive to noise in the data and returns a consistent answer for the relative intensities of the components [21].

In this work, because of a polymeric layer (Chapter 3, Figure 3.22A), the tail is elongated at the higher BE side, and there seems to be a feature that can only be ascribed to shake-up electrons, at 288.7 eV. To illustrate this point, Figure 2.18 shows that the same C 1s data can be fitted with either six (excluding shake-up feature) or seven (including shake-up feature) peaks. When shake-up was excluded from the calculations (Figure 2.18A), the fit is poor towards the higher binding energies, and the FWHM of the peaks are 1.40 eV. On the other hand, for the seven-peak fit, the FWHM is 1.12 eV (Figure 3.18B), which closely correlates with literature from computational calculations and a wide body of experimental evidence [22–25].

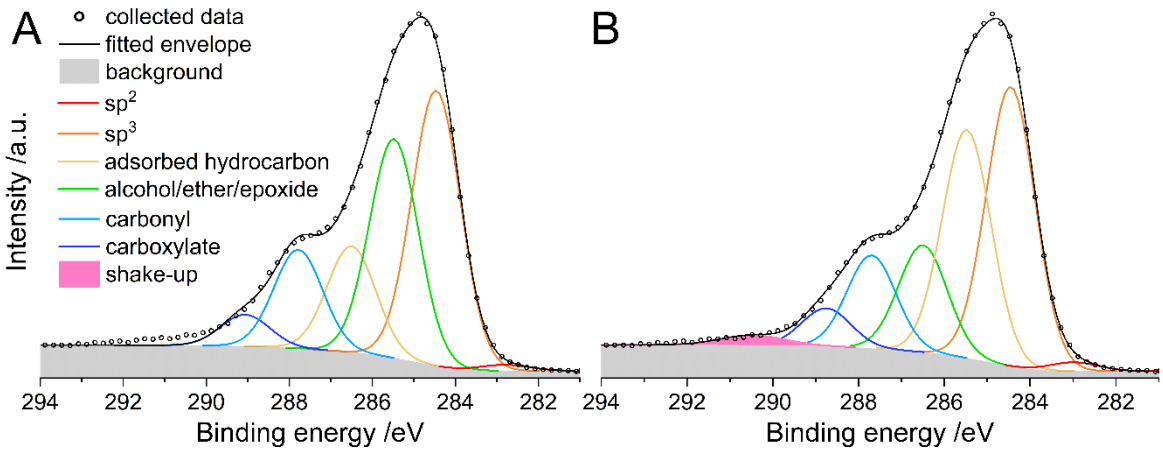


Figure 2.18 The same sample fitted without (A) and with (B) the shake-up feature.

Quantification of atomic distribution

Due to the variety of XPS instruments and operating modes, simply comparing sample intensities is not practicable. A useful way to compare XPS intensities is by stating those intensities as a proportion of the total, namely as percentage atomic concentrations. This is calculated as the ratio of the intensity of each peak to the total intensity of electrons in the measurement. The peak intensities are affected by both the amount of the element present on the surface and the sensitivity of that element to X-rays. Assuming the photon flux remains constant during data acquisition (usually true), the atomic fraction of one element, A, in a two-component model can be determined by the following expression:

$$\% \text{ A} = \frac{I_{\text{A}} F_{\text{B}}}{I_{\text{A}} F_{\text{B}} + I_{\text{B}} F_{\text{A}}}, \tag{2.21}$$

where I_{A} and I_{B} are intensities from the individual species, F_{A} and F_{B} are the empirically derived atomic sensitivity factors, which can be found in the literature. This calculation is embedded within the fitting software and works on the assumption that the sample composition is uniform within the XPS sampling depth (on the order of 5 nm).

2.2.5 Operational parameters

All spectra were recorded on a Thermo K-Alpha instrument. The samples were simply clipped onto the tray in the preparation chamber before it was automatically transported to the analysis chamber (< 10^{-9} mbar). The photon source was aluminium K-alpha radiation, at 1486.6 eV, the constant analyser energy was set at 50 eV, and the X-ray monochromator had a resolution of 0.1 eV. Ten accumulations were acquired to increase the signal-to-noise ratio. The beam size was the maximum possible (400 μm) to obtain a representative sample of the surface composition. For both techniques, the BDDs did not exhibit any charging behaviour, so no other treatments were applied prior to examination.

2.3 Scanning electron microscopy

Scanning electron microscopy (SEM) is used to produce high-resolution images by raster-scanning an electron beam across conductive samples.

The electrons are generated either thermionically or by a field-emission gun. After passing through an aperture, they are focused, to a very fine focal spot of 1 to 5 nm, through a series of condenser and objective lenses before reaching the sample. The primary electron beam interacts with the sample, generates Auger electrons, secondary electrons (SEs), backscattered electrons (BSEs), and X-rays. The region of interaction is teardrop-shaped, as shown in Figure 2.19.

The resolution of a microscope is approximately equal to half the wavelength of the

illuminating beam. An electron beam has much smaller wavelengths than light, and a skilled SEM operator can obtain image resolutions of a few nanometres [2] [26]. The magnification of an SEM does not depend on the power of the objective lenses as in optical microscopy. Rather, the electromagnetic condenser and objective lenses control the beam size, which improves the resolution. Magnification results from the ratio of the dimensions of the raster on the specimen and the raster on the display device. The smaller the raster scan area, the higher the magnification. As display screens vary in size across different SEM models, quoting the magnification is not as informative as providing a scale bar.

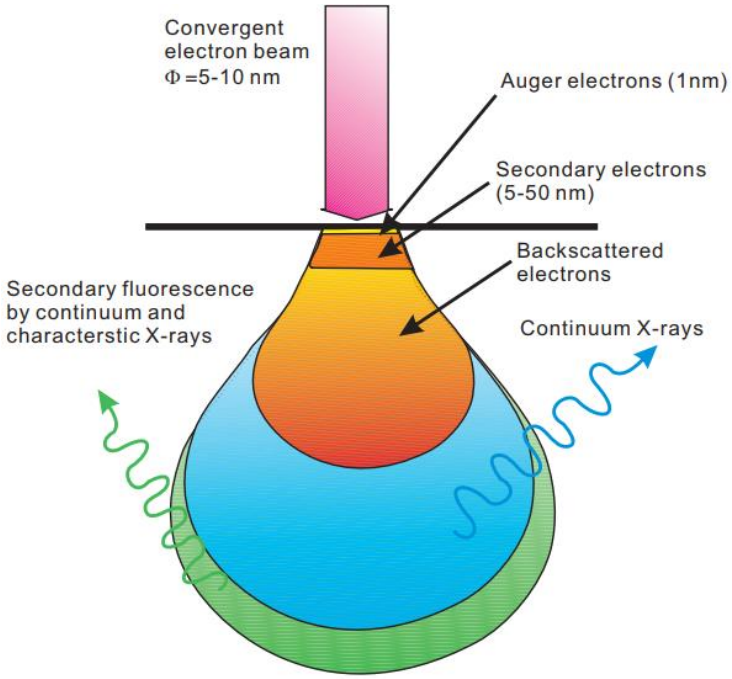


Figure 2.19 The interaction volume of a surface struck by an electron beam [27].

The electrons from the sample are collected via a scintillator and a photomultiplier tube, and this amplified response is simultaneously scanned across the monitor screen in the same raster pattern as the incident beam, thereby producing a spot-by-spot correlation between the signal level of the sampled point and the brightness of the display. Approximately half

[2] The wavelength of an electron beam is estimated by

$$\lambda = \frac{h}{\sqrt{2meV_O}} = \frac{1.23 \times 10^{-9}}{\sqrt{V_O}},$$

which for an operating voltage (V_O) of 25 kV gives a wavelength of 7.8×10^{-12} m [28].

of all SEs are produced near the point of impact of primary electrons, and due to their low energy (< 50 eV) only those from the top 5–50 nm of the surface can escape. The SEM is operated mainly in two modes, collecting either the BSEs or the SEs. The SE mode gives good stereographic representation of the surface morphology, and the BSE mode shows a contrast that depends on the mean atomic numbers of the sample's constituent elements.

In this work, the surfaces of the BDDs were imaged by the JOEL-6500F system (field-emission) operating at ~10^{-6} mbar, at 25 keV, with a beam current of ~ 130 μA, at the David Cockayne Centre for Electron Microscopy at Begbroke. The diamond did not exhibit any charging behaviour, so no sputtering was applied prior to examination. At these current densities, damaging processes may occur under electron-beam irradiation. For example, atom displacement, creation of defects, and, in the case of diamond, graphitisation [22]. In view of this, the time to image each area was kept to a minimum, which was also convenient for ensuring the whole surface was representatively sampled.

References

[1] R. G. Compton and G. H. W. Sanders, “Getting started,” in *Electrode Potentials*, Oxford: OUP, 1996, pp. 1–37.

[2] R. G. Compton and G. H. W. Sanders, “Allowing for non-ideality: activity coefficients,” in *Electrode Potentials*, Oxford: OUP, 1996, pp. 40–54.

[3] R. G. Compton and C. E. Banks, “Chapter 4 Cyclic voltammetry at macroelectrodes,” in *Understanding Voltammetry*, 2nd edn, London: Imperial College Press, 2011, pp. 107–155.

[4] H. H. Girault and M. Parsons (translator), “Chapter 4 Transport in solution,” in *Analytical and Physical Electrochemistry*. Lausanne: EPFL Press, 2004, pp. 132–138.

[5] A. Einstein and A. D. Cowper (translator) “Investigations on the theory of the Brownian movement,” *Annalen der Physik.*, vol. 17, p. 549, 1905, https://www.damtp.cam.ac.uk/user/gold/pdfs/teaching/old_literature/Einstein1905.pdf

[6] A. J. Bard and L. R. Faulkner, “Basic potential step methods,” in *Electrochemical Methods: Fundamentals and Applications*. John Wiley & Sons Ltd, 2001, p. 164.

[7] P. Monk, *Fundamentals of Electroanalytical Chemistry*. Chichester: John Wiley & Sons Ltd, 2002.

[8] M. C. Granger *et al.*, “Standard electrochemical behaviour of high-quality, boron-doped polycrystalline diamond thin-film electrodes,” *Analytical Chemistry*, vol. 72, no. 16, pp. 3793–3804, 2000, doi: 10.1021/ac0000675.

[9] R. Bowler, T. J. Davies, M. E. Hyde, and R. G. Compton, “Electrochemical cell for surface analysis,” *Analytical Chemistry*, vol. 77, no. 6, pp. 1916–1919, 2005.

[10] G. Attard and C. Barnes, “2.1 X-ray photoelectron spectroscopy,” in *Surfaces*. Oxford: Oxford University Press, 1998, pp. 38–43.

[11] P. Mérel, M. Tabbal, M. Chaker, S. Moisa, and J. Margot, “Direct evaluation of the sp3 content in diamond-like-carbon films by XPS,” *Applied Surface Science*, vol. 136, no. 1–2, pp. 105–110, 1998, doi: 10.1016/S0169-4332(98)00319-5.

[12] S. Kaciulis, “Spectroscopy of carbon: From diamond to nitride films,” *Surface and Interface Anaysis.*, vol. 44, no. 8, pp. 1155–1161, 2012, doi: 10.1002/sia.4892.

[13] M. A. Brisk and A. D. Baker, “Review Shake-up satellites in X-ray photoelectron spectroscopy,” *Journal of Electron Spectroscopy and Related Phenomena*, vol. 7, pp. 197–213, 1975, doi: 10.1016/0368-2048(75)80061-2.

[14] S. Hofmann, “Introduction and outline,” in *Auger- and X-ray Photoelectron Spectroscopy in Materials Science: A User-oriented Guide*, G. Ertl, H. Luth, and D. L. Mills, Eds. Heidelberg: Springer, 2013, pp. 3–7.

[15] D. A. Shirley, “High-resolution x-ray photoemission spectrum of the valence bands of gold,” *Physical Review B*, vol. 5, no. 12, pp. 4709–4714, 1972, doi: 10.1103/PhysRevB.5.4709.

[16] S. Tougaard, “Practical algorithm for background subtraction,” *Surface Science*, vol. 216, no. 3, pp. 343–360, 1989, doi: 10.1016/0039-6028(89)90380-4.

[17] M. R. Linford, "The Gaussian-Lorentzian sum, product, and convolution (Voigt) functions used in peak fitting XPS narrow scans, and an introduction to the impulse function," *Vacuum Technology and Coating*, vol. 7, pp. 2–9, 2014, http://www.researchgate.net/publication/263965482_The_Gaussian-Lorentzian_Sum_Product_and_Convolution_(Voigt)_Functions_Used_in_Peak_Fitting_XPS_Narrow_Scans_and_an_Introduction_to_the_Impulse_Function_.

[18] J. Filik, P. W. May, S. R. J. Pearce, R. K. Wild, and K. R. Hallam, "XPS and laser Raman analysis of hydrogenated amorphous carbon films," *Diamond and Related Materials*, vol. 12, no. 3–7, pp. 974–978, 2003, doi: 10.1016/S0925-9635(02)00374-6.

[19] G. K. Wertheim, M. A. Butler, K. W. West, and D. N. E. Buchanan, "Determination of the Gaussian and Lorentzian content of experimental line shapes," *Review of Scientific Instruments*, vol. 45, no. 11, pp. 1369–1371, 1974, doi: 10.1063/1.1686503.

[20] F. Deng *et al.*, "Grafting polymer coatings onto the surfaces of carbon nanotube forests and yarns via a photon irradiation process," *Applied Physics Letters*, vol. 100, no. 21, 2012, doi: 10.1063/1.4720509.

[21] K. Axis, "Peak fitting in XPS," *CasaXPS 2.3.14 Manual*. Casa Software Ltd., p. 19, 2006, http://www.casaxps.com/help_manual/manual_updates/peak_fitting_in_xps.pdf.

[22] C. H. Goeting, F. Marken, A. Gutiérrez-Sosa, R. G. Compton, and J. S. Foord, "Electrochemically induced surface modifications of boron-doped diamond electrodes: an X-ray photoelectron spectroscopy study," *Diamond and Related Materials*, vol. 9, no. 3–6, pp. 390–396, 2000, doi: 10.1016/S0925-9635(99)00267-8.

[23] L. A. Hutton, J. G. Iacobini, E. Bitziou, R. B. Channon, M. E. Newton, and J. V. Macpherson, "Examination of the factors affecting the electrochemical performance of oxygen-terminated polycrystalline boron-doped diamond electrodes," *Analytical Chemistry*, vol. 85, pp. 7230–7240, 2013, doi: 10.1021/ac401042t.

[24] A. Fujimoto, Y. Yamada, M. Koinuma, and S. Sato, "Origins of sp3 C peaks in C 1s X-ray photoelectron spectra of carbon materials," *Analytical Chemistry*, vol. 88, no. 12, pp. 6110–6114, 2016, doi: 10.1021/acs.analchem.6b01327.

[25] J. C. Arnault, "X-ray photoemission spectroscopy applied to nanodiamonds: From surface chemistry to in situ reactivity," *Diamond and Related Materials*, vol. 84, no. January, pp. 157–168, 2018, doi: 10.1016/j.diamond.2018.03.015.

[26] A. Zielinski, M. Cieslik, M. Sobaszek, R. Bogdanowicz, K. Darowicki, and J. Ryl, "Multifrequency nanoscale impedance microscopy (m-NIM): A novel approach towards detection of selective and subtle modifications on the surface of polycrystalline boron-doped diamond electrodes," *Ultramicroscopy*, vol. 199, December 2018, pp. 34–45, 2019, doi: 10.1016/j.ultramic.2019.01.004.

[27] J. Hu, "Electronic thin film materials," University of Oxford, 2007.

[28] D. J. Stokes, "Principles of SEM," in *Principles and Practice of Variable Pressure/Environmental Scanning Electron Microscopy (VP-ESEM)*. Chichester: John Wiley & Sons Ltd, 2008, pp. 17–62.

Chapter 3

Investigation of the *in situ* activation of diamond electrodes for dopamine detection

3.1 Introduction

Maintaining high electron-transfer kinetics and reproducible performance of electrodes is of primary concern for the experimentalist in electrochemistry [1–3]. Boron-doped diamond (BDD), despite its resistance to fouling (Section 1.1.3), still suffers from fouling, for example in the detection of dopamine, and it would be advantageous to be able to restore its activity by electrochemical means. This increases the reproducibility of measurements by removing the need for disassembly and assembly of the set-up, which is required for mechanical cleaning and introduces human errors Some cleaning procedures also have significant influence on electrochemical properties. These methods can be performed *in situ* (where the electrode stays in contact with the analyte solution) or *ex situ* (where the electrode is in blank buffers), and they can be mechanical [4], chemical [5], physical [6], electrochemical [7], or a combination of these [8].

Perhaps the most widespread practice is mechanical polishing, which is particularly suited for small disk electrodes (⌀ < 3 mm) inset to a rod [9,10], such that the electrode surface under investigation is flush with the end of the rod. The hardness of the slurry particles is chosen to match the material of the electrode—for example, alumina for platinum or gold, and nano-diamonds for BDD. The fineness of the slurries is increased to

produce a mirror polish. Alumina polishing removes physically adsorbed or deposited particles—for example, drop-coated carbon black on glassy carbon (GC) [11]. Sometimes this method is also suitable for removing adsorbates chemically bonded to the surface—for example, alkanethiols on gold [12]. This method of treating unpolished BDD electrodes can leave slurry residues, if not rinsed properly, but it does not change the oxygen-termination of the surface.

Chemical cleaning at room temperature can selectively remove deposited material from the electrode and leave the carbon substrate undamaged: for example, nitric acid dissolves silver [13], and aqua regia dissolves gold [14,15]. At higher temperatures, vigorous boiling in acid can remove loosely attached organic material or non-diamond carbon [16,17]. Most electrode casings are not built to withstand this harsh treatment, and this method is suitable only where the electrode is removable. These methods are cost-effective and easy to perform in a wet laboratory environment.

Physical treatments are often employed when total refurbishment of the BDD surface is required. Given that BDD grown by chemical vapour deposition (CVD) is naturally hydrogen-terminated, hydrogen plasmas have been used widely to obtain a 'factory setting' for electrodes of unknown history as the hydrogen atoms preferentially etch away sp^2 carbons, leaving a clean sp^3 underlayer [18]. Various studies have shown that hydrogen-terminated BDD is more reactive because of high surface conductivity and electron-transfer kinetics [19,20]. Oxygen plasma has also been used to produce ether and carboxyl surface groups [21]. Laser-induced periodic surface structuring has been shown to alter the nanostructure of the surface and tune the electrochemical properties of BDD [22]. Although effective, these techniques require complex equipment and many parameter refinements.

Practically, electrochemical cleaning involves little beyond existing set-ups, and the solution in which it is carried out can be easily changed. Cyclic voltammetry in weak acid

to establish cleanliness or active area is almost universal for all electrode materials [23]. It is also employed to recondition the electrode to a stable chemical termination and can remove persistent chemical deposits without damage to the underlying electrode [24]. Cathodic pre-treatment by applying −3 V for 3 to 30 minutes in 0.5 M H_2SO_4 can reactivate an aged BDD electrode [25]. Similarly, anodic treatment of 3 V for 30 minutes was also reported, but this reduced the electron-transfer rate and formed a passivation layer [26].

Various electrochemical pre-treatments were sought to obtain reproducible electrode activation, on a variety of carbon-based electrodes as well as BDD [27,28]. There is a general observation for the increase in reversibility after cathodic treatments. This could be correlated with a shift in the flat-band potential of the BDD [26,29] and with the increase in surface conductivity from hydrogen termination of the electrode surface [19,25].

In 2013, De Sanoit et al. patented an *in situ* electrochemical cleaning technique for diamond electrodes which simplifies the electrode activation and reduces process time [30]. The proposed method utilised high-density current pulses, in alternating cathodic and anodic potential regions. Work using this method mostly came from the same group, and they reported on the sensing of uric acid, indole, and 3-methylindole [31,32]. However, little investigation has been done into whether or why the procedure was more effective than others. This electro-activation technique does not suit non-BDD, more reactive, electrode materials, or even nanoparticle-decorated diamond electrodes, as the decorations tend to be less stable than the substrate.

The work described in this chapter explores the application of De Sanoit's activation procedure to the important molecule dopamine (DA), which is well known to be a very strong electrode fouler. Its reliable and consistent fouling quality makes it an appropriate molecule to test the robustness of De Sanoit's electrode-cleaning procedures. In this case, we used it to investigate the underlying chemical mechanisms of the current-pulsing

reactivation method. Our investigation of this method aims also to further the development of similar activation procedures.

Dopamine has maintained heightened academic and public interest. It is one of the neurotransmitters responsible for motivation and contentment levels [33], and illnesses such as Alzheimer's disease, depression, and addiction have been linked to its expression and binding. The molecular structure of DA comprises a catechol and a side-chain amine, and both exhibit electro-active behaviour that lends itself well to electrochemical analysis (Figure 3.1). Each oxidation event entails the loss of two hydrogens and two electrons. Consequently, there have been numerous reports on the monitoring of DA in vivo and in vitro with carbon electrodes [34–36].

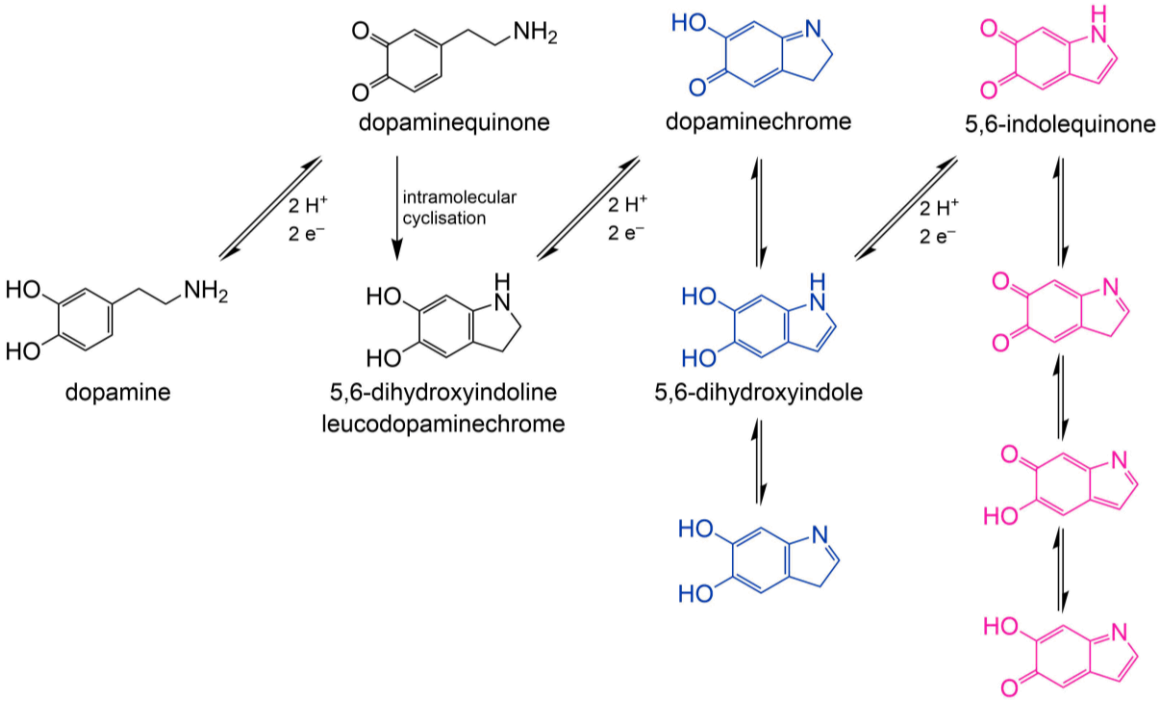


Figure 3.1 The mechanisms of dopamine oxidation and structures of its products. The coloured structures are tautomers of each other [37,38].

Dopamine forms semiconducting or insulating, extremely sticky, self-assembling polymers, depending on the conditions (such as pH and exposure to UV radiation) under which it is prepared [39–41]. Electrodes become fouled from the physical deposition of polymeric films formed after oxidation of DA, and the chemical of adsorption of these

biomolecules. Polydopamine (PDA) is chemically and physically robust, and contains the same catechol motif as found in mussel adhesive proteins, which are responsible for their enormous power of adhesion to all kinds of surface [39]. As such, PDA is used to coat metal oxides [42], carbon nanotubes [43], and medical devices [44], and to facilitate cell adhesion [45]. There is ongoing debate about the exact structure of PDA, and Figure 3.2 shows the complexity that structures proposed for it can accommodate. On a molecular level, it is assumed that carbonyl or unsaturated carbonyls act as electrophilic sites to allow functionalisation by fluorescent labels or enzymes for applications such as drug delivery and biosensing [46,47]. For our purposes, DA is both a worthwhile target molecule and a model fouling agent to investigate the mechanism of surface reactivation.

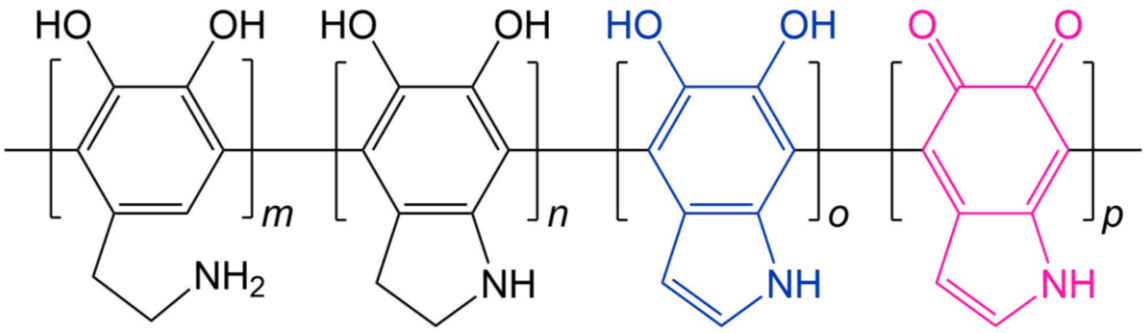


Figure 3.2 Proposed structure of PDAs; each unit can be replaced by its tautomers [48].

This project described in this chapter aims to extend the work of de Sanoit et al [30] to apply BDD electrodes to biosensing. It is the first investigation into whether this cleaning procedure can be used to overcome the major fouling and polymerisation problem presented by dopamine. The sensitivity and reproducibility of mechanical, chemical, and electrochemical means of cleaning was investigated. The chemical characterisation was performed by CV in dilute nitric acid and phosphate buffer, and physical characterisations by XPS and SEM.

3.2 Experimental details

All experiments were performed with unpolished polycrystalline BDDs purchased from Element Six (Harwell, UK). The potassium nitrate (KNO_3), dopamine hydrochloride (DA), and hexaamine ruthenium (III) chloride ($Ru(NH_3)_6Cl_3$, 98%) were purchased from Sigma Aldrich (Gillingham, UK) and used without further purification. Sulfuric acid (H_2SO_4, 98%) was from Fisher (Loughborough, UK). Stock solutions of 1 mM DA was made up in phosphate buffer at pH 7 freshly before each day's experiments. Before each CV, the potentiostat was held at 0 V for 5 seconds before the cell was switched on.

3.2.1 BDD cleaning

Mechanical cleaning was trialled. The electrodes were mechanically polished for ~5 minutes with a polish pad soaked in alumina (Buehler) slurries of increasing fineness (0.2, 0.1, 0.05 μm), followed by sonication first in 1:1 acetone–water mixture and then in water to remove any alumina remnants.

Chemical cleaning meant heating the electrodes at ~200℃ in concentrated H_2SO_4 (98%) saturated with KNO_3 for 30 minutes. The electrodes were rinsed in DI water then boiled again in only H_2SO_4 (98%) for 30 minutes. After this, the old (with unknown surface history) and new (partially hydrogen-terminated) BDD electrodes were considered to have been oxygen-terminated.

Both mechanical and chemical cleaning can be enhanced by electrochemical means, where the electrode is scanned cyclically in 0.1 M HNO_3, at 0.1 Vs^{-1}, from 0 V to 2.5 V to –1.7 V to 0 V, for at least 30 cycles, or until the CV looks like Figure 3.3. At this point, it is deemed pristine. The electrodes were then sonicated in DI water for 5 minutes and sealed in vials of fresh D.I. water until required. Each electrode was dried with N_2 gas before being screwed into its holder. Each electrode remains in its holder for a set of experiments until either one parameter has been tested or it is too fouled to continue *in situ*. The background

electrolyte is sodium phosphate buffer (NaPBS) adjusted to pH 7.0.

3.2.2 Surface analysis

Surface analyses were carried out within an hour after electrochemistry. The electrodes were dissembled from their holders, rinsed with DI water, dried with N_2, transported dry and upright, and examined. Ten accumulations of each XPS range were collected to reduce noise. Each of the components of the complex envelope was described using a Gaussian–Lorentzian sum function, where the mixing ratio was 90:10. Microscopy and XPS were performed as close to each other as possible. For XPS, the BDDs were simply clipped onto the holder, and for SEM they were stuck onto stubs with copper tape. The samples did not exhibit any charging behaviour, so no other treatments were applied prior to examination.

3.3 Results and discussions

3.3.1 Pristine oxygen-terminated BDD

To achieve a consistent surface before the electrodes were exposed to dopamine, and to establish the most reliable way to erase electrode history, two sets of BDDs were either polished or boiled in acid, followed by cyclic scans in acid. Figure 3.3 shows the state of the surfaces that is considered pristine, which can be reached by both methods. However, as the BDDs are plates only 1 mm thick, it is not a trivial exercise to polish them by hand on a fast spinning turntable, and there is always the possibility of contamination by alumina.

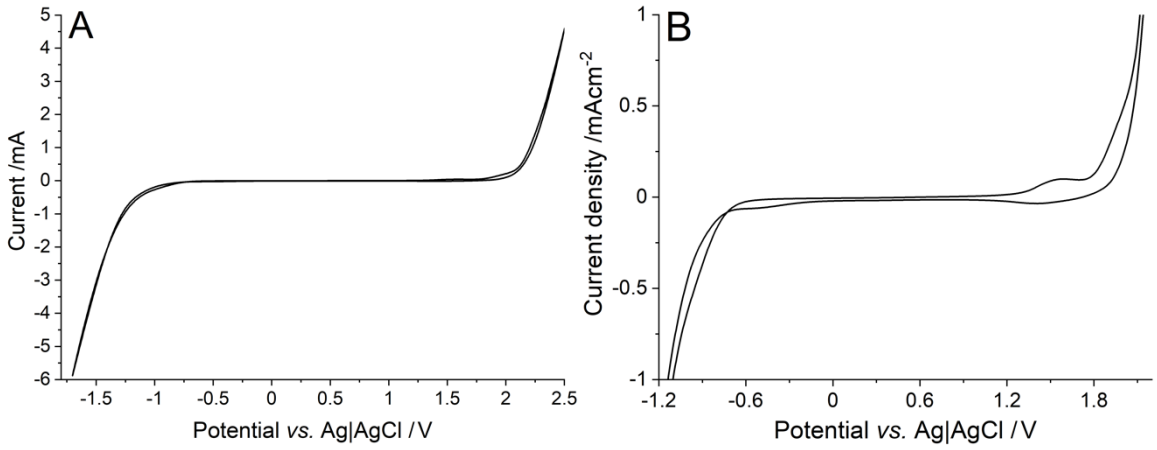


Figure 3.3 (A) A pristine BDD electrode scanned at 0.1 Vs^{-1} from 0 to 2.5 to –1.7 to 0 V in 0.1 M HNO_3. (B) A re-scaled version of A to show the currents more clearly.

The potential range and the scan rate of the cleaning scans were fixed; and the number of cycles required to achieve a clean surface was dependent on the initial state of the electrode. Figure 3.3B shows the response of an electrode that is deemed to be sufficiently clean. The response around +1.3 V has also been observed by other researchers, and the consensus is that this feature is associated with the oxidation and reduction of defective diamond. To produce electrode surfaces of the same degree of cleanliness, more cleaning scans had to be applied after mechanical cleaning, meaning that sometimes measurements could not be taken for more than two hours. In contrast, after a chemical bath, which was practically simple, only ten or so scans would be required.

Boiling in a sulfuric–nitric acid mix oxygen-terminated the BDD surface and removed any loosely bound organic material and non-diamond carbon [49]. A purely chemical approach would clean the whole of the BDD plate uniformly, not just of DA fouling but also of residues from the O-ring. This removes the need to unscrew the electrode housing until a whole series of experiments are complete, and we ensure the complete erasure of the surface history of the electrodes between experiments. Current density is shown in Figure 3.3B to allow comparison with all sizes of electrode, and the cut-off values ($\pm$ 1 mA cm^{-2}) are one of the accepted literature values which define the potential window of BDDs [50].

A useful indicator of electron-transfer kinetics for almost all electrode materials is the outer-sphere redox couple $Ru(NH_3)_6^{2+/3+}$ (RuHex). To illustrate the typical behaviour of our set-up, Figure 3.4 shows the responses of two pristine BDDs in a 1 mM RuHex supported by 0.1 M KNO_3, starting from 0.3 to –0.8 V, at a range of scan rates.

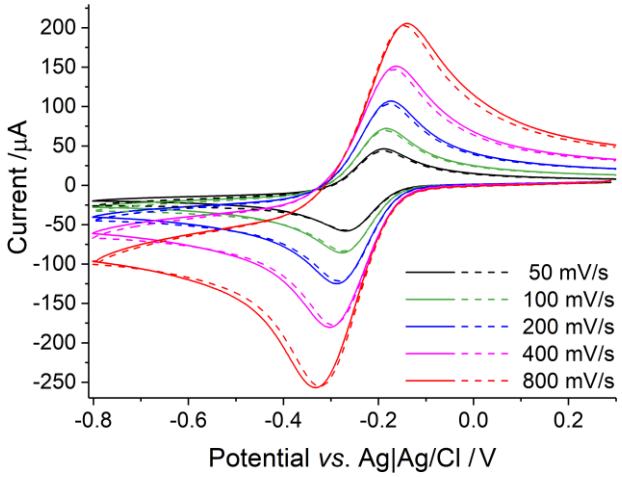


Figure 3.4 Voltammograms of two oxygen-terminated BDD electrodes (solid and dashed lines) in 1 mM $Ru(NH_3)_6Cl_3$ supported by 0.1 M KNO_3.

As the scan rate increase, the redox peak potentials move further apart from each other. This behaviour deviates from that of an ideal planar electrode, and that is due to the intrinsic differences in the electron-transfer kinetics of the different crystal facets, arising from the heterogeneous conductivity within the material [51,52]. The magnitude of the reduction peak plotted against the square root of scan rate gives the diffusion coefficient of RuHex

(III) as 5.8 (± 0.1) × 10^{-10} m^2 s^{-1}.

3.3.2 Dopamine redox

After obtaining pristine surfaces involving the *ex situ* procedures above, the electrodes were exposed to 1 mM DA at pH 7. On a pristine BBD electrode, DA exhibits a well-defined oxidation wave with its peak potential (P_{Ox}) around 0.53 V (always > 0.5 V on the acid-cleaned surface), and a weak reduction peak around –0.17 V vs. Ag|AgCl [38]. Figure 3.5 shows the decrease in the amplitude of P_{Ox} as the number of scans increases, and its potential shifts in a more anodic direction as the number of scans increases.

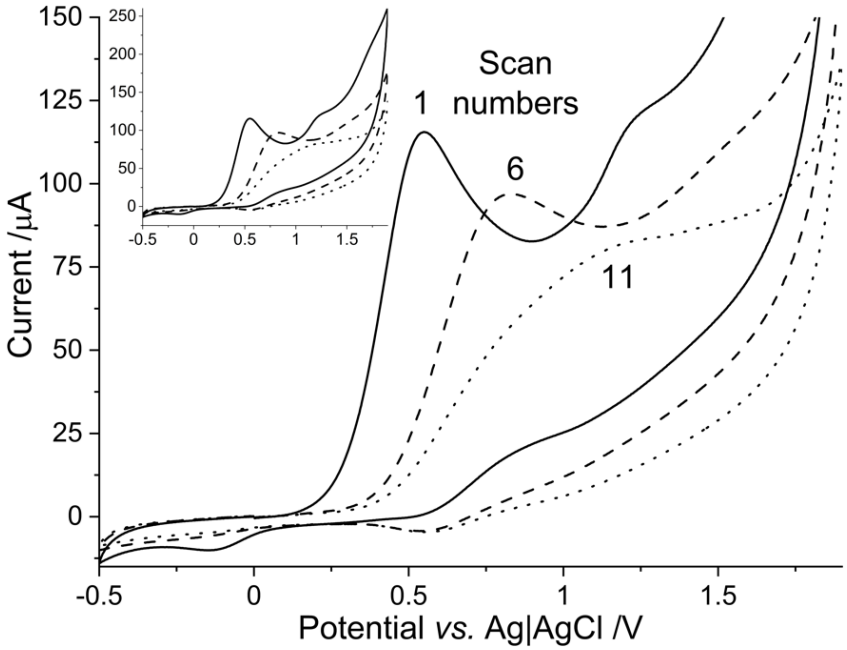


Figure 3.5 Voltammograms in 1 mM DA and 0.1 M NaPBS with a scan rate of 0.1 V s^{-1}. Inset, the same CVs displayed to their full range of 1.8 V.

The decrease in peak height and increase in oxidation potential as the scan number increases indicate a severely blocked surface where the conversion efficiency of unoxidized material is hampered, and a decrease in the rate of electron transfer [54,55]. The solid, dashed, and dotted lines depict respectively the scan numbers 1, 6, 11.

A possible explanation for the attenuation of peak magnitude is that, through prolonged scanning, the concentration of oxidisable species in the reactor decreases via faradaic

processes, or the electrode has become fouled and less sensitive. To check this, a pristine electrode was first scanned in 1 mM DA for five cycles, after which the solution was poured out, the electrode surface was rinsed with DI water, a 1 mM RuHex solution was poured in, and a voltammogram was recorded. The results are shown in Figure 3.6.

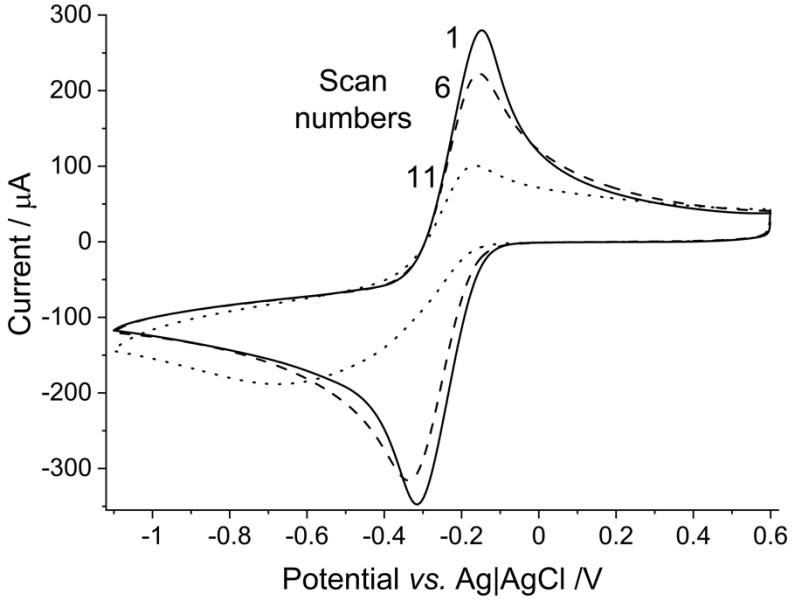


Figure 3.6 CVs of 1 mM RuHex in 0.1 M NaPBS; scanned at 0.1 V s^{-1}.

Even with this redox couple that is generally insensitive to surface changes [56], its oxidation peak decreases, and the reduction peak loses definition and shifts along the x-axis. The last two figures together indicate that both DA and RuHex are losing access to active electrode areas, and this is observed as decreased efficiency of the electron transfer process.

3.3.3 Reactivation with the patented method

Now we have demonstrated consistent and severe fouling with DA as a model system, the problem ahead lies in reactivating the electrode. This could be done *in situ* in the presence of DA, or have the electrode thoroughly rinsed and placed in a blank buffer, *ex situ*. From repeated experiments, both environments produced the same results with the patented method [30]. After this discovery, for simplicity, subsequent pulsing procedures were performed in the same DA solutions as the CV measurements were taken.

The potentiostat could be controlled either by setting a constant potential or a constant current density. The latter was chosen, as this can be controlled independently of the make-up of the solution or variations in system resistances in other set-ups. The potentiostat was able to output a maximum amplitude of 10 mA in a stable fashion. Because this method required the fast switching of the cell, 100 ms was the shortest pulse length the machine could handle while maintaining smooth operation and data export.

Figure 3.7 shows a schematic of some representative eight bipolar pulses (the exact number can vary) applied to a pristine electrode polarised in a 1 mM DA solution. The current flowing in the application of pulses at ± 10 mA cm^{-2} is shown in black, and the potential responses are shown in blue.

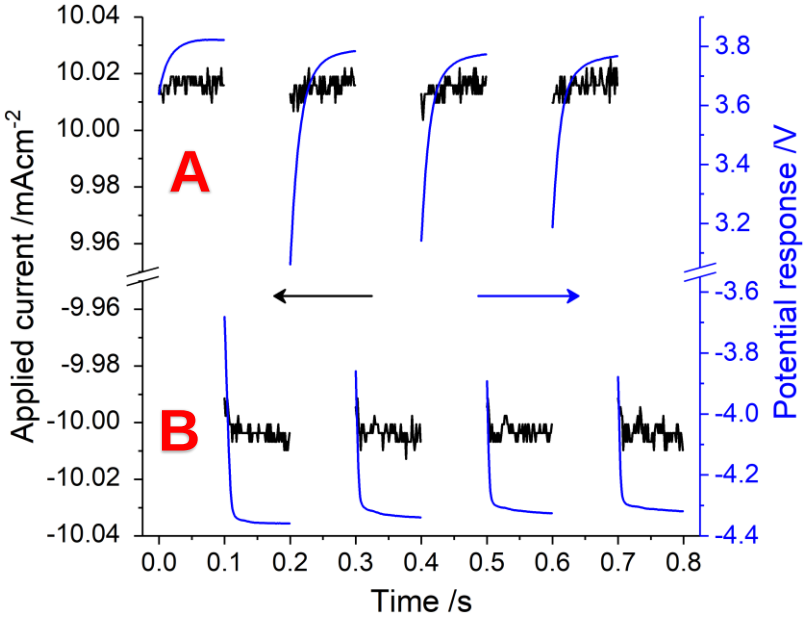


Figure 3.7 The currents applied in black (left axis) and their corresponding potentials in blue (right axis) in 1 mM DA at pH 7 for the bipolar case, where the signals and responses may be split into (A) anodic and (B) cathodic components.

In works by De Sanoit et. al. and Kiran et. al., the activation methods were qualified as a train of current pulses of any polarization lasting for less than 10 s, and the higher the current amplitude the more effective the activation [30,55]. Figure 3.8 shows the effectiveness of the method. The black line shows the CV response of a pristine electrode

in 1 mM DA. After recording it, 20 pulses of ± 10 $mAcm^{-2}$ were applied, finishing with a cathodic pulse, and the solution was stirred to dislodge bubbles on the electrode surface. When the solution had settled (waiting for 30 s), the next CV was recorded (red line). This process of CVs, current pulsing, stirring, and waiting was repeated to produce each coloured line. The electrode was not moved throughout.

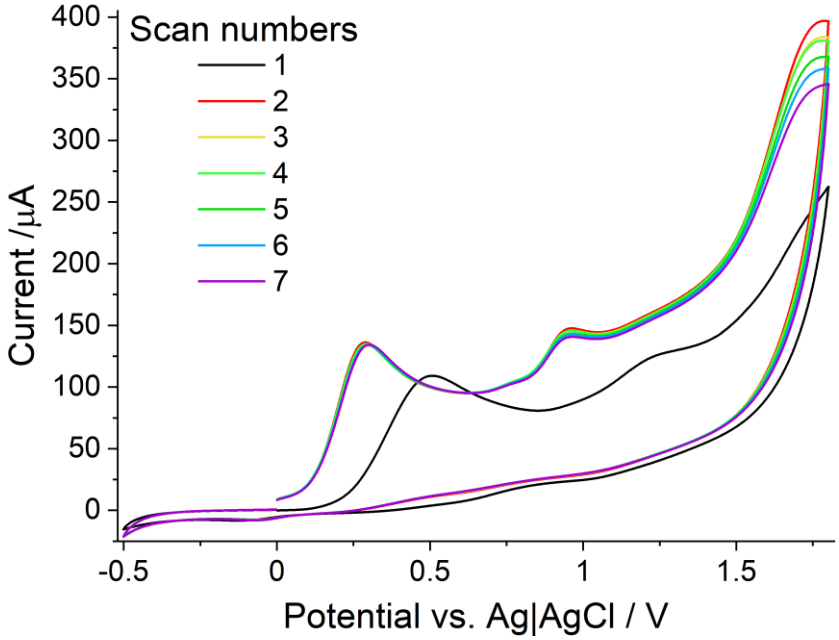


Figure 3.8 Consecutive CVs in 1 mM DA. Black, the first scan with a pristine BDD; rainbow, subsequent scans recorded after *in situ* application of 20 bipolar pulses.

To test the length of the pulse train for cleaning effectiveness, 10, 20, and 60 bipolar pulses were tested: 10 did not clean adequately, 20 seemed adequate, and 60 were no better. Each pulse was chosen to last 100 ms, to compromise between speed and electronic delay, which was exacerbated with increased number of pulses (e.g. ~7 seconds for 20 pulses, and ~18 seconds for 60 pulses).

The cumulative faradaic charge from five fouling CV scans is ~8 mC. During each cleaning pulse, 1 mC passes per 100 ms. This implies that, if all the nett charge collected has taken part in the polymerisation of DA, then ten pulses should be enough to remove all the oxidised species. However, the process is not 100% efficient, as side reactions such as electrolysis of water occurs, and so more than ten pulses are required [30]. Next, we were

interested to see whether the efficiency of this technique would depend on the severity of fouling.

To obtain Figure 3.9A, a pristine electrode was scanned for two cycles in 1 mM DA and then treated with bipolar pulses in the same solution. Next, the bubbles were cleared off the surface, the solution was allowed to settle, and another two cycles recorded. The difference between each set of two cycles is the anodic extent to which the electrode was subjected. The scans started at 0 V and the anodic maximum increased from 0.6 V (indigo) to 1.8 V (red) while the the cathodic limit remained at – 0.5 V. Even after the current pulsing treatment, the extent of the fouling is still hugely dependent on the scan range. Figure 3.9B shows the drop in peak current between the two cycles, where each colour represents a scan range, and the values are plotted against the anodic maximum.

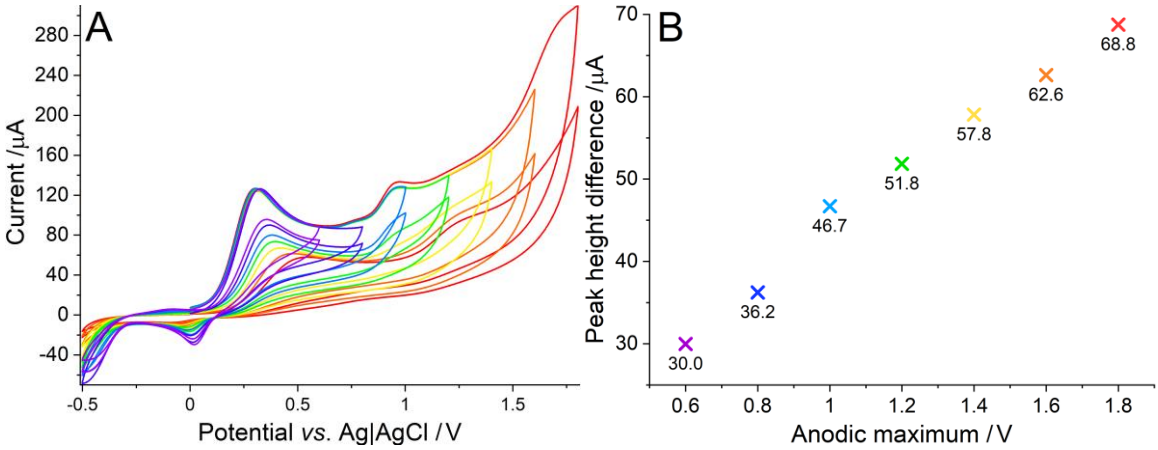


Figure 3.9 (A) CVs in 1 mM DA, starting at 0 V, scanning to a range of oxidation potentials (0.6 to 1.8 V), at a scan rate of 0.1 V/s. The cathodic limit was – 0.5 V. (B) The extent of fouling illustrated by drop in oxidation peak current.

Two deductions come from this experiment. First, when the anodic maximum is small (0.6 V), the drop in peak oxidation current is small, and this peak height difference increases linearly with the extension of the anodic maximum (Figure 3.9B). Second, the bipolar treatment was effective at creating an electrode surface that oxidised the DA reproducibly (overlaying of the P_{Ox} in the first cycles Figure 3.9A), regardless of the amount of

polymeric build-up. As an example, the drop in peak height for the green CVs (anodic maximum of 1.2 V) is 51.8 μA and for the yellow CVs (anodic maximum is 1.4 V) is 57.8 μA, yet the first scans of both CVs almost completely overlay each other.

So, it is the anodic maximum that has a greater effect on the degree of fouling, and the bipolar treatment ensures that the first, but only the first, scan after its application is reliable. Thus, the bipolar treatment did not provide long-term protection.

It is notable that the surface produced by the bipolar treatment is different to the pristine surface as shown by the difference between the first scan and the scans of the pulse-cleaned surfaces as seen in Figure 3.8. Broadly it is known that the overpotential for DA oxidation increases with the level of oxidation of the diamond electrode [57,58], as seen in Figure 3.9, so the implication is that the pulse-cleaned electrode is less oxidised than the pristine surface. It can be noted that the last pulse applied in the procedure is cathodic, which will be expected to contribute to this. To elucidate the workings of the bipolar method, we examined each polarisation separately.

3.3.4 Separation of polarisation

The anodic and cathodic parts of a bipolar pulse train were tested separately to investigate how unidirectional polarisations affect the electrode performance, and to see the effect of combining them. The magnitude of the voltage response was also dependent on the signs of the current pulses. Figure 3.10 shows some representative unidirectional pulses applied to a pristine electrode in a 1 mM DA solution. The current flowing in the application of pulses at ± 10 mA cm^{-2} is shown in black, and the potential responses are shown in red (anodic) and blue (cathodic). The alternative pulses are shown in bold to highlight the length of each pulse.

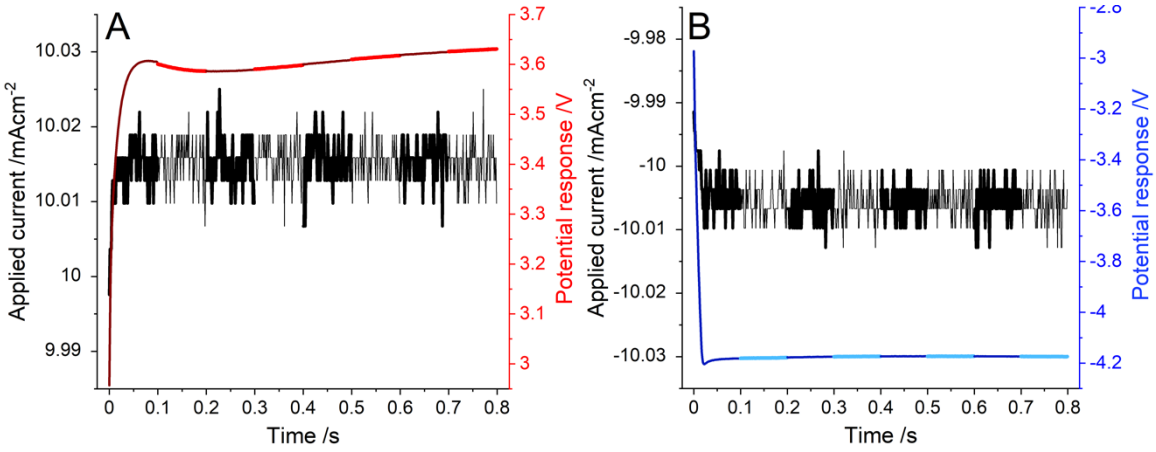


Figure 3.10 Anodic (left) and cathodic (right) pulses applied separately to a pristine electrode in 1 mM DA. To differentiate each 100 ms of current applied (black) and their potential responses (red and blue), thin and thick lines are drawn.

As can be seen from Figure 3.10A, the anodic potential response reached +3.5 V, whereas the cathodic response to reach the same current magnitude was – 4.2 V (Figure 3.10B). Under both polarisations, plumes of bubbles were observed from the onset. At these potentials in aqueous environments, we can expect products from water-splitting. Hydrogen is produced during cathodic polarisation, and oxygen evolves under anodic conditions [59]. The bubbles physically disturb the diffusion field near the electrode, making the solution too turbulent for the analytical Cottrell equation, which assumes steady-state mass transfer.

Figure 3.11 shows the CVs recorded in 1 mM DA, first with a pristine electrode (black line). Then twenty pulses of either anodic (Figure 3.11A) or cathodic (Figure 3.11B) polarisations were applied to the electrode, after which another CV was recorded (red). This process was repeated six times. After each pulse train, the solution was vigorously stirred to clear the bubbles off the electrode and to avoid the effects of electrostatic pre-concentration by the strong polarisation; then a wait time of 30 seconds was added for solution quiescence.

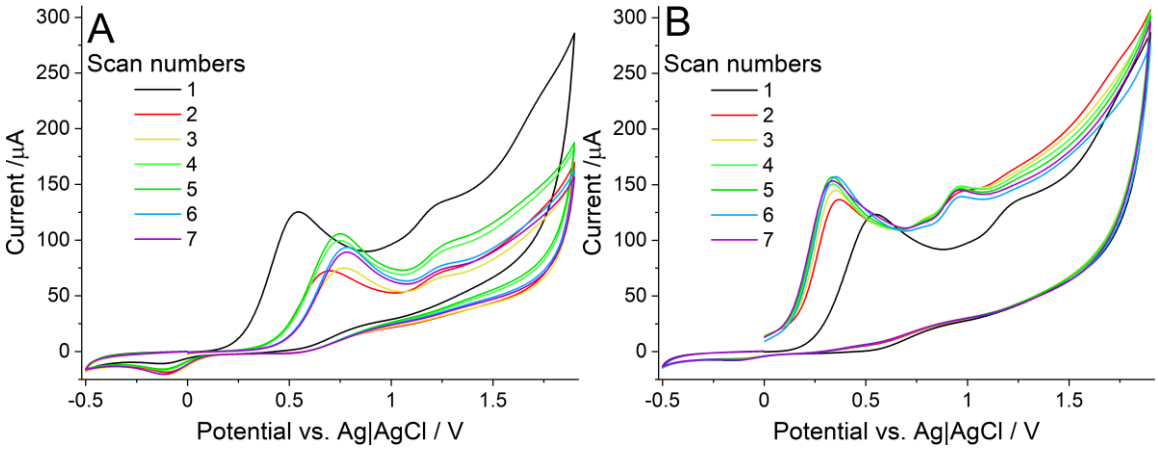


Figure 3.11 Consecutive CVs in 1 mM DA in 0.1 M NaPBS at pH 7.0. Black, the first scan with a pristine BDD; rainbow, subsequent scans recorded after application of 20 (A) anodic and (B) cathodic pulses *in situ*.

One notable difference in the electrode response is the prominence of the reduction peak after anodic polarisation (Figure 3.11A), compared to the reduction peaks after cathodic polarisation (Figure 3.11B), as might be expected. However it is notable that the magnitude of the reduction peak after anodic polarisation increases as the scan number increases from 2 to 7, even though the overall oxidation activity of the electrode decreases. Indeed just one oxidising scan is enough to cause a noticeable decrease in the activity of the electrode. This suggests that the reaction pathways change as the electrode becomes increasingly fouled: for the clean electrode, the primary process observed is the irreversible polymerisation of DA onto the electrode surface. As fouling advances, the process switches over more to the reversible (in the chemical rather than electrochemical sense) oxidation and reduction of DA producing the enhanced reduction peak.

Voltammograms recorded after anodic treatment (Figure 3.11A) show that the placement of the DA P_{Ox} shift in a generally positive direction (from 0.53 to 0.74 V), as the scan number increases from 2 to 7. This x-axis shift is also accompanied by a significant fluctuation and drop in the peak magnitude. The lack of a simple pattern in the P_{Ox} shift means that the surface is not behaving consistently.

Three processes could have caused this behaviour: thickening of the polymer layer to physically insulate the active electrode area [60]; electrical degradation of the polymer chains producing CO_2, as well as forming C–O bonds and cross-linking neighbouring polymer chains [61]; and major morphological change during electrochemical degradation of the polymer matrix which blocks ion transport through the polymer–solution mix on the surface, thus reducing the intrinsic conductivity of the film [62]. The presence of the reduction peak and the erratic placement of the oxidation peak suggest that fouling species accumulate on the electrode after anodic polarisation, and so it is not a good method to aid electroanalysis of DA.

Voltammograms recorded after cathodic treatment (Figure 3.11B) shows no change in the DA P_{Ox} as the scan number increases from 2 to 7. The biggest shift is between the first and second scans, where the P_{Ox} shifts to a lower potential, decreasing the peak separation. There is also a consistent increase in the oxidation peak current from scans 1 to 7. These two factors indicate that the electron-transfer kinetics have improved through the gradual reduction in the level of oxidation of the diamond electrode that is inherent to the pristine diamond surface

During cathodic polarization, hydrogen atoms are produced as part of the hydrogen evolution reaction. These highly energetic atoms attack the adsorbates indiscriminately and produce a mixture of soluble monomeric and polymeric quinones (Figure 3.1). Cathodic polarisation has also been reported to partially hydrogen-terminate the BDD surface, increasing its conductivity [27], which would also improve the electron-transfer kinetics.

For practical detection and quantification of dopamine, the focus is on the magnitude and overpotential of the oxidation peak. The placements of that peak position are displayed in Figure 3.12, where the error bars are calculated from at least seven repeats.

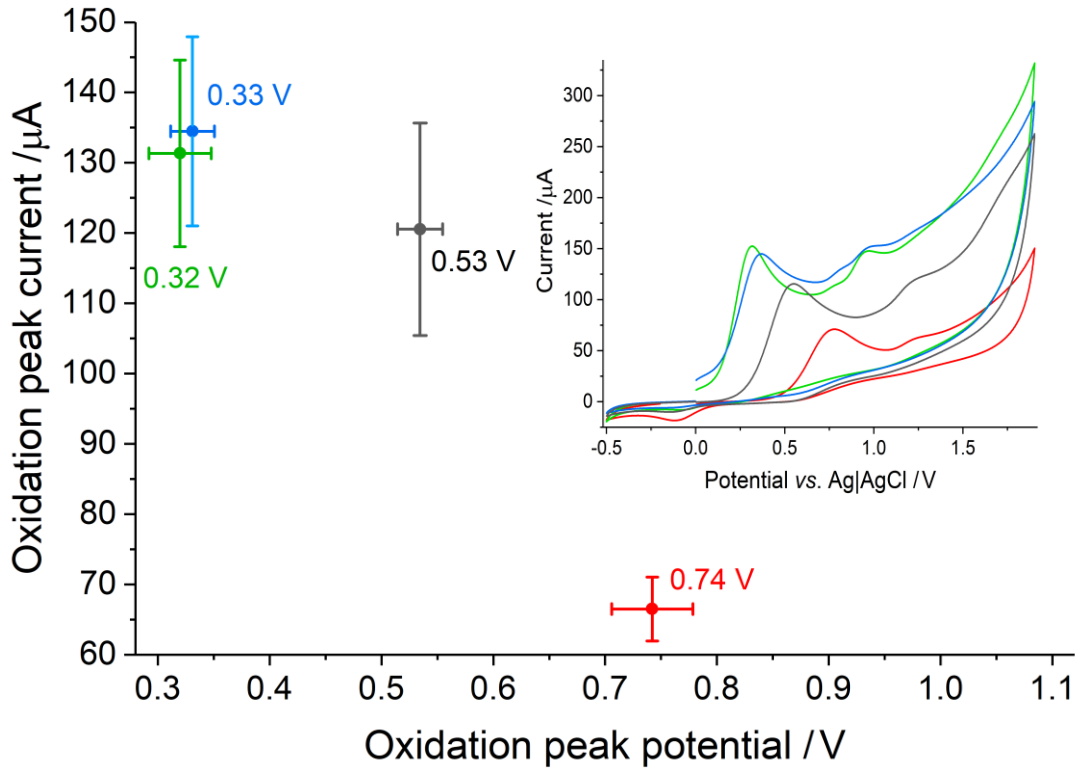


Figure 3.12 Comparison of all BDD surface conditions investigated in this project. Black: acid-cleaned, pristine BDD. Blue, cathodically pulsed. Red: anodically pulsed. Green: bipolarly pulsed. Inset, representative CVs of each condition which gave rise to the range of peak potentials and currents in the outer graph.

There are clear differences caused by the electrode treatment on the placement of P_{Ox}. Anodic polarisation produced low peak currents and high oxidation potentials, showing it to be a less effective treatment than acid-cleaning. In Figure 3.12, the range of P_{Ox} overlap after bipolar and cathodic pulses, with the cathodically-pulsed BDDs exhibiting slightly higher currents in general, meaning that either of these procedures could be chosen as a surface-reactivation method. However, the reasons why bipolar treatment was chosen is explained in the next section.

3.3.5 Stability

The placement of the oxidation peak varies as the scan numbers change. This movement of the peak is best represented by a 'moving' scatter plot, where only the position of the DA P_{Ox} is considered and plotted on a map so that its coordinates are its potential and current.

The journey of the P_{Ox} as the scan number increases is shown in Figure 3.13. Each scatter symbol represents one type of polarising treatment applied after each CV scan; for example, triangles show the placements of DA P_{Ox} recorded after bipolar pulses were applied.

The 'walk' for each symbol starts at the position of the DA P_{Ox} of an acid-cleaned, pristine BDD electrode. This start always falls within the vicinity of the dashed box, but the wide range of peak potentials and currents of those points demonstrate the variability in electrode response for the 'pristine' surface. Follow the direction of the arrows, to the position of the DA P_{Ox} of the next scan, after polarisation. For example, follow the red points where, even after one application of anodic treatment the P_{Ox}, the peak shifts by + 0.15 V and the current drops by almost 50%. Then, after further anodic treatments, the peak current fluctuates and the potential stays around 0.8 V.

The cathodic and bipolar treatments, used in the presence of DA, produced more-active electrode states than do the initial pristine electrode. The number of 100-ms pulses was fixed at twenty, their magnitude was always 10 mA cm^{-2}, and the scans were repeated eight times without removing the electrode from the solution. Displayed this way, the supreme stability of applying bipolar pulses versus the other options is obvious. With cathodic-only treatment, despite the huge fluctuations of currents, the peak potential hovers at a steady 0.35V and shows a heightened activation state compared to the acid-cleaned BDD. It may seem obvious to choose the cathodic-only treatment, as it activates the electrode surface to achieve higher currents on average. However, for reproducibility and stability through many repeats, bipolar currents were best. This indicates that anodic pulses have a stabilizing effect on the surface chemistry; and that for the pristine electrode to achieve a heightened state of activation, the effect from the application of the cathodic components must outweigh that of the anodic ones.

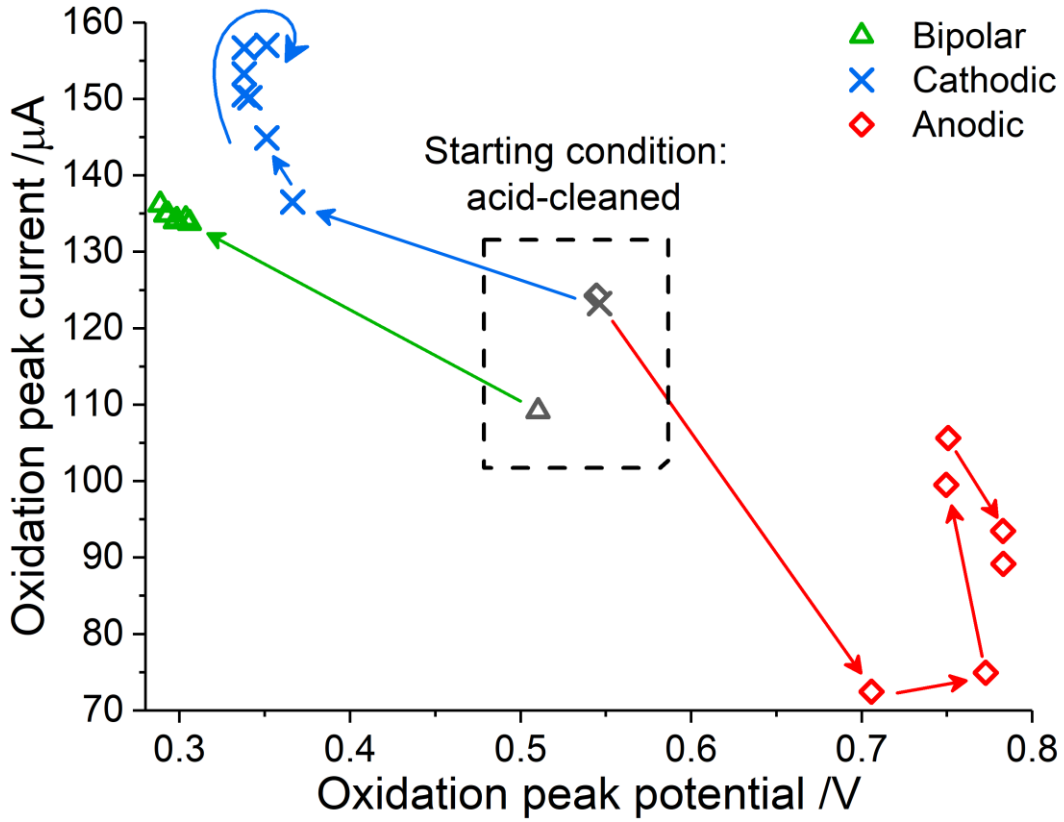


Figure 3.13 Start with pristine BDDs in 1 mM DA; their oxidation peak potentials and currents fall within the bounds of the dashed-line box. Then follow the arrows to track the movement of the current and potential of the DA oxidation peak after each type of polarisation.

3.3.6 Importance of pulses

It is stated in the patent by Scorsone et al. that 'one or several pulses with maximum current or voltage amplitudes and the shortest possible time were preferred' for the quickest activation [30]. We know that this works—but is it because the polarisation was being applied for an extended amount of time or because it was pulsed? This section addresses this question by fixing the direction of polarisation and changing the format of its application: pulsed or continuous.

To obtain Figure 3.14, first a pristine electrode was used to record five CV scans in 1 mM DA, where only the first is shown (black line) and the other four are to build up the fouling layer. To the now fouled electrode, still in the same solution, a uni-directional polarisation was applied, to equal the total duration of twenty of 100 ms pulses. Then a

waiting time of 30 s was added after the solution was vigorously stirred, and another scan recorded. In Figure 3.14, the black lines in both graphs show the response of a pristine BDD electrode, and the coloured lines represent CV responses recorded after either anodic (Figure 3.14A) or cathodic (Figure 3.14B) polarisations were applied.

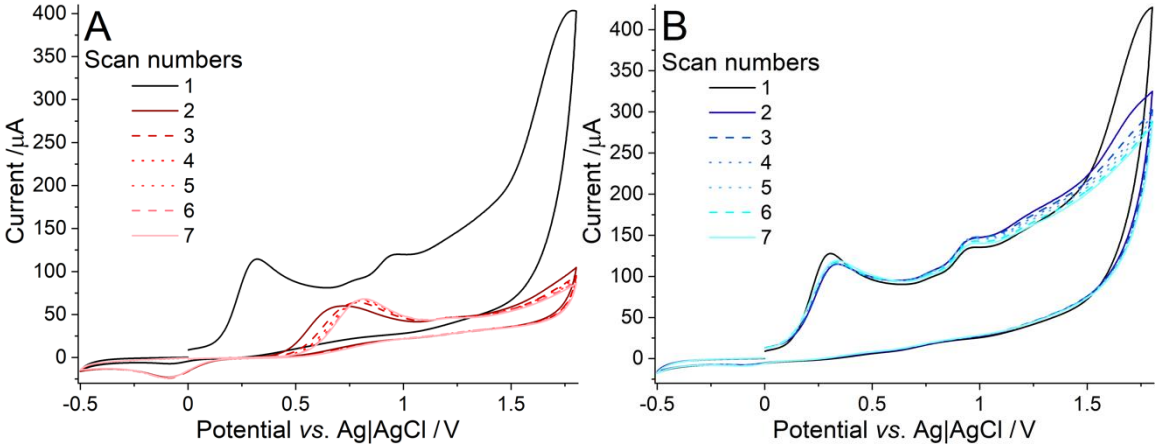


Figure 3.14 Consecutive CVs in 1 mM DA. Black, the first scan with a pristine BDD; subsequent scans recorded after application of (A) 2 s of anodic, (B) 2 s of cathodic unpulsed polarisation *in situ*.

Instead of the fluctuations seen under pulsed conditions (Figure 3.11), with continuous anodic polarisation, the current of DA oxidation peak decreased, and its potential increased (scans 2 to 7 in Figure 3.14A). This was similar to the electrode responses after twenty anodic pulses and corresponds to a reduction in the activation of the surface. However, this behaviour after anodic polarisation in either pulsed or continuous forms was not expected, as Rodrigo et al. and Oliveira et al. reported that anodic polarisation was able to return the activity of a BDD electrode [28,29]. Continuous anodic polarisation also caused an increase in the reduction-peak height, as was also seen after pulsed application, more so than acid-cleaning (black line, scan number 1) or cathodic polarisation (Figure 3.14B). To summarise, both pulsed and continuous anodic polarisation seem to exacerbate the fouling, and with continuous application the trend towards decreased electrode activity is less erratic and more definite.

In Figure 3.14B, a 2 s cathodic pulse was applied after the first scan, which caused a decrease in the peak current of scan 2, and the peak potential did not change. However, after subsequent applications of the cathodic 2 s pulse, the behaviour of electrode was highly reproducible (scans 2 to 7). Water splits at these pulse potentials (– 4.2 V) to evolve hydrogen via adsorbed hydrogen atoms. These highly reactive species can attack PDA adsorbed on the electrode surface as well as reduce nearby oxidised-DA species. This is true whether the cathodic polarisation is applied in one 2 s pulse or applied in twenty 100 ms pulses.

Figure 3.15 shows CVs obtained after a train of uni-directional pulses (solid lines), and those obtained after a single polarisation for the equivalent duration (dashed lines) were applied to fouled electrodes.

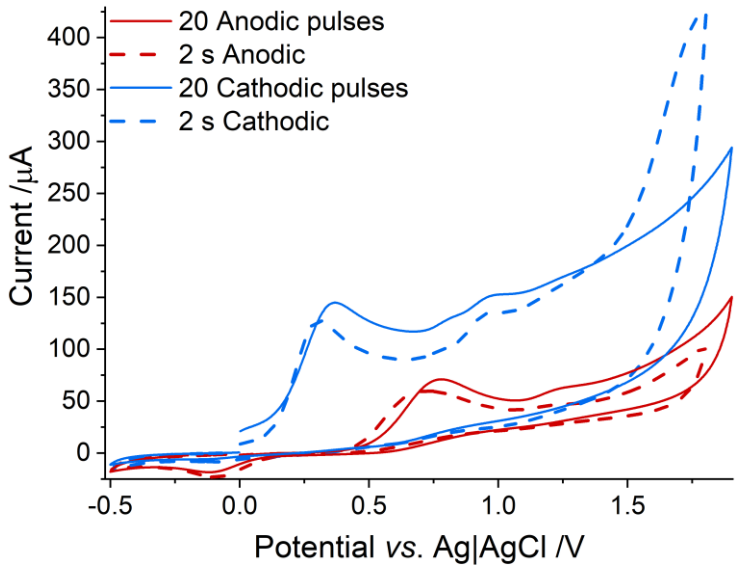


Figure 3.15 Representative CVs to show the difference in response between BDDs which have been treated with one long pulse or twenty short pulses.

In the interest of obtaining high oxidation peak currents, twenty 100 ms pulses were always slightly more effective than a single polarisation. Figure 3.16 shows the differences in applied current waveforms of pulses versus no pulses.

In Figure 3.16 A, the thin red and black lines represent the twenty anodic pulses, and the thicker pink line represents a single 2s anodic polarisation. Figure 3.16B, the navy and

black lines represent the twenty pulses, and the light blue line represents a single 2 s cathodic polarisation.

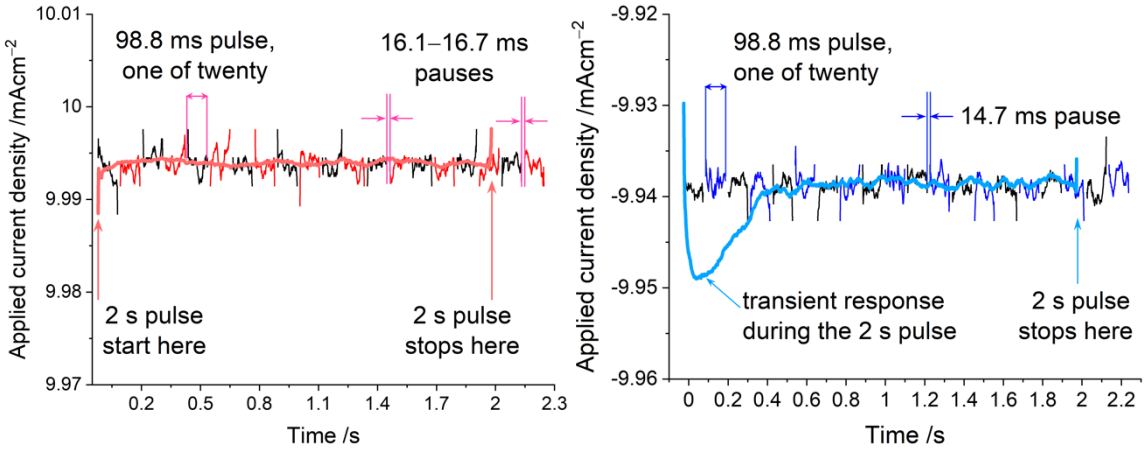


Figure 3.16 Comparison of twenty pulses and an equivalent 2 s pulse.

The short pulses are supposed to last 100 ms each, which they do, with a deviation of 1–2%. There are pauses between the pulses (about 15% of the pulse length); however, the bubbling happens continuously. During these pauses the surface discharges momentarily, which perhaps allows for some physical rearrangement (or 'relaxation') of the adsorbates as the electrode discharges. Some macroscopic structural change would explain why the CVs recorded after pulsed polarisation are erratic (Figure 3.11), while those recorded after a non-pulsed polarisation move with a concerted trend (Figure 3.13).

Another feature of having the pauses means that the total time taken to apply twenty 100 ms pulses actually was 10% to 13% longer than 2 s. The more pulses there are in a train, the greater the time difference will be between the applied and theoretical waveforms. This, however, does not affect the total current which passes through the electrode—only the schedule in which it is delivered. For the single two-second application, the transient surge in the current output for 400 ms was unexpected. However, this surge was too small to cause any significant change to the end effect of the electrode; +0.01 mA cm^{-2} for 400 ms is only a 0.02% increase in the total current passed in the two seconds.

In general, whether pulsed or not, anodic treatments oxidise the surface and make it less

active; cathodic treatments reduce the surface and make it more active. Pulsing, however, produces greater peak heights and an increased oxidation overpotential for both uni-directional polarisations compared with a steady 2 s polarisation. This suggests that any rearrangement that may happen at the electrode surface during the pauses increases the rate of electron transfer at the surface yet decreases the voltage efficiency of the cell.

3.3.7 Reproducibility

Figure 3.17 shows CVs when the electrode was pre-treated with bipolar pulses before every scan. The data are displayed in this manner because, as can be seen in the inset, the currents are so reproducible that they overlap each other.

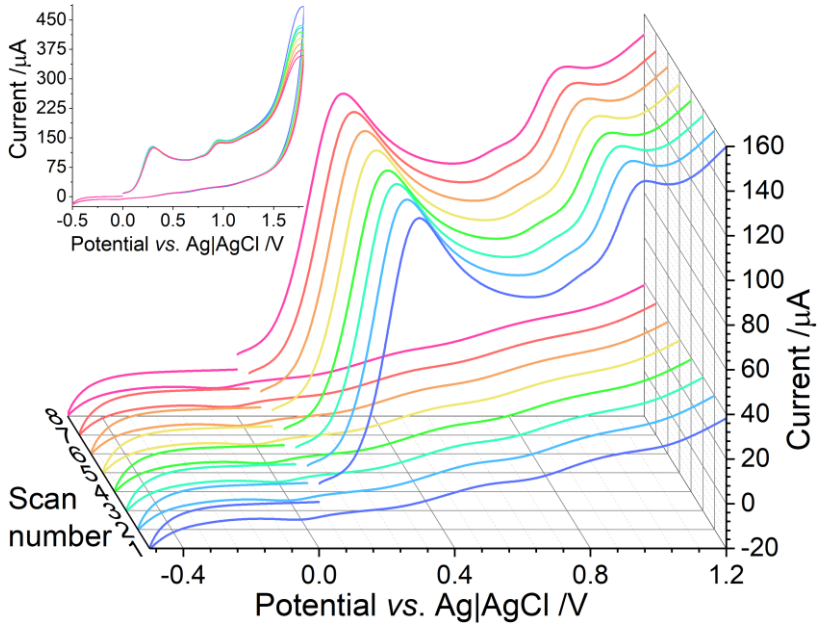


Figure 3.17 Twenty bipolar pulses were applied *in situ* prior to recording each CV in this series, in 1 mM DA at pH 7.0. Inset shows all CVs overlaid without cropping.

At the higher oxidation potentials, the background current decreases at the scan number increases, as the electrode undergoes repeated polarisation treatments. This suggests that the potential window of the BDD have effectively increased, with lower capacitance at high potentials.

Effective though the bipolar pulses are, this report would like to highlight the fleeting nature of surface pre-treatments by electrochemical means in severely fouling analyte. Even

after a single fouling CV, reactivation is necessary. This suggests that long-lasting chemical changes at the BDD surface from the ‘‘activation’’ process do not endure, and that the reproducibility derives from temporary but significant chemical modification of partial regions on the BDD surface, or that electronic effects are the main cause of the change in the rate of electron transfer.

3.3.8 Scanning electron microscopy

Figure 3.18 shows SEM images of six BDD surfaces imaged within an hour of performing electrochemistry. The six conditions are: clean, fouled, clean and then subjected to cathodic pulses, fouled and then subjected to cathodic pulses, clean and then subjected to bipolar pulses, and fouled and then subjected to bipolar pulses. They are representative of the whole active surface, and the contrast and brightness have not been altered after acquisition.

Figure 3.18D is an example of a pristine electrode. The polycrystalline nature of the diamond surface is clearly resolved, and individual crystals of 5–100 μm size can be seen. Differences in electrochemical reactivity in different zones on the BDD surface have been reported in the literature [63,64], and the differing electronic and electron emission properties of the individual crystallites would explain the ‘shading’ effect on certain facets. After extensive CV in DA (Figure 3.18A), fouled BDD had a very cloudy appearance, confirming that the whole surface is fully covered with polydopamine [65]. Thick irregular patches of polymeric material are clearly visible and is especially concentrated at the grain vertices and boundaries. In some places, there are nodules, suggesting that there is preferential growth on existing deposition islands. This film caused a reduction in the contrast between the faces and grain boundaries, making the whole surface appear dull when compared with Figure 3.18D.

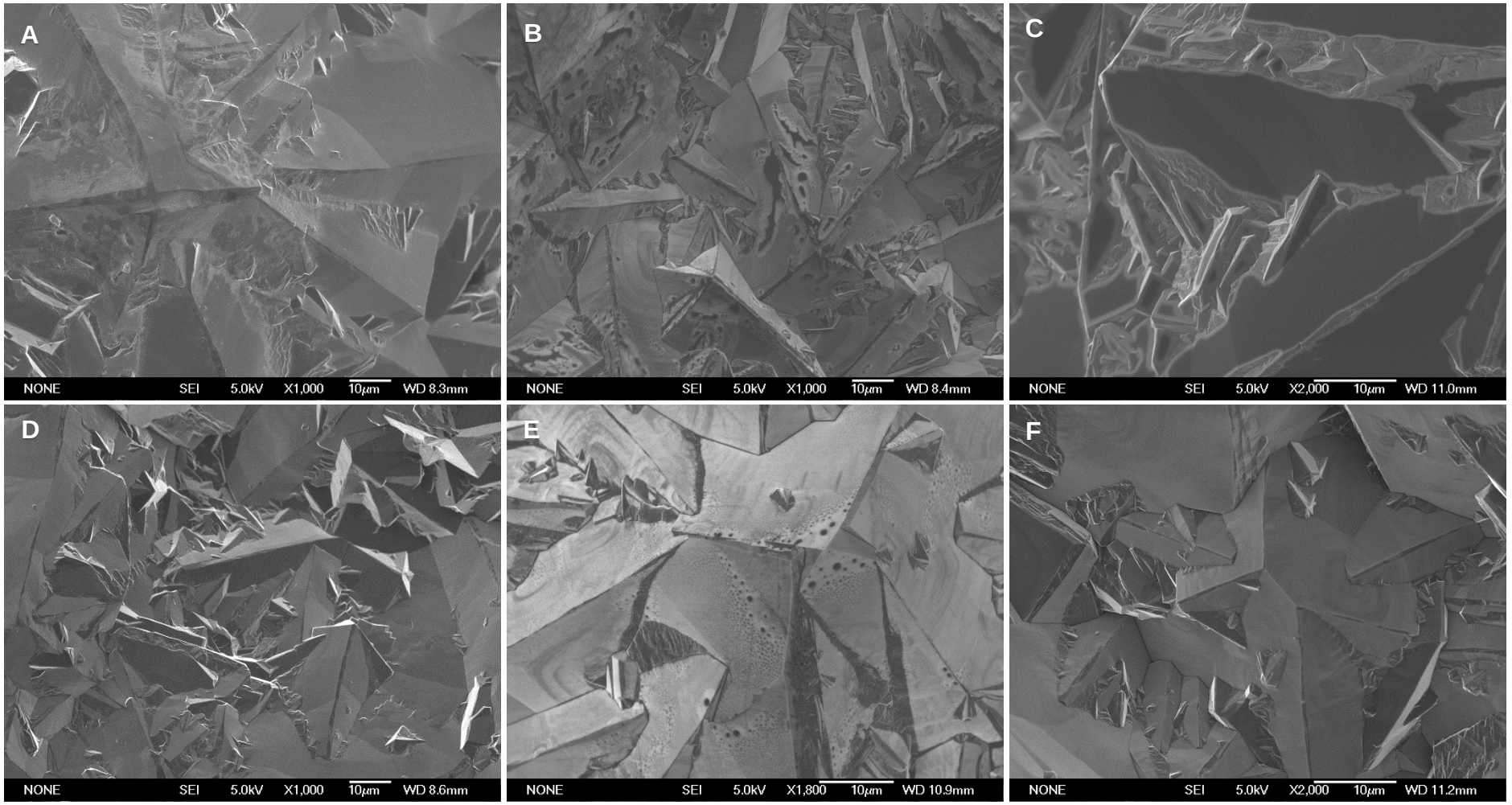


Figure 3.18 (A) An extensively fouled BDD electrode surface after repeated scans in 1 mM DA. (B) A fouled surface after 20 bipolar pulses. (C) A fouled surface after 20 cathodic pulses. (D) A pristine, acid-cleaned oxygen-terminated surface. (E) A pristine surface after 20 bipolar pulses. (F) A pristine surface after 20 cathodic pulses.

For the bipolarly pulsed BDD surfaces (Figure 3.18B,E), the underlying diamond shows much the same contrast as the clean surface. There remained islands of PDA on the surface, some being more than 20 μm long. Panning around with the SEM has shown that the islands preferentially disappeared from the grain boundaries and gather in the middle of the crystal faces. Given the inhomogeneous doping and growth of the BDD plates, it is reasonable to suppose that vertices and joints contain more sp^2 defects, which favour greater electrochemical activity. Surprisingly, on samples that had cathodic-only pulses (Figure 3.18C,F), the grain boundaries appear significantly brighter than the grain faces, and neither were polluted. As only cathodic currents were applied, no •OH could have been generated [66], so this desorption PDA would be attributed to electro-generated H_2 bubbles which were observable by eye. Cathodic pulses have also been linked to hydrogen-termination of BDD surfaces, which suggests that the termination is preferential at the grain boundaries, thus accounting for the stark contrasts [17,25]. Additionally, striations of uncertain origin radiating from the interlocked grains were observed in all BDDs that have been polarised (more clearly visible in Figure 3.18B,E,F), which possibly arose from uneven plasma distributions during growth [64].

This variation in the physical appearance of the samples was also investigated by X-ray photoelectron spectroscopy (XPS), which is a quantitative surface technique that provides elemental and structural information.

3.3.9 Photoelectron X-ray spectroscopy

Spectra were obtained from six freshly prepared BDD electrode surfaces: fouled, fouled then bipolarly pulsed, fouled then cathodically pulsed, acid-cleaned (pristine), pristine then bipolarly pulsed, and pristine then cathodically pulsed. Three random points were sampled from each surface. High-resolution spectra were also recorded for the carbon, oxygen, and nitrogen region. Figure 3.19 shows the survey spectra of all six samples.

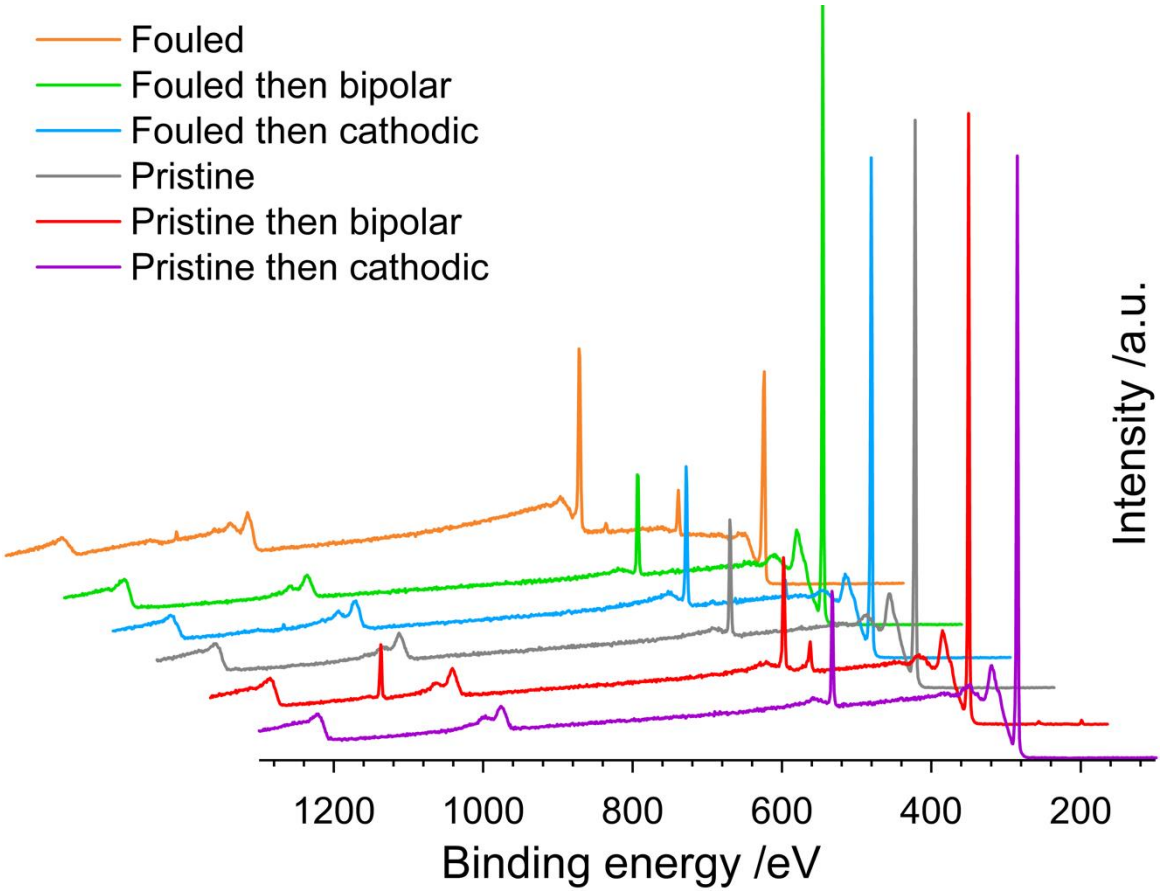


Figure 3.19 Survey spectra of six BDD surfaces.

There is a drastic increase in the background and decrease in the height of the main peaks from the fouled electrode (orange line) in comparison with the other five. Tougaard explains this rising background in terms of the depth-distribution of atoms [67,68]. If all the C atoms are in a surface thin layer, very few electrons will lose energy as they exit the surface, and the peak intensity is high and the background low (all lines except the orange). With C atoms buried at large depths, most electrons will have lost energy through inelastic collisions on their way out and are taken away from the peak-energy and end up in the background at lower energies. This implies that the C concentration is less in the film than in the underlying diamond. Consequently, the peak intensity carries very limited quantitative information. Also, as the amount of material is related to the area of the peak not just the height, if we look at Figure 3.21 where the C 1s peak is much broader than the others, this will translate to the reduced peak height as in the survey spectrum.

Other qualitative observations that can be made of Figure 3.19 is that the red line (pristine then bipolarly pulsed) has distinctive extra peaks (sodium 1s and Auger, and nitrogen 1s) compared to the other five survey spectra, and that the greatest similarity exists between the acid-cleaned sample and the fouled-then-bipolarly-pulsed one. Both will be discussed later in this section.

The atomic percentage from the survey spectra were calculated after applying the Shirley background [69]. The values are displayed in Table 3.1.

Table 3.1 The percentages of carbon, nitrogen, oxygen, sodium in all samples. Blank entries indicate readings undetectably different from zero.

Sample	**carbon**	**oxygen**	**nitrogen**	**sodium**	**phosphorus**	**O:C**
Fouled	70.5	22.5	6.5	0.4		0.32
Fouled bipolar	92.8	7.2				0.08
Fouled cathodic	86.8	11.4	1.7			0.13
Acid-cleaned (pristine)	91.8	8.2				0.09
Pristine bipolar	88.7	8.7		2.1	0.5	0.10
Pristine cathodic	91.9	8.1				0.09

Taking the Figures 3.11–3.13 and values in Table 3.1 together, we see that there is a correlation between good electrochemical performance (both in terms of sensitivity and reproducibility) and samples with small O:C ratios. This fits with the theory discussed in Section 1.1.4 that a more oxidised BDD surface is less reactive. Above a threshold of ~9% oxygen, nitrogen is present, which indicates a sufficient coverage of DA molecules, with their amine groups as the most likely source of nitrogen. The surprising discovery in the survey spectra is the sodium presence: First, that it is there; and second, the only electrode treatment to have resulted in significant sodium is the pristine-then-bipolarly-pulsed one. The sodium 1s and Auger regions for all samples are shown in Figure 3.20.

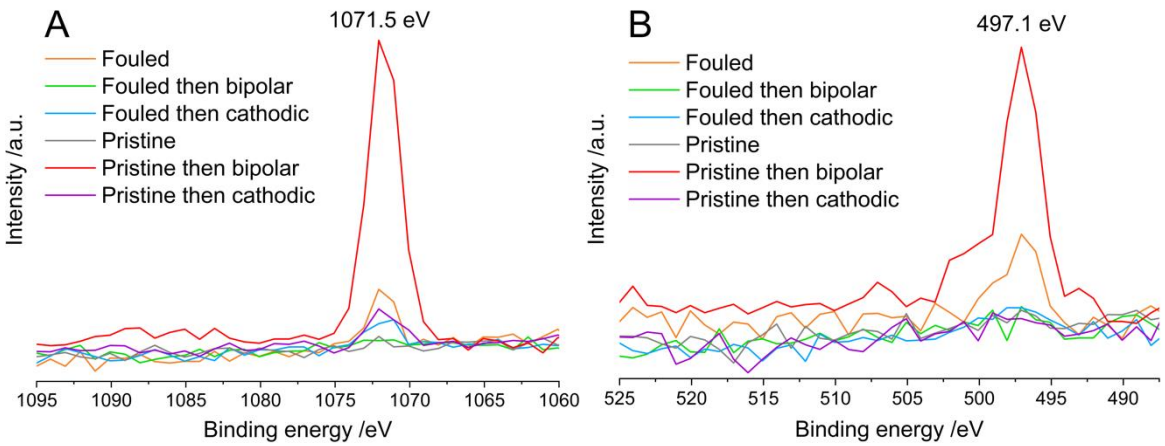


Figure 3.20 Survey spectra scaled for the (A) sodium 1s, and (B) Auger peaks.

The highest sodium presence is in the pristine-then-bipolarly-treated sample, where the 1s peak is accompanied by a strong Auger peak at ~497eV. This combination occurs if the sodium is buried, such as under carbon [70]. And although there is also some sodium on the highly fouled sample, it is much less. This suggests that it is probably there only through experimental errors, such as not rinsing adequately after being immersed in the DA solution, especially as the pristine-then-bipolarly-pulsed sample also shows phosphorus, which means that both components are likely to be from sodium phosphate in the supporting electrolyte.

Next, we shall turn our attention to the carbon peak. It provides quantitative data on the chemical nature of the oxidised carbon on the surface. Figure 3.21 shows the normalised peaks of the carbon 1s region.

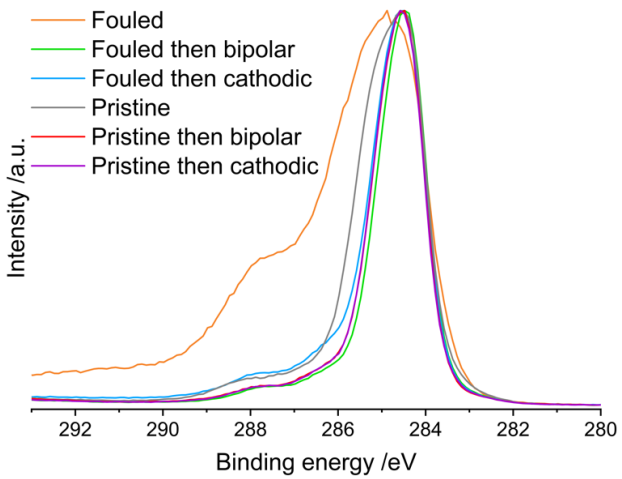


Figure 3.21 Normalised high-resolution carbon 1s spectra of six BDD surfaces.

The normalisation of all spectra demonstrates the stark differences between the fouled sample and the other five ‘clean’ samples. It also shows that the differences arising from the different cleaning methods are subtler. The component fittings of the C 1s spectra are shown in Figure 3.22. There, they are shown to the same y-scale as the fouled-then-bipolarly treated sample to display the differences in intensity of the raw data.

All the high-resolution carbon 1s spectra were fitted with one set of mathematical constraints, designed to capture all possible chemical arrangements and to provide a well-fitted envelope, thus allowing the calculation of average peak positions and group assignations. All components were constrained to have equal and average FWHM, which averaged to 1.0 ± 0.1 eV. The summary of this information is laid out in Table 3.2.

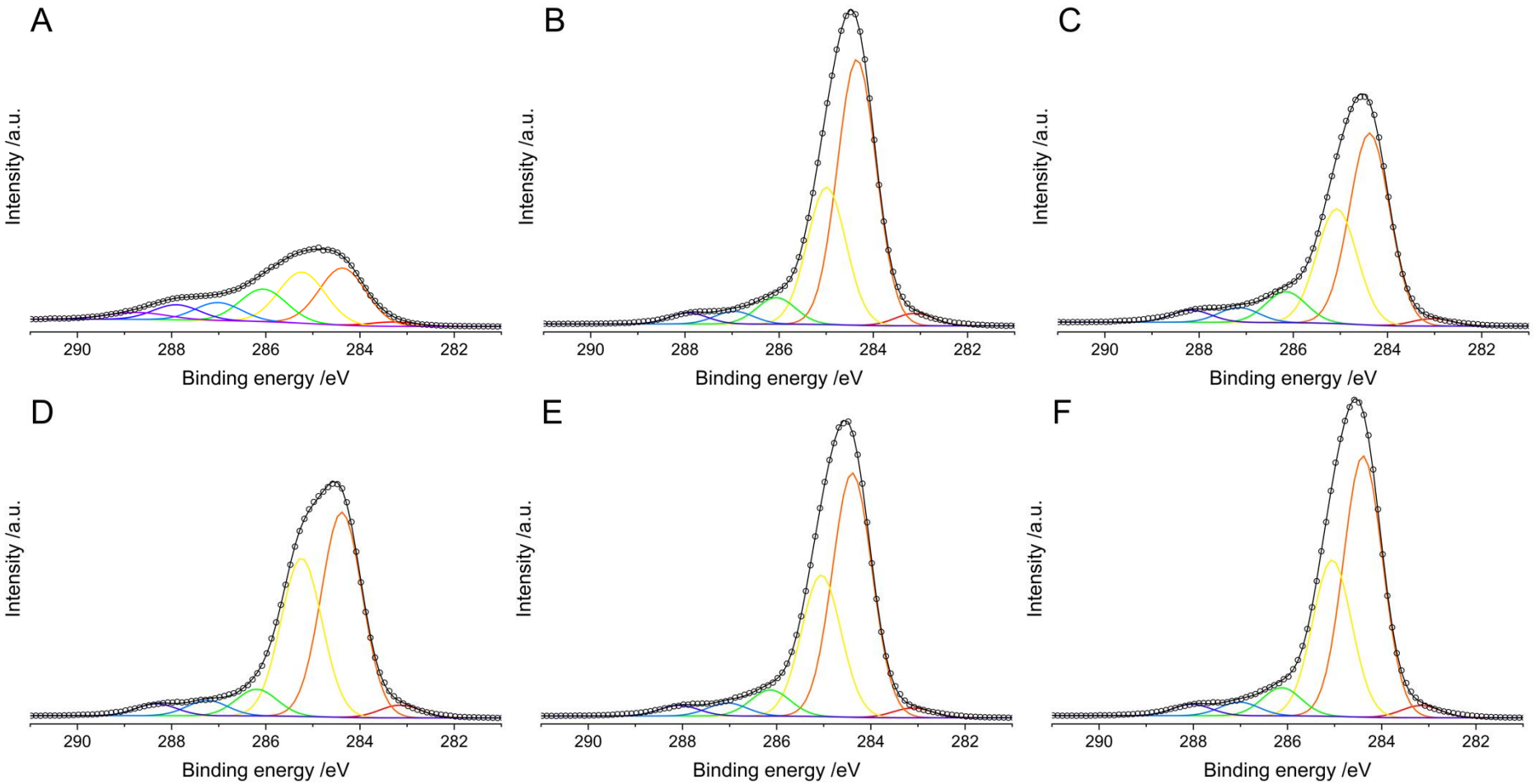


Figure 3.22 Carbon 1s spectra normalised to the fouled-then-bipolarly-pulsed sample. (A) Fouled. (B) Fouled then bipolarly pulsed. (C) Fouled then cathodically pulsed. (D) Pristine. (E) Pristine then bipolarly pulsed. (F) Pristine then cathodically pulsed. Legend: sp^2, sp^3, adsorbed hydrocarbons, alcohol/ether/epoxide, carbonyl, carboxylate, π→π* shake-up satellite, collected data, fitted envelope.

Table 3.2 The binding energies of carbon functionalities and their distribution percentages for all six samples

Functionalities	**Peak centre /eV**	**Shifts /eV**	**Area percentage**					
			Fouled	**Fouled then bipolar**	**Fouled then cathodic**	**Pristine**	**Pristine then bipolar**	**Pristine then cathodic**
sp^2	283.1	–1.3	2.3	2.6	2.0	3.1	2.2	2.7
sp^3	284.4	0.0	30.5	59.3	52.0	47.6	53.3	51.7
Adsorbed hydrocarbons	285.1	+0.7	27.3	27.4	30.3	37.0	33.1	34.3
Alcohol	286.1	+1.7	17.4	5.7	8.5	6.0	5.9	6.0
Carbonyl	287.1	+2.7	9.6	2.8	4.1	3.5	3.2	2.9
Carboxylate	288.1	+3.7	8.0	2.3	3.3	2.8	2.3	2.5
$\pi \rightarrow \pi^*$ shake-up	288.7	+4.4	4.8					

A peak area of less than 3% was detected for all samples at 283.2 eV, corresponding to sp^2 carbon, which can be related to the contribution from grain boundaries of the microcrystalline BDD films. A satellite peak (288.7 eV) was only seen in the severely fouled sample, as is consistent with measurements from species containing extended delocalised electrons (e.g. aromatic rings) such as in PDA. There is a correlation between good electrochemical performance (both in terms of sensitivity and reproducibility) and samples with high levels of sp^3 and low levels of oxidised-carbon states.

Comparing the fouled and pristine samples (Table 3.2), we see that, while boiling the BDD electrodes in acid removes a large amount of higher-oxidised species from the surface, it also leaves a lot of adsorbed-hydrocarbons behind. Of the four pulsed samples, where the sp^2, sp^3, alcohol, carbonyl, and carboxylate areas were not so different, the fouled-then-bipolarly-pulsed one has the lowest adsorbed-hydrocarbon area and showed the best reproducibility in voltammetry (Figure 3.13). Samples represented by the four rightmost columns has similar amounts of adsorbed hydrocarbons, which suggests that its presence affects surface stability, which manifests as variability in the oxidation response.

Comparing the worst and best performers, respectively the fouled and the fouled-then-bipolarly-pulsed samples, the sp^2 and adsorbed-hydrocarbon percentages stay constant, but bipolar pulses removed substantial amounts of oxidised carbon species from 39.8% down to 10.8%, and increased the sp^3 area from 30.5% to 59.3%. This is attributed to the physical lifting off of the adsorbed polymer layers to expose clean BDD underneath, as well as the termination of the surface with hydrogen under cathodic polarisation.

Further insights on the nature of the adsorbates and electrode treatments can be gleaned from the nitrogen 1s region (Figure 3.23).

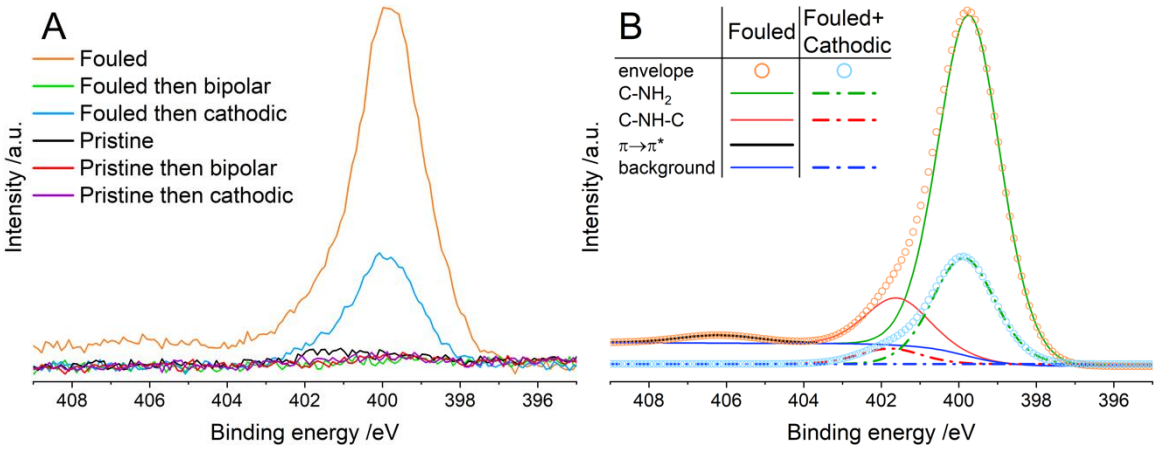


Figure 3.23 High resolution spectra of the nitrogen regions.

Pairing Figure 3.20A and Figure 3.23A, we see that only the fouled electrode shows both sodium and nitrogen. Otherwise, the samples that show nitrogen do not necessarily show sodium. Nitrogen presence on the fouled electrode was expected, as the adsorbates would inevitably show some amine characteristic intrinsic to DA, and perhaps as the polymer layers form, they could trap sodium ions from the supporting electrolyte. The fouled-then-cathodically-pulsed sample surprisingly also shows some nitrogen (1.7%), about a third of that of the fouled electrode (6.5%). The proportions of each fitted component in Figure 3.23B are displayed in Table 3.3.

Table 3.3 Fitted components of the high-resolution N 1s spectra

	Primary amine ($R–NH_2$)	**Secondary amine ($R_1–NH–R_2$)**	**π→π* Shake-up**
Binding energy	399.8 eV	401.9 eV	406.1 eV
Fouled /%	88.8	4.6	6.6
Fouled then cathodic /%	91.0	9.0	

Only the fouled and the fouled-then-cathodically-pulsed samples show a sizeable nitrogen peak, even though both the bipolarly pulsed samples also had visible adsorbates (Figure 3.18B,E). Table 3.3 shows that primary amine (at 399.8 eV, from $C–NH_2$ in dopamine) had the dominant presence, and there were about a tenth as many secondary amines (406.1 eV, from polydopamine C–NH–C) as primary. Only for the fouled sample

is there a shake-up satellite (406.1 eV) just as in the carbon 1s region. Satellites are more likely to occur where the outgoing electrons undergo more than the usual number of inelastic collisions, such as through an amorphous polymer. This observation is in line with SEM observations (Figure 3.18A), where the adsorbates are thickly clustered at the grain boundaries (sometimes into nodules hundreds of nanometres in diameter), showing the formation of polymers. This ratio of primary to secondary amines suggest that the amine tail was preserved during polymerisation, instead of forming into a five-membered heterocycle, such that Figure 3.2 may be modified into Figure 3.24, with a roughly even proportion of C–O and C=O groups (Table 3.2).

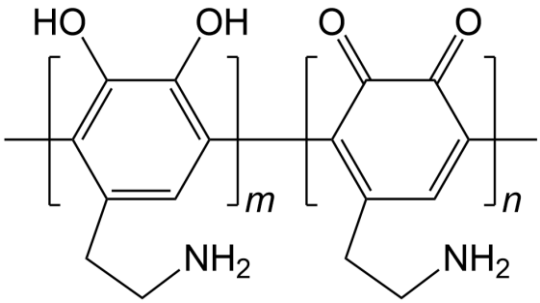


Figure 3.24 The likely structure of the polydopamine formed via electrooxidation.

The XPS data backs up our electrochemical observations that, for an electrode that has never been scanned in DA, applying either cathodic or bipolar polarisations will produce surfaces more active than the acid-cleaned one, by reducing the presence of adsorbed hydrocarbons. Although the cathodic-only treatment will rid a fouled surface of adsorbates (Figure 3.18C,F), it also leaves more adsorbed hydrocarbons (affecting stability) and more oxidised carbon species (affecting sensitivity) than the bipolar treatment.

3.4 Conclusions

The important neurotransmitter dopamine (DA) is known to form extremely adherent polymer layers during oxidation at electrode surfaces, which prevent reproducible electrochemical measurements with common electrode materials. In this project, we used electrodes made from BDD in an attempt to avoid this problem, as the material is naturally more resistant to fouling. This choice of material allowed us to apply more extreme electrochemical procedures for cleaning and stabilising the electrode surface and observe how these affect DA oxidation.

Diamond was observed to foul rapidly during voltametric studies with DA. The extent of fouling largely depended on how much the electrode is scanned in the anodic range. So increased numbers of scans and increasingly anodic potential limits increase the extent of fouling. A thick (>100 nm) adsorbed layer was observed, via SEM, to be deposited on the electrode surface during these studies. Unsuprisingly, the longer the electrode spent at positive potentials, the thicker this layer grew and more seriously affected were subsequent measurements. Voltammetry with $Ru(NH_3)_6Cl_3^{3+}$ demonstrated that this deposit was sufficiently insulating to hinder reliable quantification of the analyte concentration. Analysis of the XPS nitrogen 1s spectra showed that this layer consisted mostly of primary amines with some secondary amines, indicating that polymers were formed, where the amine tail was preserved instead of forming into a five-membered heterocycle.

As chemical and mechanical methods to try to remove this fouling layer required the complete disassembly of our electrode housing, which prevented the exact replication of experiments, *in situ* electrochemical cleaning procedures were investigated. Anodic, cathodic, and bipolar polarisation, applied with or without the presence of DA, were used to investigate their effect on the electron-transfer kinetics for dopamine CVs. The marker for the efficacy of these treatments was the DA oxidation potential and its magnitude.

Anodic polarisation, applied either in a series of short pulses or in one go, in DA solution, increased the oxidation potential and halved the current response on the next scan. This effect was similar to that exhibited by the fouled surface, except that the redox response did not progressively become more positive with added cycles of polarisations. We also discovered that a pulse of two seconds allowed the electrode to reach a stable limit of poor reactivity faster than with twenty 100 ms pulses. At potentials beyond +2.5 V, significant amounts of hydroxyl radicals are produced which could break down polymer chains. The vigorous oxygen bubbles can then lift these off. However, at the same time, fresh DA is still being oxidised, and continues to form into sticky chains. These competing effects meant that anodic polarisation alone did not reactivate the electrode.

Cathodic polarisation, applied in a series of short pulses in DA solution or in blank buffer, tended to decrease the oxidation potential and increase peak magnitude, though with poor stability. However, when the same is applied in its unpulsed form, the opposite happened, where the activity of the electrode is not much better than in the acid-cleaned case. There are natural advantages to applying cathodic pulses in the case of DA. First, this is the region where the oxidised DA will undergo reduction and thus be prevented from participating in future polymerisation reactions, so already the number of likely fouling culprits is less. Second, for our BDD electrode, –1.5 V is the threshold for hydrogen production. So, for the same 100 ms pulse, cathodic polarisation produces more radicals than the anodic. Thus, the adsorbates are more attacked. Finally, there is significant generation of hydrogen bubbles during cathodic polarisation. This, paired with greater damage inflicted by radicals, means that there can be greater loss of adsorbed polymer mass compared than with the same situation under anodic pulses.

Overall, it was observed that many pulses worked better than one lengthy application, anodic polarisation has a stabilising effect, and cathodic polarisation increased the activity

of the surface higher than did acid-cleaning. The most effective activation was a train of twenty 100 ms current pulses of amplitude 10 mA cm^{-2} applied *in situ* prior to recording CVs, and it is important to end the pulse train with cathodic polarisation. These pulses, used in the presence of DA, produced more-active surface states than those found with pristine BDD electrodes. Moreover, the responses were highly stable and reproducible over successive scans.

For electrodes in general, the one drawback of this cleaning method is that it requires the electrode material to be chemically inert, to be able to withstand large currents, and to be without surface additions that could be dislodged along with the undesired deposits. The work described in this chapter affirms that BDD, which accords with these requirements, is highly suited to electrochemical studies of molecules likely to cause fouling problems, such as dopamine—especially if minimal mechanical disruption to the measurement set-up is desired, such as in medical implants.

References

[1] P. Chen and R. L. McCreery, "Control of electron transfer kinetics at glassy carbon electrodes by specific surface modification," *Analytical Chemistry*, vol. 68, no. 22, pp. 3958–3965, 1996, doi: 10.1021/ac960492r.

[2] D. Kotnik, M. Novič, W. R. LaCourse, and B. Pihlar, "Cathodic re-activation of the gold electrode in pulsed electrochemical detection of carbohydrates," *Journal of Electroanalytical Chemistry*, vol. 663, no. 1, pp. 30–35, 2011, doi: 10.1016/j.jelechem.2011.09.026.

[3] P. Gan, R. G. Compton, and J. S. Foord, "The voltammetry and electroanalysis of some estrogenic compounds at modified diamond electrodes," *Electroanalysis*, vol. 25, no. 11, pp. 2423–2434, 2013, doi: 10.1002/elan.201300362.

[4] A. Dekanski, J. Stevanović, R. Stevanović, B. Ž. Nikolić, and V. M. Jovanović, "Glassy carbon electrodes: I. Characterization and electrochemical activation," *Carbon*, vol. 39, pp. 1195–1205, 2001, doi: 10.1016/S0008-6223(00)00228-1.

[5] C. Moreno-Castilla, M. A. Ferro-Garcia, J. P. Joly, I. Bautista-Toledo, F. Carrasco-Marin, and J. Rivera-Utrilla, "Activated carbon surface modifications by nitric acid, hydrogen peroxide, and ammonium peroxydisulfate treatments," *Langmuir*, vol. 11, no. 11, pp. 4386–4392, 1995, doi: 10.1021/la00011a035.

[6] E. Vanhove et al., "Stability of H-terminated BDD electrodes: An insight into the influence of the surface preparation," *Physica Status Solidi (A) Applications and Materials Science*, vol. 204, no. 9, pp. 2931–2939, 2007, doi: 10.1002/pssa.200776340.

[7] I. Duo, C. Levy-Clement, A. Fujishima, and C. Comninellis, "Electron transfer kinetics on boron-doped diamond Part I: Influence of anodic treatment," *Journal of Applied Electrochemistry*, vol. 34, no. 9, pp. 935–943, 2004, doi: 10.1023/B:JACH.0000040525.76264.16.

[8] Z. J. Ayres, S. J. Cobb, M. E. Newton, and J. V. Macpherson, "Quinone electrochemistry for the comparative assessment of sp^2 surface content of boron doped diamond electrodes," *Electrochemistry Communications*, vol. 72, pp. 59–63, 2016, doi: 10.1016/j.elecom.2016.08.024.

[9] L. Hutton, M. E. Newton, P. R. Unwin, and J. V. Macpherson, "Amperometric oxygen sensor based on a platinum nanoparticle-modified polycrystalline boron doped diamond disk electrode," *Analytical Chemistry*, vol. 81, no. 3, pp. 1023–1032, 2009, doi: 10.1021/ac8020906.

[10] Y. Wang, E. I. Rogers, and R. G. Compton, "The measurement of the diffusion coefficients of ferrocene and ferrocenium and their temperature dependence in acetonitrile using double potential step microdisk electrode chronoamperometry," *Journal of Electroanalytical Chemistry*, vol. 648, no. 1, pp. 15–19, 2010, doi: 10.1016/j.jelechem.2010.07.006.

[11] L. Jiang, G. W. Nelson, J. Abda, and J. S. Foord, "Novel modifications to carbon-based electrodes to improve the electrochemical detection of dopamine," *ACS Applied Materials & Interfaces*, vol. 8, no. 42, pp. 28338–28348 2016, doi: 10.1021/acsami.6b03879.

[12] P. Jolly, N. Formisano, J. Tkáč, P. Kasák, C. G. Frost, and P. Estrela, "Label-free impedimetric aptasensor with antifouling surface chemistry: A prostate specific antigen case study," *Sensors and Actuators, B: Chemical*, vol. 209, pp. 306–312, 2015, doi: 10.1016/j.snb.2014.11.083.

[13] X. Cai, E. E. L. Tanner, C. Lin, K. Ngamchuea, J. S. Foord, and R. G. Compton, "The mechanism of electrochemical reduction of hydrogen peroxide on silver nanoparticles," *Physical Chemistry Chemical Physics*, vol. 20, no. 3, pp. 1608–1614, 2018, doi: 10.1039/c7cp07492a.

[14] J. Svanberg-Larsson et al., "A comparison of explicitly-terminated diamond electrodes decorated with gold nanoparticles," *Electroanalysis*, vol. 28, no. 1, pp. 88–95, 2016, doi: 10.1002/elan.201500442.

[15] "A unique gold medal," NobelPrize.org, 1998. https://www.nobelprize.org/prizes/about/the-nobel-medals-and-the-medal-for-the-prize-in-economic-sciences/ (accessed May 20, 2020).

[16] M. C. Granger et al., "Standard electrochemical behaviour of high-quality, boron-doped polycrystalline diamond thin-film electrodes," *Analytical Chemistry*, vol. 72, no. 16, pp. 3793–3804, 2000, doi: 10.1021/ac0000675.

[17] L. A. Hutton, J. G. Iacobini, E. Bitziou, R. B. Channon, M. E. Newton, and J. V. Macpherson, "Examination of the factors affecting the electrochemical performance of oxygen-terminated polycrystalline boron-doped diamond electrodes," *Analytical Chemistry*, vol. 85, pp. 7230–7240, 2013, doi: 10.1021/ac401042t.

[18] N. Yang et al., "Conductive diamond: synthesis, properties, and electrochemical applications," *Chemical Society Reviews*, 2018, doi: 10.1039/C7CS00757D.

[19] W. Gajewski et al., "Electronic and optical properties of boron-doped nanocrystalline diamond films," *Physical Review B - Condensed Matter and Materials Physics*, vol. 79, no. 4, pp. 1–14, 2009, doi: 10.1103/PhysRevB.79.045206.

[20] M. I. Landstrass and K. V. Ravi, "Resistivity of chemical vapor deposited diamond films," *Applied Physics Letters*, vol. 55, no. 10, pp. 975–977, 1989, doi: 10.1063/1.101694.

[21] Y. Tanaka et al., "Electrochemical properties of N-doped hydrogenated amorphous carbon films fabricated by plasma-enhanced chemical vapor deposition methods," *Electrochimica Acta*, vol. 56, no. 3, pp. 1172–1181, 2011, doi: 10.1016/j.electacta.2010.11.006.

[22] A. F. Sartori et al., "Laser-Induced Periodic Surface Structures (LIPSS) on heavily boron-doped diamond for electrode applications," *ACS Applied Materials and Interfaces*, vol. 10, no. 49, pp. 43236–43251, 2018, doi: 10.1021/acsami.8b15951.

[23] G. J. Offer and A. R. Kucernak, "Calculating the coverage of saturated and sub-saturated layers of carbon monoxide adsorbed onto platinum," Journal of *Electroanalytical Chemistry*, vol. 613, no. 2, pp. 171–185, 2008, doi: 10.1016/j.jelechem.2007.10.028.

[24] N. Elgrishi, K. J. Rountree, B. D. McCarthy, E. S. Rountree, T. T. Eisenhart, and J. L. Dempsey, "A practical beginner's guide to cyclic voltammetry," *Journal of Chemical Education*, vol. 95, no. 2, pp. 197–206, 2018, doi: 10.1021/acs.jchemed.7b00361.

[25] G. R. Salazar-Banda, L. S. Andrade, P. A. P. Nascente, P. S. Pizani, R. C. Rocha-Filho, and L. A. Avaca, "On the changing electrochemical behaviour of boron-doped diamond surfaces with time after cathodic pre-treatments," *Electrochimica Acta*, vol. 51, no. 22, pp. 4612–4619, 2006, doi: 10.1016/j.electacta.2005.12.039.

[26] H. B. Suffredini, V. A. Pedrosa, L. Codognoto, S. A. S. Machado, R. C. Rocha-Filho, and L. A. Avaca, "Enhanced electrochemical response of boron-doped diamond electrodes brought on by a cathodic surface pre-treatment," *Electrochimica Acta*, vol. 49, no. 22-23 SPEC. ISS., pp. 4021–4026, 2004, doi: 10.1016/j.electacta.2004.01.082.

[27] R. Trouillon, Y. Einaga, and M. A. M. Gijs, "Cathodic pretreatment improves the resistance of boron-doped diamond electrodes to dopamine fouling," *Electrochemistry Communications*, vol. 47, pp. 92–95, 2014, doi: 10.1016/j.elecom.2014.07.028.

[28] M. A. Rodrigo, P. A. Michaud, I. Duo, M. Panizza, G. Cerisola, and Ch. Comninellis, "Oxidation of 4-chlorophenol at boron-doped diamond electrode for wastewater treatment," *Journal of The Electrochemical Society*, vol. 148, no. 5, p. D60, 2001, doi: 10.1149/1.1362545.

[29] S. C. B. Oliveira and A. M. Oliveira-Brett, "Voltammetric and electrochemical impedance spectroscopy characterization of a cathodic and anodic pre-treated boron doped diamond electrode," *Electrochimica Acta*, vol. 55, no. 15, pp. 4599–4605, 2010, doi: 10.1016/j.electacta.2010.03.016.

[30] J. De Sanoit, R. Kiran, and E. Scorsone, "Method of activating a doped diamond electrode," US 2013/0313120 A1, 2013

[31] R. Kiran, E. Scorsone, P. Mailley, and P. Bergonzo, "Quasi-real time quantification of uric acid in urine using boron doped diamond microelectrode with *in situ* cleaning," *Analytical Chemistry*, vol. 84, no. 23, pp. 10207–10213, 2012, doi: 10.1021/ac301177z.

[32] D. K. Belghiti, E. Scorsone, J. de Sanoit, and P. Bergonzo, "Simultaneous detection of indole and 3-methylindole using boron-doped diamond electrodes," *Physica Status Solidi (A) Applications and Materials Science*, vol. 213, no. 10, pp. 2662–2671, 2016, doi: 10.1002/pssa.201600187.

[33] W. Schultz, "Updating dopamine reward signals," *Current Opinion in Neurobiology*,

vol. 23, no. 2, pp. 229–238, 2013, doi: 10.1016/j.conb.2012.11.012.

[34] A. C. Michael and J. B. Justice, "Oxidation of dopamine and 4-methylcatechol at carbon fiber disk electrodes," *Analytical Chemistry*, vol. 59, no. 3, pp. 405–410, 1987, doi: 10.1021/ac00130a006.

[35] K. T. Kawagoe and R. M. Wightman, "Characterization of amperometry for in vivo measurement of dopamine dynamics in the rat brain," *Talanta*, vol. 41, no. 6, pp. 865–874, 1994, doi: 10.1016/0039-9140(94)E0064-X.

[36] B. D. Bath, H. B. Martin, R. M. Wightman, and M. R. Anderson, "Dopamine adsorption at surface modified carbon-fiber electrodes," *Langmuir*, vol. 17, no. 22, pp. 7032–7039, 2001, doi: 10.1021/la0106844.

[37] R. A. Zangmeister, T. A. Morris, and M. J. Tarlov, "Characterization of polydopamine thin films deposited at short times by autoxidation of dopamine," *Langmuir*, vol. 29, no. 27, pp. 8619–8628, 2013, doi: 10.1021/la400587j.

[38] S. Chumillas, T. Palomäki, M. Zhang, T. Laurila, V. Climent, and J. M. Feliu, "Analysis of catechol, 4-methylcatechol and dopamine electrochemical reactions on different substrate materials and pH conditions," *Electrochimica Acta*, vol. 292, 2018, doi: 10.1016/j.electacta.2018.08.113.

[39] H. Lee, S. M. Dellatore, W. M. Miller, and P. B. Merssersmith, "Mussel-inspired surface chemistry for multifunctional coatings," *Science*, vol. 318, no. 5849, pp. 426–430, 2007, doi: 10.1126/science.1147241.

[40] X. Du et al., "Uv-triggered dopamine polymerization: Control of polymerization, surface coating, and photopatterning," *Advanced Materials*, vol. 26, no. 47, pp. 8029–8033, 2014, doi: 10.1002/adma.201403709.

[41] G. Loget, J. B. Wood, K. Cho, A. R. Halpern, and R. M. Corn, "Electrodeposition of polydopamine thin films for DNA patterning and microarrays," *Analytical Chemistry*, vol. 85, no. 21, pp. 9991–9995, 2013, doi: 10.1021/ac4022743.

[42] E. Amstad, T. Gillich, I. Bilecka, M. Textor, and E. Reimhult, "Ultrastable iron oxide nanoparticle colloidal suspensions using dispersants with catechol-derived anchor groups," *Nano Letters*, vol. 9, no. 12, pp. 4042–4048, 2009, doi: 10.1021/nl902212q.

[43] B. Fei et al., "Coating carbon nanotubes by spontaneous oxidative polymerization of dopamine," *Carbon*, vol. 46, no. 13, pp. 1795–1797, 2008, doi: 10.1016/j.carbon.2008.06.049.

[44] J. lei Wang et al., "Electropolymerization of dopamine for surface modification of complex-shaped cardiovascular stents," *Biomaterials*, vol. 35, no. 27, pp. 7679–7689, 2014, doi: 10.1016/j.biomaterials.2014.05.047.

[45] M. E. Lynge, R. van der Westen, A. Postma, and B. Städler, "Polydopamine—a nature-inspired polymer coating for biomedical science," *Nanoscale*, vol. 3, no. 12, pp. 4916–4928, 2011, doi: 10.1039/c1nr10969c.

[46] A. N. Zelikin, "Drug releasing polymer thin films: New era of surface-mediated drug delivery," *ACS Nano*, vol. 4, no. 5, pp. 2494–2509, 2010, doi: 10.1021/nn100634r.

[47] Y. Yu, Y. Wu, J. J. Liu, Y. Zhan, and D. Wu, "Ultrasmall dopamine-coated nanogolds: preparation, characteristics, and CT imaging," *Journal of Experimental Nanoscience*, vol. 11, no. 1, pp. S1–S11, 2016, doi: 10.1080/17458080.2015.1102343.

[48] J. Liebscher et al., "Structure of polydopamine: A never-ending story?," *Langmuir*, vol. 29, no. 33, pp. 10539–10548, 2013, doi: 10.1021/la4020288.

[49] S. J. Cobb, Z. J. Ayres, M. E. Newton, and J. V. Macpherson, "Deconvoluting surface-bound quinone proton coupled electron transfer in unbuffered solutions: toward a universal voltammetric pH electrode," *Journal of the American Chemical Society*, vol. 141, no. 2, pp. 1035–1044, 2019, doi: 10.1021/jacs.8b11518.

[50] J. V. Macpherson, "A practical guide to using boron doped diamond in electrochemical research," *Physical Chemistry Chemical Physics*, vol. 17, no. 5, pp. 2935–49, 2015, doi: 10.1039/c4cp04022h.

[51] A. J. Bard, F. R. F. Fan, J. Kwak, and O. Lev, "Scanning Electrochemical Microscopy. Introduction and Principles," *Analytical Chemistry*, vol. 61, no. 2, pp. 132–138, 1989, doi: 10.1021/ac00177a011.

[52] H. V. Patten, L. A. Hutton, J. R. Webb, M. E. Newton, P. R. Unwin, and J. V. Macpherson, "Electrochemical 'read–write' microscale patterning of boron doped diamond electrodes," *Chemical Communications*, vol. 51, no. 1, pp. 164–167, 2015, doi: 10.1039/c4cc07830f.

[53] Y. Wang, J. G. Limon-Petersen, and R. G. Compton, "Measurement of the diffusion coefficients of $[Ru(NH_3)_6]^{3+}$ and $[Ru(NH_3)_6]^{2+}$ in aqueous solution using microelectrode double potential step chronoamperometry," *Journal of Electroanalytical Chemistry*, vol. 652, no. 1–2, pp. 13–17, 2011, doi: 10.1016/j.jelechem.2010.12.011.

[54] R. G. Compton and C. E. Banks, "Partially blocked electrodes," in *Understanding Voltammetry*, 2nd edn, London: Imperial College Press, 2011, pp. 197–200.

[55] R. Kiran, E. Scorsone, J. de Sanoit, J.-C. Arnault, P. Mailley, and P. Bergonzo, "Boron doped diamond electrodes for direct measurement in biological fluids: An *in situ* regeneration approach," *Journal of The Electrochemical Society*, vol. 160, no. 1, pp. 67–73, 2013, doi: 10.1149/2.014302jes.

[56] R. Trouillon and D. O'Hare, "Comparison of glassy carbon and boron doped diamond electrodes: Resistance to biofouling," *Electrochimica Acta*, vol. 55, no. 22, pp. 6586–6595, 2010, doi: 10.1016/j.electacta.2010.06.016.

[57] A. Fujishima, T. N. Rao, E. Popa, B. V. Sarada, I. Yagi, and D. A. Tryk, "Electroanalysis of dopamine and NADH at conductive diamond electrodes," *Journal of Electroanalytical Chemistry*, vol. 473, no. 1, pp. 179–185, 1999, doi: 10.1016/S0022-0728(99)00106-0.

[58] D. A. Tryk, H. Tachibana, H. Inoue, and A. Fujishima, "Boron-doped diamond electrodes: The role of surface termination in the oxidation of dopamine and ascorbic

acid," *Diamond and Related Materials*, vol. 16, no. 4-7 SPEC. ISS., pp. 881–887, 2007, doi: 10.1016/j.diamond.2007.02.002.

[59] M. Carmo, D. L. Fritz, J. Mergel, and D. Stolten, "A comprehensive review on PEM water electrolysis," *International Journal of Hydrogen Energy*, vol. 38, no. 12, pp. 4901–4934, 2013, doi: 10.1016/j.ijhydene.2013.01.151.

[60] B. Stöckle et al., "Precise control of polydopamine film formation by electropolymerization," *Macromolecular Symposia*, vol. 346, no. 1, pp. 73–81, 2014, doi: 10.1002/masy.201400130.

[61] F. R. Simões, L. A. Pocrifka, L. F. Q. P. Marchesi, and E. C. Pereira, "Investigation of electrochemical degradation process in polyaniline/polystyrene sulfonated self-assembly films by impedance spectroscopy," *Journal of Physical Chemistry B*, vol. 115, no. 38, pp. 11092–11097, 2011, doi: 10.1021/jp2041668.

[62] J. Tamm, U. Johanson, M. Marandi, T. Tamm, and L. Tamm, "Study of the properties of electrodeposited polypyrrole films," *Russian Journal of Electrochemistry*, vol. 40, no. 3, pp. 388–392, 2004.

[63] K. Juttner and D. Becker, "Characterization of boron-doped diamond electrodes by electrochemical impedance spectroscopy," *Journal of Applied Electrochemistry*, vol. 37, pp. 27–32, 2007, doi: 10.1007/s10800-006-9228-6.

[64] Z. J. Ayres, J. C. Newland, M. E. Newton, S. Mandal, O. A. Williams, and J. V. Macpherson, "Impact of chemical vapour deposition plasma inhomogeneity on the spatial variation of sp^2 carbon in boron doped diamond electrodes," *Carbon*, vol. 121, pp. 434–442, 2017, doi: 10.1016/j.carbon.2017.06.008.

[65] C. Tao, S. Yang, J. Zhang, and J. Wang, "Surface modification of diamond-like carbon films with protein via polydopamine inspired coatings," *Applied Surface Science*, vol. 256, no. 1, pp. 294–297, 2009, doi: 10.1016/j.apsusc.2009.08.024.

[66] S. Siahrostami, G. L. Li, V. Viswanathan, and J. K. Nørskov, "One- or two-electron water oxidation, hydroxyl radical, or H_2O_2 evolution," *Journal of Physical Chemistry Letters*, vol. 8, no. 6, pp. 1157–1160, 2017, doi: 10.1021/acs.jpclett.6b02924.

[67] S. Tougaard, "Practical algorithm for background subtraction," *Surface Science*, vol. 216, no. 3, pp. 343–360, 1989, doi: 10.1016/0039-6028(89)90380-4.

[68] S. Tougaard, "QUASES-Tougaard Manual—Quantitative Analysis of Surfaces by Electron Spectroscopy. Version 5.1.," 2011.

[69] D. A. Shirley, "High-resolution x-ray photoemission spectrum of the valence bands of gold," *Physical Review B*, vol. 5, no. 12, pp. 4709–4714, 1972, doi: 10.1103/PhysRevB.5.4709.

[70] "Sodium," Thermo Fisher Scientific Inc. XPS Simplified, 2013. https://www.jp.xpssimplified.com/elements/sodium.php

Chapter 4

Electrochemical characterisation of 2-amino-9-fluorenone and its interaction with DNA

4.1 Introduction

Combustion-engine exhaust products are either particulates or molecular chemicals such as CO_2, CO, NO_2, and polycyclic aromatic hydrocarbons (PAHs) [1]. The PAHs persist in the environment, where they degrade to oxy and amino derivatives, some of which are suitable for electrochemical detection in aqueous environments [2]. The detection of such molecules is important because many of them are harmful to human health, being known mutagens. The work in this chapter investigates one such derivatised PAH: 2-Amino-9-fluorenone (2-AFN).

2-Amino-9-fluorenone (Figure 4.1) is a relatively newly identified environmental pollutant. The chemical is an amino derivative of fluoren-9-one, which in turn is the oxidation product, via metabolic or photolytic degradation, of PAHs such as fluoranthene and fluorene [2]. 2-AFN is also one of the major photoproducts from irradiating 2-aminofluorene with UV-A (320–400 nm) [3]. Furthermore, exposing solutions of 2-AFN to UV-A oxidised the nitrogen group, leading to the formation of the direct-acting mutagen 2-nitro-fluorenone [4]. This photoreaction is a physical mimic of enzymatic metabolism, and the 2-nitro-fluorenone was stable for several weeks when stored in sealed vials in the dark [5]. While the direct mutagenicity of 2-AFN has not been studied, the ease with which

it is converted from amino-fluorene into nitro-fluorenone by simple UV-A irradiation, which accounts for approximately 95% of the UV radiation reaching the Earth's surface [6], means that it is a worthy candidate of study. The carbonyl group on 2-AFN is cathodically reducible, and its amino group is anodically oxidisable [7], which means that it metabolises easily, reacts readily with a wide range of biomolecules, and is well suited for investigation using electrochemistry.

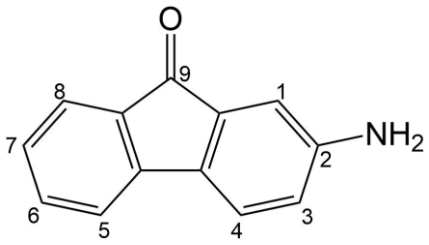


Figure 4.1 Chemical structure of 2-amino-9-fluorenone (2-aminofluoren-9-one).

Chemical identification of 2-AFN and other fluorenones and their kinetics of formation have been studied via mass spectrometry, chromatography, electrochemistry, UV–vis spectroscopy, and photochemistry since the 1980s. In their pioneering work, Empis and Herold (1986) performed the first cyclic voltammetry experiments on 9-fluorenones with different substituents at positions 2 or 3, and studied the effect of these substitutions on half-wave potential [8]. Later, Zeisig and Möller (1995) investigated the genotoxic effect of 2-AFN, along with fluorene, pyrene, and their nitro, amino and acetylamino derivatives, *in vitro*, using ^{32}P-postlabelling high-performance liquid chromatography, and it was observed that these species form adducts with DNA (calf thymus) in varying quantities [9]. In 2006, 2-AFN in water was used as a fluorescent probe for the molecular recognition of β-cyclodextrin, which is a toroidal saccharide polymer that mimics enzymes used in drug delivery and is important for supramolecular chemistry research [10]. In his thesis submitted in 2010, Vyskočil developed electrochemical techniques to detect oxo-derivatives of fluorene [11]. More recently, Hájková and her colleagues have carried out several voltammetric studies of 2-AFN on mercury and glassy-carbon electrodes [14,15].

The long-lasting nature of its contamination of water and soil highlights the need for continuous monitoring in those environments [14]. Given the material advantages of BDD for aqueous electrochemistry in difficult settings (Section 1.2), this present research is well placed to extend the work of Vyskočil et al. and put the abilities of BDD to the test.

2-Amino-9-fluorenone was originally found in groundwater near sites of processing and purification of natural gas [15]. It and its derivatives have since been found in urban environments [16], and their incorporation has been associated with a non-negligible increase in human cancer risk [17].

Practically, to investigate the interaction between 2-AFN and real genetic material, short double-stranded DNA (dsDNA) would be the primary candidate. Nucleic acids are made of many nucleotides. Nucleotides contain a nucleobase (purine or pyrimidine), a ribose sugar (or its deoxy form), and a phosphate group which makes it negatively charged. Nucleosides are nucleotides without the phosphate, and consequently neutral. The decision was made to work with nucleosides, as they produce responses closer to natural DNA oxidation [18]. In the region for 2-AFN oxidation, and therefore also where DNA is probed, guanosine (G) and adenosine (A) are the bases which were expected to be oxidised (Figure 4.2).

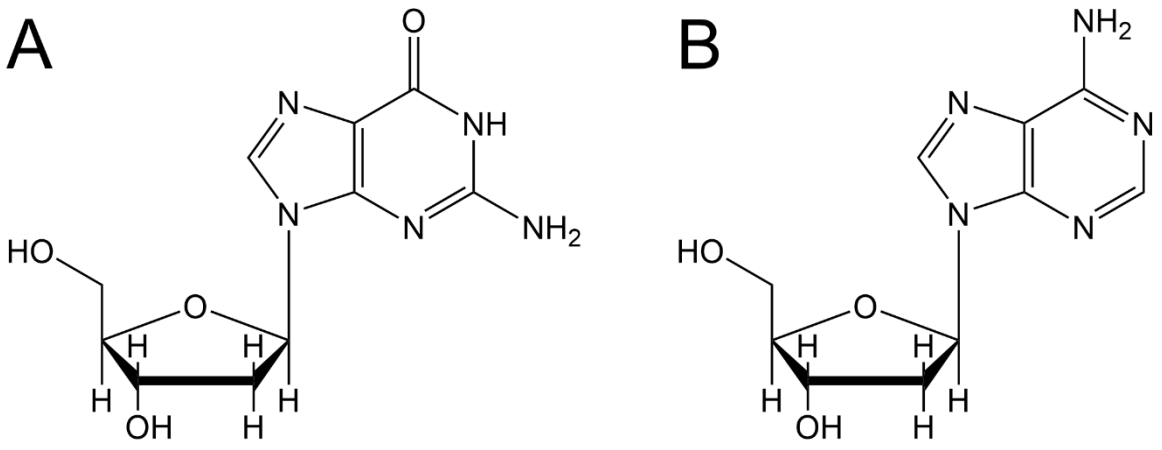


Figure 4.2 The nucleosides studied in this work. (A) Guanosine. (B) Adenosine.

Investigating the electrochemistry of nucleosides first would provide the proximate

peak potentials, detection limits, and linear regions before the more complex dsDNA experiments later. This would form an instructive stepping stage to refine the voltammetry parameters to optimise the signal strengths from both 2-AFN and dsDNA. Also, G and A are important bases to study in terms of disease monitoring. Guanosine modulates glutamate transport and suppresses the destructive effects of Alzheimer's and Parkinson's diseases [19], while the modulation of A is beneficial for epilepsy, chronic pain, cerebral ischemia, and alcoholism [20,21]. The relative popularity of certain DNA-adduct classes depends on their ease and method of detection. A good body of literature exists for G-adducts, whether in chemical assays or as theoretical calculations [22,23]. This helps to link gathered electrochemical data with structural information.

A majority of the electrochemical work involving nucleic acids is in sensor development for mediating designated chemical reactions [24–26]. This work aims to detect and quantify the level of DNA damage. Aside from the bonding of pollutants to certain bases, planar aromatic structures can insert between the stacked base pairs. This can cause a subtle lengthening of the DNA helix, increasing strain within the sugar–phosphate backbone and untwisting of the helix. These effects may expose oxidation sites and alter the electrochemical response. The approach in this work generates a measurable response from label-free and reagentless interactions, which makes it a simple and robust way to observe supramolecular interactions.

This work explores the use of bipolarly pre-treated BDD electrodes (1) to evaluate the voltammetric behaviour of 2-AFN, nucleosides, and DNA strands, (2) to compare the performance of bare BDD with other electrode materials, and (3) to study the interaction between 2-AFN and double-stranded DNA. The third aim is of considerable interest, given that DNA-electrochemical biosensors can simulate *in vivo* nucleic acid interactions with carcinogenic compounds, and is a growing area of research [27].

4.2 Experimental details

All BDD electrodes (Element Six) were treated by acid boiling and cyclic scanning in weak nitric acid before exposure to buffer solutions and analytes, as described in Section 3.2.1. The pH was measured using the Mettler-Toledo pH meter (Leicester, UK) with a combined glass electrode by the same producer.

4.2.1 Reagents and solutions

The 2-amino-9-fluorenone, guanosine, adenosine, dsDNA (low-molecular-weight salmon sperm, product no. 31149, solubility of 10 mg/mL, <100 base pairs), sodium acetate, and acetic acid were purchased from Sigma-Aldrich (Gillingham, UK), and were used without further purification. Solutions (100 μM) of 2-AFN were prepared by weighing. The solids were first dissolved in a minimal volume of methanol (< 3 mL), and the rest of the volume made up with 0.1 M sodium acetate buffer (NaAcB) at pH 4.0. To reach a wider pH range without changing the composition of the background electrolyte, the universal Carmody buffer was trialled [28]. So, experiments at pH 4.0 were carried out in both NaAcB and Carmody buffer; and later experiments were done only in Carmody buffer. Stock and dilute solutions were stored in glassware in the dark at laboratory temperature (22 ± 1°C). Carmody buffers of a wide range of pH were made in batches when necessary and stored in glass bottles, and stringently checked for cleanliness.

Stock solutions of adenosine and guanosine were made fresh on the day of each experiment. Due to the imprecision in the molecular weights of dsDNA, its dilutions are stated in mg/mL rather than in molar concentrations. The dsDNA powder and its stock solutions were stored at –18°C. After the desired reaction concentrations were mixed in a separate vessel, they were kept in an ice bath until a few minutes before electrochemical measurements. Each mixture was then allowed to come to room temperature and exposed to the BDD only for the duration of each voltammogram.

4.2.2 Voltammetry parameters

Investigative CVs were performed using 50 μM solutions, scanned from –0.4 to +1.2 V at a variety of scan rates from 10 to 400 mV s^{-1}. In DPV, the potential was scanned from 0 to +1.7 V against a 1.0 M Ag|AgCl reference, which was sufficient to cover the oxidations of both 2-AFN and the DNA peaks. The step size was 4.6 mV, at a modulation amplitude 46 mV for 4 ms, and with an interval of 45.7 ms. This produced a scan rate of 100.2 mV s^{-1}.

4.3 Results and discussions

4.3.1 Cyclic voltammetry

The first experiments with 2-AFN were done with a pristine oxygen-terminated BDD electrode. That meant that the BDD plate was boiled in concentrated H_2SO_4 (98%) saturated with KNO_3 for 30 min, rinsed, and then again boiled in H_2SO_4 (98%) only. After this, all electrodes were cyclically scanned in 0.1 M HNO_3, at 0.1 V s^{-1}, starting at 0 V, and then between +2.5 to –1.7 V, for at least 30 cycles. Only then was the electrode rinsed, dried, and then exposed to 2-AFN. Scans in 50 μM 2-AFN and buffer are shown in Figure 4.3.

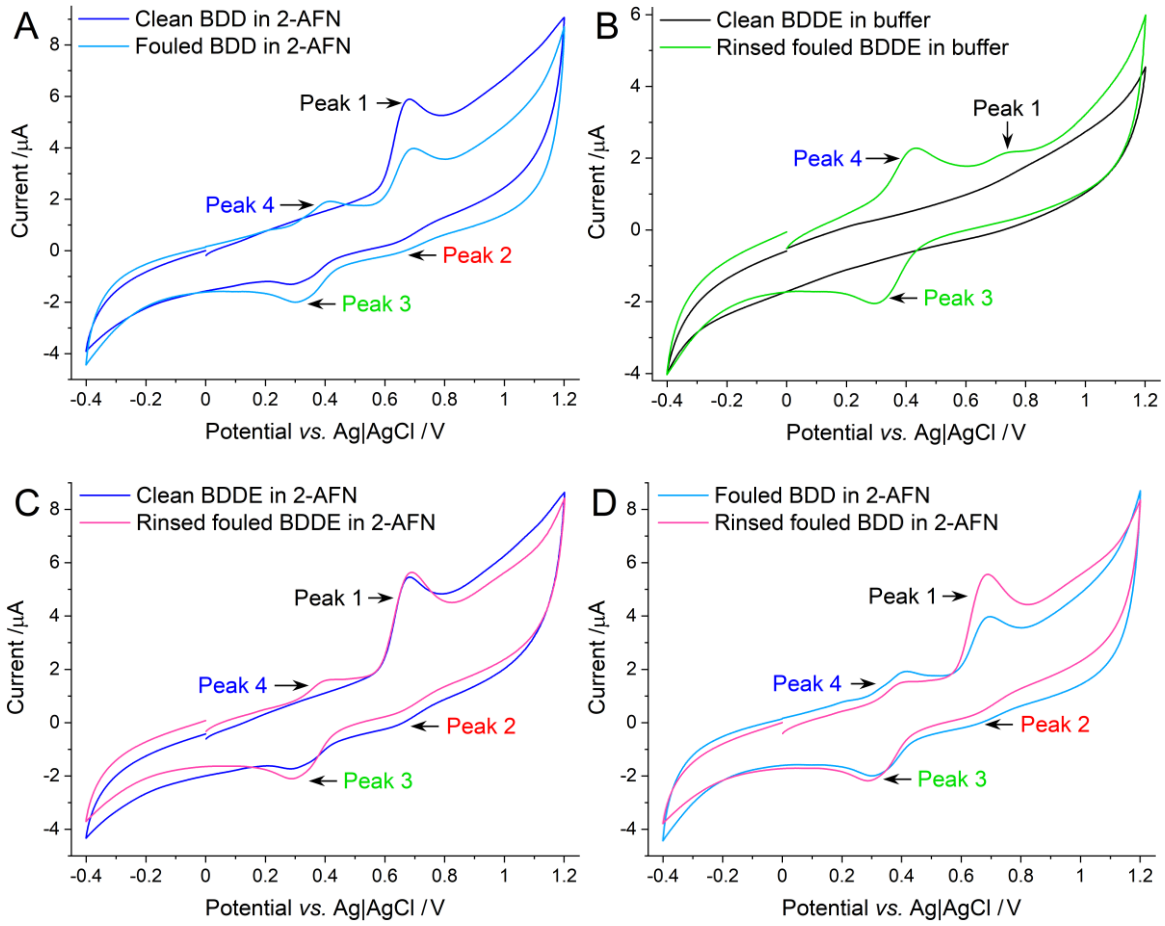


Figure 4.3 (A) Clean-BDDE CVs in 50 uM of 2-AFN in 0.2 M pH 4.0 sodium acetate buffer at a scan rate of 100 mV s^{-1}. (B,C) Compared CVs of rinsed fouled BDDE with CVs of clean BDDE in buffer and in 2-AFN, respectively. (D) Compared responses of rinsed and not-rinsed fouled BDD in 2-AFN.

From the first scan in Figure 4.3A, it can be seen that 2-AFN undergoes irreversible oxidation at a BDD electrode (unequal peaks 1 and 2), followed by a secondary reduction. From the second scan, the huge drop in the peak 1 magnitude and the appearance of peak 4 suggests that some subsequent chemical or electrochemical process occurs. Figure 4.3B shows that peaks 3 and 4 cannot be removed by rigorous rinsing with D.I. water, and also that rinsing does not perfectly remove all the analyte (as peak 1 persists). Figure 4.3C shows that, if a fouled electrode is rinsed and then replaced in the same analyte solution, it is just as active in oxidising 2-AFN (similar peak 1 heights) as a clean electrode. Figure 4.3D

shows that the rinsed fouled electrode is better than a fouled unrinsed electrode at oxidising 2-AFN (peak 1 for the former is higher). Both the fouled and fouled-and-rinsed electrodes exhibit a higher reduction peak 3 than that of the clean electrode, and peak 4 always shows. This suggests that a fouled electrode encourages greater reduction of some products from the forward scan.

In summary, a single CV scan of an acid-cleaned BDD electrode oxidises and reduces 2-AFN (peaks 1 and 2). This deposited groups on the surface (peaks 3 and 4) which cannot be removed by rinsing, and deposited material which fouls but can be washed off by rinsing. Thus, repeated measurements in 2-AFN causes significant deviation of the electrode surface from its clean state, and a process needs to be created to allow further work with this molecule to be reproducible.

4.3.2 Surface restoration

Application of the electro-activation technique discussed in Chapter 3 naturally recommended itself. As discussed in Chapter 3, during activation, the electrode surface is alternately highly anodically or cathodically polarized. During anodic polarization, hydroxyl breaks down polymer chains, and the associated generation of gaseous species aids desorption of adsorbed organic compounds by electro-generated gaseous species [29]. Under cathodic conditions, hydrogen radicals attack the adsorbates indiscriminately and aid the diffusion of these products away from the electrode [30]. At the same time, the pulses mildly increase the hydrogen-termination of the whole BDD surface [31]. Because of this, each pulse train always ends with cathodic polarisation.

In any case, it was found that twenty bipolar pulses (±10 mA cm^{-2} of 100 ms each) did not adequately produce an electrode that excluded peak 4, so the number of pulses was increased to forty, and then to sixty, until peak 4 does not appear in a first scan. This pulsing technique not only removes any adsorbates from the surface, but also produces a BDD

surface that is more active than the acid-cleaned BDD surface. However, this pre-treatment depends on the solution in which it is carried out, and Figure 4.4 shows the data. For Figure 4.4A, the electrochemical pre-treatment and analysis were carried out in the same 50 µM 2-AFN solution (*in situ*), and for Figure 4.4B the pre-treatment was carried out in blank buffer (*ex situ*). In both figures, this pre-treatment was applied before every scan.

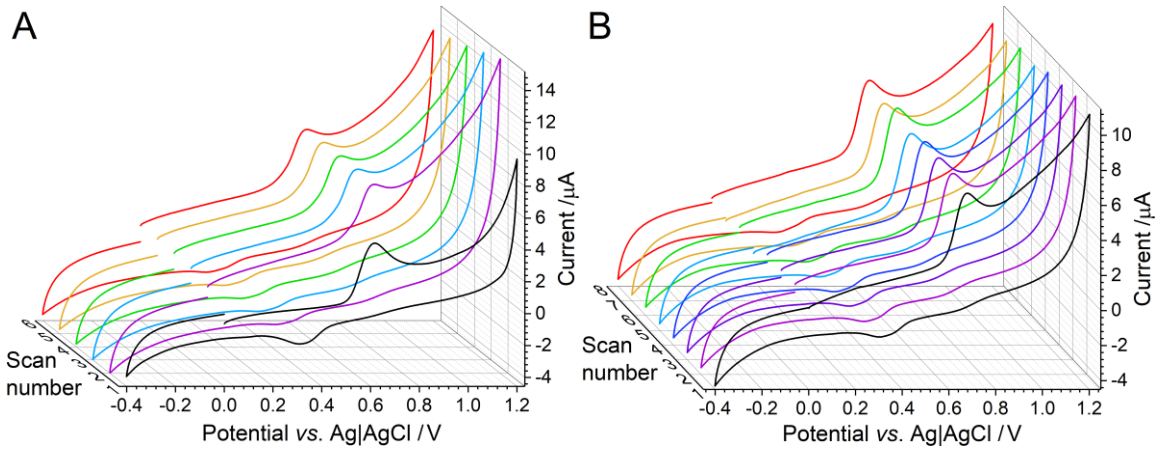


Figure 4.4 Sixty ±10 mA cm^{-2} pulses of 100 ms were applied (A) *in situ* and (B) *ex situ* prior to recording the CVs in 50 µM 2-AFN dissolved in 0.1 M NaAcB at pH 4.0. The scan rate was 100 mV s^{-1}.

In both activation situations, from scan number 2, the oxidation and reduction peak potentials of all subsequent scans stayed constant. The big differences are in Figure 4.4A, where the second (purple) scan shows increased redox currents and higher peak potentials than the first (black). Both were recorded after an acid-cleaned electrode was bipolarly pulsed *in situ*.

Even though there are minor variations in the magnitude of the peak currents in Figure 4.4B, the peak definition and positions did not change throughout the eight scans. At this stage, it was more useful to obtain reproducibility efficiently than know the exact chemical structure of adsorbate on the surface. So a conclusion was reached that, for future scans, polarisations in a blank buffer solution, *ex situ*, should be applied. This way, we avoid generating irrelevant reaction products during the pulsing procedure itself.

4.3.3 Successive scans

Armed with the pulsing procedure, investigations into 2-AFN oxidation could be more freely conducted efficiently. The potential range was between –0.4 V and +1.2 V, with each scan starting and ending at 0 V. Figure 4.5A shows the CVs from twenty successive scans in 50 µM 2-AFN, and Figures 4.5B,C show the first two scans and their baselines.

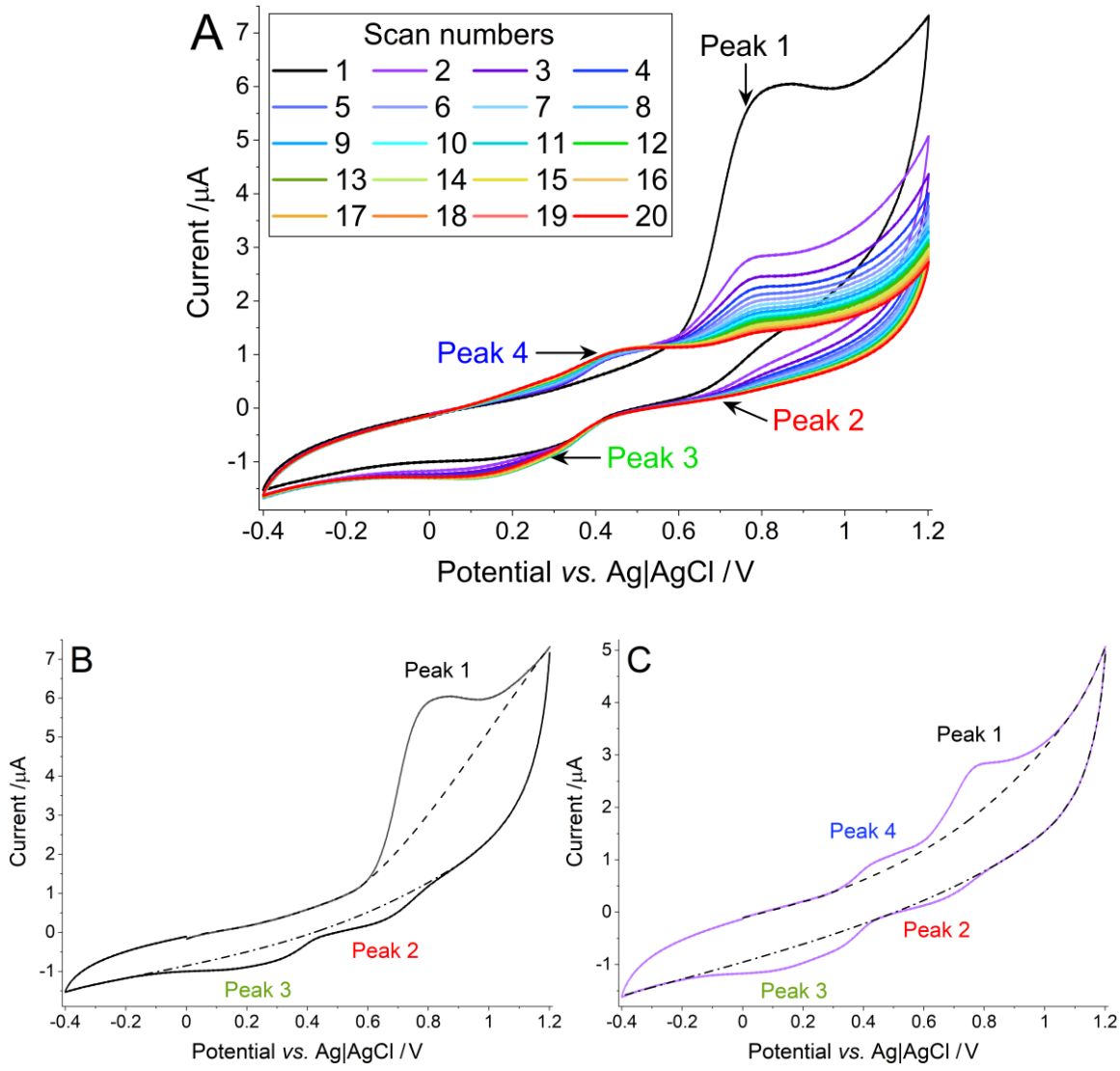


Figure 4.5 Cyclic voltammograms taken at 100 mV s^{-1} in 50 µM 2-AFN in 0.1 M NaAcB. (A) Twenty scans successively. (B) The first scan. (C) The second scan. Dotted lines charts in B and C show the baselines for the forward and back scans.

Four peaks were identified via manual subtraction of their baselines. The first scan (Figure 4.5B) shows one oxidation peak at 0.78 V (peak 1) and two reduction peaks at

+0.67 V (peak 2) and +0.28 V (peak 3). On the second scan (Figure 4.5C), a new peak appears at +0.44 V (peak 4) which moves to +0.46 V by the 20th scan. From the peak separation (larger than 59 mV) and inequality in the redox peak magnitudes, it can be concluded that 2-AFN undergoes irreversible oxidation. For the rest of this chapter, all CV peaks will be referred to with these labels.

The most drastic changes are between scans 1 and 2: the magnitude of peak 1 decreased by 0.48 µA, peak 2 decreased by 0.17 µA, and a new peak 4 appears with a magnitude of 0.08 µA. Thereafter, peaks 3 and 4 quickly increase in magnitude to approximately constant values, and peaks 1 and 2 decrease steadily to never regain their original height. Throughout the twenty scans, the total charge from reduction stays around 2.25 µC, whereas the total charge from oxidation events decreases from 8.25 µC in the first scan to 2.74 µC in the second, to settle around 1.38 µC by the twentieth. This means that the first scan already encompasses all the major redox events affecting the greatest change in subsequent electrode behaviour.

Given that the electrode surface cannot be restored to a clean state by rinsing, and that peak 4 appears only after the first reverse scan is complete, it is highly likely that peak 4 is an electroactive adsorptive feature. Scan-rate experiments were performed to check this hypothesis.

4.3.4 Scan-rate dependence

The electrodes were exposed to 50 µM of 2-AFN at pH 4.0 for two cycles at one scan rate, then taken out and bipolarly pulsed in a blank buffer, and then placed back in the analyte solution for scans of another rate. Figure 4.6 shows the influence of scan rate, ν, on the redox features in the first and second scans.

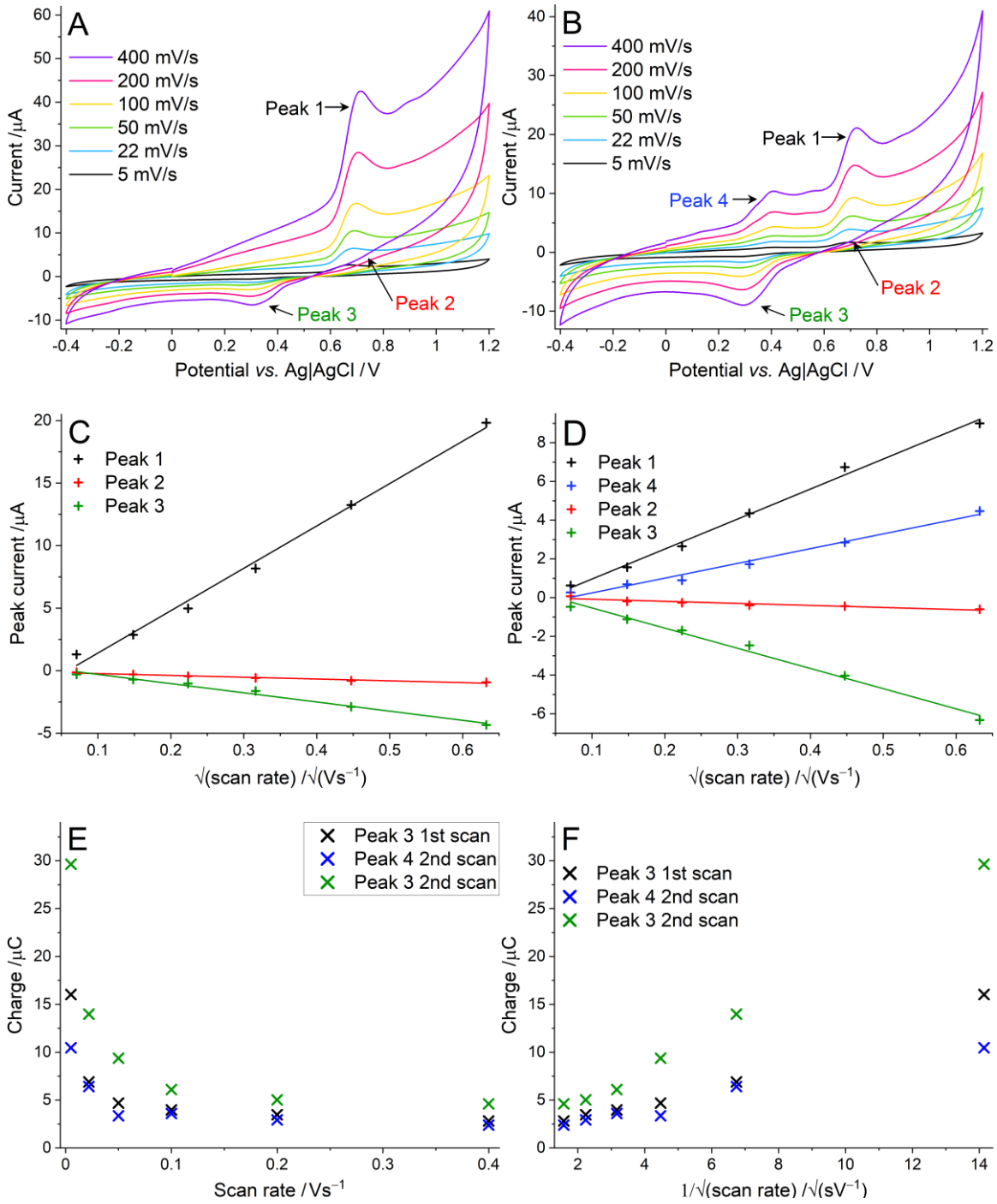


Figure 4.6 (A,B) Respectively the first and second CVs scans in 50 µM of 2-AFN at pH 4.0, at different scan rates (from 5 to 400 mV s^{-1}). (C,D) The peak currents from the first and second scans, respectively, plotted against the square root of the scan rate. (E,F) The charge encompassed by peaks 3 and 4 from both scans plotted against respectively the scan rate and the inverse of the square root of the scan rate.

Figures 4.6A,B show the peak potential of both redox peaks move further apart as ν increases, in line with previous observations of the electrode kinetics of these BDD plate electrodes. Figures 4.6C,D show the linear relationships of the peak currents versus the square root of the scan rate (i_p *vs.* $\sqrt{\nu}$), suggesting that the both the oxidation and reduction of 2-AFN is controlled by diffusional mass transport [32]. Furthermore, Table 4.1 shows the coefficient of determination, R^2, when linear regression was fitted to peak currents plotted against either ν or $\sqrt{\nu}$. The higher R^2 values conclusively show that a linear relationship only exists with respect to $\sqrt{\nu}$ for all peaks in both scans.

Table 4.1 The coefficients of determination, R^2, for all first and second scans peaks

	Scan 1, R^2		**Scan 2, R^2**	
	i_{Ox} *vs.* $\sqrt{\nu}$	i_{Ox} *vs.* ν	i_{Ox} *vs.* $\sqrt{\nu}$	i_{Ox} *vs.* ν
Peak 1	0.991	0.973	0.997	0.960
Peak 2	0.967	0.839	0.970	0.860
Peak 3	0.998	0.958	0.998	0.954
Peak 4			0.994	0.975

Only for peak 1 of scan 1 can it be assumed that the concentration of unoxidized 2-AFN in the solution is zero, and that there is no electrostatic or adsorptive behaviour prior to applying a potential. This fulfils the initial boundary conditions for deriving meaningful analytical information from that linear relationship. According to the reversible Randles–Sevčik equation $i_P = 2.69 \times 10^5 n^{\frac{3}{2}}[A]_{bulk} A\sqrt{D}\sqrt{v}$, assuming a geometric electrode area of 44.2 mm^2, and a one-electron oxidation, in 0.1 M sodium acetate buffer at pH 4.0, the diffusion coefficient of 2-AFN was calculated to be $8.1\,(\pm 0.6)\times10^{-10}$ m^2 s^{-1}, which is similar to that of other molecules of a similar size [33].

From Figure 4.6 it is clear that peaks 3 and 4 are a redox couple, as the amounts of charge transferred for both essentially overlap. Figure 4.6E shows that the charge decreases

with increasing scan rate, reaching a near-constant value above 100 mV s^{-1}. This would be the case whether the surface has been passivated by an adsorbed species or not. As at high scan rates, there is less time for the diffusion to take place, simply to a bare surface or having to penetrate through some polymeric pores. However, the experiment of transferring the electrode out the system (Figure 4.3B) demonstrates that peaks 3 and 4 are associated with surface-bound species. If the concentration of the bound species is constant, then the current of both peaks would be proportional to ν and not to $\sqrt{\nu}$. However, if the amount of material deposited is itself a function of scan rate, so that the concentration of the bound species changes with time, then the effect of a $\sqrt{\nu}$ dependence would become more prominent. The total charge under the curve can be expressed as a sum of surface-capacitive charge (a constant) and a diffusion-controlled charge (proportional to $1/\sqrt{\nu}$) [34]. The linear behaviour of peaks 3 and 4 in Figure 4.6F suggest that the amount of charge could be due to species having concentrations dependent on the scan rate.

From the voltammetry evidence so far, it is certain that adsorption occurred, though the nature of the adsorbates is unclear. As redox of the carbonyl group is a well-known proton-dependent reaction, and since proton exchange is expected in the polymerisation process, the next experiment varied the pH of the analyte solution to investigate the redox properties of the two functional groups of 2-AFN.

4.3.5 pH dependence

Previous research on 2-AFN detection with glassy carbon electrodes found that the position of the peak potentials varied linearly with respect to the pH of the supporting electrolyte [13]. The aim was to repeat this experiment with BDD electrodes and use the information to decipher the cause of the extra peaks 3 and 4. From this point on, sodium acetate buffer was replaced by Carmody universal buffer to restrict the variety of buffer compounds as pH changed. The baseline-subtracted CVs for the first oxidation and reduction scans are

shown in Figures 4.7A,C, and for the second oxidation scans in Figure 4.7E, and their corresponding peak potentials are shown in Figures 4.7B,D,F.

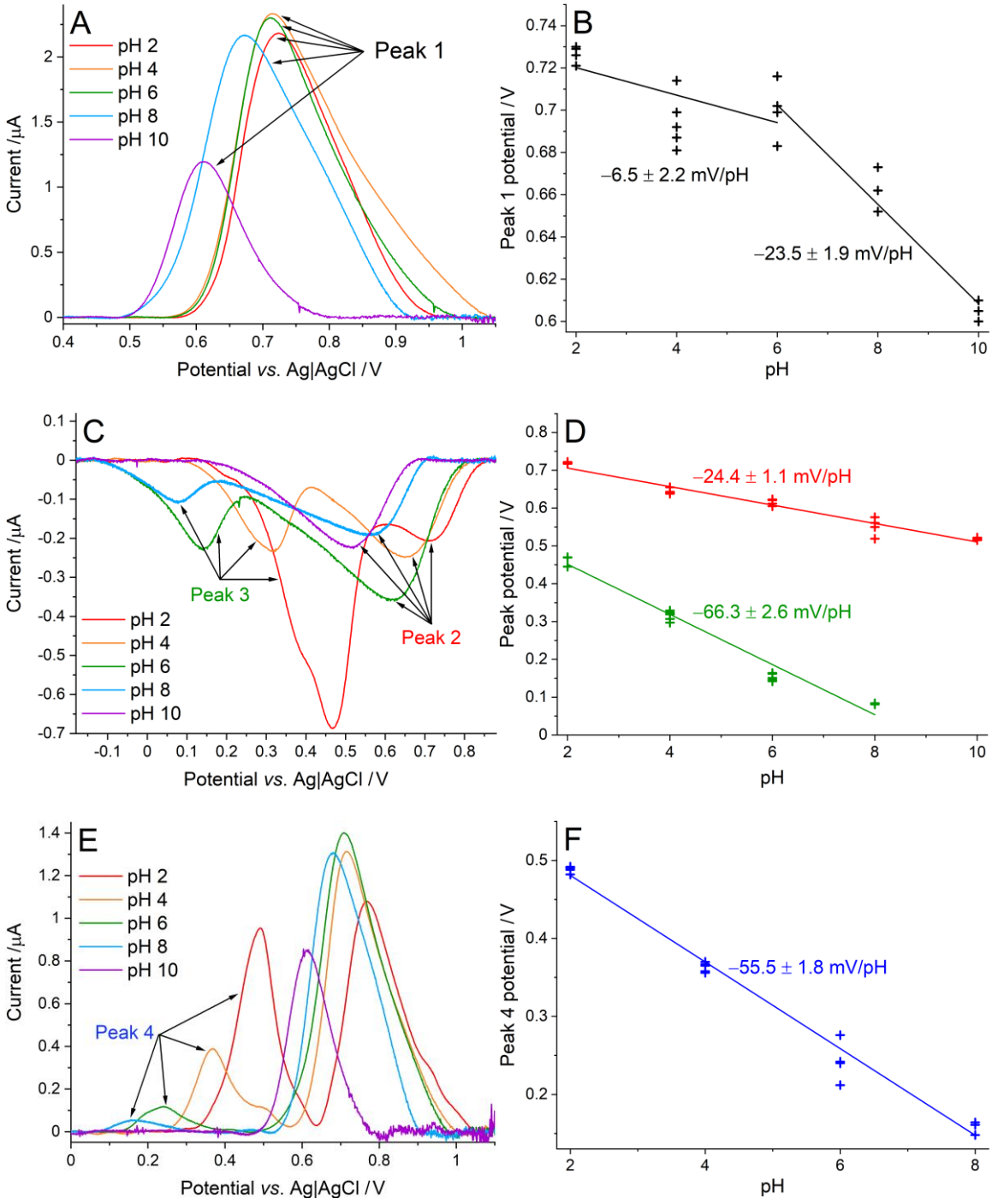


Figure 4.7 (A,C) The background-subtracted forward and reverse scans of the first CV at different pH values between 2.0 and 10.0. The scan rate was 100 mV s^{-1}. (E) Forward scans of the second cycle. (B,D,F) Scatter chart plotting the movement of the oxidation and reduction peak potentials. Charts A,C,E

Figure 4.7A shows peak 1 from the first forward scan, and Figure 4.7B shows the peak potentials of all repeated experiments. If a linear regression is fitted for all the data points in Figure 4.7B, its slope would be –13.1 mV/pH, which is a weak correlation that has no known chemical reference. However, by viewing the data as two segments, peak 1 is essentially independent of pH below pH 6.0 (–6.5 mV/pH) and has a proton dependence at above pH 6.0 (–23.5 mV/pH). The pH-dependence of peak 2 is –24.4 mV/pH for all pH values. The separation between peaks 1 and 2 is ~53 mV, suggesting that they form a redox pair. In the electrochemically reversible case, the Nernst equation takes into account the number of protons and electrons transferred, such that the potential changes according to

$$potential = const - 2.303\frac{m}{n}\frac{RT}{F}pH$$

where *m* is the number of protons, *n* is the number of electrons, and *R, T, and F* are the usual quantities [35]. How the potential behaves depends on the proton concentration and the equilibrium constant K for the proton-transfer step. In one case, where $[H^+] \ll K$ (above pH 6.0), assuming that $m = 1$ and $n = 2$, the theoretical slope is –23.4 mV/pH. In the other, where $[H^+] \gg K$ (below pH 8.0), the potential stays constant, as all the 2-AFN is already in its protonated form. Given the above analysis, peak 1 could be attributed to the two-electron–one-proton oxidation of the amino group (NH_2) to its radical cation $NH_2^{\bullet+}$, which is stabilised by its delocalised π-system, leading to the formation of dimers in acidic conditions [12,36].

Further oxidation of the dimer could also lead to head-to-tail polymerisation by the radical, similar to aniline polymerisation [37]. Although the big drop in peak 1 current between scans 1 and 2 suggests that the oxidation product is partially blocking the electrode surface, work with aminofluorene and diaminofluorene show that their polymers are conductive [36,38]. So, given the similarity in the three polymers' structures, it is possible that 2-AFN dimers or polymers are conductive, but they hinder the diffusion of unoxidised

monomers from reaching the electrode surface.

There is a general decrease in all peak magnitudes and negative shift of peaks 3 and 4 with increasing pH, such that they disappear at pH values above 8.0. Peak 3 occurs at a potential of –25.5 mV relative to peak 2 at pH 2.0 (Figure 4.7C), and its potential moves at –66.3 mV per pH unit (Figure 4.7D), which differentiates its behaviour as very different to that of peak 2. Furthermore, on the subsequent forward scan, peak 4 appears at a potential of –27.9 mV relative to peak 1 at pH 2.0 (Figure 4.7E), and moves at a rate of –55.5 mV/pH, as shown in Figure 4.7F. This feature has not been reported previously. Both potential shifts fit closely to the theoretical slope of a one-electron–one-proton reaction of –58.4 mV/pH at 21 °C, which strongly suggest that peak 3 is the reduction of the carbonyl group and peak 4 is the subsequent oxidation of the newly formed hydroxyl.

Taking Figures 4.7B,D,F, it can be seen that polymers are formed from oxidising the amino group, especially at acidic pH; and Figures 4.6C,D show that monomers and dimers containing both functional groups reach the electrode in a diffusion-limited manner as shown by the $\sqrt{\nu}$ dependence of peaks 1 and 2. However, Figure 4.3 shows that, although these reaction products are not strongly adsorbed (there is approximately a 40 mV separation between peaks 3 and 4), there are some remnants which require more than rinsing to remove.

To summarise, 2-AFN can be oxidised and small amounts reduced (peaks 1 and 2); after that, conductive species dependent on concentration and scan rate (peaks 3 and 4) strongly bind to the BDD surface; then an insulating layer of oxidised 2-AFN polymers binds weakly to the surface, thus fouling it, although some of this can be washed off.

The voltammetry confirmed the formation of polymers. The following sections detail investigations, using scanning electron microscopy and x-ray photoelectron spectroscopy, into the properties of the adsorbed species.

4.3.6 Scanning electron microscopy

Figures 4.8 and 4.9 show SEM images of the electrode surfaces imaged as soon as possible after treatments (within an hour). Sample A was a freshly acid-cleaned BDD electrode; while sample B was an electrode fouled by three scans in 50 µM of 2-AFN at pH 4; samples C and D were identically fouled as B, and then had sixty bipolar pulses of 10 mA cm^{-1} applied respectively in the presence of 2-AFN (*in situ*) and in blank buffer (*ex situ*). The contrast and brightness have not been altered after acquisition. Sample C showed the most stark and irregular contrast between the grain faces and boundaries after sixty pulses *in situ*.

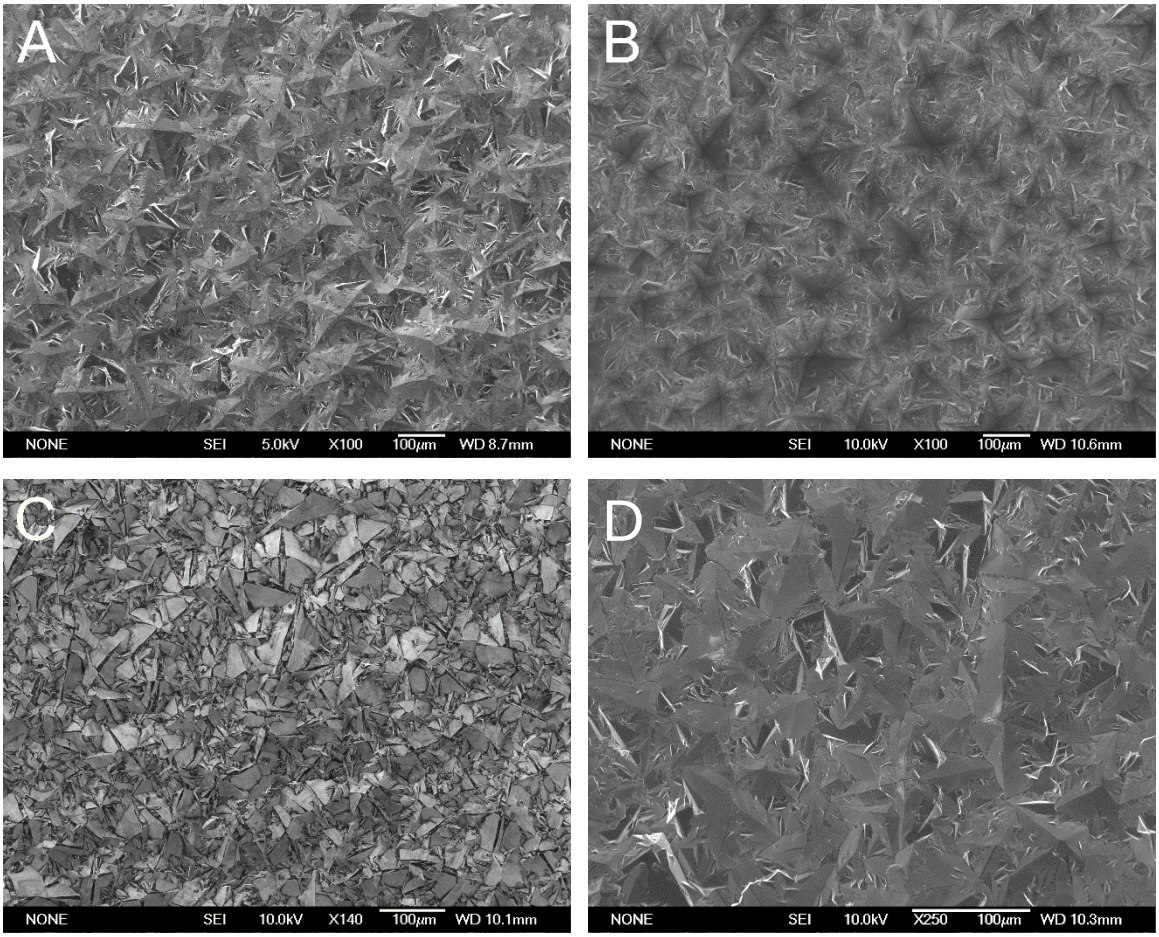


Figure 4.8 Scanning electron micrographs of (A) a pristine oxygen-terminated BDD surface, (B) a fouled electrode surface after successive CVs in 50 µM of 2-AFN at pH 4.0, (C) a fouled electrode after bipolar pulses *in situ*, and (D) a fouled electrode after bipolar pulses *ex situ*.

Due to the differing electronic and electron-emission properties arising from the orientations of the crystallites, individual crystals of 5–100 μm could clearly be seen for all the BDD samples. The fouled surface (Figure 4.8B) showed consistently darker regions at the apexes of the BDD, whereas the 'valleys' still appeared sharp and clear. It is possible that oxidation and subsequent adsorption happens more vigorously where the interfacial excess free energy is higher (at edges and boundaries), and hence fouling occurs preferentially where the density of boundaries is higher (at apexes) rather than more centrally on the faces.

Figure 4.9 shows the same four samples under higher magnification.

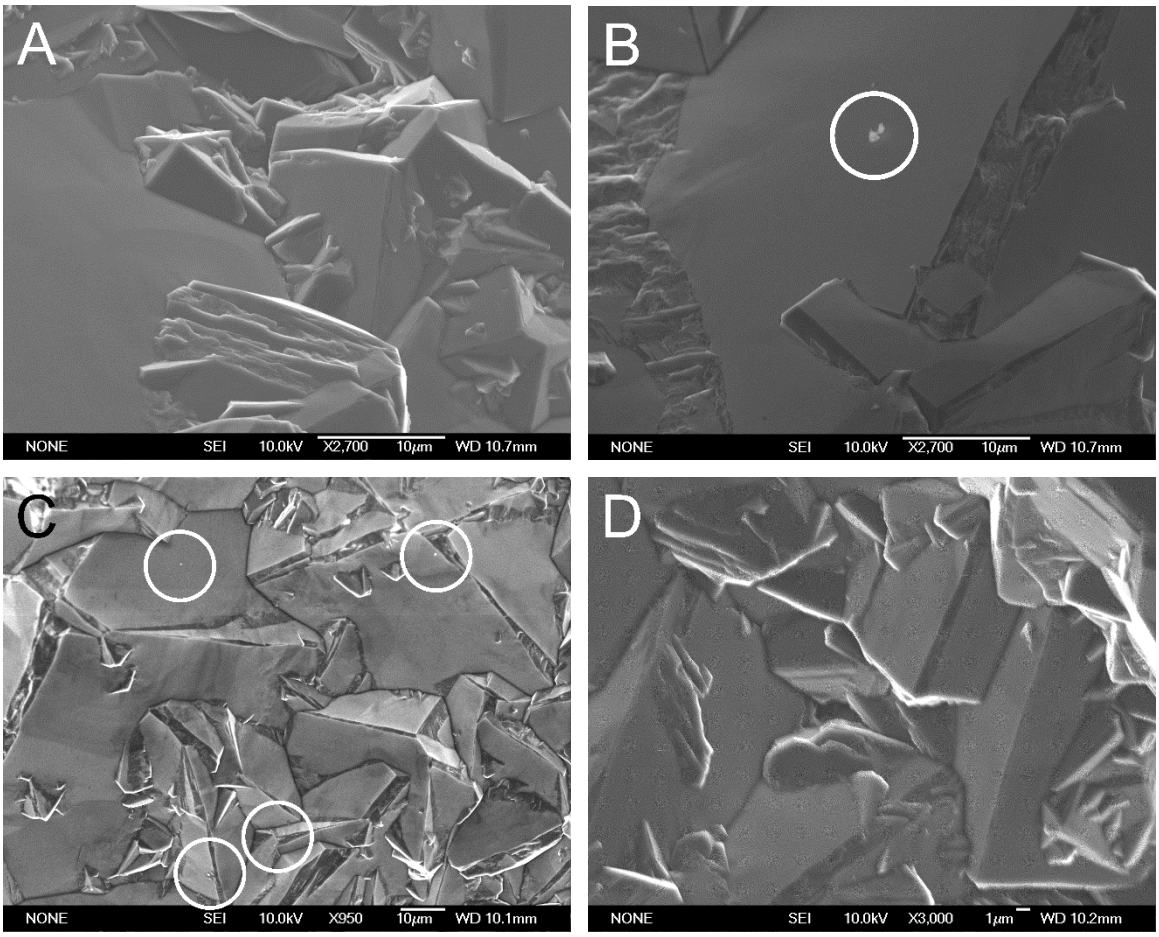


Figure 4.9 Higher magnifications of the same regions as the samples in Figure 4.8. Note the striations on the grain faces after polarisation. (A) pristine, (B) fouled, (C) fouled then bipolarly pulsed *in situ*, and (D) fouled then bipolarly pulsed *ex situ*.

Circled in samples B and C are what appear to be clustered foreign particles on top of which are otherwise unadorned surfaces. These bright white dots appear sparsely distributed and have no preferential sites. The only likely source for them is from 2-AFN polymerisation caused by extensive oxidation through repeated CV scans (sample B, fouled) and high current density polarisations (sample C, pulsed *in situ*).

In samples C and D, concentric bands around the apexes and striated bands on the flat faces are visible, which only appear in samples that have undergone bipolar pulsing. Differences in the electrochemical reactivity in various regions on the BDD surface have been reported in the literature, where the differences are attributed to appreciably differing amounts of sp^2 carbon across the wafer [39, 40]. Changes in sp^2 content across the BDD films indicates spatial variations in parameters such as temperature and the concentrations of methane and atomic hydrogen encountered during growth, especially in cases where the microwave CVD reactor has been designed to facilitate the overlap of transverse magnetic resonant modes to create a larger plasma at low power densities [40]. As the cleaning was carried out in acidic aqueous solutions, it can be expected that adsorbed molecules were oxidised by hydroxyl ions, that electrogenerated H_2 and O_2 bubbles helped the desorption of bigger, clustered, pieces of adsorbate (circled in Figures 4.9B,C), and that cathodic polarisations would have partially terminated the exposed diamond carbons with hydrogen. It is this last factor that may have amplified the differences between the sp^2 and sp^3 growth regions on the BDD and caused the striations visible in Figures 4.9C,D.

Both samples C and D are electrodes capable of performing accurate detection, though D has better reproducibility. Also, the difference in appearance between samples A and C is marked in comparison with that between A and D, further recommending the application of the pulse-cleaning treatment to be carried out in blank buffer.

4.3.7 X-ray photoelectron spectroscopy

The effects of exposure to 2-AFN, and bipolar pulses on the fouled BDD electrodes, were investigated by XPS. Figure 4.10 shows the survey spectra for the four conditions to which the electrodes were subject.

Survey and high-resolution carbon and nitrogen XPS spectra were obtained from four freshly prepared BDD electrode surfaces: (1) acid-cleaned, (2) extensively scanned in 2-AFN (fouled), (3) fouled then bipolarly pulsed *in situ* (in the presence of 2-AFN and its redox products), and (4) bipolarly pulsed *ex situ* (in buffer only).

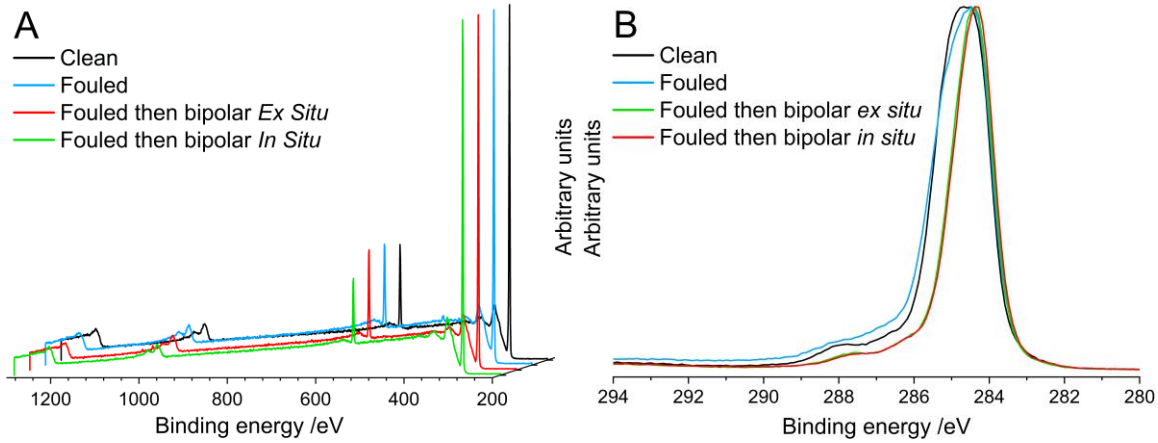


Figure 4.10 (A) Survey XPS spectra of pristine and fouled BDD electrodes. (B) Fouled samples after bipolar pulsing in and out of 50 µM 2-AFN.

These spectra shows that fouling species are deposited liberally everywhere on the surface. The two large peaks in both survey spectra (Figure 4.10A) are assigned to C 1s (~285 eV) and O 1s (~532 eV) core electrons, and the two small features above 900 eV are the carbon and oxygen Auger peaks. As can be seen in Figure 4.10B, although there is a clear difference in electrochemical behaviour between the acid-cleaned and fouled BDD electrodes, XPS in the carbon 1s region does not differentiate them much (obvious differences exist in the nitrogen 1s region) as both contain a lot of oxidised-carbon functionalities. This is because the vigorous acid-boiling treatment that electrodes undergo is supposed to produce a highly oxidised BDD surface in a reproducible way, and the fouled

samples do not have enough 2-AFN adsorbed to elicit stronger XPS signals. Spectra in this region also cannot differentiate between the surfaces pulsed in different solutions, but this was expected, as it was also the case in voltammetry, after the first round of pulses.

The most important comparison would be between a fouled surface and one that has been bipolarly cleaned, to illustrate the differences in levels of oxidation of the BDD surfaces. Figure 4.11 shows the component fitting of high-resolution spectra of (A) a fouled electrode and (B) one that was fouled and then bipolarly pulsed in blank buffer.

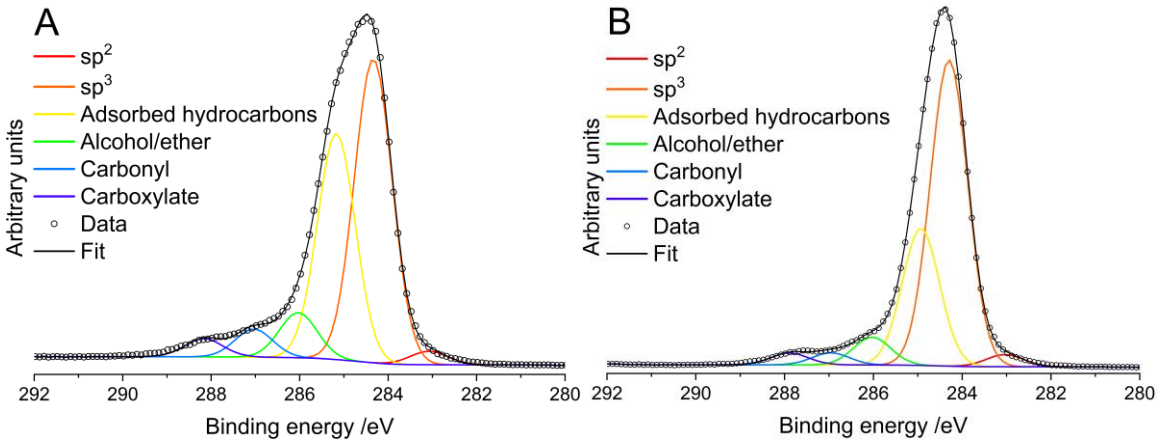


Figure 4.11 High-resolution XPS spectra of the carbons 1s region for (A) a fouled electrode and (B) a fouled electrode that has undergone *ex situ* bipolar pulses.

The same parameters that were used to fit the XPS spectra from the dopamine project were employed here (Section 3.3.9). The sp^3 to oxidised-carbons ratio is much higher in Figures 4.11B than in Figures 4.11A. This change occurs after pulsing and suggests that the fouling takes place at sp^3 carbons. Table 4.2 shows the percentage atomic concentration of the various components on the electrode surfaces. The positions of the component peaks are as follows: sp^2 283.1 eV, sp^3 284.3 eV, adsorbed hydrocarbon 285.0 eV, alcohol or ether 286.0 eV, carbonyl 286.9 eV, and carboxylate 288.0 eV.

Table 4.2 Percentage atomic concentrations of C groups, averaged over 3 areas

	sp^2 C	**sp^3 C**	**Adsorbed hydrocarbon**	**Σ Higher oxidation states**

Clean	2.4 ± 0.1	45.2 ± 0.4	39.8 ± 0.2	12.6 ± 0.1
Fouled	2.1 ± 0.1	48.0 ± 0.2	35.6 ± 0.3	14.2 ± 0.1
Bipolar *ex situ*	2.4 ± 0.0	59.3 ± 1.0	27.8 ± 0.7	10.5 ± 0.1
Bipolar *in situ*	2.5 ± 0.1	58.6 ± 1.0	28.3 ± 0.7	10.6 ± 0.1

After bipolar pulses, the percentages of the adsorbed hydrocarbons and higher oxidation functionalities (alcohol, carbonyl, and carboxylate) decrease, and sp^3 content increases. This trend fits the hypothesis that bipolar pulses have the effect of reducing the oxidation of the BDD surface. The tiny peak found at ~283 eV comprises less than 3% of the total peak area, corresponds to sp^2 carbon, and is unchanged by any of the chemical or electrochemical treatments.

High-resolution of the nitrogen 1s region is shown in Figure 4.12A for all four samples, where only the fouled sample showed a peak. Figure 4.12B shows how that peak was fitted.

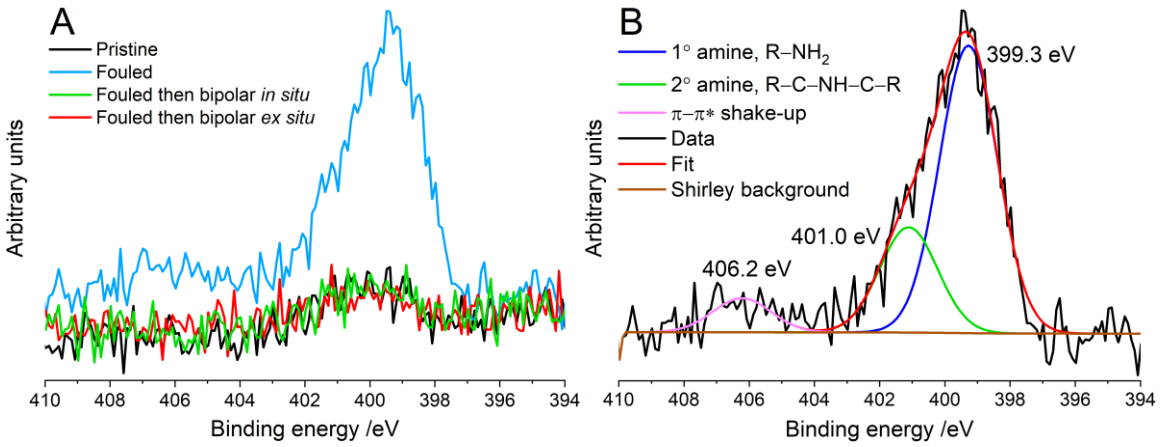


Figure 4.12 (A) High-resolution XPS spectra of the nitrogen 1s region for all samples. (B) The functional groups fitted to the fouled electrode's spectrum.

The increased presence of nitrogen was expected for all samples that had been exposed to 2-AFN, as the pre-peak in the second scan indicates that some adsorption would have occurred after even one CV scan. However, a sizable N 1s peak was only observed for the fouled sample, and three component peaks could be fitted under it [39, 40]. The position and atomic percentage of each component in Figure 4.12B is listed in Table 4.3.

Table 4.3 Fitted components of the fouled XPS nitrogen 1s spectrum

	Primary amine ($R–NH_2$)	**Secondary amine ($R_1–NH–R_2$)**	**$\pi \rightarrow \pi^*$ shake-up**
Binding energy	399.3 eV	401.0 eV	406.2 eV
Percentage concentration	70.0	24.4	5.6

The largest component is the primary amine, 2-AFN, at 399.3 eV. A peak at 406.2 eV is either commonly assigned as nitrate or as a shake-up satellite from nitrogen-rich polymers. Electrochemistry and SEM both point to the polymerisation of 2-AFN into secondary amines, whereas the only source of nitrate would be the degradation of 2-AFN into nitro-fluorenone from UV-A exposure [4]. But that is unlikely, as the analyte solutions were stored in the dark in a laboratory without natural lighting. This not only takes care of the 406.2 eV feature, but also the 401.0 eV component, as a simple secondary amine formed from polymerisation [37].

Although the electrochemical activation is quick and effective, reactivation is necessary even after one voltammetry scan in 2-AFN. This shows that the chemical changes derived from pulsing do not endure. This is an important detail to be remembered for all experiments.

4.3.8 Differential pulse voltammetry

Differential pulse voltammetry is widely used to improve the electroanalytical parameters for the direct measurements of concentrations, namely, the lowest limit of detection and the sensitivity range. Cyclic voltammograms collected at pH 4.0 gave the highest currents and the best peak definition; so experiments on the limit of detection were performed at pH 4.0.

Wide scan ranges were tested, for example, from –1 to 0 V, 0 to +1.7 V, and –0.5 to +1.2 V, and the scan directions were also reversed across similar potential ranges to capture all redox features. To evaluate the sensitivity of the BDD electrode towards 2-AFN, DPVs

were recorded in increasing concentrations of 2-AFN, from 0 to 100 µM, at pH 4.0. Figure 4.13 shows the Δ*i*–*E* curves, showing a single, well-defined oxidation peak. In comparison with CVs (Figure 4.4), the detection time is halved, and the oxidation peak is better defined for the same concentration of solution at the same scan rate. This is because of the low capacitive-current characteristic of this technique and physical properties of the electrode.

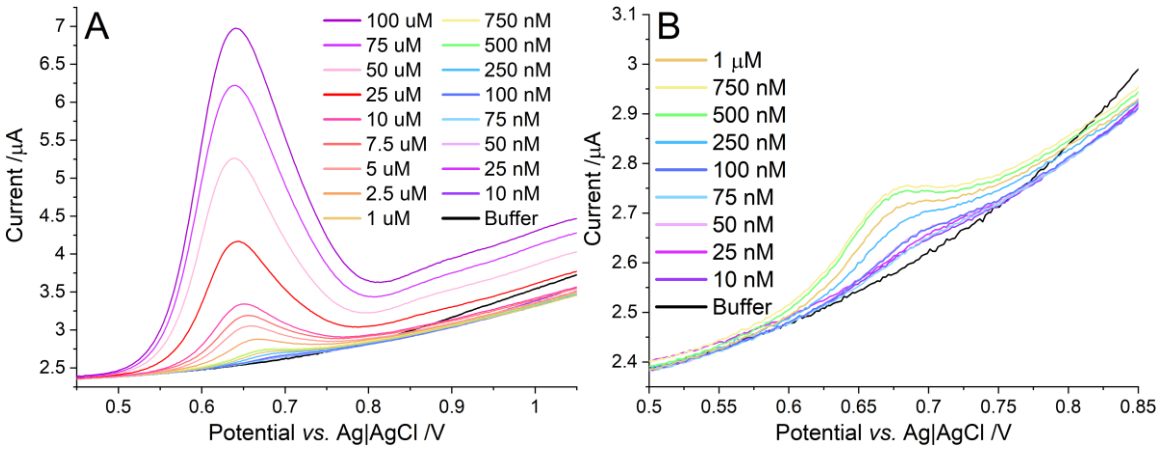


Figure 4.13 Differential pulse voltammograms of 2-AFN at pH 4, the scan rate was 22 mV s^{-1}. (A) The black line is a blank buffer, rainbow lines are [2-AFN] at 10, 25, 50, 75, 100, 250, 500, and 750 nM, and at 1, 10, 50, 75, and 100 µM. (B) A scaled version showing DPVs below 1 µM, displaying a clear peak even at 10 nM.

As can be seen from Figure 4.13, the oxidation peak shifts to more positive potentials at lower analyte concentrations (from +0.643 ± 0.009 V at 100 µM to +0.697 ± 0.010 V at 10 nM). Figure 4.14 shows the extracted peak current values from the DPVs plotted against concentration.

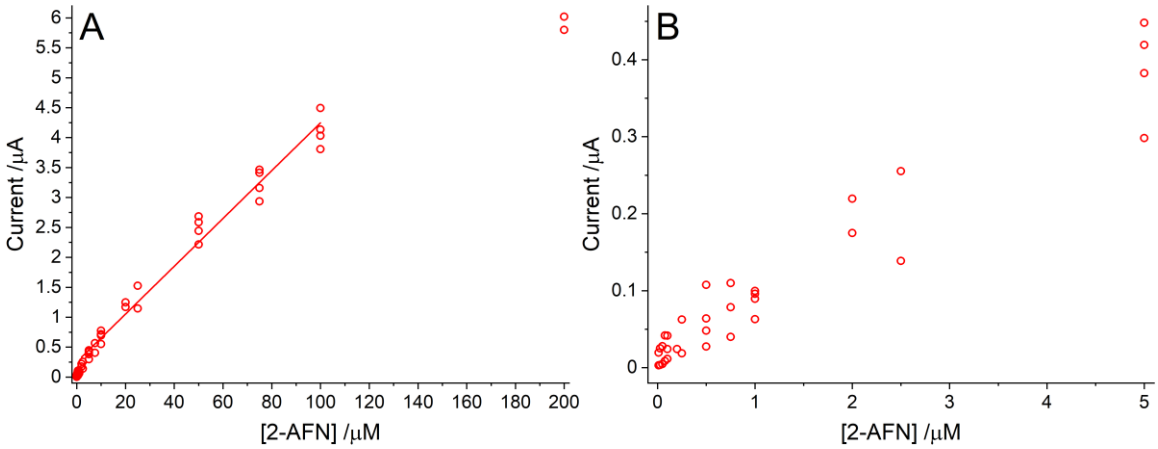


Figure 4.14 (A) All peak currents *vs*. [2-AFN], at 0, 10, 25, 50, 75, 100, 250, 500, and 750 nM, and then in greater increments to 200 μM, showing the calibration line in the linear region between 2 and 100 μM with its upper and lower limits bound. (B) Peak currents below 5 μM to show that a peak can still be discerned.

The BDD electrode can detect the oxidation of 2-AFN to a concentration of 10 nM, which is an order of magnitude more sensitive than previously reported [13]. The most distinct voltammograms were obtained with a step potential of 4.6 mV, modulation amplitude of 46 mV, a modulation time of 4 ms, and an interval time of 45.7 ms.

In Figure 4.14, a linear relationship was observed between 2 and 10 nM, with a correlation coefficient r of 0.991, and a coefficient of determination, r^2, of 0.981. The functional relationship for the peak current and concentration of 2-AFN is

$$i_{2\text{-AFN}} = (0.0399 \pm 1.03\times10^{-3}) \times [\text{2-AFN}] + (0.254 \pm 0.0506), \qquad (4.1)$$

where $i_{2\text{-AFN}}$ is expressed in μA and the 2-AFN concentration is in μM. This equation can be used to find the concentration of an unknown solution containing only 2-AFN and will be used in studying its interaction with dsDNA in solution in later experiments.

4.3.9 Sensing of nucleosides

These experiments aim to find the oxidation potentials of guanosine (G) and adenosine (A) at pH 4.0, and whether they vary with respect to concentration, so that peaks can be assigned

correctly in the later dsDNA experiments. The highest concentration was 250 μg mL^{-1}, chosen such that the number of free bases in the stock would equal the number of bound bases in dsDNA stock (1 mg mL^{-1}), assuming a 25% presence.

Figures 4.15 show the DPVs collected from serial dilutions of G and A. The potential was scanned from 0 to +1.7 V, using the same NOVA procedure as for the 2-AFN DPVs. When the DPVs became visibly indistinct from that of the concentration above, no more dilutions were made.

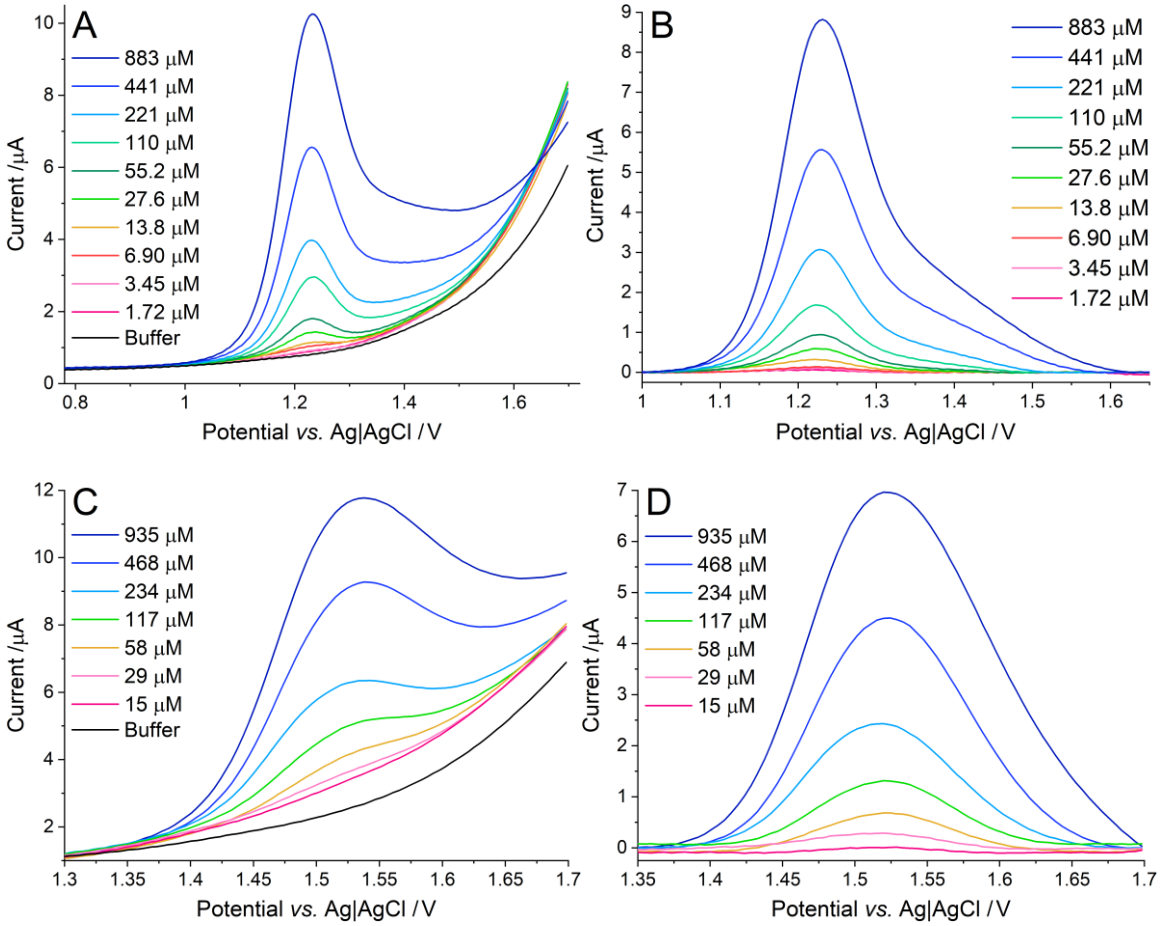


Figure 4.15 (A,C) As-recorded DPVs, respectively, of guanosine and adenosine at pH 4.0, at a scan rate of 100 mV s^{-1}. (B,D) The baseline-subtracted versions of charts A and B.

The oxidation potentials of guanosine (1.225 ± 0.006 V, Figures 4.15A,B) and adenosine (1.520 ± 0.004 V, Figures 4.15C,D) at pH 4.0 did not change with concentration.

For both G and A, oxidation occurs in the guanine or adenine moieties. Compared to A, the additional carbonyl group of G increases the delocalised zone of its electrons, meaning that they are held to the molecule less strongly, and so less energy is required to extract an electron, observed as lower oxidation potential.

Below 3.45 μM for G and 29 μM for A, the peaks become difficult to distinguish from the next concentration down. Baseline correction was employed on all curves to produce Figures 4.15B,D. Afterwards, the shapes of the voltammograms became clearer, revealing a hump after the main G peak (Figure 4.15B) which seemed to depend on concentration, and is probably an electron abstraction from one of the many oxidation products.

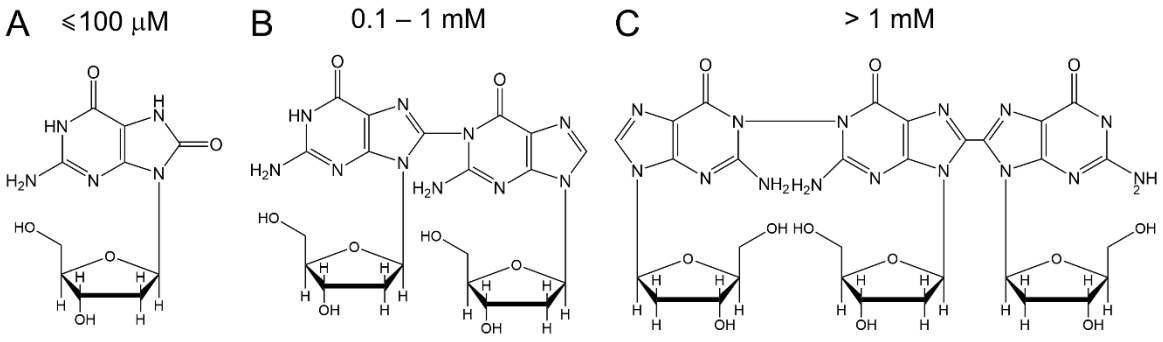


Figure 4.16 The major oxidation products of G at three significant concentration ranges. (A) 8-oxo-guanosine. (B) 8-(1-guanosyl)guanosine. (C) 8-(8-guanosyl)-1-(1-guanosyl)guanosine.

An extensive NMR study by Subramanian and Dryhurst in 1987 showed that 8-oxo-guanosine is the predominant product up to 100 μM (Figure 4.16A), and that a dimer increasingly replaces this as concentrations increase to around 1 mM (Figure 4.16B), while above 1 mM complex trimers form (one example of which is shown in Figure 4.16C) [43]. As the observed asymmetry disappears at below 100 μM, it is likely that the hump can be attributed to the oxidation of the dimer.

The peak currents extracted from Figures 4.15B,D are plotted against concentration, in Figure 4.17, where A shows that of guanosine, and B adenosine.

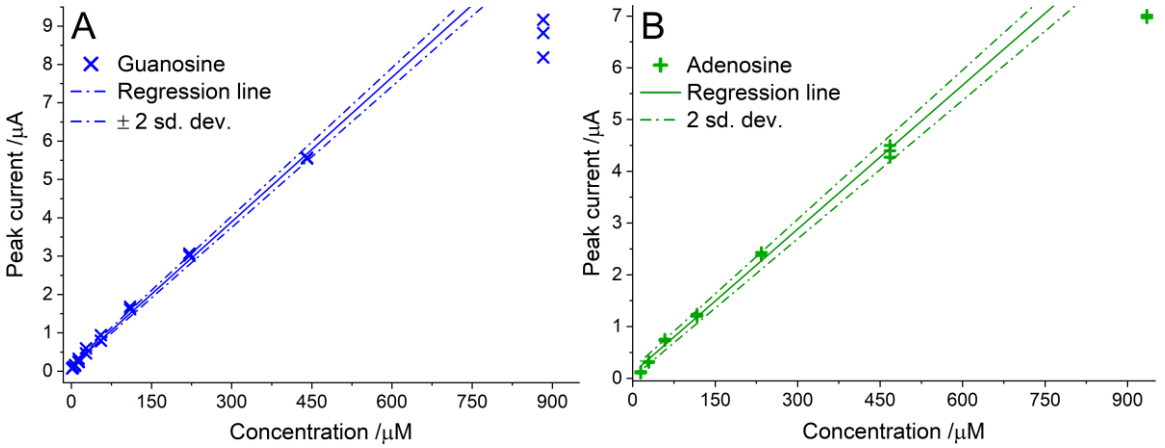


Figure 4.17 (A,B) Peak currents plotted respectively, for G and A, at the whole range of concentrations measured. Also shown are the calibration lines, with upper and lower limits, showing a linear range below 500 μM for both species.

For both nucleosides, Figure 4.17 shows that linear regression lines may be drawn through most of the points, from the lowest detectable concentrations, 3.45 μM for G and 15 μM for A, up to 441 and 468 μM respectively. Only these ranges are called the linear region: beyond these concentrations, the peak currents do not fall within the dash–dot lines at two standard deviations of the slope and two standard deviations of the intercept. The equations of the regression lines in the linear region are

$$i_G = (1.257\times10^{-2} \pm 1.602\times10^{-4}) \times [G] + (0.123 \pm 0.025), \quad (4.2)$$

$$i_A = (9.266\times10^{-3} \pm 1.722\times10^{-4}) \times [A] + (0.104 \pm 0.043), \quad (4.3)$$

where G and A concentrations are in μM, and i_G and i_A are in μA.

From these experiments, both nucleosides have well-defined oxidation peaks at pH 4.0, which do not change with respect to concentration, and are sufficiently far apart (~300 mV) to allow for simultaneous detection. This will be useful for assigning correct peaks in dsDNA oxidation. Also, knowing the linear detection ranges allows the estimation that, if dsDNA solutions were to contain between 0.98 and 125 $\mu g\,mL^{-1}$ of G and between 7.75 and 133 $\mu g\,mL^{-1}$ of A, then peaks can be expected, and can be expected to increase linearly with concentration. (The concentrations are presented thus as the molecular weights of

dsDNA are not known.)

4.3.10 Sensing of DNA strands

The stock solution made from dsDNA powder (salmon, <100 base pairs) was 1 mg mL^{-1}. Several concentrations close to 1000 µg mL^{-1} were chosen as well as much more dilute solutions to capture the full range of expected concentration changes in the two 2-AFN experiments to follow. Figure 4.18 shows the raw and baseline-subtracted DPVs obtained from dsDNA with a BDD preconditioned in blank buffer with 60 bipolar pulses.

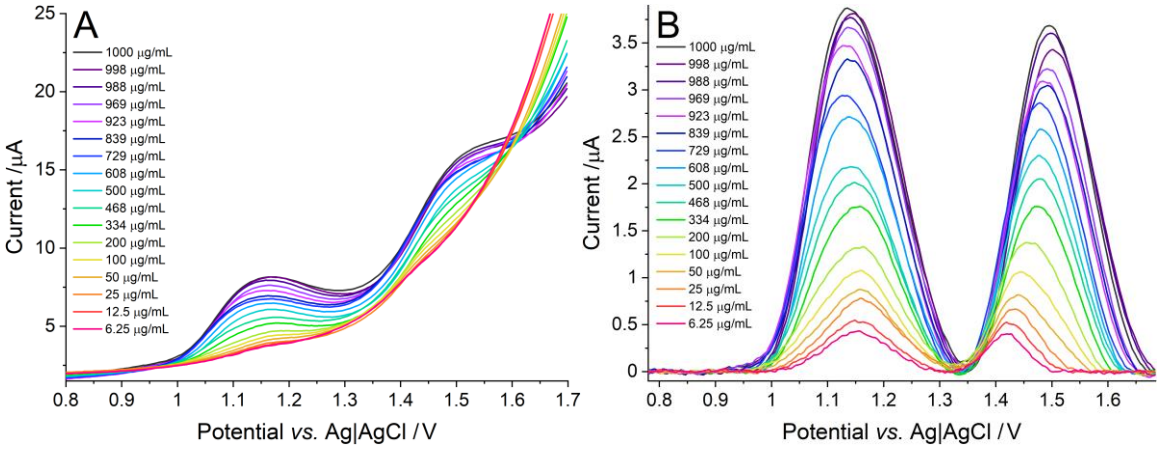


Figure 4.18 DPVs measured at a scan rate of 100 mV s^{-1} in dsDNA at pH 4.0 shown (A) directly and (B) with the baselines subtracted.

With the experience gained from the work described in Section 4.9, the two peaks in the DPVs in Figure 4.18 correspond to the oxidation of deoxyguanosine (dsG) at ~1.2 V and the deoxyadenosine (dsA) peak at ~1.5 V. Below 400 µg mL^{-1}, the average oxidation potential of dsG and dsA are 1.160 ± 0.004 V and dsA 1.450 ± 0.013 V, and above 400 µg mL^{-1} the peak potential decreases for dsG, to 1.137 ± 0.008 V, and increases for dsA, to 1.487 ± 0.008 V. The oxidation of bases in dsDNA occurs at a potential of 65–70 mV lower than for their corresponding free nucleoside. The decreased difficulty of oxidising deoxynucleotides in comparison with the free nucleosides at pH 4.0 is an expected effect due to the vastly different electronic environments of free and bound G and A, especially with the presence of the phosphate groups in the macromolecule.

The limit of detection was visually deemed to be 6.25 μg mL^{-1}, as at this concentration the lines become indistinguishable from that of 12 μg mL^{-1} without baseline subtraction, and the errors from this operation would then be comparable to the peak currents. In any case, as can be seen in Figure 4.19, the peaks from concentrations below 25 μg mL^{-1} do not fit within two standard deviations (dash-dot lines) of the linear regression estimations, which otherwise fits all but one or two of the other points.

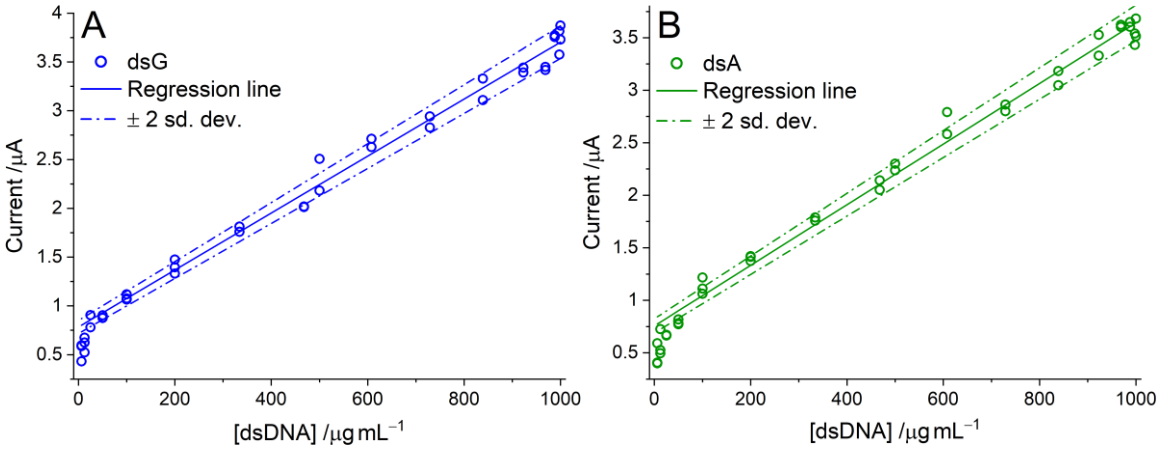


Figure 4.19 (A,B) Peak currents respectively, of dsG and dsA, for the whole range of [dsDNA] measured: 6.25–1000 μg mL^{-1}. The regression lines, with upper and lower limits, are drawn for the linear range between 25 and 1000 μg mL^{-1}.

The linear relationship between dsG and dsA peak currents and dsDNA concentration between 25 and 1000 μg mL^{-1} respectively are

$$i_{dsG} = (0.00292 \pm 5.06\times10^{-5}) \times [\text{dsDNA}] + (0.783 \pm 0.0331), \quad (4.4)$$

$$i_{dsA} = (0.00288 \pm 5.14\times10^{-5}) \times [\text{dsDNA}] + (0.757 \pm 0.0336), \quad (4.5)$$

where [dsDNA] is in μg mL^{-1} and the peak current calculated is in μA.

With the simplistic 25% assumption of G and A bases in dsDNA, it may be reasonable to expect the peak currents from 1000 μg mL^{-1} dsDNA to be similar to those of 883 and 935 μM of G and A. However, the currents from dsDNA are much lower. At planar undecorated electrodes, several factors stand in the way of producing well-defined peaks. First, the oxidation sites of G and A are hidden in the helix skeleton, shielded by the un-

electroactive deoxyribose and phosphate groups [43,44]. Second, these macromolecules have much lower diffusion coefficients—so that, even if there is an abundance of each nucleotide proportionally, it takes longer for them to diffuse to the electrode [33]. The polar sugar–phosphate group of the nucleotide also causes greater solvation energy compared to the base, further affecting how close any oxidation site can approach the electrode [46]. In the positive potential regions, there is also a steric effect caused by the electrostatic interaction between the negatively charged phosphate group and the positively charged BDD surface, which orients the bases further from the electrode surface toward the solution bulk, thus increasing the energy necessary for reorganisation of the nucleotide at the surface after adsorption and prior to charge transfer [18]. All the above acts to alter the energy required to extract electrons from dsDNA, which can be observed as variations in peak positions and widths.

These experiments defined the detection limits and linear ranges for dsG and dsA oxidation when no interferents are present. Thus, the results form a control data set, against which the values from the next experiment, when 2-AFN is added, can be interpreted.

4.3.11 dsDNA interactions with 2-AFN

In these experiments, 2-AFN is expected to intercalate between the bases in dsDNA, causing steric strain to the strands, and acting as electronic shielding to purine electron loss leading to the increase of oxidation potential and decrease of oxidation current. The BDD's sensitivity in detecting this activity will be investigated.

There are two ways to observe how 2-AFN and dsDNA interact. First, by keeping the concentration of dsDNA constant and adding 2-AFN, it can be seen how dsDNA affects the detection of low concentrations of 2-AFN. Second, by keeping a constant concentration of 2-AFN and increasing the amount of dsDNA, how quickly the nucleic acids 'consume' 2-AFN can be seen. From the same experiment, observations can also be made on whether

an excess of 2-AFN interferes with detection of small amounts of dsDNA. From both experiments, any deviations in the 2-AFN, dsG, and dsA signals could be directly attributed to their interactions in the mixture.

Between each measurement, sixty bipolar pulses were applied to the electrode in a blank buffer to ensure that the pre-measurement condition of the electrode is consistent. Meanwhile, the analyte solution volume was checked with a 10 mL volumetric flask and made up to the mark with blank buffer if required. Once the bipolar treatment was complete, this solution was poured into the electrode cell and new aliquots were pipetted in. The mixture was then stirred and allowed to stand at room temperature before recording.

Adding 2-AFN to 1 mg mL^{-1} dsDNA

The DPVs shown in Figure 4.20A were made in a series of six solutions containing 30.6 µmoles of dsDNA bases (calculated using the average molecular weight of a nucleotide, 327 g mol^{-1}, in 10 mg of dsDNA powder) and varying amounts of 2-AFN (0, 1, 5, 9.9, 48.1, and 95 µM). These concentrations were chosen to maximally make use of the wide linear range of the BDD for 2-AFN oxidation, as found in Section 4.3.8. The volumes added were from a high-concentration 2-AFN stock solution (1 mM) to minimise changes to the reaction volume, leading to dsDNA concentrations in the range 952–1000 µg mL^{-1}.

Figures 4.20A,B show the DPVs obtained from the mixed solutions, while Figures 4.20 C,D,E show the peak currents from all three species in mixture, overlaid on their values in standalone solutions.

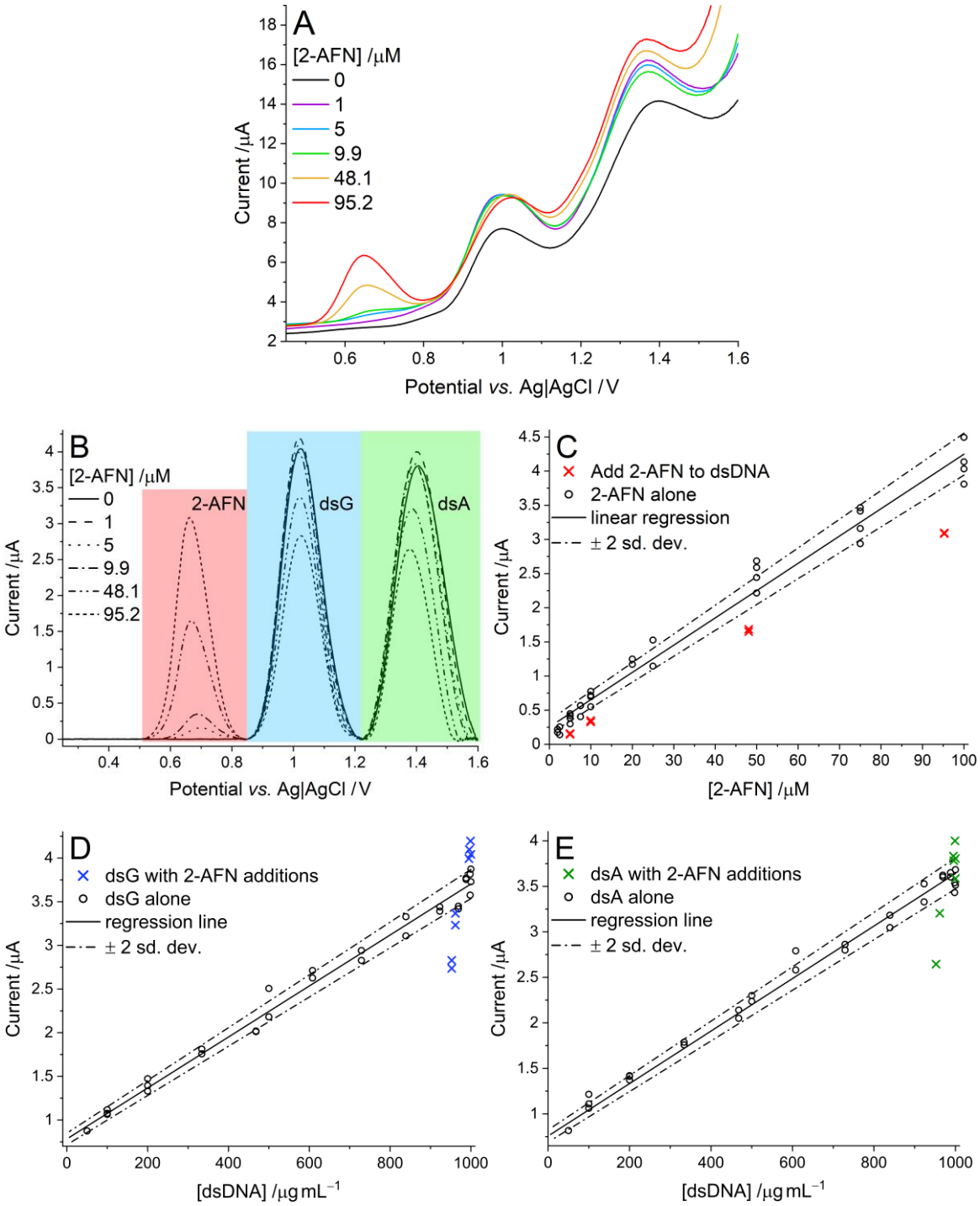


Figure 4.20 (A,B) Raw and baseline-corrected DPVs in 1 mg mL^{-1} dsDNA with increasing amounts of 2-AFN, at a scan rate of 22 mV s^{-1}, at pH 4.0. (C,D,E) The 2-AFN, dsG, and dsA peaks extracted from chart B overlaid on the calibration line obtained by serial dilutions of 2-AFN and dsDNA. Charts C, D, and E show the original data in their linear ranges, with upper and lower boundaries representing two standard deviations.

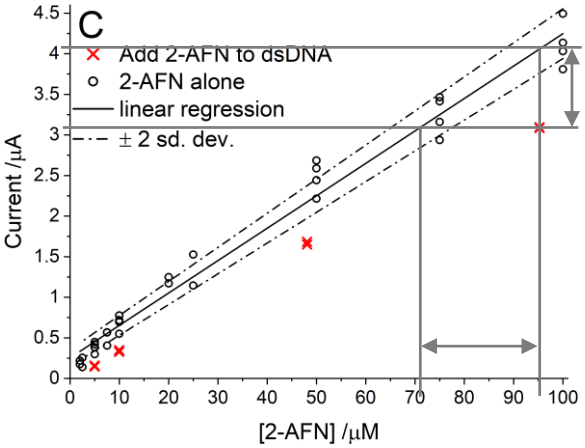
Figure 4.20C shows that 2-AFN was not detected at 1 µM. This was unexpected, as even 10 nM of 2-AFN had produced a well-defined peak when it was the only species in solution (Figure 4.13B). The non-detection indicates that dsDNA hinders the detection of small amounts of 2-AFN, either because at 1 µM, a majority of the 2-AFN molecules have quickly intercalated into the dsDNA macrostructure, or because the presence of lengthy charged macromolecules disrupted the diffusion of 2-AFN towards the electrode such that its presence cannot be distinguished.

A second observation is that, with increasing 2-AFN concentration, the 2-AFN peaks increased while the dsDNA peaks decreased. In Figures 4.20C,D,E, the oxidation peak currents of each species in the mixture is compared to that of each species alone. Figure 4.20B shows the 2-AFN peaks from Figure 4.20A overlaid with the calibration line obtained from Figure 4.14A. At 5 µM and above, the peak currents increase linearly with increasing concentration. However, all peak currents are within two standard deviations of the calibration line, meaning that there is significant difference between the behaviour of 2-AFN in mixture with dsDNA and that of 2-AFN alone.

Although the volume of each 2-AFN injection was designed to be low (tens of microlitres), the additions still caused small changes to the reaction-cell solution volume, which reduces the dsDNA concentration slightly. This is why the dsG (Figure 4.20D) and the dsA (Figure 4.20E) peaks are plotted against the theoretical concentration of dsDNA, which are then shown superimposed on the calibration line obtained from Figures 4.19A,B. In both figures, the centroid of the crosses lies within the upper and lower bounds (dash-dot lines) of the regression line, as would be expected. However, both peak currents decrease much faster than would be predicted from Figure 4.19. To explain the quantitative results from Figure 4.20, it may be helpful to consider a worked example.

As seen in Figure 4.20C, at 95 µM 2-AFN, the current from the mixture is much lower

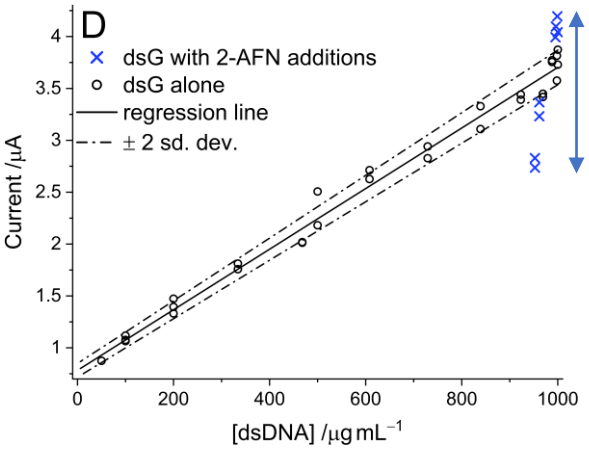
than expected if there was no interaction. At that point, the mixture is equivalent to containing 30.6 µmoles of dsDNA bases and 1 µmole of 2-AFN.



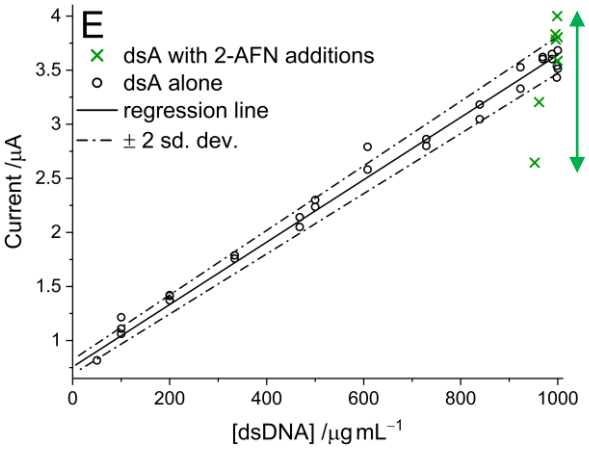
Reading from the calibration line, the concentration that would have generated the experimental currents is 71 µM.

In a 10 mL reaction volume, this means that effectively 0.24 µmoles of 2-AFN is no longer available for oxidation.

Due to the 2-AFN additions, the final changes in the reaction volume will decrease the dsDNA concentration, from 1000 to 952 µg mL^{-1}. This would have produced current decreases of 0.140 µA in dsG and 0.138 µA in dsA.



The actual observed drop in the dsG current is 1.26 µA, which would be equivalent to a dsDNA concentration drop from 1000 to 568 µg mL^{-1}.



The actual observed drop in the dsA current is 1.05 µA, which would be equivalent to a dsDNA concentration drop from 1000 to 636 µg mL^{-1}.

This first experiment shows that a significant amount of 2-AFN can be incorporated into the dsDNA macrostructure, and the amount incorporated disproportionally affects the ability of dsDNA to undergo oxidation at the BDD electrode. Specifically, 0.24 µmoles of 2-AFN caused sufficient damage to decrease the peak magnitudes of dsG and dsA equivalent to 12.6 µmoles and 10.6 µmoles.

Adding dsDNA to 50 µM 2-AFN

To find the amount of dsDNA that will affect the 2-AFN sensitivity, small volumes from a 10 mg mL^{-1} stock solution of dsDNA were added to 10 mL of 50 µM 2-AFN. The DPVs shown in Figure 4.21A were recorded in solutions containing 10, 50, 99.5, 577, and 952 µg mL^{-1} of dsDNA. These concentrations were chosen to make maximal use of the wide linear range of the BDD for dsDNA oxidation. At the end of the experiment the mixture would contain 0.5 µmoles of 2-AFN and 29.1 µmoles of bases.

Figures 4.21A,B show that even 10 µg mL^{-1} of dsDNA elicited clear signals for dsG and dsA, and at that concentration the 2-AFN signal was not affected. After each addition of dsDNA, the reaction solution volume changes, leading to slight decreases in the 2-AFN concentration (from 50 µM to 47.6 µM). Hence, in Figure 4.21C the peak 2-AFN currents from the mixed solutions are shown overlaid on data when 2-AFN was the sole analyte. There, when the concentration of dsDNA was less than 100 µg mL^{-1}, the 2-AFN signal overlaps the original data and lies within two standard deviations, meaning that these current variations could simply be caused by small concentration changes. However, when the concentration of dsDNA increased above 100 µg mL^{-1}, the 2-AFN peak height decreased significantly by more than two standard deviations, meaning that dilution alone cannot explain this drop in the apparent amount of 2-AFN in solution. The total drop is equivalent to a concentration change from 50 to 29 µM, suggesting that 0.21 µmoles of 2-AFN has been incorporated into the dsDNA strands.

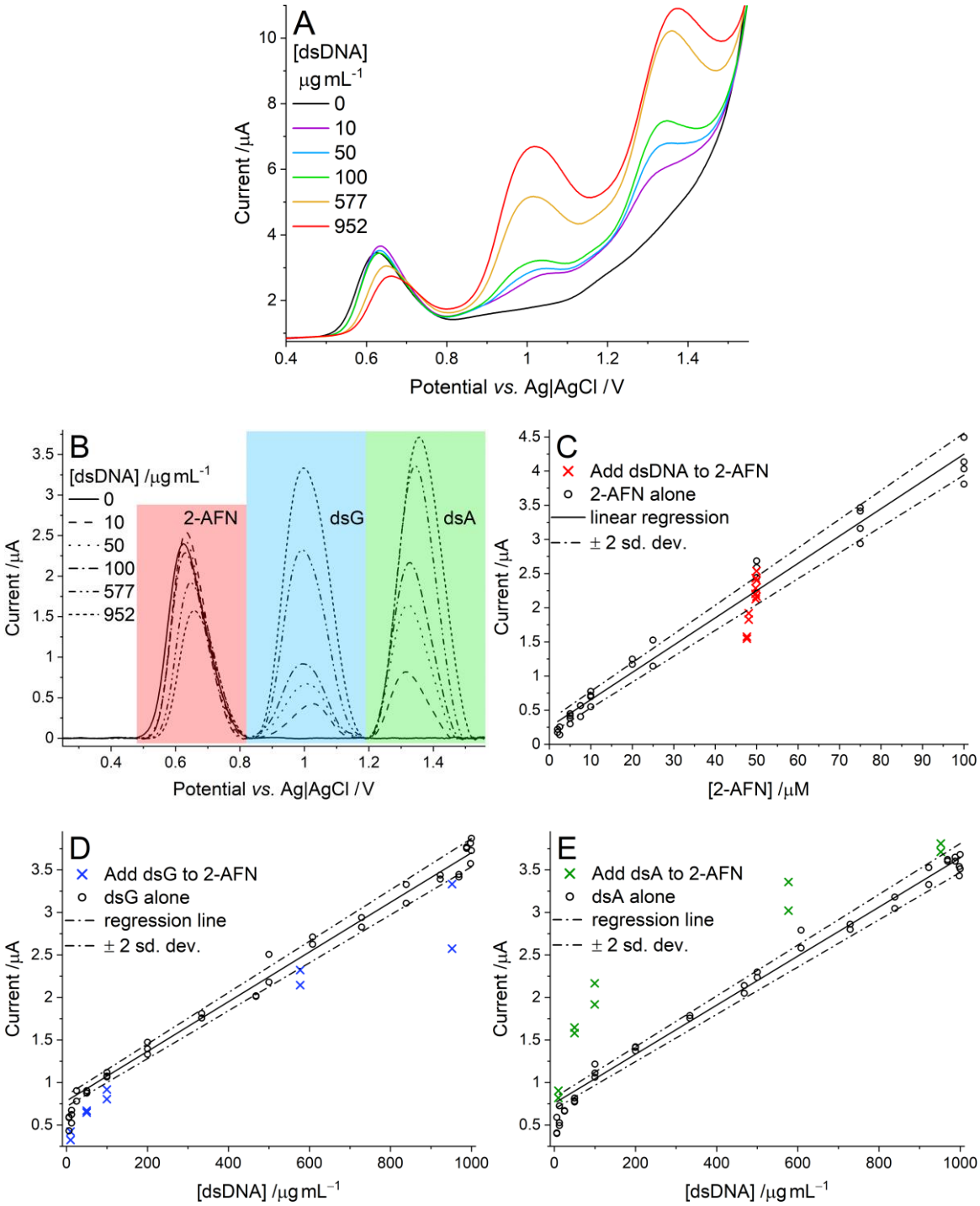


Figure 4.21 (A,B) Raw and baseline-corrected DPVs in 50 μM of 2-AFN with increasing amounts of dsDNA, at a scan rate of 22 mV s^{-1}, at pH 4.0. (C,D,E) The 2-AFN, dsG, and dsA peaks extracted from chart B overlaid on the calibration line obtained by serial dilutions of 2-AFN and dsDNA. Charts C, D, and E show the original data in the linear range, with upper and lower boundaries of two standard deviations of the slopes.

Figures 4.21D,E show that the oxidation peak currents of dsG and dsA from this experiment are consistently lower compared with the data obtained from serial dilutions of dsDNA with no 2-AFN. The presence of 2-AFN enhances the dsA signal while dramatically suppressing the dsG peak.

The observations made from Figure 4.21 could be because 2-AFN initially existing in excess relative to the number of dsDNA bases (~0.3 µmoles of bases to 0.5 µmoles of 2-AFN) but, as more strands are added (above 100 µg mL^{-1}, ~3.1 µmoles of bases), their large capacity for intercalation significantly lowers in the amount of free-floating 2-AFN.

This second experiment shows that a mixture containing 50 µM of 2-AFN does not affect the detection limits of dsDNA in the same solution. Below a threshold concentration of dsDNA (100 µg mL^{-1}), accurate sensing of 2-AFN is also unaffected. The dsDNA data show that the incorporation of 2-AFN tends to suppress the oxidation of the G bases, possibly through preferential bonding, which could then lead to greater exposure of or easier access to the A bases, observed as higher peak currents.

Oxidation potentials of 2-AFN, dsG, and dsA in mixture

From both experiments in this section, the peak potentials observed for 2-AFN, dsG, and dsA oxidation, in their free-floating state and when they are mixed, also reveal interesting information, shown in Tables 4.5 and 4.6.

Table 4.4 The oxidation potentials of 2-AFN in solutions without and with dsDNA

	⩽10 µM 2-AFN	**>10 µM 2-AFN**
no dsDNA	0.667 ± 0.015	0.643 ± 0.009
<400 µg mL^{-1} dsDNA	n/a	0.638 ± 0.009
>400 µg mL^{-1} dsDNA	0.681 ± 0.013	0.656 ± 0.009

Several trends can be found in Table 4.4. Taking the average of all 2-AFN potentials, which is 0.659 ± 0.017 when no dsDNA is present, it decreases to 0.638 ± 0.009 V when dsDNA is present but below 400 µg mL^{-1}. The seeming decrease actually mostly overlaps

the range of potentials from higher concentrations of 2-AFN (>50 μM), suggesting that even after intercalation a considerable proportion is still free. Thus, at this low concentration of dsDNA, its effect on 2-AFN oxidation is very small, but the effect of 2-AFN on dsG is huge.

The average of all 2-AFN potentials (0.659 ± 0.017 at zero [dsDNA]) increases to 0.665 ± 0.016 V when [dsDNA] is greater than 400 μg mL^{-1}. Coupled with this, the dsA potential dropped from 1.488 ± 0.008 V to 1.363 ± 0.018 V. The increase in 2-AFN potential when large quantities of dsDNA are in solution could be either because harder-to-oxidise adducts form between 2-AFN and nucleosides, or simply becuase such large quantities of 2-AFN get incorporated into the strands that its solution concentration decreases to below 2 μM, or by a combination of both. As the potential is on the high end of the expected range even for low concentrations, and the difficulty in oxidising 2-AFN increases significantly, the former option must play the greater part.

Table 4.5 The oxidation potentials of 2-AFN in solutions without and with dsDNA

	<400 μg mL^{-1} dsDNA		**>400 μg mL^{-1} dsDNA**	
	dsG	dsA	dsG	dsA
no 2AFN	1.158 ± 0.005	1.454 ± 0.015	1.136 ± 0.007	1.488 ± 0.008
⩽10 μM 2-AFN	n/a		0.999 ± 0.020	1.379 ± 0.026
>10 μM 2-AFN	1.012 ± 0.012	1.326 ± 0.006	1.006 ± 0.013	1.363 ± 0.018

As seen in Table 4.5, regardless of the concentration of dsDNA, when it was mixed with 2-AFN in any proportion, there was a constant decrease in the dsG potential, from 1.146 ± 0.013 V to 1.005 ± 0.016 V. This suggests that the guanine base is highly sensitive to the presence of 2-AFN, such that the formation of a guanine-AFN adduct or the intercalation at the base happens preferentially—so much so, that further increases in 2-AFN presence do not disrupt the dsG oxidation beyond what has already occurred.

When [2-AFN] was greater than 10 µM and [dsDNA] was smaller than 400 µg mL^{-1} (more than 0.1 µmol of 2-AFN to ~3.1 µmol of bases), the dsA potential decreased even more: from 1.454 ± 0.015 V to 1.326 ± 0.006 V. This means that the adenine bases react proportionally to the concentration of 2-AFN, whereas the guanine bases were simply overwhelmed, no matter the amount. The decrease in the dsA oxidation potential could be attributed to the same reason as for dsG potentials, that the intercalation of large quantities of 2-AFN into the helix stretched and unwound the strands, revealing the purine rings, and facilitiating easier electron removal. Based on the literature, the amine group is expected to bond to the C8 position in guanine covalently [9]. There are two possible conformations when 2-AFN forms an adduct with guanine, leading to different types of distortion in the double-helix structure (Figure 4.22A).

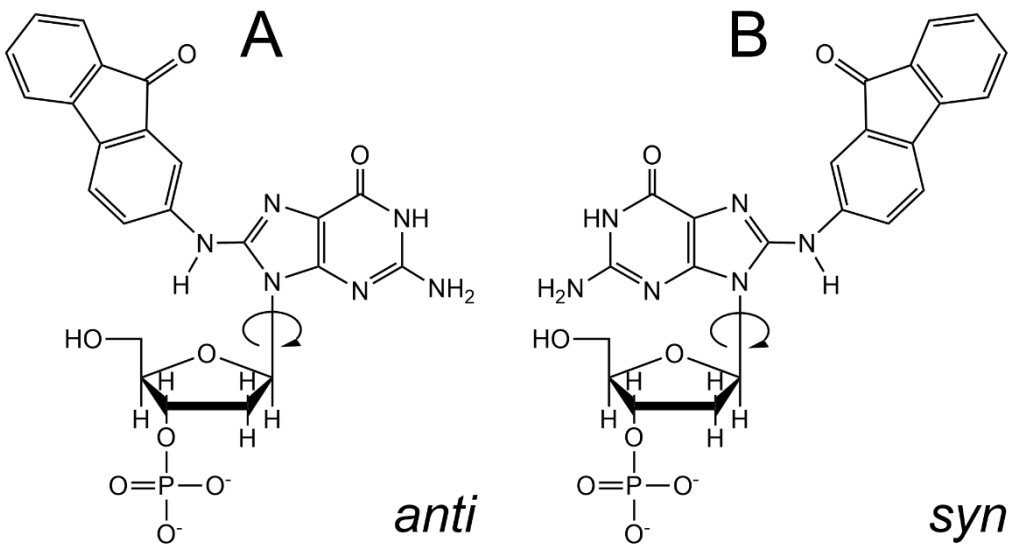


Figure 4.22 The two conformations of 2-AFN covalently bonding to the guanine base at the C8 position: *anti* or *syn* N-(2'-deoxyguanosin-8-yl)-2-aminofluorenone monophosphate. (A) The major groove conformation: the 2-AFN sticks out of the double helix and the guanine stays in the normal *anti* glycosidic bond conformation. (B) The base-displacing intercalation: the guanine adopts the *syn* glycosidic bond conformation, the fluorenyl rings are inserted into the helix, and both the adducted guanine and its partner cytosine are extruded into the major groove.

In the major groove conformation, the guanine remains in the normal *anti* glycosidic bond conformation, and the fluorenyl ring system sticks out of the double helix. In the base-displacing intercalation conformation (Figure 4.22B), the guanine adopts the *syn* glycosidic bond conformation, where the fluorenyl rings are inserted into the helix, which forces the strands to bulge and pushes both the adducted guanine and its partner cytosine into the major groove. A small amount of untwisting accompanies both conformations.

Experiments in this section confirm that the concentration of the damaging agent, 2-AFN, impacts the structural integrity of dsDNA. There is enormous capacity for 2-AFN uptake into the helix, such that up to 5 μM of 2-AFN is consumed before there are sufficient free molecules to be detectable. With the increasing concentration of 2-AFN, deeper degradation of dsDNA occurred, causing the decrease of dsG and dsA DPV peaks. Intercalation was not the only process occurring. The increase in oxidation potential of 2-AFN in the mixture means that the dsG was harder to oxidise, indicating that guanine–AFN adducts were formed.

4.4 Conclusions

The work described in this chapter investigated the voltammetric behaviour of 2-amino-9-fluorenone (2-AFN) and its interaction with dsDNA. Optimising the polarisation cleaning method found in Chapter 3 was effective in creating reproducible BDD electrode surfaces for the detection of 2-AFN, guanosine, adenosine, and dsDNA.

Voltammetry of 2-AFN was recorded in solutions at pH 2.0 to 10.0, where the optimal condition was found to be pH 4.0. At a molecular level, 2-AFN diffuses to the electrode and undergoes proton-dependent irreversible oxidation in the anodic region to form dimers or longer polymer chains. Then these and the monomers also take part in reversible reduction of the carbonyl group. Both redox events are observed in the positive potential region. Physical techniques such as SEM and XPS corroborate with the electrochemical

evidence that polymers are formed in conditions below pH 10.0.

The detection limit of 2-AFN at a bare BDD electrode was measured to be 10 nM using differential pulse voltammetry, which is an order of magnitude better than previously reported with any other electrode material. If BDD electrodes were to be used for quantitative detection, a wide linear range of between 2 and 100 µM is reliable. The detection limits were 3.45 to 441 µM for G and 15 to 468 µM for A. The well-defined peaks observed in DPV are directly assignable to the electro-oxidation of deoxyguanosine and deoxyadenosine groups in the dsDNA macromolecule.

Compared with the free-floating nucleosides, the decreases in the peak potentials and currents in dsG and dsA are attributed to the negatively charged nature of the macromolecule and the much lower diffusion coefficients. The linear regions for dsG and dsA oxidation were 6.25–1000 $\mu g\,mL^{-1}$ (4.75 to 765 µM) and 25 and 1000 $\mu g\,mL^{-1}$ (19 to 765 µM), respectively.

After incubation of 2-AFN with dsDNA, relative-concentration-dependent changes in the oxidation potentials of all three species confirm the preferential binding of 2-AFN with the guanine moieties. The formation of the 2-AFN–DNA adducts made 2-AFN oxidation more difficult, increasing the oxidation potential by ~20 mV. The incorporation of large quantities of 2-AFN in turn increased the intramolecular strain between the bases and along the sugar-phosphate backbone, leading to possible exposure of the oxidation centres of surrounding bases, which made their oxidation easier. At the same time, the peak currents decreased beyond the expected range, suggesting that the intercalation also altered the diffusion behaviour of the now laden strands

When dsDNA was added to 2-AFN, damage to the DNA was evident in the changes in the significant deviations in the dsG and dsA peak currents from the statistical average. In this case, 0.21 µmoles of 2-AFN (out of 0.5 µmoles) had been removed from the solution

by 29.1 µmoles of bases. Similar observations were made for the experiment where 1 µmole of 2-AFN was incrementally added to 30.6 µmoles of dsDNA. The dsDNA current decreased substantially (10-fold) beyond expectations, indicating that between 10.6 and 12.6 µmoles of bases have lost their ability to be oxidised. As the amount of 2-AFN incorporated was directly proportional to the amount of damage observed, 0.24 µmoles of 2-AFN may be assumed to have been integrated. The amount of DNA damage inflicted is 44 to 53 times the number of 2-AFN molecules incorporated, confirming its place among the ranks of powerful mutagens.

The work in this chapter shows that BDD as an electrode material outpaces current sensitivities for the detection of 2-AFN. The fouling resistance of BDD means that it can probe solution interactions between DNA and 2-AFN, both qualitatively and quantitatively.

References

[1] W. E. Bechtold, T. R. Henderson, and A. L. Brooks, "Isolation, identification and bacterial mutagenicity of 2-nitro-9-fluorenone from diesel-exhaust particle extracts," *Mutatation Research Letters*, vol. 173, pp. 105–109, 1986, doi: 10.1016/0165-7992(86)90085-0.

[2] H. Yu, "Environmental carcinogenic polycyclic aromatic hydrocarbons: Photochemistry and phototoxicity," *Journal of Environmental Science and Health. Part C—Environmental Carcinogenesis and Ecotoxicology Reviews*, vol. 20, no. 2, pp. 149–183, 2002, doi: 10.1081/GNC-120016203.

[3] R. T. Okinaka, J. W. Nickols, and T. W. Whaley, "Phototransformation of 2-aminofluorene into N-oxidized mutagens," *Carcinogenesis*, vol. 5, no. 12, pp. 1741–1743, 1984.

[4] G. F. Strniste, J. W. Nickols, R. T. Okinaka, and T. W. Whaley, "2-Nitrofluoren-9-one: a unique mutagen formed in the photo-oxidation of 2-aminofluorene," *Carcinogenesis*, vol. 7, no. 3, pp. 499–502, 1986.

[5] G. F. Strniste, J. W. Nickols, and R. T. Okinaka, "Photochemical oxidation of 2-aminofluorene: Correlation between the induction of direct-acting mutagenicity and the formation of nitro and nitroso aromatics," *Mutatation Research*, vol. 151, no. 1, pp. 15–24, 1985, doi: 10.1016/0027-5107(85)90177-0.

[6] National Aeronautics and Space Administration and S. M. Directorate, "Ultraviolet waves," *NASA Science*, 2010. http://science.nasa.gov/ems/10_ultravioletwaves

[7] F. A. Asswadi, "Novel anodic oxidation of 1-amino-9-fluorenone and its electrochemical behavior," *International Journal of Scientific and Engineering Research*, vol. 7, no. 8, pp. 2340–2351, 2016.

[8] J. M. A. Empis and B. J. Herold, "Substituent effects in fluoren-9-one ketyls. Part 2. The electrolytic reduction of fluoren-9-ones studied by cyclic voltammetry and electron spin resonance spectroscopy," *Journal of the Chemical Society Perkin Transactions II*, pp. 425–430, 1986.

[9] M. Zeisig and L. Möller, "^{32}P-HPLC suitable for characterization of DNA adducts formed *in vitro* by polycyclic aromatic hydrocarbons and derivatives," *Carcinogenesis*, vol. 16, no. 1, pp. 1–9, 1995, doi: 10.1093/carcin/16.1.1.

[10] I. V. M. V. Enoch and M. Swaminathan, "Fluorimetric study on molecular recognition of β-cyclodextrin with 2-amino-9-fluorenone," *Journal of Fluorescence*, vol. 16, no. 4, pp. 501–510, 2006, doi: 10.1007/s10895-006-0074-z.

[11] V. Vyskočil, "New electrochemical methods for determinations of nitro and oxo derivatives of fluorene," PhD Thesis, Charles University of Prague, 2010.

[12] A. Hájková, J. Hranicek, J. Barek, and V. Vyskočil, "Voltammetric determination of trace amounts of 2-aminofluoren-9-one at a mercury meniscus modified silver solid

amalgam electrode," *Electroanalysis*, vol. 25, no. 1, pp. 295–302, 2013, doi: 10.1002/elan.201200408.

[13] A. Hájková, J. Barek, and V. Vyskočil, "Voltammetric determination of 2-aminofluoren-9-one and investigation of its interaction with DNA on a glassy carbon electrode," *Electroanalysis*, vol. 27, no. 1, pp. 101–110, 2015, doi: 10.1002/elan.201400427.

[14] P. W. O'Keefe, O. Ekabo, E. Braun-Howland, D. Swarr, and B. Stockholm, "Microbial reduction of 9-fluorenone to 9-hydroxyfluorene in carbon-filtered water: A confounding factor in an aquatic bioassay of 9-fluorenone with larvae of the midge, *Chironomus tentans* (Fabr.)," *Bulletin of Environmental Contamination and Toxicology*, vol. 75, no. 6, pp. 1060–1066, 2005, doi: 10.1007/s00128-005-0857-y.

[15] W. Wilcke and B. Bandowe, "Persistent organic pollutants in soil: sources, concentrations, and fate," *National Environmental Research Institute Technical Report* No. 402, pp. 33–38, 2011.

[16] L. Möller, I. Lax, and L. C. Eriksson, "Nitrated polycyclic aromatic hydrocarbons: A risk assessment for the urban citizen," *Environmental Health Perspectives Supplements*, vol. 101 (Suppl. 3), pp. 309–315, 1993, doi: 10.2307/3431744.

[17] L. Möller, I. Lax, U. -B Torndal, and L. C. Eriksson, "Risk assessment of nitrated polycyclic aromatic hydrocarbons," *Risk Analysis*, vol. 13, no. 3, pp. 291–299, 1993, doi: 10.1111/j.1539-6924.1993.tb01081.x.

[18] A. M. Oliveira-Brett, J. A. P. Piedade, L. A. Silva, and V. C. Diculescu, "Voltammetric determination of all DNA nucleotides," *Analytical Biochemistry*, vol. 332, no. 2. pp. 321–329, 2004, doi: 10.1016/j.ab.2004.06.021.

[19] T. Dal-Cim *et al.*, "Neuroprotection promoted by guanosine depends on glutamine synthetase and glutamate transporters activity in hippocampal slices subjected to oxygen/glucose deprivation," *Neurotoxicity Research*, vol. 29, no. 4, pp. 460–468, 2016, doi: 10.1007/s12640-015-9595-z.

[20] D. Boison, "Adenosine as a neuromodulator in neurological diseases," *Current Opinion in Pharmacology*, vol. 8, no. 1, pp. 2–7, 2008, doi: doi:10.1016/j.coph.2007.09.002.

[21] D. P. Dohrman, "The role of the neuromodulator adenosine in alcohol's actions," *Alcohol Health and Reseearch World*, vol. 21, no. 2, pp. 136–143, 1997.

[22] A. C. Povey, "DNA adducts: endogenous and induced," *Toxicologic Pathology*, vol. 28, no. 3, pp. 405–414, 2000.

[23] H. Mu *et al.*, "Nucleotide excision repair of 2-acetylaminofluorene-and 2-aminofluorene-(C8)-guanine adducts: Molecular dynamics simulations elucidate how lesion structure and base sequence context impact repair efficiencies," *Nucleic Acids Research*, vol. 40, no. 19, pp. 9675–9690, 2012, doi: 10.1093/nar/gks788.

[24] R. Gasparac, B. J. Taft, M. A. Lapierre-Devlin, A. D. Lazareck, J. M. Xu, and S. O.

Kelley, "Ultrasensitive electrocatalytic DNA detection at two- and three-dimensional nanoelectrodes," *Journal of the Americal Chemical Society*, vol. 126, no. 39, pp. 12270–12271, 2004, doi: 10.1021/ja0458221.

[25] I. Ivanov, J. Stojcic, A. Stanimirovic, E. Sargent, R. K. Nam, and S. O. Kelley, "Chip-based nanostructured sensors enable accurate identification and classification of circulating tumor cells in prostate cancer patient blood samples," *Analytical Chemistry*, vol. 85, no. 1, pp. 398–403, 2013, doi: 10.1021/ac3029739.

[26] E. E. Ferapontova, "DNA electrochemistry and electrochemical sensors for nucleic acids," *Annual Review of Analytical Chemistry*, vol. 11, no. 1, pp. 197–218, 2018, doi: 10.1146/annurev-anchem-061417-125811.

[27] A.-M. M. Chiorcea-Paquim, S. C. B. Oliveira, V. C. Diculescu, and A. M. Oliveira-Brett, "Applications of DNA-electrochemical biosensors in cancer research," *Comprehensive Analytical Chemistry*, vol. 77, pp. 237–286, 2017, doi: 10.1016/bs.coac.2017.06.003.

[28] W. R. Carmody, "Easily prepared wide range buffer series," *Journal of Chemical Education*, vol. 38, no. 11, p. 559, 1961, doi: 10.1021/ed038p559.

[29] B. Marselli, J. Garcia-Gomez, P.-A. Michaud, M. A. Rodrigo, and C. Comninellis, "Electrogeneration of hydroxyl radicals on boron-doped diamond electrodes," *Journal of The Electrochemical Societry*, vol. 150, p. D79, 2003, doi: 10.1149/1.1553790.

[30] R. Kiran, E. Scorsone, P. Mailley, and P. Bergonzo, "Quasi-real time quantification of uric acid in urine using boron doped diamond microelectrode with in situ cleaning," *Analytical Chemistry*, vol. 84, no. 23, pp. 10207–10213, 2012, doi: 10.1021/ac301177z.

[31] C. H. Goeting, F. Marken, A. Gutiérrez-Sosa, R. G. Compton, and J. S. Foord, "Electrochemically induced surface modifications of boron-doped diamond electrodes: an X-ray photoelectron spectroscopy study," *Diamond and Related Materials*, vol. 9, no. 3–6, pp. 390–396, 2000, doi: 10.1016/S0925-9635(99)00267-8.

[32] R. G. Compton and C. E. Banks, "Chapter 4 Cyclic voltammetry at macroelectrodes," in *Understanding Voltammetry*, 2nd edn, London: Imperial College Press, 2011, pp. 107–155.

[33] E. L. Cussler, "Chapter 5 Values of diffusion coefficients," in *Diffusion — Mass Trasport in Fluid Systems*, 3rd edn, Cambridge University Press, 2009, pp. 126–134.

[34] D. Kumar, A. K. Tomar, G. Singh, and R. K. Sharma, "Interlayer gap widened 2D α-$Co(OH)_2$ nanoplates with decavanadate anion for high potential aqueous supercapacitor," *Electrochimica Acta*, vol. 363, p. 137238, 2020, doi: 10.1016/j.electacta.2020.137238.

[35] R. G. Compton and C. E. Banks, "4.11 The influence of pH on cyclic voltammetry,"

in *Understanding Voltammetry*, 2nd edn, London, 2011, pp. 147–150.

[36] T. Imamoglu and A. M. Önal, "Electrochemical polymerisation of 2-aminofluorene in ethylalcohol/water medium," *European Polymer Journal*, vol. 40, no. 8, pp. 1875–1880, 2004, doi: 10.1016/j.eurpolymj.2004.03.019.

[37] E. Steckhan, "Chapter 15 Anodic oxidation of nitrogen-containing compounds," in *Organic Electrochemistry*, 4th edn, H. Lund and O. Hammerich, Eds. New York and Basel: Marcel Dekker, 2001, pp. 551–555.

[38] F. A. Asswadi, U. S. Yousef, A. S. Hathoot, M. Abdel Azzem, and A. Galal, "Electropolymerization of diaminofluorene and its electrochemical properties," *Arabian Journal of Chemistry*, vol. 8, no. 4, pp. 433–441, 2015, doi: 10.1016/j.arabjc.2011.03.016.

[39] K. Juttner and D. Becker, "Characterization of boron-doped diamond electrodes by electrochemical impedance spectroscopy," *Journal of Applied Electrochemistry*, vol. 37, pp. 27–32, 2007, doi: 10.1007/s10800-006-9228-6.

[40] Z. J. Ayres, J. C. Newland, M. E. Newton, S. Mandal, O. A. Williams, and J. V. Macpherson, "Impact of chemical vapour deposition plasma inhomogeneity on the spatial variation of sp^2 carbon in boron doped diamond electrodes," *Carbon*, vol. 121, pp. 434–442, 2017, doi: 10.1016/j.carbon.2017.06.008.

[41] G. Beamson and D. Briggs, *High Resolution XPS of Organic Polymers - The Scienta ESCA300 Database*. Wiley Interscience, 1992.

[42] A. Mohtasebi, T. Chowdhury, L. H. H. Hsu, M. C. Biesinger, and P. Kruse, "Interfacial charge transfer between phenyl-capped aniline tetramer films and iron oxide surfaces," *Journal of Physical Chemistry C*, vol. 120, no. 51, pp. 29248–29263, 2016, doi: 10.1021/acs.jpcc.6b09950.

[43] P. Subramanian and G. Dryhurst, "Electrochemical oxidations of guanosine formation of some novel guanine oligonucleosides," *Journal of Electroanalytical Chemistry and Interfacial Electrochemistry*, vol. 224, no. 1–2, pp. 137–162, 1987, doi: https://doi.org/10.1016/0022-0728(87)85089-1.

[44] M. Fojta, "Electrochemical sensors for DNA interactions and damage," *Electroanalysis*, vol. 14, no. 21, pp. 1449–1463, 2002, doi: 10.1002/1521-4109(200211)14:21<1449::AID-ELAN1449>3.0.CO;2-Z.

[45] T. A. Ivandini, B. V. Sarada, T. N. Rao, and A. Fujishima, "Electrochemical oxidation of underivatized-nucleic acids at highly boron-doped diamond electrodes," *Analyst*, vol. 128, no. 7, p. 924, 2003, doi: 10.1039/b301483e.

[46] W. Saenger, "Chapter 17 Water and Nucleic Acids," in *Principles of Nucleic Acid Structure*, C. R. Cantor, Ed., Springer-Verlag, 1984, pp. 368–384.

Chapter 5

Detection of carbamate and organophosphate pesticides with bare BDD

5.1 Introduction

Previous chapters have demonstrated the high sensitivity of BDD at high oxidation potentials and described reliable and quick cleaning methods. Continuing the theme of detection and quantification of molecules which impact health, this chapter covers pollutants with more immediate consequences for life: pesticides.

Carbamate and organophosphate compounds are widely used by farmers for their high insecticidal activity [1]. Here we investigated four carbamates—fenobucarb (FC), carbaryl (CB), carbofuran (CF), and aldicarb (AC) (Figure 5.1)—and one organophosphate: malathion (MT) (Figure 5.4). They work by inhibiting the enzyme acetylcholinesterase (AChE), which leads to a build-up of the neurotransmitter acetylcholine at motor-neuron synapses, and causes seizures [2]. Application in the liquid form is effective because insects have spiracles on their exoskeletons to allow air to enter the tracheal tubes which deliver oxygen (and these inhibitors) directly into the tissues [3].

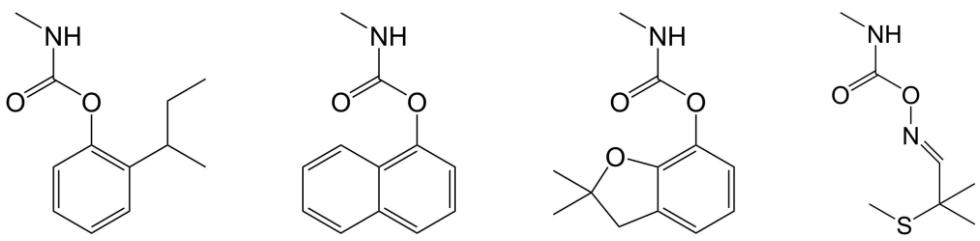


Figure 5.1 Carbamate pesticides: fenobucarb, carbaryl, carbofuran, and aldicarb.

The two major problems with industrial pesticide use are direct poisoning from occupational exposure and contamination of drinking water by run-off from farms [4]. In the US, annual insecticide usage decreased from 45 million kilograms in 2002 to 30 million kg in 2012, of which organophosphates account for ~50% [5]. And between 2008 and 2012, 16–18% of the total world pesticide expenditures were by the US. Carbamates are much more potent, and so they take up a lesser weight percentage [5]. These compounds hijack the nervous system of the target organisms, and they affect other organisms in the food chain indiscriminately through accumulation [6].

Apart from intentional ingestion, most people are exposed to carbamate pesticides by handling their neat forms while making dilutions for crop protection, or contacting contaminated water from farm run-offs. The term LD50 describes the lethal dose required to kill 50% of test animals. The values in Table 5.1 are provided to give an idea of the level of toxicity of these compounds to laboratory rats. The aim of this project to be able to detect and, preferably, distinguish these pesticides.

Table 5.1 The hazardous threshold concentrations as issued by safety authorities

Carbamate	**LD50 for rats, mg/kg**	**Equivalent lethal human dose**	**Commercially available concentration**
Fenobucarb	♂250 ♀185 [7]	15.2 g	500 g/L (Baycarb® 500 EC) [8]
Carbaryl	♂850 ♀500 [7]	47.3 g	479 g/L (Carbaryl 4L) [9]
Carbofuran	2 – 5 [10]	0.25 g	479 g/L (Furadan 4F) [11]
Aldicarb	0.9 [12]	0.06 g	Granules, 150 g/kg (Temik® 150G) [13]

Existing electrochemical sensing methods mostly use AChE, where it is either physically or chemically trapped to a sensing platform, which is often conductive. Acetylcholinesterase is layered atop bare electrodes, or adsorbed onto nanomaterials to

assist loading (to increase surface area, or to act as a scaffold) on conductive substrates [4,5]. A multitude of substrate materials have been tested, in particular: platinum [14], gold [15], fluorine-doped tin oxide [16], glassy carbon [17], screen-printed carbon [18], and BDD [19]. A long list of trialled nanomaterials includes maghemite [20], silver [21], gold [22], graphene oxide [23], and carbon nanotubes [24]. After the biosensor is complete, it can either be exposed directly to the pesticide solution (Figure 5.2 A,C,D) or used in solutions where the pesticide has been incubated with AChE (Figure 5.2 B) [14–16,25]. Then, electrochemical signals are recorded, which relate to the concentration of the pesticide and degree of enzyme inhibition, respectively.

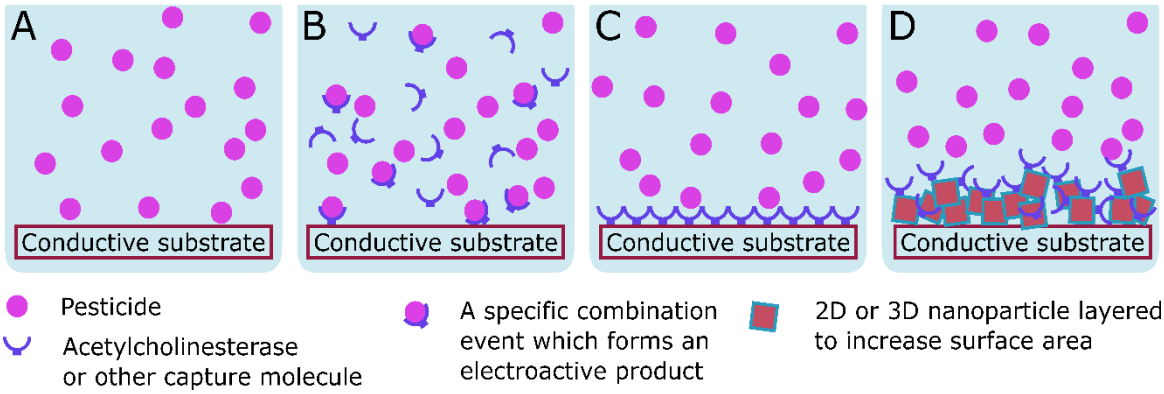


Figure 5.2 Various existing schemes to detect pesticides in solution.

Similar to the general idea shown in Figure 5.2B, the analyte itself can be modified before detection. Carbamates have been reported to undergo acid-catalysed, neutral, and alkaline hydrolysis, as well as photolysis [26]. The latter two are most likely to occur in conditions common to aquatic environments, and both have been used to simulate carbamate degradation in nature [27,28]. Alkaline hydrolysis is of particular interest here, as it has been reported to change the oxidation characteristics of carbamates [29,30]. The mechanism in Figure 5.3 shows the alkaline hydrolysis of the N-alkyl substituted carbamate carbaryl [31], a process that is expected to be similar for the other carbamate pesticides. Structure 1 is the original carbaryl (CB) and structure 2 is the hydrolysed carbaryl (H-CB), and both are expected to be electroactive.

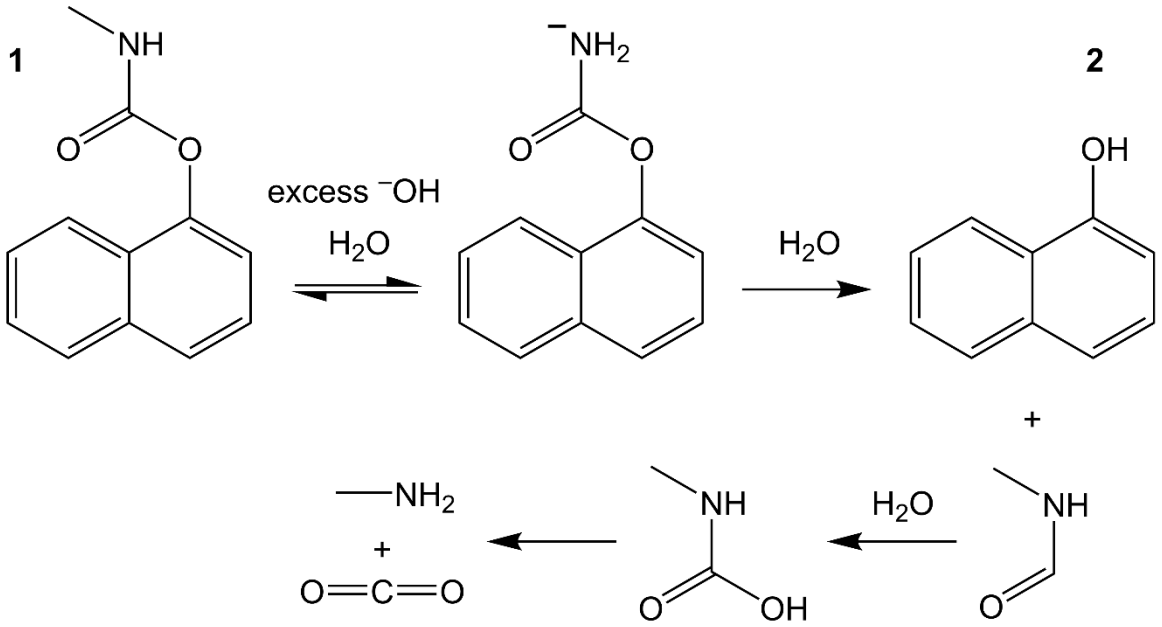


Figure 5.3 Mechanism for the alkaline hydrolysis of carbaryl (structure **1**). The intended product with a lower oxidation potential is structure **2**: 1-naphthol.

Organophosphates generally have low solublity in water, and MT (Figure 5.4) is often sold as a dilute suspension [32]. Although MT is one of the more well-known pesticides, we have not found reports of its interactions with bare electrode materials, as the focus remains with the development of biosensors involving microorganismic and biomolecular deposition [33], just as in carbamate electrochemistry. However, some work has been done which employs a different approach, and we consider that now.

Aptamers have been synthethised and used to capture MT. They allow more specific binding and identification than does AcheE, and have a longer shelf-life [21]. In 2018, Nie et al. linked aptamers to silver NPs, incubated them with MT, and used surface-enhanced Raman scattering to count the proportion of silver NPs now attached with aptamer-MT [21]. A colorimetric test uses the size-dependent colour properties of gold NPs to monitor the presence of MT, where MT and a cationic peptide compete for binding with an aptamer. In an MT binding event, the peptide is freed, which causes NP aggregation and turns the suspension from red to blue [22].

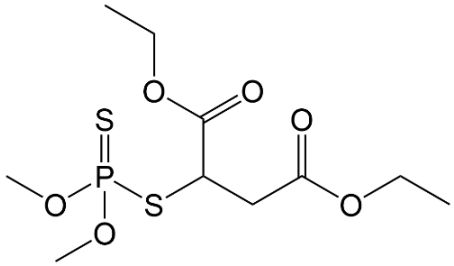


Figure 5.4 Chemical structure of malathion (MT), a common organophosphate.

From the works referenced here that involve decorated electrodes, the fabrication time can take from a few hours to a few days [34–36]. These sensors are specific to neurotoxic pesticides because of the AChE enzyme. However, they are subject to enzyme longevity issues, and require dexterity and experience to prepare. The main reason why previous work relied so heavily on enzymes and nanomaterials is the potential window of the electrode. As such, BDD is well placed to provide an alternative.

The first objective of this work is to discover whether the electroactive behaviour of the pesticides FC, CB, CF, AC, and MT may be observed with oxygen-terminated BDD without enzymes, and if this detection caused any surface changes to the electrode. The second is to investigate the possibility of specific identification with alkaline hydrolysis of the carbamates, both in buffers and in river water. With both forms of pesticide, the limit of detection was investigated. The final aim is to compare the sensing capabilities of bare BDD with other methods (electrochemical or otherwise), also making a comparison of the limit of detection and linear range, which are both crucial aspects for developing real applications using electrochemistry.

5.2 Experimental details

Given the high potentials of the pesticide oxidation, the usual cyclic cleaning in 0.1 M HNO_3, at 100 mV s^{-1}, was adjusted to go from 0 V to 3 V to –2 V to 0 V. This was done for at least 30 cycles, or until the voltammograms appeared flat and the currents in the regions of interest were between ± 0.5 μA.

5.2.1 Solutions

All the carbamate pesticides (analytical grade) were obtained from Sigma Aldrich and used without further purification. Stock solutions of each pesticide in buffer were prepared by weighing. For CF and FC, a small volume of acetone (< 3 mL) was used to dissolve the solids, and then the solution was made up in a volumetric flask. A fresh solution was made for each day of experiments. The concentration of 200 μM was found to be a good compromise between dissolution of solids and minimising weighing errors. For multiple-analyte solutions, the solids were weighed and placed in the same flask before being dissolved with acetone if necessary and made up to volume with buffer. For experiments involving river water, it directly replaced buffer solutions without further treatment.

5.2.2 Alkaline hydrolysis

To make stock solutions of hydrolysed carbamates (either single or multiple), the solids were weighed and dissolved in acetone first, and then about 10 mL of water was washed down the neck of the volumetric flask. To this was added 10 mL of 0.5 M NaOH (in excess of the quantity of carbamate). The solutions were mixed thoroughly (in a volumetric flask) and left for at least 10 minutes at room temperature. Following this hydrolysis procedure, glacial acetic acid was added dropwise in a beaker to adjust the pH to 7.0. The solution was then poured back into the volumetric flask and made up with pH 7.0 Carmody buffer. For solutions of any combination of carbamates or hydrolysed carbamates, their stock solutions were pipetted in appropriate ratios and made up with Carmody buffer in glass vials.

5.2.3 Voltammetry parameters

Analytical CVs of each carbamate were carried out between 0.4 and 1.6 V (exploration was carried out between –1.5 and 2.2 V) versus the 1.0 M Ag|AgCl electrode, at a scan rate of 100 mV s^{-1}, unless otherwise stated. Randles–Sevčik type experiments were performed using the same parameters but with a scan rate that ranged from 10 to 400 mV s^{-1}. Square-

wave voltammetry was performed from 0 to 2.2 V. Its frequency was 28.5 Hz, with a modulation amplitude of 100 mV, and a potential step of 3.5 mV, to achieve a scan rate of 100 mV s^{-1}. For a slower scan rate of 10 mV s^{-1}, the frequency was reduced to 2.85 Hz, which was useful in confirming the limit of detection.

5.3 Malathion results and discussions

5.3.1 Cyclic voltammetry

Neat malathion (MT) is immiscible with water, and so to make a 1 mM aqueous solution at pH 7.0 it was first thinned out in a minimal volume of acetone before dilution in buffer. Figures 5.5 shows the experience with MT as a representative organophosphate pesticide.

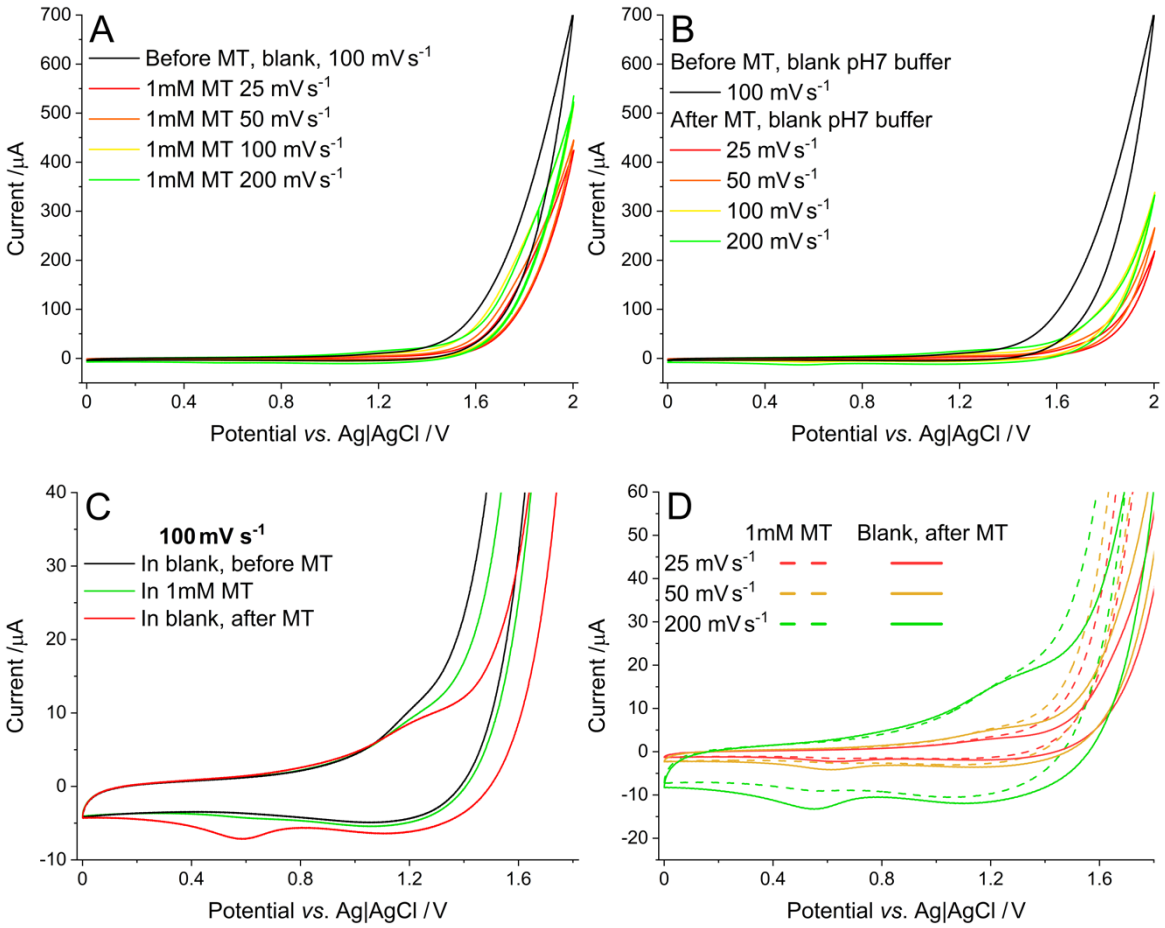
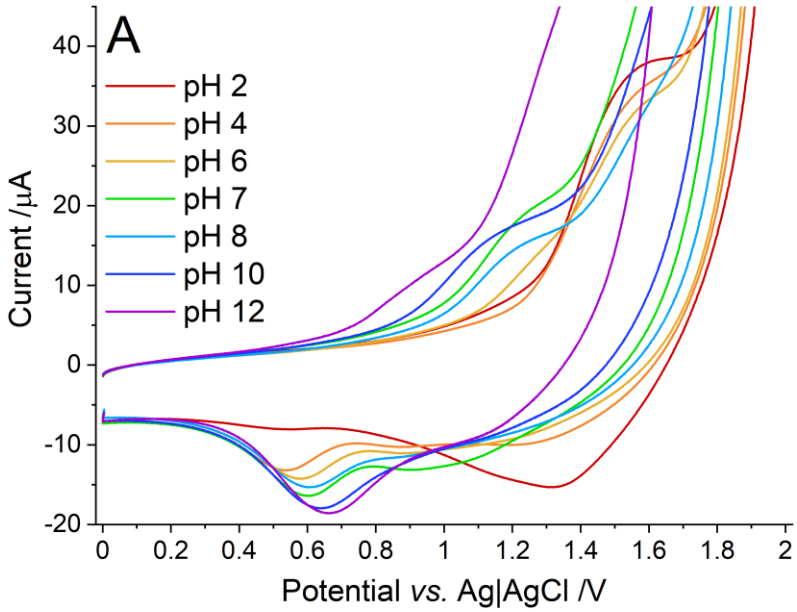


Figure 5.5 (A) CVs in 1 mM MT at pH 7.0. (B) CVs in blank buffer after recording A. (C,D) Scaled selected parts of A and B, to show greater detail.

Figures 5.5A,C show that there is little difference between the CV recorded in blank buffer and that recorded in 1mM MT. Although interestingly the currents recorded in buffer at high anodic potentials exceed those observed in the presence of MT. This suggests that the electrode is becoming passivated in some way by the presence of MT. This modification of the electrode becomes clear through the following experiment: once the scans in MT were complete, the electrodes and cell were rinsed, and CVs of the same scan rates were recorded in blank buffer (Figure 5.5B and D) and a new reduction feature at ~0.5 V become visible. Just from the initial exposure of MT in a simple scan rate experiment, this reduction feature will prove to be permanent as the following two sections will show.

Figure 5.6 shows the response of a BDD electrode which had been extensively scanned in 1 mM MT, then cleaned, and then scanned in blank Carmody buffers of pH values between 2.0 and 12.0, from 0 to +2 V. By ‘cleaned’ we mean that exposed electrodes were given all of the following treatments: scrubbed in detergent, hand polished in alumina slurry, left in aqua regia overnight, sonicated in acetone, boiled in concentrated nitric then sulphuric acid, subjected to extensive scans in dilute nitric acid. All attempts to restore the electrode response as in blank buffer (when there should be no visible peaks) were made.



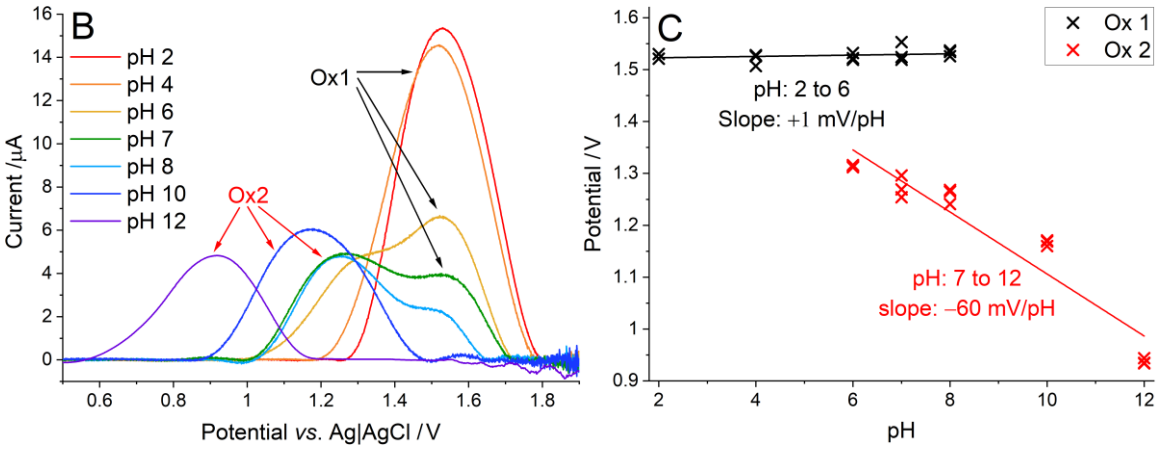


Figure 5.6 (A) CV responses of a BDDE that had been used for extensive scans in MT, cleaned, and then scanned in buffers of pH values between 2.0 and 12.0, at 100 mV s^{-1}. (B) The baseline-subtracted forward waves from A. (C) Oxidation potentials against pH.

As pH increases, oxidation of the background electrolyte is easier, seen as lower potentials for the onset of rapidly rising currents at 1.8 V for pH 2.0 and 1.2 for pH 12.0 (Figure 5.6A). Each scan shows a pair of redox peaks, and there is a generalised trend for them to move together negatively as pH increases. Figure 5.6B shows representative forward waves which have had their baselines removed to allow better peak definition. The increase in pH values brings on a gradual disappearance of one oxidation peak at 1.5 V (pH 2.0–8.0), and the appearance of a new peak between 0.9 and 1.3 V (pH 6.0 and higher); this suggests that there are two species: one that is independent on pH (black line in Figure 5.6C). Its peak does not shift with pH, suggesting that no protons are transferred during the electrochemical process, and so this species must already be protonated. A second species is active only above pH 4.0; its oxidation-peak potential increases (it becomes harder to oxidise) as pH increases (red line in Figure 5.6C). The oxidation of the second species follows the –59 mV change per pH value, theorised for a simple one-proton–one-electron oxidation.

The same electrode was then scanned in blank pH 7.0 buffer only, this time changing

the scan range. The scans start at 0 V at 100 mV s^{-1} and ends at –0.5 V, and the anodic turn-around potential is increased from 1.4 to 2.5 V in 0.1 V increments. As the scan range increases, Figure 5.7 A shows the increase in the background current in the anodic region, from buffer electrolyte dissociation as expected, and Figure 5.7 B shows the increase in the new reduction peaks.

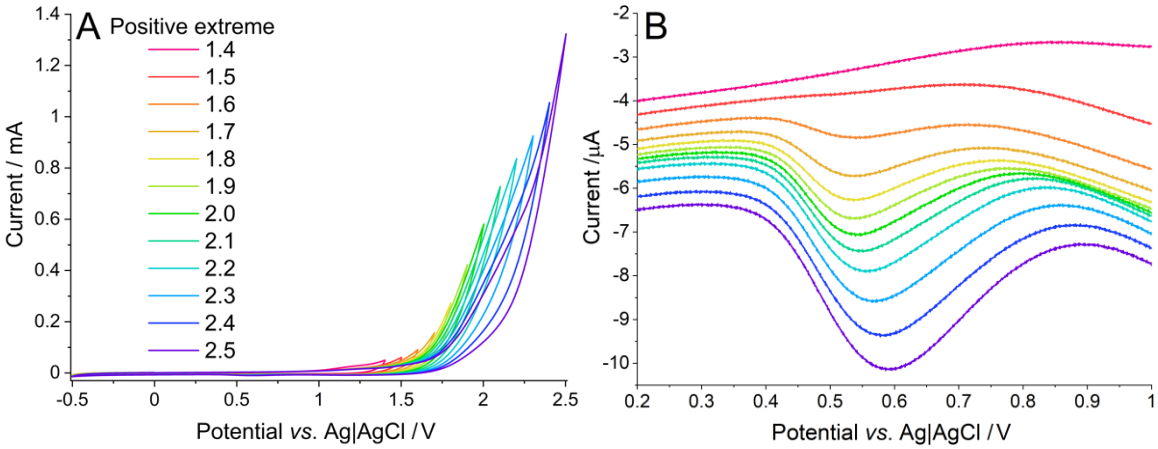


Figure 5.7 Responses of a BDD electrode that has been subjected to extended voltammetry in 1mM MT, in pH 7.0 buffer at scan rates from 25 to 200 mV s^{-1}. (A) CV scans started and ended at 0 V; the cathodic extreme was fixed at –0.5 V, and the anodic extreme varied from 1.4 to 2.5 V. (B) The reduction region in more detail. The colour legend in chart A applies to both charts A and B.

Two features were observed with the increase in the anodic extreme. As the anodic extreme was increased, the reduction peak potential shifted more positively, and the area encompassed by that peak (amount of charge transferred) also increased; both these are described by linear relationships. On average, a 0.1 V increase in the anodic extreme led to an + 8 mV shift in the position of the reduction peak and a 1.1 µC increase in charge (from 1.5 µC with an extreme of 1.7 V to 8.9 µC with an extreme of 2.5 V, Figure 5.7B). This means that, as we spend longer applying anodic polarisation, more groups get oxidised which can then be subsequently reduced, and that the reduction event required higher potential to complete.

Quinone reduction has been shown to fall within +1 and –0.6 V on other carbon electrodes, where they are intrinsic naturally [37,38]. The peaks were integrated (from +0.35 to +0.95 V) to obtain the charge passed, Q, and converted to surface coverage, Γ (mol cm^{-2}), using the equation $Q = nFA\Gamma$, where n is the number of electrons transferred (2), F is Faraday's constant (96,485 C mol^{-1}), and A is the electrode surface area (0.442 cm^2). For the curve scanning back from 2.5 V, the charge under the peak is 8.9 µC on average, which gives Γ as 1.04×10^{-10} mol cm^{-2} or around 10 % of a monolayer.

The origin of the reduction peaks seen as diamond electrodes are scanned from anodic to cathodic potentials is not especially well-understood. They could arise from the oxidation of diamond itself, which is then reduced on the cathodic scan. However, this is perhaps unlikely since very high-quality BDD electrodes (very low sp^2 content) have been quoted as having Γ between 1.5×10^{-16} and 7.5×10^{-16} mol cm^{-2} [39,40]. It therefore is more likely the case that these reduction peaks are associated with non-diamond carbon.

After MT exposure, a reduction feature exists around 0.6 V, which is compatible with the reduction of more stable oxidised carbon centres such as quinones. The overall conclusion therefore is that electrochemical treatment of diamond electrodes with MT brings about irreversible changes in the nature of the non-diamond carbon present on the electrodes used. This “irreversible” reduction feature was robust to aggressive cleaning methods and only removable by hydrogen-plasma etching.

5.3.2 XPS of electrodes after malathion exposure

To investigate these changes further, the electrodes exposed to MT were investigated using surface spectroscopic methods. XPS is one of a few methods able to provide surface chemical information for chemically complicated and relatively disordered materials such as polycrystalline diamond electrodes. To deconvolute the functional groups under the carbon 1s peak (Figure 5.8B), several constraints were strictly followed.

To restrain the number of peaks to the minimum required to describe the C 1s peak consistent with reasonable chemical concepts, the full-width half maximum (FWHM) was kept below 1.2 eV [40–42], in line with previous reports on apparatus similar to that employed here; the peak centres were constrained to have a ± 0.3 eV leeway to compromise between fitting well yet capturing all possible functionalities [43]; and the Gaussian–Lorentzian mix was set to 90:10 (because metallic species are lacking although the sample is a semimetal) [44]. The fitting considerations were covered in more detail in Section 2.2.4.

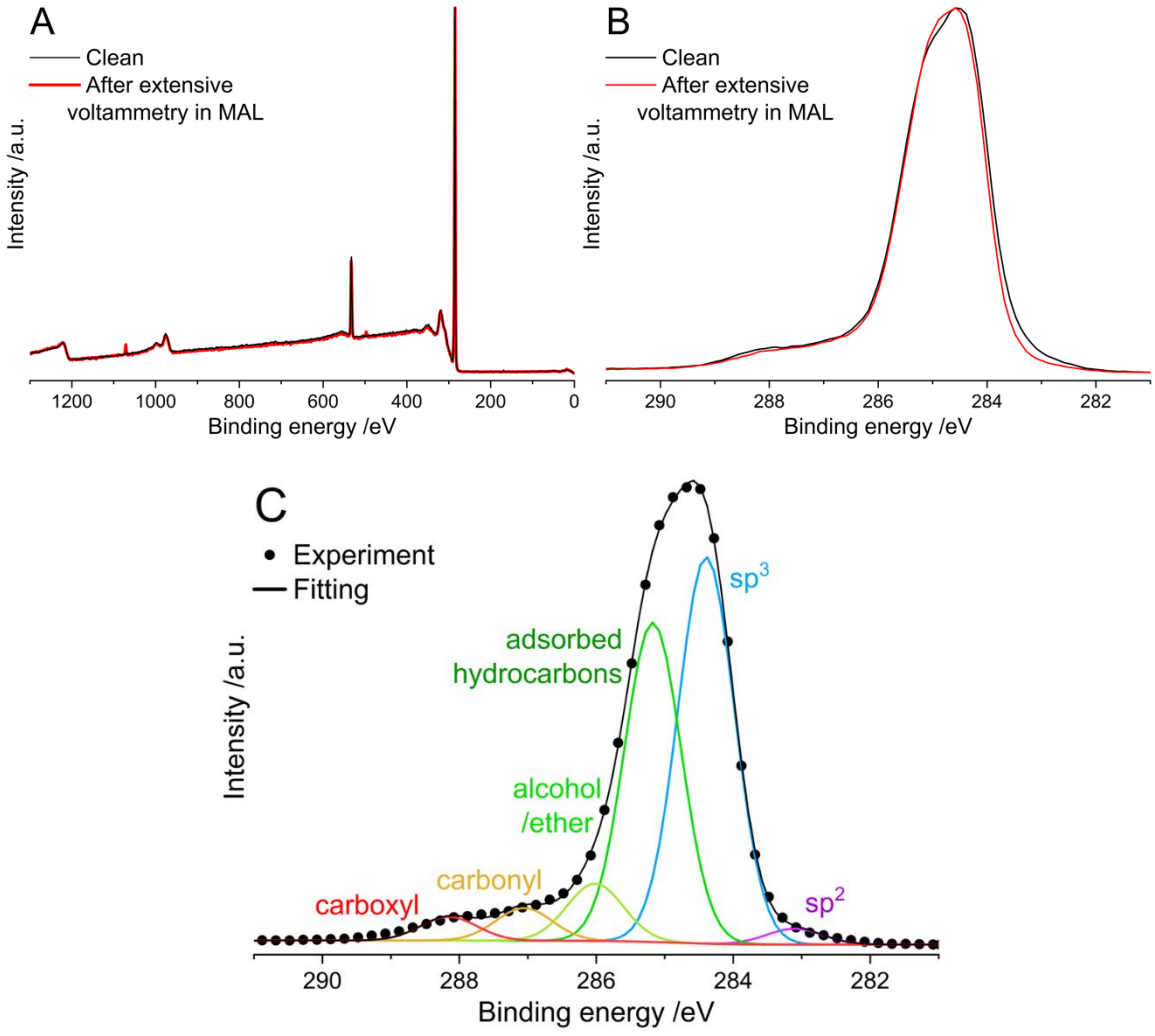


Figure 5.8 (A) Survey and (B) high-resolution spectra of a BDDE before and after exposure to malathion. (C) The deconvoluted carbon 1s spectrum after exposure.

Figure 5.8A shows that the survey spectra before and after MT treatment are essentially similar and overlay significantly at the carbon and oxygen 1s and Auger peak positions.

Even though there seems to be electrochemical evidence for a change in chemical nature, this is not easily seen in XPS. Table 5.2 shows the results of deconvolution of peaks under the carbon 1s spectra for all BDD electrodes used in the present research. The same fit was suitable for both before and after exposure to malathion, since no significant differences between the two was detectable in the carbon 1s region (Figure 5.8B).

Table 5.2 The positions and atomic coverage of deconvoluted C 1s functional groups

Functionalities	**Peak centre /eV**	**Shifts /eV**	**Atomic percentages**	
			Before	**After**
sp^2 hybridisation	283.1	– 1.3	3.1	1.9
sp^3 hybridisation	284.4	0	47.6	45.9
Hydrogenated surface carbons	285.2	+ 0.8	37.0	38.5
alcohol	286.1	+ 1.7	6.0	6.8
carbonyl	287.2	+ 2.8	3.5	3.9
carboxyl	288.2	+ 3.8	2.9	3.0

From the survey spectra (Figure 5.8A), the percentages of elements detected are listed in Table 5.3. The electrode which had been used to perform CVs in 1mM MT showed a slightly higher amount of sodium. The only source of sodium is the sodium triphosphate in the Carmody buffer. As we neither expected MT to polymerise nor observed it, the sodium most likely to be a residual from inadequate rinsing. Aside from the C1s spectrum (Figure 5.8B), high-resolution scans were also taken from the oxygen, nitrogen, sulphur, phosphate, and silicon regions, but no abnormalities were observed.

Table 5.3 Atomic percentages of carbon, oxygen, and sodium functionalities

Survey spectra regions		**Carbon**	**Oxygen**	**Sodium**
Atomic percentages	**Before**	90.59	9.22	0.19
	After	91.03	8.32	0.65

There is no significantly detailed evidence of changes in the BDD surface in either the survey or high-resolution spectra to suggest what functionality caused the interesting pH-dependent reduction feature on exposure to MT. Since the coverage is only 10% of a monolayer, it is possible that the change is too small to be seen in XPS. However, it is also possible that the change is due to some unstable transitory species, with quinone-like electrochemical behaviour, that is oxidised by the forward scan, and then reduced straightaway by the reverse scan, but does not survive removal from solution and subsequent manipulation in air and (XPS) vacuum This instability indicates that some in situ surface-sensitive technique with fast time-resolution may be required for more detailed characterisation. This mystery meant that those contaminated BDDs were retired from subsequent work. Electrodes made from BDD are well-known to be resistant to irreversible modifications by simple electrochemical means. However, this 'MT-modified' BDDE may become advantageous in applications such as pH sensing.

5.4 Carbamates results and discussions

5.4.1 Cyclic voltammetry at pH 7.0

Cyclic voltammograms were recorded for fenobucarb (FC), carbaryl (CB), carbofuran (CF), and aldicarb (AC) at 100 $mV\,s^{-1}$ at pH 7.0. Figure 5.9 shows representative CVs of the four carbamates at 100 μM, the stock concentration, and more dilute concentrations, which are closer to the doses of these pesticides that one would wish to detect.

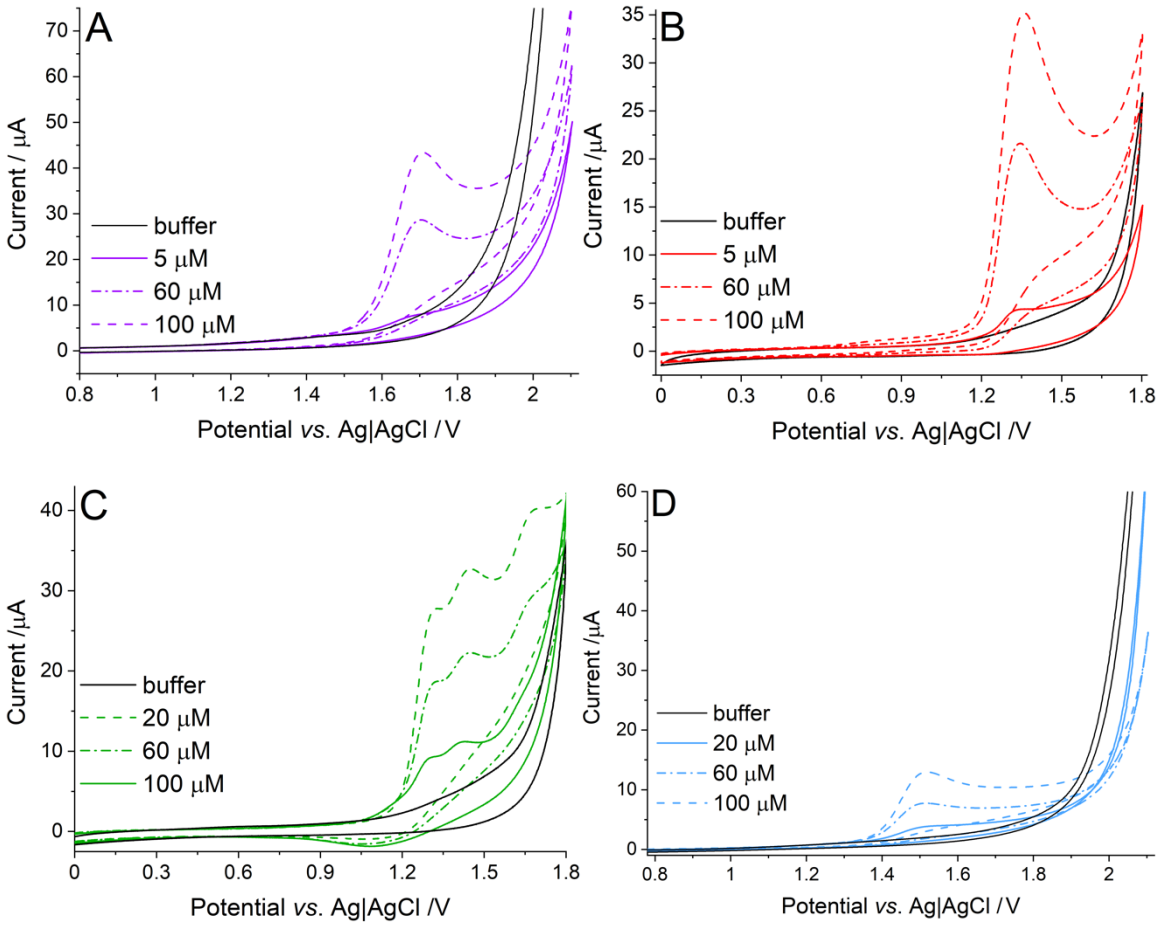


Figure 5.9 CVs of various concentrations of carbamates at pH 7.0. (A) fenobucarb (FC), (B) carbaryl (CB), (C) carbofuran (CF), and (D) aldicarb (AC). The scan rate was 100 mV s^{-1} for charts A, B, and C, and was 25 mV s^{-1} for chart D.

Our major route of quantification involves being able to distinguish the size and position of the oxidation features. Oxidation of CF showed peaks at three potentials, suggesting that three electrons from differing centres were lost during oxidation; and a broad reduction peak was observed at 1.10 V. Compared with the oxidation of CB at 1.35 V, FC at 1.70 V, and AC at 1.55 V, these electrochemical differences could be ideally placed for simultaneous detection of both compounds.

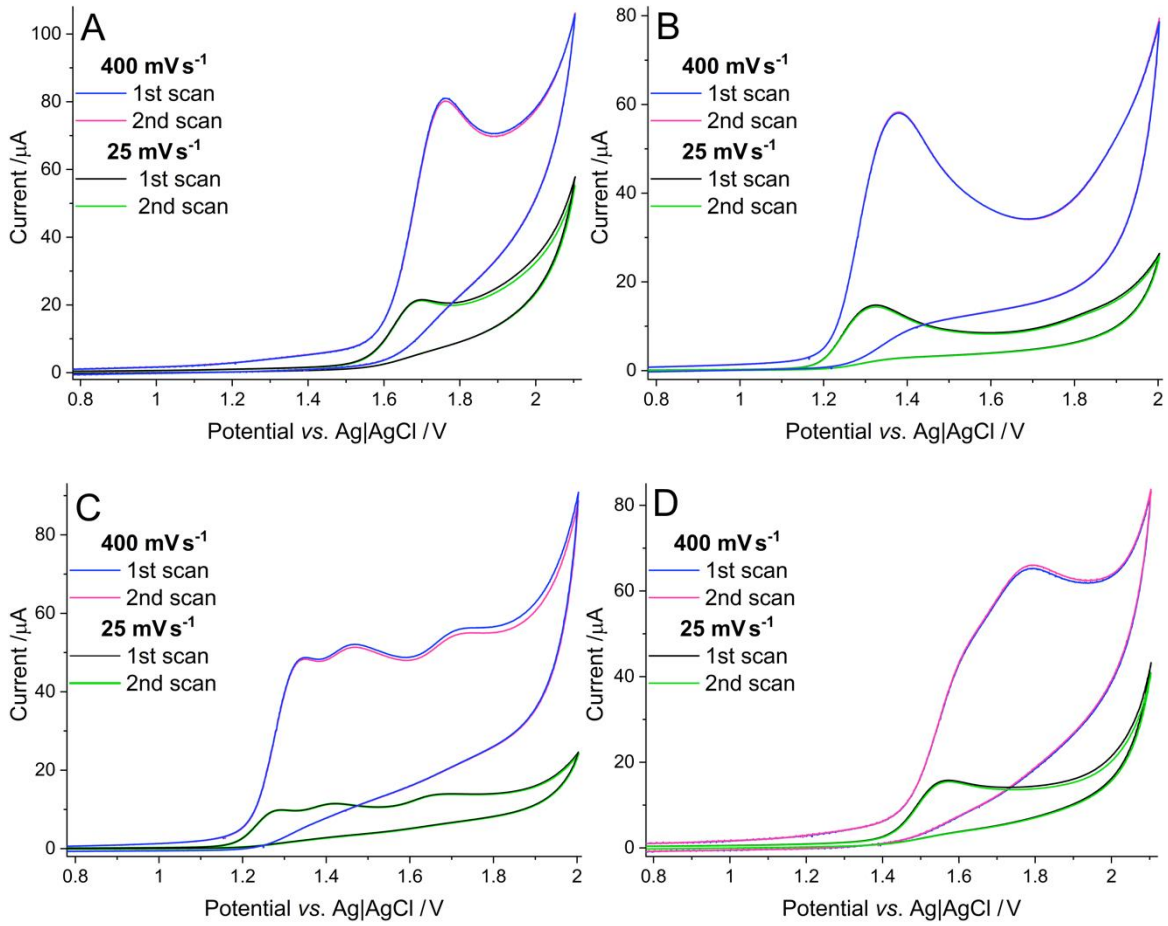


Figure 5.10 Solutions of 100 µM at pH 7.0 of (A) FC, (B) CB, (C) CF, and (D) AC. The scan rates shown here are 25 mV s^{-1} and 400 mV s^{-1}.

As shown in Figure 5.10, consecutive CVs in the same solution overlap closely, and are highly reproducible, without any fouling observed or cleaning procedure applied. Surfaces before and after exposure to carbamates were also examined by XPS, and overlapping spectra suggested that insignificant to non-existent fouling accumulates during detection, and that the electrode surface remains active. This is a characteristic feature of the BDD electrodes: its intrinsic resistance to fouling means that no cleaning steps were required in between experiments. However, we note the remarkable exception of malathion as described in Section 5.3.

5.4.2 Alkaline hydrolysis

Although there are few electrochemical studies on carbamate pesticides, researchers have

used various chromatography techniques and mass spectrometry to study them [43,44]. One method used to separate and distinguish samples is alkaline hydrolysis.

Hydrolysis is the substitution of hydrogen for part of the carbamate group under basic conditions. This procedure turns carbamates into complicated phenols, which are well known to be electroactive. Table 5.4 shows the name, and the insets in Figure 5.11 show the structures of the hydrolysed species. The expected electrochemical behaviour is that the oxidation will be easier after hydrolysis, because the hydroxyl groups on the phenol ring will be more responsive to electron transfer than the carbamate group.

Table 5.4 Alkaline hydrolysis effectively removes the pesticide's carbamate group

Pesticide	**Hydrolysed pesticide**
fenobucarb	2-*sec*-butyl-phenol
carbaryl	1-naphthol
carbofuran	benzofuranol
aldicarb	aldicarb sulfoxide (also produced by photodegradation)

For each of the hydrolysed carbamate molecules, CVs were recorded. The solid lines in Figure 5.11 show original carbamate response, the dashed lines show the response from the hydrolysed carbamate, and the chemical structures of both are inset into each graph. The scans started at 0 V, at a rate of 0.1 V s^{-1}. All other parameters were kept constant.

For three of the four samples, the hydrolysed pesticide showed oxidation peaks at much lower potentials (aldicarb being the exception), with weak reduction features. The dotted lines in Figures 5.11 are representative of the decrease in the oxidation peak heights and loss of waveform definition that are caused by alkaline hydrolysis. Generally, these effects are undesirable for electroanalysis and could make low-concentration quantification inaccurate. However, if the mixture of pesticides in solution is carefully chosen, then hydrolysis serves as a technique for simultaneously observing co-existing species.

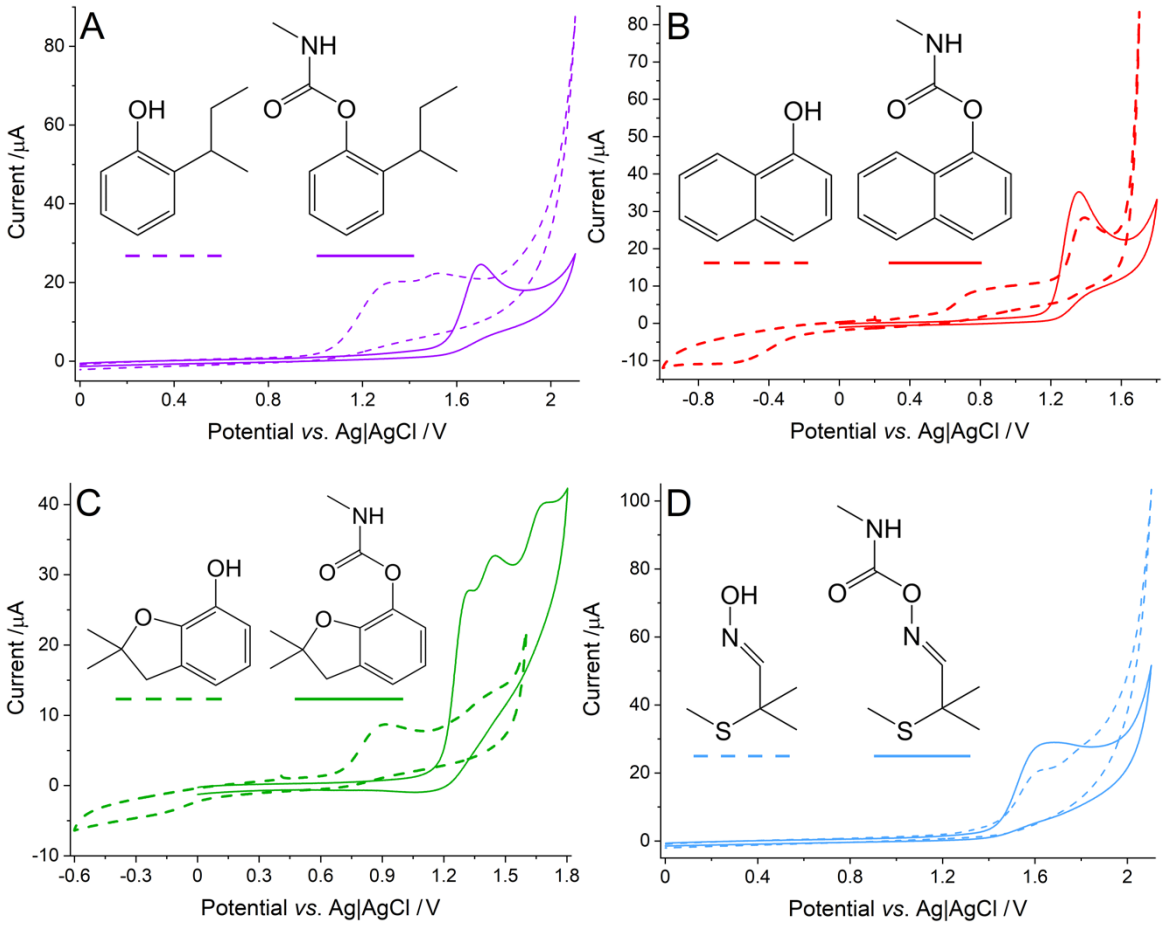


Figure 5.11 The solid lines are responses from the 100 μM solutions of the four carbamates: (A) FC, (B) CB, (C) CF, and (D) AC; the dashed lines are for the corresponding hydrolysed forms. The scan rate was 100 mV s^{-1}.

After hydrolysis for CB and CF, their original oxidation peaks decrease in height, extra reduction peaks were observed, and more oxidation peaks appear at more negative potentials. For FC, no reduction features appeared after hydrolysis, but the same negative move for the oxidation peak was observed, appearing to separate into two peaks. Oxidation and reduction peaks of AC moved slightly closer together after hydrolysis, signifying an increase in electrode kinetics, meaning that the hydrolysed species are more electroactive and are more easily oxidised. The specific movements are laid out in Table 5.5.

Table 5.5 Oxidation peak potentials of carbamates before and after hydrolysis

	Fenobucarb	**Carbaryl**	**Carbofuran**	**Aldicarb**
Oxidation before	1.703	1.363	1.320, 1.448, 1.680	1.631
Oxidation after	1.309, 1.525	0.795, 1.391	0.911, 1.402	1.605
Reduction before	n/a	n/a	1.07, 0.684	1.420
Reduction after	n/a	– 0.570	0.700, – 0.194	1.505

Hydrolysis is effective in causing big shifts in the oxidation potential for FC, CB, and CF—but not for AC. So, it is a useful technique, but not always applicable. These results suggest that the carbamate group was a key stabilising feature of the compounds, preventing easy oxidation of the phenol structure. Reduction peaks are from the carbonyl groups after the phenols have been oxidised, because they do not exist when the scan direction is reversed (i.e. starting at 0 V and scanning towards – 0.6 V first).

5.4.3 pH-dependence of the carbamates

The part of the CVs encompassing all oxidation activities, recorded at a range of pH values, is shown in Figure 5.12. For each forward wave, an exponential baseline has been removed to allow clearer differentiation of the peaks.

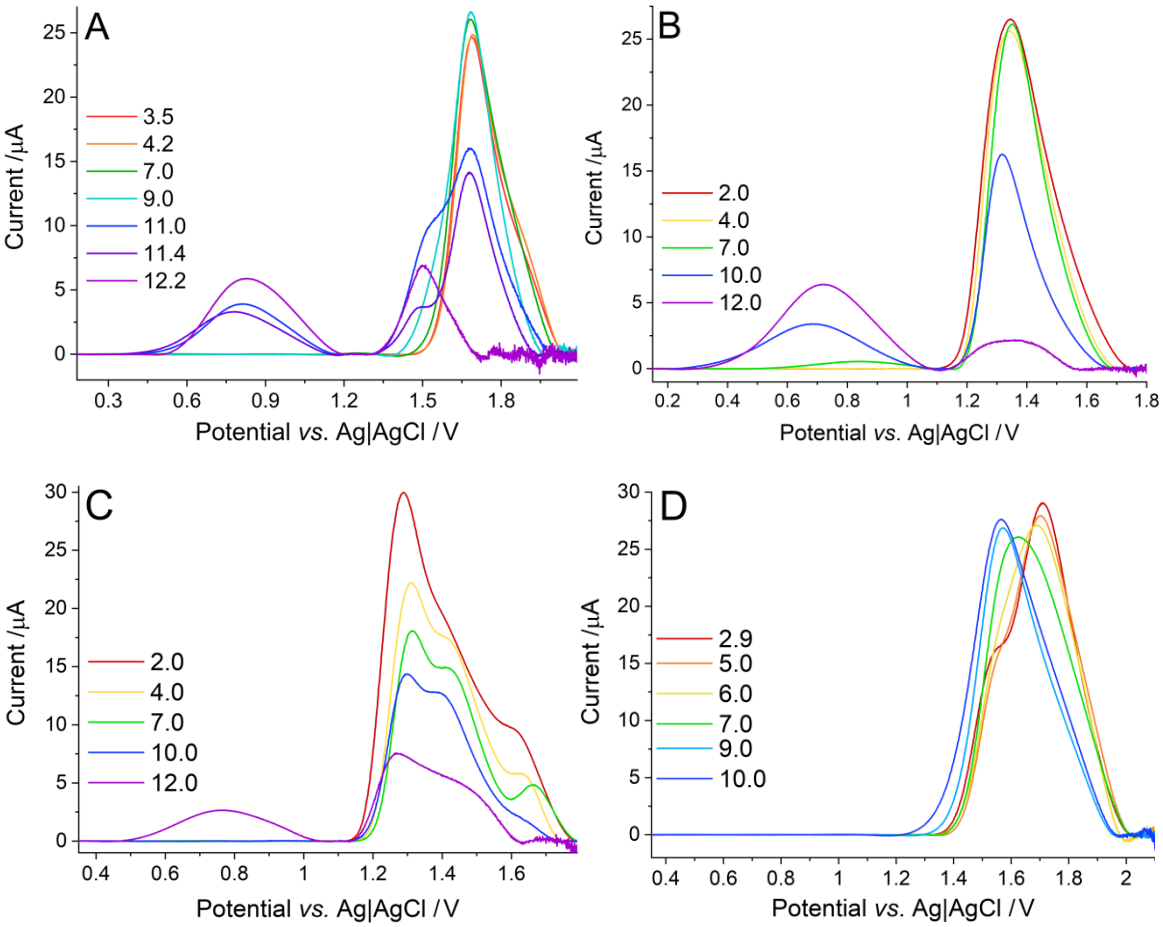


Figure 5.12 The baseline-subtracted forward CV scans of (A) FC, (B) CB, (C) CF, and (D) AC in a range of pH conditions. The scan rate was 100 mV s^{-1}.

The general trend is that peaks do not shift with pH, but new species appear at higher pHs, suggesting changes in speciation. In Figures 5.12A,B,C, as alkalinity increases, the oxidation peaks at higher potential become less prominent; and when alkalinity increases past a threshold, new features at lower potentials appear, similar to hydrolysed carbamates. As pH increases from 2.0 to 10.0, the main CF oxidation peaks decrease in magnitude, indicating that carbamates are becoming less stable. For FC, CB, and CF, it could be

expected that they share similar oxidative behaviour, such as the appearance of the pre-peak at 0.7–0.8 V, because the differences between their structures are much smaller than any of their individual differences from AC.

Fenobucarb displays a broad oxidation peak at ~0.8 V when pH values are above 11.0, indicating that it is the hydrolytic threshold alkalinity for FC. The separation of one peak (1.7 V) into two distinct features (1.5 and 1. 7 V) as pH increases even slightly from 11 to 11.4 indicates either that more than one electron is lost after hydrolysis, or that several hydrolysis products exist simultaneously.

At pH 10.0 and 12.0 for CB and at pH 12.0 for CF, a considerable pre-peak appears around 0.7 V in accordance with a similar peak observed after alkaline hydrolysis. This suggests that some incomplete hydrolysis occurs at high pH values, but incompletely, as the original feature is still observed. Although pH affects the magnitude of the current response for both CB and CF (Figures 5.12B,C), the peak potentials do not change (until hydrolysis occurs), so we can say that they do not undergo proton-assisted electron transfer.

Aldicarb (Figure 5.12D) at pH 2.0 shows a smooth transition: from a peak at 1.6 V containing a small hump at 1.5 V, to a single broader peak at neutral pH, to a single sharp peak at 1.5 V at pH 10.0. This observation is in line with the knowledge that AC can be hydrolysed in both acid and alkaline conditions [26]. This suggest that, at pH 2.0, the peak and hump correspond to acid-hydrolysed and non-hydrolysed AC respectively; the single peak at pH 7.0 represents only non-hydrolysed AC; and at pH 10.0, the alkaline hydrolysis of AC is sufficiently complete to obscure features that might be due to non-hydrolysed AC.

5.4.4 Scan-rate dependence

The electron-transfer behaviour of any analyte can be probed by changing the scan rate used in cyclic voltammetry. Figure 5.13 shows the representative CVs of the carbamates at different scan rates.

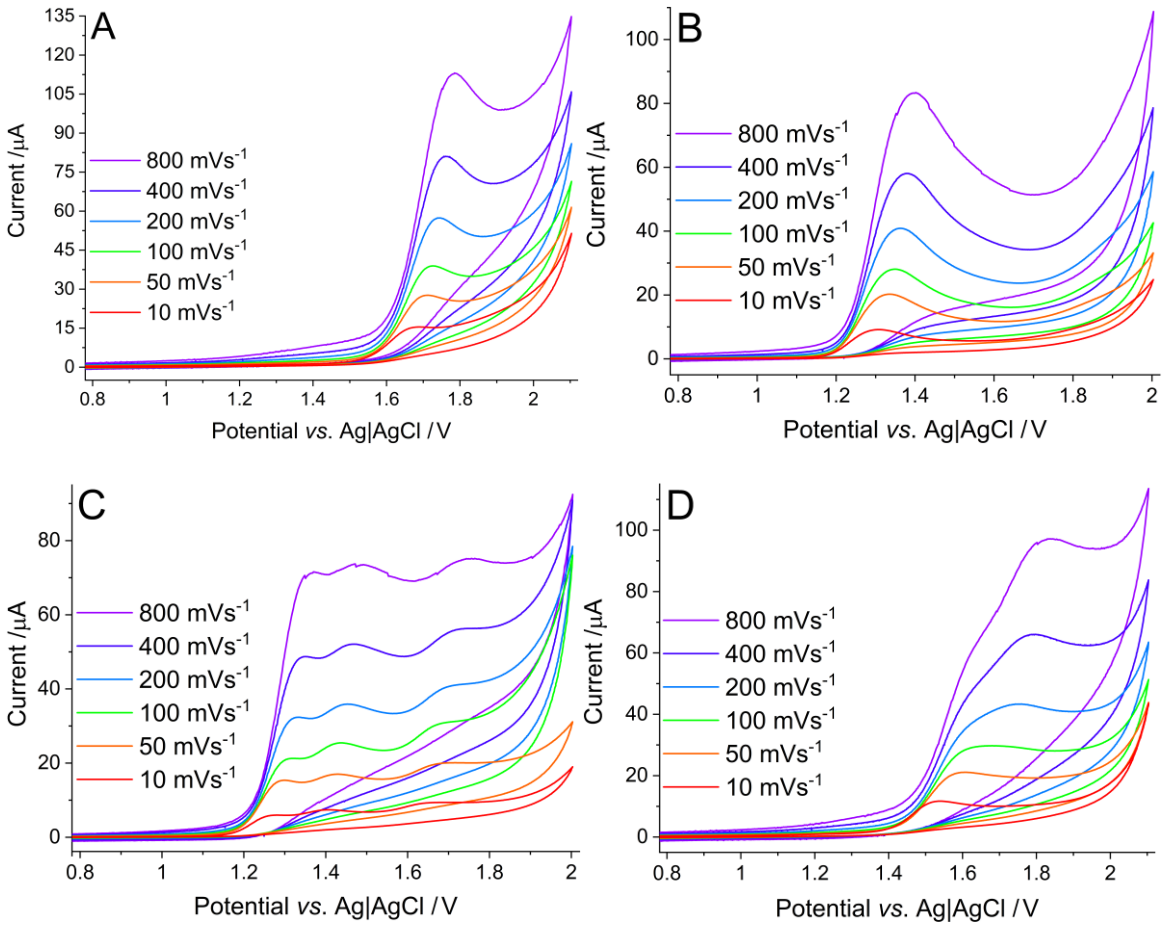


Figure 5.13 Representative CVs from 100 µM solutions of (A) FC, (B) CB, (C) CF, and (D) AC at scan rates of 10, 50, 100, 200, 400, and 800 mV s^{-1}.

With increasing scan rates, the peak currents of all carbamates increase, as there is increased flux to the surface. In the case of FC, CB, and CF, the oxidation peaks move anodically while maintaining their basic waveform, whereas the waveform of AC changes dramatically as the scan rate increases. For AC, initially there is only a single well-defined peak, at 1.5 V, at 10 mV s^{-1}, which moves to 1.6 V at above 50 mV s^{-1} and is joined by a second peak at 1.8 V which is visible at above 200 mV s^{-1} (Figure 5.13D). The appearance of the second wave shows that this deformation is not simply an issue of slow electron transfer across the surface, which could be the reason for the shift of the 1.5 V peak: rather, there are two kinetic processes. At 800 mV s^{-1}, the second process at the higher overpotential overshadows the first process at 10 mV s^{-1}. Put another way, only at high

enough scan rates is there sufficient time resolution to distinguish two electron-transfer events.

With some compounds, their concentration in solution affects the shape of their CV response [45,46] depending on how well they maintain their diffusion characteristics and interactions with the electrode surface. The concentration of AC was checked as a possible parameter in causing the waveform changes. Voltammograms were recorded at 10 mV s^{-1} (Figure 5.14A) and 800 mV s^{-1} (Figure 5.14B) in seven solutions containing various concentrations of AC at pH 7.0.

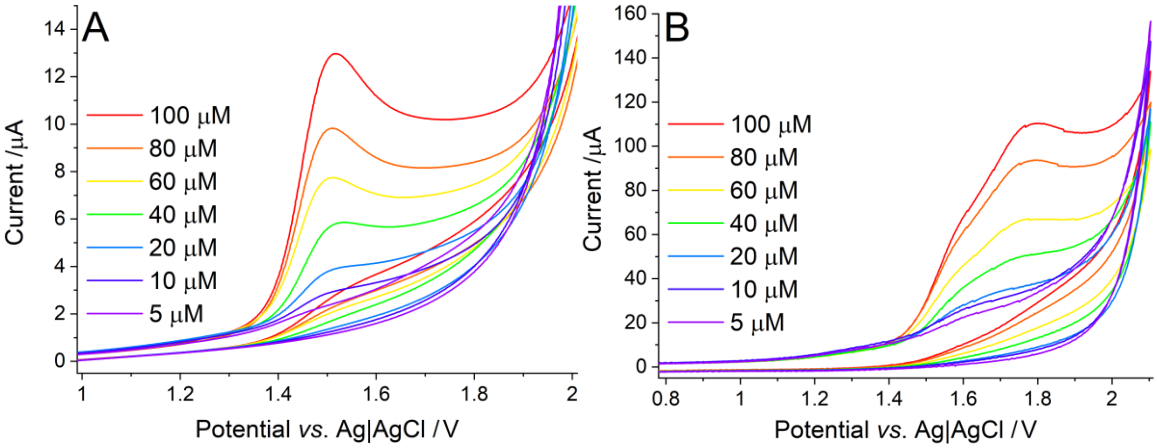


Figure 5.14 Aldicarb concentrations scanned at (A) 10 mV and (B) 800 mV s^{-1}.

At 10 mV s^{-1}, only the oxidation event at 1.52 V is observed, with good peak definition. At 800 mV s^{-1}, a gradual change in waveform similar to that in Figure 5.13D is observed; only this time, the second peak at 1.8 V becomes increasingly prominent at concentrations above 20 µM.

Taking Figures 5.12D, 5.13D, and 5.14B together, there are several aspects to consider while analysing the oxidation of AC. The higher potential peak is favoured in acid, and the lower potential peak is more prominent in alkaline conditions. This clearly implies that the reaction kinetics depend on proton concentration; the presence of more protons results in oxidation at higher potentials. With the concentration kept constant, two peaks appear at the higher scan rate, which suggests that there are two electron-transfer events. Perhaps

these two electrochemical steps are separated by a chemical step which is fast—hence the appearance of two peaks only at high scan rates when the chemical step is not rapid enough to remove the first oxidised species from solution.

The oxidation of AC could thus fall into two reaction categories, ECE or EC_2E. The ECE is where a chemical step yields a product which itself is electrochemically active (A $– e^- \rightarrow$ B, then B $\rightarrow$ C, then C $– e^- \rightarrow$ X). However, as the oxidation of the B species is substantially slower than the first electron transfer (Figure 5.13B), this strongly implies that the transfer of the second electron results in a large conformational change as suggested by Marcus theory. Figure 5.14B is significant here, as it shows two peaks appearing when the absolute concentration of AC increases, suggesting that the chemical step has second-order kinetics, EC_2E (A $– e^- \rightarrow$ B, then B + B $\rightarrow$ C, then C $– e^- \rightarrow$ X). In such a process, an increased concentration of A yields an increased concentration of B (increased prominence of the second peak), and since the rate of B depletion is proportional to $[B]^2$, this depletion will occur faster at higher initial concentrations of A. These effects were not examined in detail, but the considerations mentioned above could qualitatively explain the observations.

Previous experience with organic molecules cautioned us to explicitly check that these pesticides did not adsorb on or otherwise poison the electrode's surface. This was done qualitatively by scrutinising for changes to the waveform after consecutive scans in the same solution and, when no changes were observed (Figure 5.10), quantitatively by analysing how the oxidation peak currents changed with respect to scan rate. Due to the shifting and appearance of new oxidation features, the peak currents from the first oxidation peak of each carbamate and hydrolysed carbamate were extracted and plotted against the square root of the scan rate, in Figure 5.15. That peak was chosen because of its visibility at every scan rate, and the peak at the lowest potential was analysed for hydrolysed carbamates because that peak shows the unique features of hydrolysis.

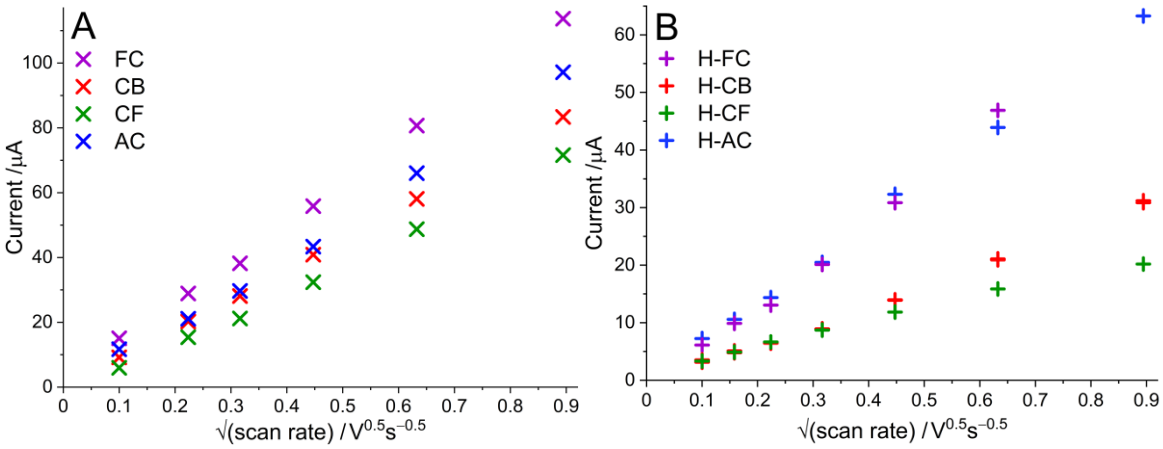


Figure 5.15 Dependence of the current of the first oxidation peak with respect to the square root of the scan rate, recorded at pH 7.0. (A) shows the response from original carbamates and (B) shows the hydrolysed carbamates.

For both original and hydrolysed carbamates, the oxidation current changed linearly with the square root of the scan rate, indicating that the oxidation peaks were formed purely by diffusion-controlled processes and that no adsorption was detectable by electrochemical means. This agrees with the observations shown in Figure 5.10, in which no cleaning steps were required in between experiments for reproducibility.

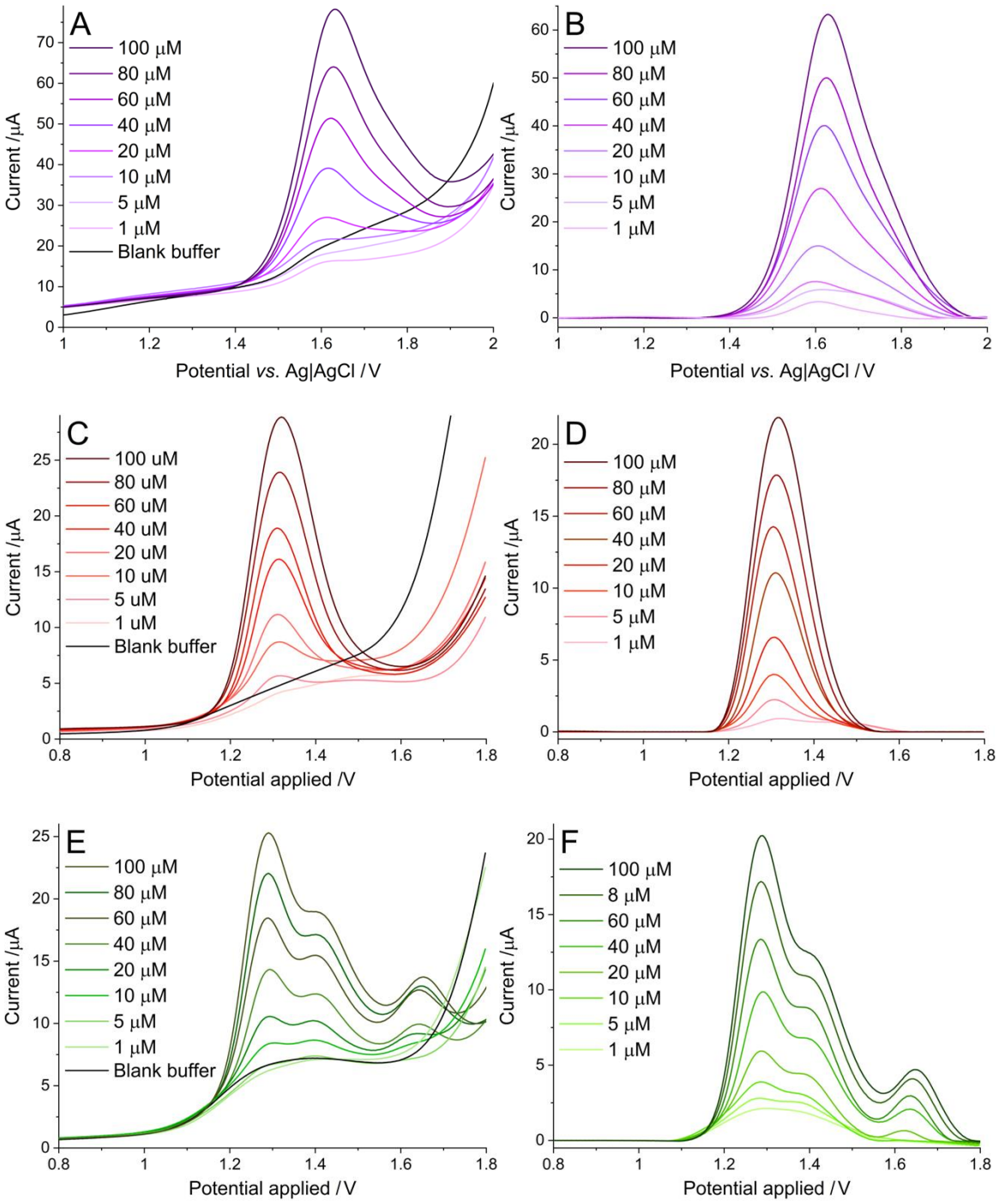
5.4.5 Square-wave voltammetry

Cyclic voltammetry is an exploratory tool, but to achieve low detection limits and fast quantification, square-wave voltammetry was used. The parameters for most of these voltammograms were optimised at 28.5 Hz, 0.1 V amplitude, and 3.5 mV increment, starting at 0 V and scanning towards 2.2 V. The scan range was set to be extra wide to catch all observable oxidation activity, and the scan rate was equivalent to 100 mV s^{-1}.

Individual pesticides

To create a calibration curve for finding the concentration of a single carbamate in an unknown solution, each solution contained only one species to eliminate possible interference from the others. The variation in response of AC with respect to different scan

rates is marked: a lower scan rate of 10 mV s^{-1} was used to find the limit of detection for AC because, at higher scan rates, its peaks lose definition, which makes baseline subtraction more prone to error. To some extent, the same issue applied to the other three carbamates as well, so a scan rate of 100 mV s^{-1} was chosen as a compromise between wave definition and recording time.



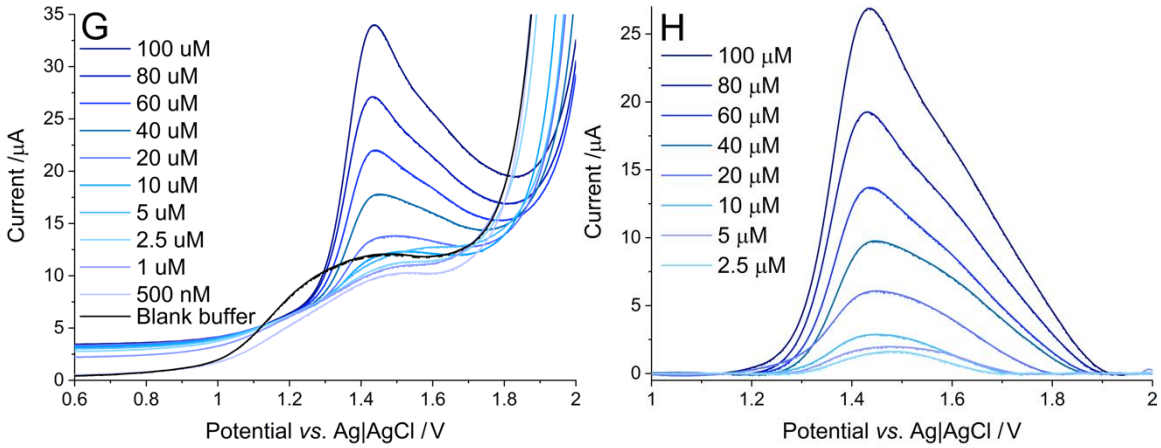


Figure 5.16 Unprocessed SWVs of (A) FC, (C) CB, (E) CF at 100 mV s^{-1}, and (G) AC at 10 mV s^{-1} show the visual detection limits at 1 µM and 2.5 µM. Graphs B, D, F, and H are of the same carbamates respectively, with the SWVs baseline-subtracted.

Without surface modifications, the detection limit for CB, CF, and FC was found visually to be 1 µM, with 2.5 µM for AC. All four show a linear response, and these data could be the basis for a calibration 'curve' for working out how much a real sample might contain of a specific carbamate. Along with overall sensitivity, an important criterion for sensing is the sensor's linear range. The larger the range, the easier it is to calibrate the sensing system, and the more accurate the interpretation.

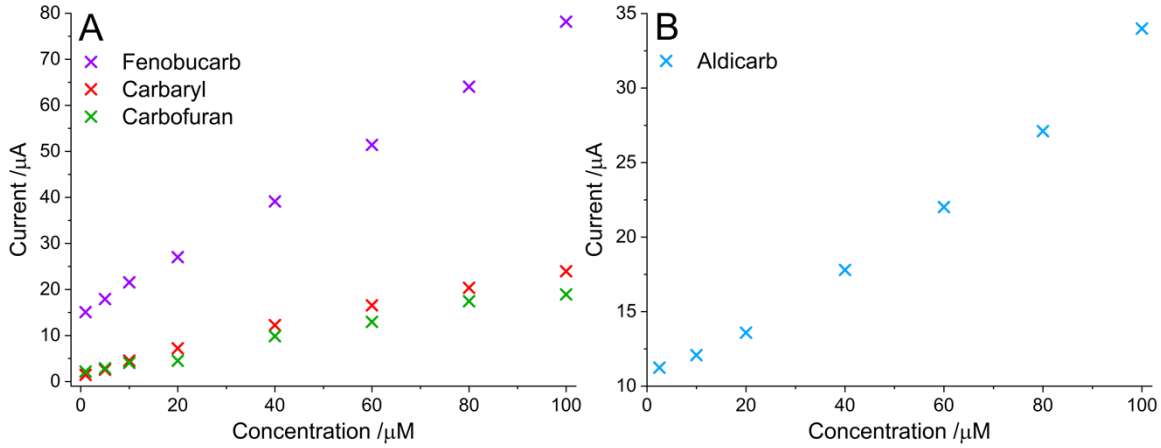


Figure 5.17 Peak currents from SWVs of different concentrations of (A) FC, CB, and CF at 100 mV s^{-1}, and (B) AC at 10 mV s^{-1}. For CF, its peak at 1.3 V was used.

The detection limits are 1.0 μM for FC, CB, and CF, and 2.5 μM for AC; and the linear range of detection for each carbamate is between its limit of detection and 100 μM. As Table 5.7 shows, while our detection limits cannot match the low detection limits of electrodes needing complicated functionalisation procedures, Table 5.7, the limits we have achieved are practically useful, and our method benefits from its simplicity and robustness.

It is interesting to note that several results listed in Table 5.7 report detection limits at least an order of magnitude below the lowest concentration in their linear range. This is in accordance with evaluating the limits as three times the standard deviation of the blank measurements [51–52], and no actual data for the limiting concentrations are shown. Our reported limits are based purely on peaks that are visually distinguishable from the blank (Figures 5.16B,D,F,H). Taking the linear range and method of evaluating limits into account, our results show competitive performance and have the key advantage of simple electrode preparation.

Table 5.7 The limits of detection and linear ranges of previous reports and how they compare with expected exposure concentrations

Carbamate	Applied concentration	Previous reports		
		Electrode modifications	Linear range	Detection limit
Fenobucarb 207.27 g/mol	51 mM [8]	nanosphere carbon black on screen printed carbon electrode (SPCE)	0.1–100 μM	0.08 μM [30]
		glassy carbon electrode (GCE)	Up to 100 μM	3.7 μM [53]
		graphene nanoribbons ionic liquid cobalt phthalocyanine on SPCE	0.025–110 μM	25.2 nM [54]
Carbaryl 201.22 g/mol	293 mM [9]	multi-walled carbon nanotube/cobalt phthalocyanine on GCE	0.33–6.61 μM	5.5 nM [55]
		AChE, carbon black, cobalt phtalocyanine, mineral oil paste	50–750 μM	1.99 μM [56]
		Boron-doped diamond electrode	2.5–30 μM	41.0 nM [57]
Carbofuran 221.25 g/mol	67 mM [11]	AChE on iron oxide–chitosan nanocomposite on GCE	5–90 nM	3.6 nM [58]
		gold nanoparticles and graphene oxide on SPCE	1–250 μM	0.22 μM [23]
		cobalt (II) oxide-decorated reduced graphene oxide on GCE	0.2–70 μM	18.9 nM [59]
Aldicarb 190.27 g/mol	12 mM [13]	AChE on Prussian blue on SPCE	0.2–20 μM	0.16 μM [60]
		europium-3-carboxycoumarin complex on GCE	0.5–10 μM	1.01 μM [61]
		molecularly imprinted polyaniline nanofiber on indium-tin oxide	50–80 nM	500 pM [62]

Previous work has not attempted the voltammetry of several carbamates in the same solution. Given the natural peak separation that exists, and that which can be enhanced by hydrolysis, some combinations of carbamates are suitable for simultaneous detection.

Equimolar mixtures

To test whether, and how well, the carbamates can be differentiated simultaneously, equimolar solutions containing carbaryl, fenobucarb, and carbofuran were investigated, with the same SWV parameters applied, Figure 5.18. These were chosen to allow a sufficient separation of oxidation potentials.

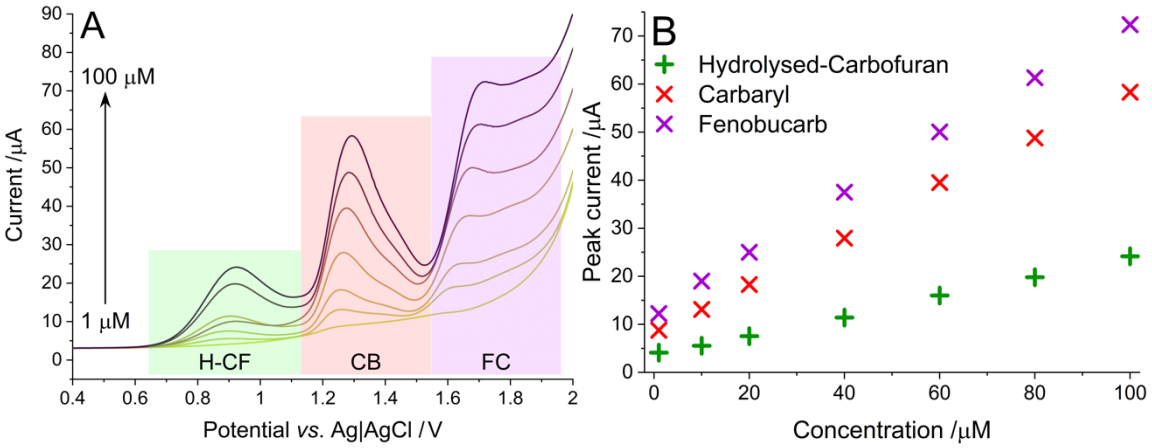


Figure 5.18 (A) SWVs of solutions containing equal amounts of hydrolysed carbofuran, carbaryl, and aldicarb, recorded at 10 mV s^{-1}. (B) Plot of the peak currents of each of the carbamate oxidation response against their concentrations.

Three distinct peaks can be seen in Figure 5.18A, each representing a different carbamate species. Normally, the lowest oxidation potential of CF is at 1.32 V, which would 'hide' the peaks from the other species (Table 5.5). However, hydrolysed carbofuran (H-CF) has an extra oxidation feature at 0.91 V, and H-CB has a similar peak at 0.80 V, so both can be detected simultaneously if one is completely hydrolysed. Aldicarb was left out, as its oxidation peak at 100 mV s^{-1} is not sharp and partially overlaps with the oxidation peaks of CB and CF.

Figure 5.18B shows the linear relationship between the peak currents of each carbamate plotted against its concentration. The limit of detection is 1 µM, and the linear range is up to 100 µM. This is the expected result, and the same result as detecting each species individually.

It is pleasing to see that distinction of the pesticides is possible when they are in equal concentrations, and this detection is very reproducible. However, what this experiment does not show is whether any one of the pesticides interferes with another if one is in excess.

Varimolar mixtures

By keeping the concentration of two species the same, fixed at 100 µM, and varying the third, it may be easier to highlight, from these SWVs, the interactions between specific species, if any. Figure 5.19A shows increasing concentrations of FC, and Figure 5.19B shows increasing amounts of CB, from 0, 1, 5, 10, 20, to 100 µM.

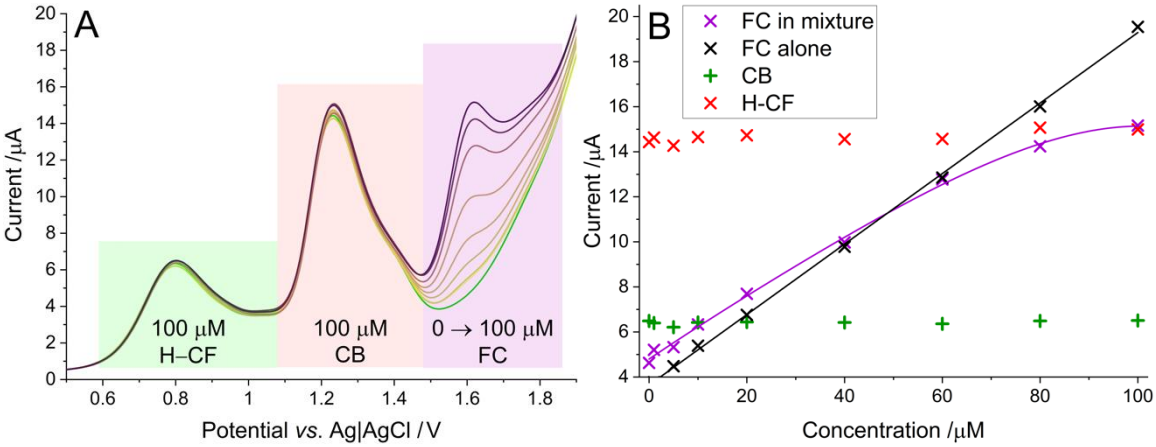


Figure 5.19 (A) Square-wave voltammograms for 100 µM of both H-CF and FC, with the CB concentration varying from 0 to 100 µM. The scan rate was 10 mV s^{-1}. (B) The extracted peak currents plotted against concentration of FC.

To obtain Figure 5.19A, appropriate volumes of a stock solution containing 200 µM of FC was added to fixed volumes containing 200 µM of H-CF and CB, and each volumetric flask was topped up with pH 7.0 Carmody buffer until the desired concentrations were reached. Apart from the increase in peak current due to the changing concentration of FC,

indicated by the green line where there is no FC in solution, and the purple line where there is 100 µM of FC, the other peaks are expected to remain constant.

Because the excess alkali used to hydrolyse CF should have been neutralised by the large addition of pH 7.0 buffer before the addition of the other two carbamates, there should be no hydrolysis of them. This is shown by the near-perfect overlaying of peaks for those species, while only the FC peak changed with increasing concentration. As demonstrated by Figure 5.17, this increase should have been linear if there were no cross-species interactions in solution. Another factor we cannot rule out in explaining this nonlinear behaviour is possible error derived from the baseline-subtraction process. As the oxidation of FC occurs at a potential where the supporting electrolyte dissociation current is very high, baselining to differentiate between oxidisable species and the background becomes a delicate art. Therefore the use of this calibration curve should be qualitative.

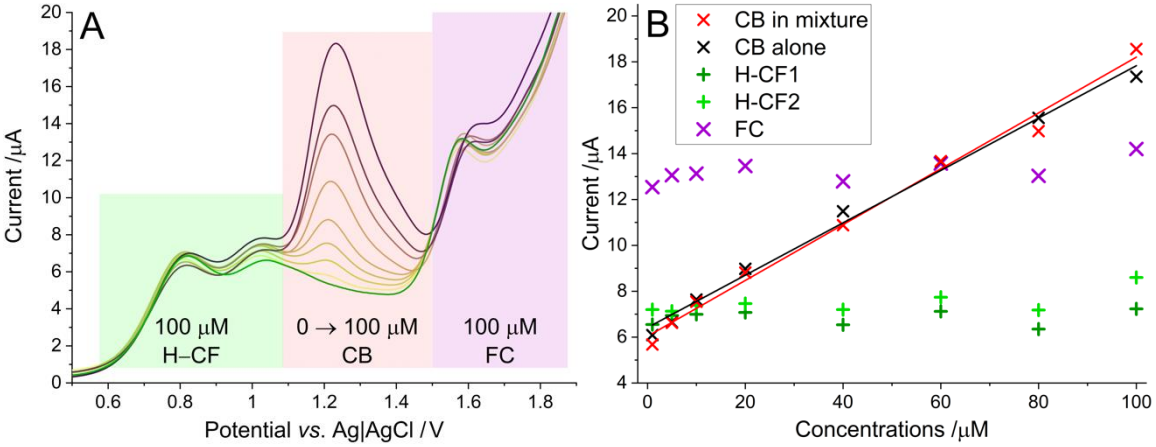


Figure 5.20 (A) Square-wave voltammograms containing 100 µM of H-CF and CB, with the FC concentration varying from 0 to 100 µM. The scan rate was 10 mV s^{-1} (B) The extracted peak currents plotted against the concentration of CB.

The solutions used in obtaining Figure 5.20A were made similarly to those used for Figure 5.19A, but this time with varying volumes of 200 µM of CB added to fixed volumes containing 200 µM of H-CF and FC. The green line shows a solution containing 100 µM of H-CF and FC and no CB, and an extra peak (compared to Figure 5.18A and Figure 5.19A)

appears at 1.05 V. The height of this peak does not change as CB concentration increases and, with reference to the peak positions in Figure 5.21, it is not entirely clear to which of the individual carbamate species it belongs.

Figure 5.20B shows that, although there are irregularities in the number and placement of peaks when the concentration of CB changes, there is a strong linear dependence between peak current and increasing concentration. This matches our observations in Figure 5.17A, and therefore we can be confident in saying that the calibration curve obtained from this configuration of the three species is more reliable than that of Figure 5.19A.

Ideally, the SWVs of Figures 5.19A and 5.20A for the highest concentrations of all three species should look the same, but only the 100 µM CB and H-CF peaks are similar. Figure 5.20A suggests that there are undesirable interactions between H-CF and FC, which is unaffected the presence of CB.

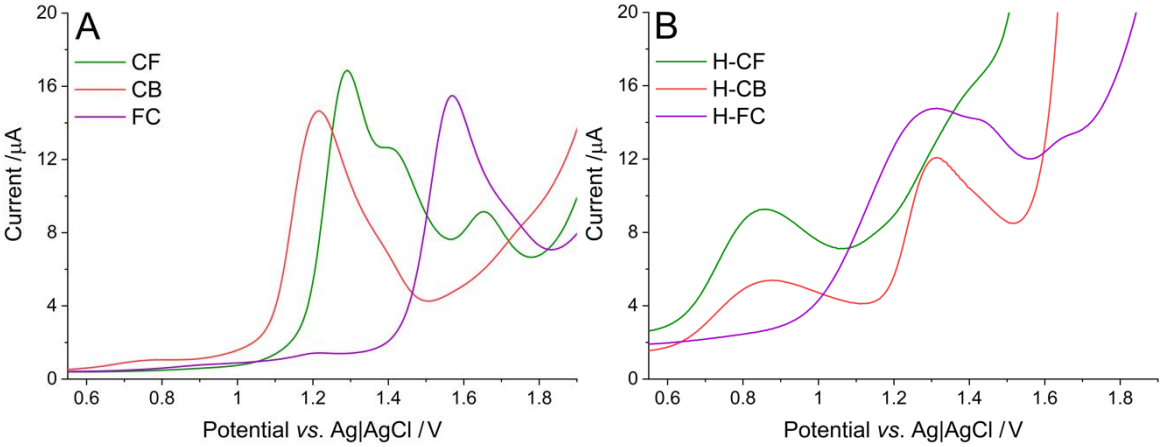


Figure 5.21 The overlaid SWVs, at 10 mV s^{-1} of 100 µM of (A) CF, CB, and FC, and (B) H-CF, H-CB, and H-FC where the solution only contained each individually.

To summarise, SWVs in equimolar and varimolar mixtures provide qualitative information about species present in solution. As the likelihood of a real situation where these specific carbamates would exist in equal amounts in the same sample is slim, Figures 5.18–20 should be used qualitatively for identification; for quantification, use the calibration curves in Figure 5.17.

5.4.6 Batch injection analysis

Aside from concerns about the detection limit and the sensing linear range, tests in real matrices are also important, and local river water (Cherwell, pH 7.1, Aug 2019) was the supporting electrolyte for experiments in this section.

Chronoamperometry is faster and requires much simpler waveforms than cyclic or pulsed voltammetry. A single potential step is applied, and the resulting current is measured with respect to time. Of the stationary-electrode techniques in a hydrodynamic system, injection analysis has the great advantage that adsorption, which is always a worry in complex matrices, is much lower.

The analytical signal from flow-injection analysis (FIA) is based on the quick introduction of a small volume of sample into a turbulently flowing carrier stream of reagent [63]. The passage of the analyte over the electrode creates a transient peak-shaped response due to the reproducible transport and high dilution of the injected volume, and the magnitude of the peak is proportional to the concentration of the analyte in the injected solution [64]. In lieu of a peristaltic pump and a carrier stream, batch-injection analysis is conceptually similar to FIA, only now the injections are made into a large (compared to injected aliquots) volume of blank solution, which can be still for simplicity, or stirred for faster analysis [65].

Some conditions need to be met to achieve the most reliable results. First, the injected volumes and concentrations need to create a local change in concentration at the electrode surface, but not make a big impact globally. Second, the volume to be injected needs to be small enough for the time taken to empty the pipette to be as short as possible, which will minimise the amount of movement in the pipette tip. Third, the injection volume should also be minimised to allow all the analyte to reach the electrode surface at almost the same time. Fourth, the background solution into which the injections are made needs to be of

sufficient volume that the global analyte concentration would approximate zero. Fifth, the potential set for the electrode should be set at the oxidation potential of each analyte, to ensure speedy consumption of the analyte. Finally, enough time should be allowed to pass for the current to subside to background levels before the injection of the next aliquot (this usually took ~60 seconds).

Figures 5.22A,B,C respectively show the results of the fixed volume (50 µL) injections of different concentrations of FC, CB, and CF (1–100 µM) into stirred river water. The electrode potential was set at +1.3 V: the potential to completely oxidise CF and CB but incompletely oxidise FC (its oxidation potential is ~1.7 V). This was chosen to investigate whether some differences in peak magnitudes would allow differentiation of the species. Aliquots of each carbamate stock solution were pipetted by hand to the centre of the BDD electrode, keeping the same vertical distance from the electrode surface. As controls, blank river water and pH 7.0 Carmody buffer were injected 3 times prior to aliquots of carbamates. For each injection, background current immediately before the peak was subtracted from the peak current, and Figure 5.22D shows the differential currents plotted against its concentration.

Chronoamperometry works quantitatively as well as square-wave voltammetry on an individual basis, but it cannot differentiate a mixture of analytes, or present information on the species in any mixture. Injections of the two control solutions elicited no currents distinguishable from the background. The minimum concentration detected was 1 µM for CB and CF, and 5 µM for FC. Fenobucarb was chosen instead of aldicarb to test the degree of differentiation, because its oxidation potential is the furthest away from the set electrode potential of +1.3 V. In any case, this experiment was simply a proof of concept, as a great deal of engineering is required to realise the practical aspect of integrating our kind of BDD plates into a flow-injection system to provide injection stability, automation, and speed.

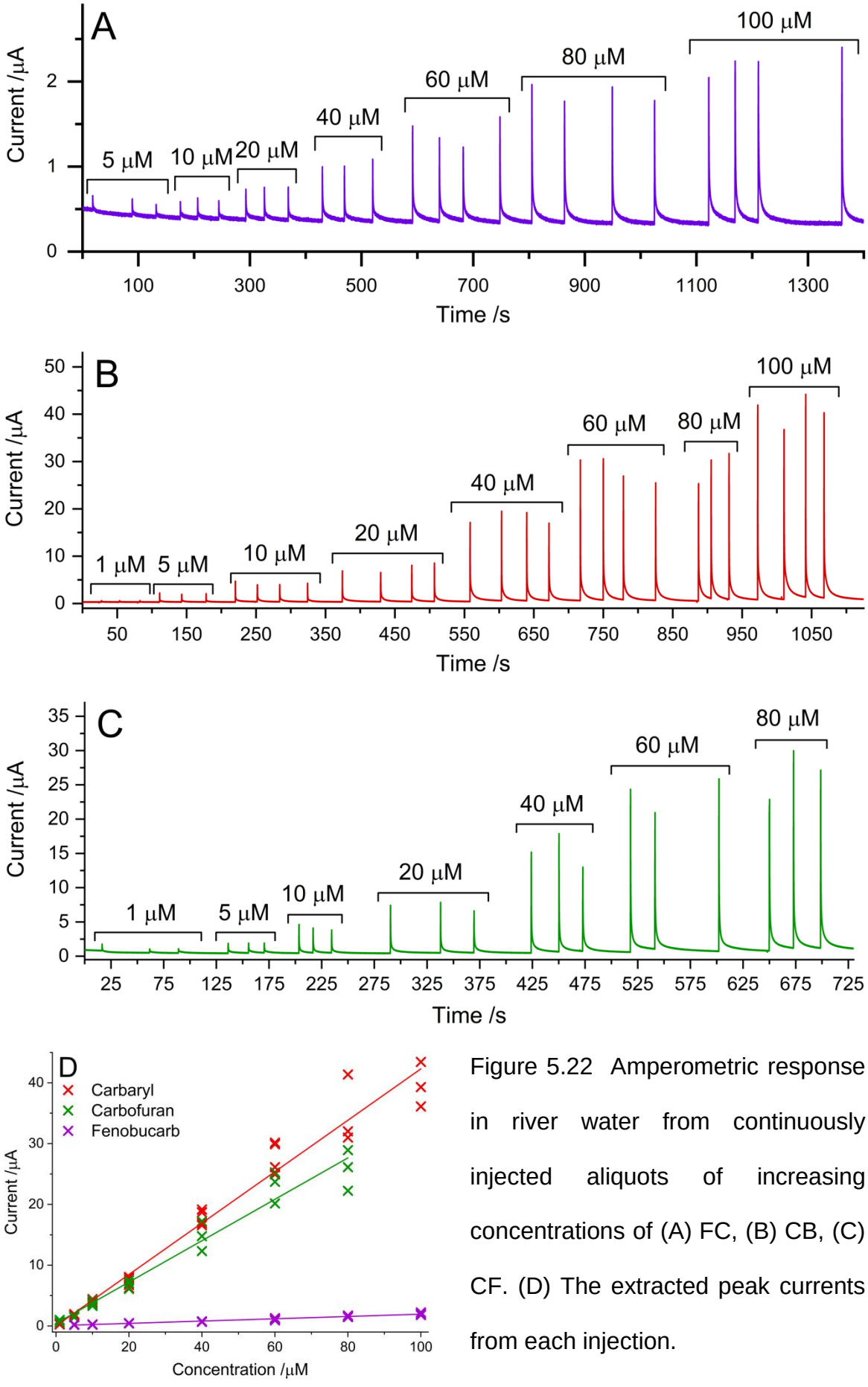


Figure 5.22 Amperometric response in river water from continuously injected aliquots of increasing concentrations of (A) FC, (B) CB, (C) CF. (D) The extracted peak currents from each injection.

5.5 Conclusions

Carbamate and organophosphate compounds are widely used by the agricultural industry for their high insecticidal activity. The work in this chapter examines their electrochemistry at diamond electrodes, and the following conclusions were reached.

Interactions with MT in the early test stages permanently altered the BDD surface to produce an irremovable feature in reduction, which can be switched on by exaggerated anodic scanning. Due to its position and pH-sensitivity, we attribute this to complex quinone-like moieties derived from the degradation of MT which modify the non-diamond carbon species initially present on oxygen-terminated diamond electrodes.

We have shown that BDD electrodes can reach detection limits of 1 μM for FC, CB, and CF, and 2.5 μM for AC. The same detection limits were obtained with local river water spiked with either CB or CF. Although these sensitivities are not as competitive as those of the complex electrodes, they are useful and easily encompass concentrations encountered during routine pesticide application. The linear ranges of our set-up are also wider than those of enzymatic/nanomaterial-based electrodes.

The interaction of the carbamates with the BDD surface is by simple diffusion, where no intermediates or fouling behaviour were observed. The reaction mechanism for AC is possibly EC_2E, and due to the unclear nature of the intermediate chemical step, care needs to be taken when choosing experimental conditions during detection. Namely, scan rates over 100 $mV\,s^{-1}$ will produce two peaks, and if AC is in a multi-species mixture, then the position of the oxidation peaks may overlap those of other species.

Real samples have multiple chemicals in them, and a method able to identify and quantify each component is attractive. Compared to mass spectrometry, electrochemistry is simple in instrument and operator requirements—and fast. We found that if CF, CB, and FC coexist in the sample, then simultaneous detection is not possible without alkaline

hydrolysis, because their oxidation features overlap. We have shown that these features can be separated nicely via hydrolysis. Due to interaction between the species, we were able to produce qualitatively useful calibration curves in varimolar situations; but when they exist in equimolar concentrations, quantitatively useful calibration curves were obtained. Therefore, our protocol enables more varied detection using electrochemistry, provided that this hydrolysis step is included.

The strengths of our BDD set-up lies in its simplicity and reproducibility. The lack of surface fouling means longer and more stable operating conditions and supports the use of this BDD material for studies with a wider range of carbamates. In the future it would be of interest to build this electrode into an adapted flow-injection analysis system and optimise it to perform on a greater number of carbamates both qualitative voltammetry and quantitative amperometry.

References

[1] W. Aktar, D. Sengupta, and A. Chowdhury, "Impact of pesticides use in agriculture: Their benefits and hazards," *Interdisciplinary Toxicology*, vol. 2, no. 1, pp. 1–12, 2009, doi: 10.2478/v10102-009-0001-7.

[2] J. A. Vale and S. M. Bradberry, "Organophosphate and carbamate insecticide," in *Critical Care Toxicology: Diagnosis and Management of the Critically Poisoned Patient*, J. Brent, K. Burkhart, P. Dargan, B. Hatten, B. Megarbane, R. Palmer, and J. White, Eds., Springer, 2017, pp. 1829–1853.

[3] Y. Sumita, H. Kawada, and N. Minakawa, "Mode of entry of a vaporized pyrethroid knockdown agent into the body of the housefly, *Musca domestica* (Diptera: Muscidae)," *Applied Entomology and Zoology*, vol. 51, no. 4, pp. 653–659, 2016, doi: 10.1007/s13355-016-0443-2.

[4] J. Verheyen and R. Stoks, "Current and future daily temperature fluctuations make a pesticide more toxic: Contrasting effects on life history and physiology," *Environmental Pollution*, vol. 248, pp. 209–218, 2019, doi: 10.1016/j.envpol.2019.02.022.

[5] D. Atwood and C. Paisley-Jones, "Pesticides Industry Sales and Usage 2008–2012," Washington, D.C., 2017. https://www.epa.gov/sites/production/files/2017-01/documents/pesticides-industry-sales-usage-2016_0.pdf.

[6] Z. Ö. Şimşek, M. Sevim, Y. Şimşek, M. Sungur, K. Gündoğan, and M. Güven, "Effects of organophosphate poisoning on endocrine system in the long term: A pilot study," *Erciyes Medical Journal*, vol. 41, no. 1, pp. 33–36, 2019, doi: 10.14744/etd.2019.19122.

[7] K. Ameno, "II.7.4 Carbamate pesticides," in *Drugs and Poisons in Humans: A Handbook of Practical Analysis*, Springer, Berlin, Heidelberg, 2005, pp. 559–570.

[8] "Baycarb® 500 EC," 2021. https://www.bayer.com/en/id/baycarb

[9] "Carbaryl 4L usage instructions." Loveland Products, pp. 1–46.

[10] R. C. Gupta, "Carbofuran toxicity," *Journal of Toxicological and Environmental Health*, vol. 43, no. 4, pp. 383–418, 1994, doi: 10.1080/15287399409531931.

[11] "Furadan 4F." FMC Corporation Agricultural Products Group, Philadelphia.

[12] A. Covaci, P. Manirakiza, V. Coucke, R. Beckers, P. G. Jorens, and P. Schepens, "A case of aldicarb poisoning: A possible murder attempt," *J. Anal. Toxicol.*, vol. 23, no. 4, pp. 290–293, 1999, doi: 10.1093/jat/23.4.290.

[13] "Temik® 150G." Bayer CropScience.

[14] M. S. Çelebi, N. Oturan, H. Zazou, M. Hamdani, and M. A. Oturan, "Electrochemical oxidation of carbaryl on platinum and boron-doped diamond anodes using electro-Fenton technology," *Separation and Purification Technology.*,

vol. 156, pp. 996–1002, 2015, doi: 10.1016/j.seppur.2015.07.025.

[15] Z. Gong, Y. Guo, X. Sun, Y. Cao, and X. Wang, "Acetylcholinesterase (AChE) biosensor for carbaryl detection based on interdigitated array microelectrodes," *Bioprocess and Biosystems Engineering*, vol. 37, no. 10, pp. 1929–1934, 2014, doi: 10.1007/s00449-014-1195-4.

[16] N. Kaur, H. Thakur, and N. Prabhakar, "Conducting polymer and multi-walled carbon nanotubes nanocomposites based amperometric biosensor for detection of organophosphate," *Journal of Electroanalytical Chemistry*, vol. 775, pp. 121–128, 2016, doi: 10.1016/j.jelechem.2016.05.037.

[17] H. Zhao *et al.*, "An ultra-sensitive acetylcholinesterase biosensor based on reduced graphene oxide Au nanoparticles β-cyclodextrin/ Prussian blue chitosan nanocomposites for organophosphorus pesticides detection," *Biosensors and Bioelectronics*, vol. 65, pp. 23–30, 2015, doi: 10.1016/j.bios.2014.10.007.

[18] Y. Chai, X. Niu, C. Chen, H. Zhao, and M. Lan, "Carbamate insecticide sensing based on acetylcholinesterase/Prussian blue multi-walled carbon nanotubes/screen-printed electrodes," *Analytical Letters*, vol. 46, no. 5, pp. 803–817, 2013, doi: 10.1080/00032719.2012.733899.

[19] F. Pino, T. A. Ivandini, K. Nakata, A. Fujishima, A. Merkoçi, and Y. Einaga, "Magnetic enzymatic platform for organophosphate pesticide detection using boron-doped diamond electrodes," *Analytical Sciences*, vol. 31, no. 10, pp. 1061–1068, 2015, doi: 10.2116/analsci.31.1061.

[20] A. Kostelnik, P. Kopel, A. Cegan, and M. Pohanka, "Construction of an acetylcholinesterase sensor based on synthesized paramagnetic nanoparticles, a simple tool for neurotoxic compounds assay," *Sensors*, vol. 17, no. 676, pp. 1–12, 2017, doi: 10.3390/s17040676.

[21] Y. Nie, Y. Teng, P. Li, W. Liu, Q. Shi, and Y. Zhang, "Label-free aptamer-based sensor for specific detection of malathion residues by surface-enhanced Raman scattering," *Spectrochimica Acta Part A: Molecular and Biomolecular Spectroscopy.*, vol. 191, pp. 271–276, 2018, doi: 10.1016/j.saa.2017.10.030.

[22] R. Bala *et al.*, "Detection of organophosphorus pesticide—Malathion in environmental samples using peptide and aptamer based nanoprobes," *Chemical Engineering Journal*, vol. 311, pp. 111–116, 2017, doi: 10.1016/j.cej.2016.11.070.

[23] A. Jirasirichote, E. Punrat, A. Suea-Ngam, O. Chailapakul, and S. Chuanuwatanakul, "Voltammetric detection of carbofuran determination using screen-printed carbon electrodes modified with gold nanoparticles and graphene oxide," *Talanta*, vol. 175, pp. 331–337, 2017, doi: 10.1016/j.talanta.2017.07.050.

[24] Z. Bin, C. Yanhong, X. Jiaojiao, and Y. Jing, "Acetylcholinesterase biosensor based on functionalized surface of carbon nanotubes for monocrotophos detection,"

Analytical Biochemistry, vol. 560, no. 301, pp. 12–18, 2018, doi: 10.1016/j.ab.2018.08.024.

[25] P. F. P. Barbosa *et al.*, "Voltammetric techniques for pesticides and herbicides detection—an overview," *International Journal of Electrochemical Science*, vol. 14, pp. 3418–3433, 2019, doi: 10.20964/2019.04.60.

[26] S. Bank and R. Jeffrey Tyrrell, "Kinetics and mechanism of alkaline and acidic hydrolysis of aldicarb," *Journal of Agricultural and Food Chemistry*, vol. 32, no. 6, pp. 1223–1232, 1984, doi: 10.1021/jf00126a005.

[27] N. Lee Wolfe, R. G. Zepp, and D. F. Paris, "Use of structure–reactivity relationships to estimate hydrolytic persistence of carbamate pesticides," *Water Research*, vol. 12, no. 8, pp. 561–563, 1978, doi: 10.1016/0043-1354(78)90133-1.

[28] N. de Bertrand and D. Barceló, "Photodegradation of the carbamate pesticides aldicarb, carbaryl and carbofuran in water," *Analytica Chimica Acta*, vol. 254, no. 1–2, pp. 235–244, 1991, doi: 10.1016/0003-2670(91)90031-Y.

[29] T. N. Rao, B. H. Loo, B. V. Sarada, C. Terashima, and A. Fujishima, "Electrochemical detection of carbamate pesticides at conductive diamond electrodes," *Analytical Chemistry*, vol. 74, no. 7, pp. 1578–1583, 2002, doi: 10.1021/ac010935d.

[30] F. Della Pelle, C. Angelini, M. Sergi, M. Del Carlo, A. Pepe, and D. Compagnone, "Nano carbon black-based screen printed sensor for carbofuran, isoprocarb, carbaryl and fenobucarb detection: application to grain samples," *Talanta*, vol. 186, pp. 389–396, 2018, doi: 10.1016/j.talanta.2018.04.082.

[31] T. Vontor, J. Socha, and M. Večeřa, "Kinetics and mechanism of hydrolysis of 1-naphthyl n-methyl- and n,n-dimethylcarbamates," *Collection of Czechoslovak Chemical Communications*, vol. 37, no. 7, pp. 2183–2196, 1972, https://doi.org/10.1135/cccc19722183.

[32] S. Kim *et al.*, "PubChem in 2021: New data content and improved web interfaces," *Nucleic Acids Research*, vol. 49, no. D1, pp. D1388–D1395, 2021, doi: 10.1093/nar/gkaa971.

[33] N. Kaur and N. Prabhakar, "Current scenario in organophosphates detection using electrochemical biosensors," *Trends in Analytical Chemistry*, vol. 92, pp. 62–85, 2017, doi: 10.1016/j.trac.2017.04.012.

[34] Y. Li, L. Shi, G. Han, Y. Xiao, and W. Zhou, "Electrochemical biosensing of carbaryl based on acetylcholinesterase immobilized onto electrochemically inducing porous graphene oxide network," *Sensors Actuators B: Chemical*, vol. 238, pp. 945–953, 2017, doi: 10.1016/j.snb.2016.07.152.

[35] T. M. B. F. Oliveira *et al.*, "Laccase-Prussian blue film-graphene doped carbon paste modified electrode for carbamate pesticides quantification," *Biosensors and*

Bioelectronics, vol. 47, pp. 292–299, 2013, doi: 10.1016/j.bios.2013.03.026.

[36] T. Hu *et al.*, "Visual detection of mixed organophosphorous pesticide using QD-AChE aerogel based microfluidic arrays sensor," *Biosensors and Bioelectronics*, vol. 136, no. March, pp. 112–117, 2019, doi: 10.1016/j.bios.2019.04.036.

[37] M. Lu and R. G. Compton, "Voltammetric pH sensing using carbon electrodes: Glassy carbon behaves similarly to EPPG," *Analyst*, vol. 139, no. 18, pp. 4599–4605, 2014, doi: 10.1039/c4an00866a.

[38] M. Lu and R. G. Compton, "Voltammetric pH sensor based on an edge plane pyrolytic graphite electrode," *Analyst*, vol. 139, no. 10, pp. 2397–2403, 2014, doi: 10.1039/c4an00147h.

[39] Z. J. Ayres, S. J. Cobb, M. E. Newton, and J. V. Macpherson, "Quinone electrochemistry for the comparative assessment of sp2 surface content of boron doped diamond electrodes," *Electrochemistry Communications*, vol. 72, pp. 59–63, 2016, doi: 10.1016/j.elecom.2016.08.024.

[40] L. A. Hutton, J. G. Iacobini, E. Bitziou, R. B. Channon, M. E. Newton, and J. V. Macpherson, "Examination of the factors affecting the electrochemical performance of oxygen-terminated polycrystalline boron-doped diamond electrodes," *Analytical Chemistry*, vol. 85, pp. 7230–7240, 2013, doi: 10.1021/ac401042t.

[41] C. H. Goeting, F. Marken, A. Gutiérrez-Sosa, R. G. Compton, and J. S. Foord, "Electrochemically induced surface modifications of boron-doped diamond electrodes: an X-ray photoelectron spectroscopy study," *Diamond and Related Materials*, vol. 9, no. 3–6, pp. 390–396, 2000, doi: 10.1016/S0925-9635(99)00267-8.

[42] A. Fujimoto, Y. Yamada, M. Koinuma, and S. Sato, "Origins of sp3 C peaks in C 1s X-ray photoelectron spectra of carbon materials," *Analytical Chemistry*, vol. 88, no. 12, pp. 6110–6114, 2016, doi: 10.1021/acs.analchem.6b01327.

[43] K. Axis, "Peak fitting in XPS," *CasaXPS 2.3.14 Manual*. Casa Software Ltd., p. 19, 2006, http://www.casaxps.com/help_manual/manual_updates/peak_fitting_in_xps.pdf.

[44] F. Deng *et al.*, "Grafting polymer coatings onto the surfaces of carbon nanotube forests and yarns via a photon irradiation process," *Applied Physics Letters*, vol. 100, no. 21, 2012, doi: 10.1063/1.4720509.

[45] A. Mostafa *et al.*, "Simultaneous quantification of carbamate insecticides in human plasma by liquid chromatography/tandem mass spectrometry," *Journal of Chromatography B: Analytical Technologies in the Biomedical and Life Sciences*, vol. 879, no. 23, pp. 2234–2238, 2011, doi: 10.1016/j.jchromb.2011.06.006.

[46] J. M. Dias Soares and H. P. de Oliveira, "Silver-based surface enhanced Raman spectroscopy devices for detection of organophosphorus pesticides traces,"

Biotechnology Progress, vol. 35, no. 4, pp. 1–8, 2019, doi: 10.1002/btpr.2809.

[47] D. S. Kim *et al.*, "Electrochemical detection of dopamine using periodic cylindrical gold nanoelectrode arrays," *Scientific Reports*, vol. 8, no. 1, pp. 1–10, 2018, doi: 10.1038/s41598-018-32477-0.

[48] R. Madhu, B. Devadas, S. M. Chen, and M. Rajkumar, "An enhanced direct electrochemistry of glucose oxidase at poly(taurine) modified glassy carbon electrode for glucose biosensor," *Analytical Methods*, vol. 6, no. 22, pp. 9053–9058, 2014, doi: 10.1039/c4ay01406e.

[49] B. Liu, B. Xiao, and L. Cui, "Electrochemical analysis of carbaryl in fruit samples on graphene oxide-ionic liquid composite modified electrode," *Journal of Food Composition and Analysis*, vol. 40, pp. 14–18, 2015, doi: 10.1016/j.jfca.2014.12.010.

[50] "GSI Chemical Database," *GSI Environmental*, 2014. https://www.gsi-net.com/en/publications/gsi-chemical-database/.

[51] A. M. Committee, "Recommendations for the definition, estimation and use of the detection limit," *Analyst*, vol. 112, no. 2, pp. 199–204, 1987, doi: 10.1039/AN9871200199.

[52] J. Inczedy, T. Lengye, and A. M. Ure, Eds., "Chapter 18 Quality assurance of analytical processes," in *IUPAC Compendium on Analytical Nomenclature, Definitive Rules 1997, "The Orange Book,"* 3rd edn, Blackwell Science, 1998.

[53] A. G. Cabanillas, T. G. Díaz, F. Salinas, J. M. Ortiz, and J. M. Kauffmann, "Differential pulse voltammetric determination of fenobucarb at the glassy carbon electrode, after its alkaline hydrolysis to a phenolic product," *Electroanalysis*, vol. 9, no. 12, pp. 952–955, 1997, doi: 10.1002/elan.1140091218.

[54] K. Kunpatee *et al.*, "A highly sensitive fenobucarb electrochemical sensor based on graphene nanoribbons-ionic liquid-cobalt phthalocyanine composites modified on screen-printed carbon electrode coupled with a flow injection analysis," *Journal of Electroanalytical Chemistry*, no. 855, p. 113630, 2019, doi: 10.1016/j.jelechem.2019.113630.

[55] F. C. Moraes, L. H. Mascaro, S. A. S. Machado, and C. M. A. Brett, "Direct electrochemical determination of carbaryl using a multi-walled carbon nanotube/cobalt phthalocyanine modified electrode," *Talanta*, vol. 79, no. 5, pp. 1406–1411, 2009, doi: 10.1016/j.talanta.2009.06.013.

[56] J. Caetano and S. A. S. Machado, "Determination of carbaryl in tomato 'in natura' using an amperometric biosensor based on the inhibition of acetylcholinesterase activity," *Sensors and Actuators B: Chemical*, vol. 129, no. 1, pp. 40–46, 2008, doi: 10.1016/j.snb.2007.07.098.

[57] L. Codognoto, S. T. Tanimoto, V. A. Pedrosa, H. B. Suffredini, S. A. S. Machado,

and L. A. Avaca, “Electroanalytical determination of carbaryl in natural waters on boron doped diamond electrode,” *Electroanalysis*, vol. 18, no. 3, pp. 253–258, 2006, doi: 10.1002/elan.200503396.

[58] T. Jeyapragasam and R. Saraswathi, “Electrochemical biosensing of carbofuran based on acetylcholinesterase immobilized onto iron oxide-chitosan nanocomposite,” *Sensors and Actuators B: Chemical*, vol. 191, pp. 681–687, 2014, doi: 10.1016/j.snb.2013.10.054.

[59] M. Wang, J. Huang, M. Wang, D. Zhang, and J. Chen, “Electrochemical nonenzymatic sensor based on CoO decorated reduced graphene oxide for the simultaneous determination of carbofuran and carbaryl in fruits and vegetables,” *Food Chemistry*, vol. 151, pp. 191–197, 2014, doi: 10.1016/j.foodchem.2013.11.046.

[60] E. Suprun, G. Evtugyn, H. Budnikov, F. Ricci, D. Moscone, and G. Palleschi, “Acetylcholinesterase sensor based on screen-printed carbon electrode modified with Prussian blue,” *Analytical and Bioanalytical Chemistry*, vol. 383, no. 4, pp. 597–604, 2005, doi: 10.1007/s00216-005-0002-0.

[61] H. A. Azab, A. Duerkop, E. M. Mogahed, F. K. Awad, R. M. Abd El Aal, and R. M. Kamel, “Fluorescence and electrochemical sensing of pesticides methomyl, aldicarb and prometryne by the luminescent europium-3-carboxycoumarin probe,” *Journal of Fluorescence*, vol. 22, no. 2, pp. 659–676, 2012, doi: 10.1007/s10895-011-1002-4.

[62] S. Saxena, G. B. V. S. Lakshmi, D. Chauhan, and P. R. Solanki, “Molecularly imprinted polymer-based novel electrochemical sensor for the selective detection of aldicarb,” *Physica Status Solidi (A) Applications and Materials Science*, vol. 217, no. 9, pp. 1–8, 2020, doi: 10.1002/pssa.201900599.

[63] J. Ružička and E. H. Hansen, “Flow injection analyses. Part I. A new concept of fast continuous flow analysis,” *Analytica Chimica Acta*, vol. 78, no. 1, pp. 145–157, 1975, doi: 10.1016/S0003-2670(01)84761-9.

[64] J. M. Freitas, T. da C. Oliveira, R. A. A. Munoz, and E. M. Richter, “Boron doped diamond electrodes in flow-based systems,” *Frontiers in Chemistry*, vol. 7, no. April, 2019, doi: 10.3389/fchem.2019.00190.

[65] J. Wang and Z. Taha, “Batch Injection Analysis,” *Analytical Chemistry*, no. 65, pp. 1053–1058, 1991, doi: 10.1021/ac00010a025.

Chapter 6

Electroanalysis of β-lactam, quinolone, and tetracycline antibiotics

6.1 Introduction

Currently, the most commonly used detection methods for antibiotics are based on chromatographic or immunological techniques, and electroanalysis is a fairly new addition to this tool set [1]. So far, only a handful of studies has used BDD electrodes for analysing antibiotics. The present section provides a brief history (Figure 6.1) of the discovery and application of antibiotics and reviews the existing studies to quantify their concentrations.

Antibacterial compounds can be produced naturally by adapted fungi and bacteria to use as a chemical weapon against other microbes competing for space and nutrients [2], [3]. Antibiotic resistance has been observed for as long as these drugs have been used [4]. The modes of action of antimicrobial agents can be divided into five categories: inhibition of cell-wall synthesis; inhibition of protein synthesis; inhibition of nucleic-acid synthesis; inhibition of folate synthesis; and disruption of the cytoplasmic membrane [5].

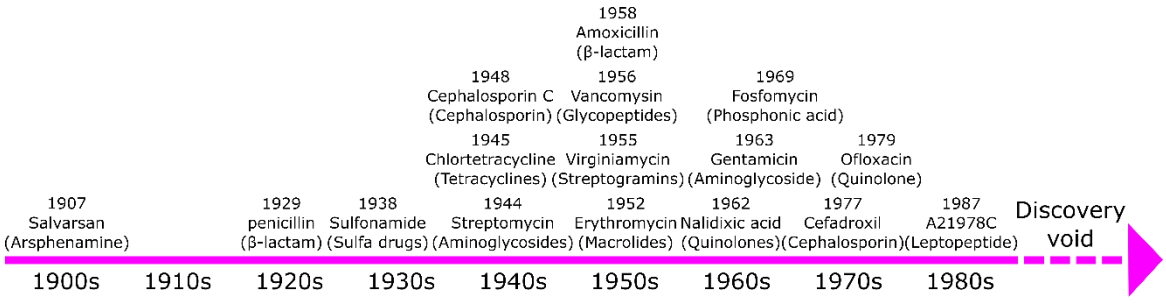


Figure 6.1 A partial timeline of antibiotic discoveries, with a void from 1987 [6–8].

From the wide range of possible analytes on the timeline, this project focuses on four major classes, with one representative compound chosen from each. The first category to be decided upon was β-lactams. This is because they have the longest history, as they were the first to be isolated and produced. The class of cephalosporins was chosen next because they are the first alternative for those allergic to β-lactams. Together, they form the first option for most conditions requiring antibiotics and have demonstrated growth-promotion advantages. Tetracyclines are the next most common antibiotic used in farming, having been discovered relatively early. Finally, the choice of the quinolones was because they are newer broad-spectrum drugs, with relatively lower side-effects and production costs which consequently put them among most widely used antibiotics worldwide. A variety and combination of these drugs, almost as soon as they entered the market, were fed to poultry to reduce their growth time from an average of 18 weeks to a mere 5 weeks [7,8]. From each class, amoxicillin (AMX), cefadroxil (CFX), ofloxacin (OFX), and tetracycline (TC) were chosen, as the basic structures that are representative of the whole class (Figure 6.2).

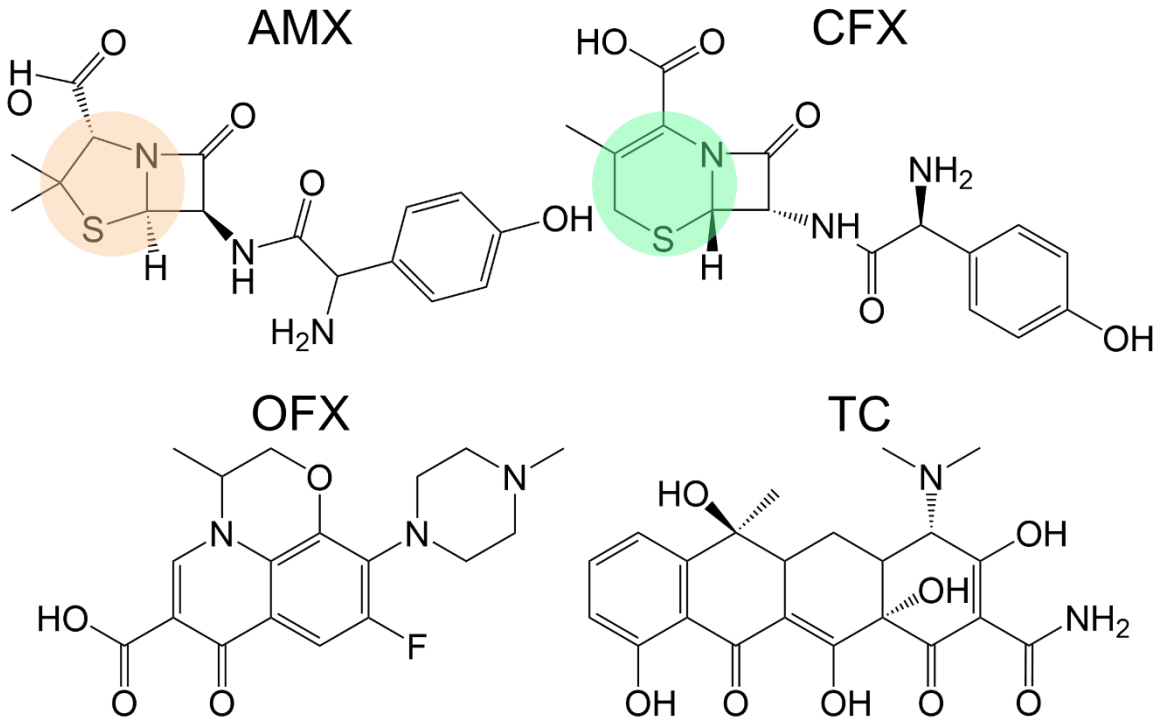


Figure 6.2 The structures of amoxicillin, cefadroxil, ofloxacin, and tetracycline.

A significant proportion of administered antibiotics (25–75%) is excreted in unaltered form. Some antibiotics resist biodegradation during wastewater treatment, and those present in organic manure can run off into natural streams. Often, pollution arises from dispersed sources that are difficult to monitor, leaving antibiotics to persist and increase in residual amount in the environment, in soil and water.

The Swann report in 1969 recommended against the use of human antibiotics for growth promotion in animal farming [11], and in each subsequent government investigation on the issue, the advice has become stricter and usage more restrictive [10,11]. However, the economics of industrial farming has meant that loopholes have been found, in particular by the use of rebranding, despite knowledge of the dangers of untreatable cross infections [12,13]. The impending obsoletion (by 2050 [16]) arising from the misuse of antibiotics could be overcome by legislation supported by research. Here, it is hoped that investigating the science around developing robust and sensitive probes can be a step in the right direction. This project will add to the small body of evidence on the electrochemical behaviour of antibiotics.

Amoxicillin (AMX) is a semisynthetic derivative of penicillin; they are both β-lactams. Cefadroxil (CFX) is a first-generation cephalosporin, meaning that it was naturally derived from the mould. They share the same β-lactam moiety but differ in their sulfur-containing groups: dihydrothiazine in CFX (green in Figure 6.2) and thiazolidine in AMX (yellow in Figure 6.2). Both drugs work by inhibiting the active site of penicillin-binding proteins, which are required for the last stage of transpeptidation in peptidoglycan synthesis [6]. By disruption of the structure of peptidoglycans, the cell wall deforms and weakens under strain, leading to cell lysis and death [17].

Cephalosporins and β-lactams can form transition-metal complexes with Cu(II), Cd(II), and Zn(II), among others [16–19], which can increase their potency [20,21]. Sanz et al

exploited this binding phenomenon to study the selective formation of CFX complexes in solution using glassy carbon (GC) electrodes [18], as Pham et al did similarly for AMX with reduced graphite oxide nanosheet electrodes [24], both in 2019. Using the same behaviour, UV-vis spectrometry and electrochemistry with a carbon paste electrode had been used to detect Cu (II) ions in solution [21].

Ofloxacin (OFX) is a second-generation fluoroquinolone; it is a synthetic antibiotic that halts the growth of bacteria. It inhibits DNA gyrase, which is responsible for reducing strain while the double helix is being unwound during replication. Without the gyrase to make DNA 'unzipping' smooth, double-strand breaks accumulate, replication forks stall, and the cells cannot reproduce [25]. Antibiotics of this class are poorly biodegradable, tend to accumulate, and are considered toxic. Hence, they are recommended only for serious infections [26].

Specific sensing of OFX has also been achieved by the joint working of aptamers and Au-NPs deposited on a GC substrate [27]. Irreversible reduction of OFX has been observed by polarography, with a proposed mechanism being the reduction of the C^7 carbonyl to an alcohol and hydrogen, which is dependent on the adsorption of OFX to the static mercury-drop electrode surface [28]. Voltammetry at a graphene/GC electrode shows that OFX oxidises differently depending on the solution pH [29]. The adsorption of the oxidation products of OFX has proved to be problematic [30]. The chemical inertness of BDD may bypass this issue. In this project, BDD electrodes will be applied, for the first time, to perform voltammetric investigation of OFX in aqueous conditions.

Tetracycline (TC) inhibits bacterial protein synthesis by reversibly binding to the 30S ribosomal subunit which prevents the addition of new amino acids to the growing polypeptide [31]. As their binding is reversible, these agents are mainly bacteriostatic rather than bactericidal [6]. The literature on TC in an electrochemical context has focused on the

treatment of water to remove it as a contaminant, using degradation by advanced oxidation processes or by the Fenton process [29–31]. A small proportion of work is on electrochemical detection schemes. A wide variety of electrode materials have been trialled: multi-wall carbon nanotube (MWCNT) [35], GC [36], MWCNT–ionic-liquid-film coated GC [37], poly(Malachite green)-modified GC [38], gold colloids on tungsten [39], and hanging mercury drop [40], in increasing degrees of sensitivity, generally with detection limits in the 1–5 micromolar range. One study by Treetepvijit et al, in 2005, which used nickel-implanted BDD thin films in a flow-injection system, achieved a limit of detection of 10 nM for TC oxidation. The present work examines the reduction of TC on BDD electrodes.

There are three aims for this project. The first aim is to explore the sensitivity of bare BDD electrodes for detecting amoxicillin, cefadroxil, ofloxacin, and tetracycline in aqueous solutions. The second aim is to investigate the oxidation mechanism of those analytes that respond to electrochemical stimulation. The final aim is to examine the application of the current pulses, from Chapter 3, to maintain surface sensitivity.

6.2 Experimental details

Prior to commencing the project, the BDD electrodes underwent acid boiling, to severely oxidise their surfaces and ‘erase’ the electrode history. Thereafter, a combination of CV cleaning scans and current pulses sufficed. The cleaning CVs scanned from 0 V to 3 V to –2 V to 0 V. For those analytes which caused a reduction in the electrode performance, current pulses of ± 10 mAcm^{-2} amplitude and 100 ms each were applied in the analyte solution before subsequent measurements to return reproducible voltammograms.

6.2.1 Solutions

Ofloxacin, tetracycline, amoxicillin, and cefadroxil (analytical grade, produce of Israel)

were obtained from Sigma Aldrich (Gillingham, UK) and used without further purification. All antibiotics easily dissolved in Carmody buffers of all pH values, and any aggregation was removable by vigorous shaking (< 30 seconds). All powders and solutions were stored at – 4°C. Fresh solutions were made for each day of experiments.

6.3 Results and discussions

6.3.1 Cyclic voltammetry

First, voltammograms were recorded at a variety of scan rates to investigate the electrochemical behaviour of AMX, CFX, OFX, and TC on bare BDD electrodes. Figure 6.3 shows the CVs obtained at high concentrations of the four analytes at pH 7.0. A large range of starting and turn-around potentials were trialled to elicit and capture any electrochemical response. The starting potentials ranged from –1.0 to 1.0 V, and the positive extremes varied from 1.6 to 2.2 V, and the negative extreme varied from –0.5 to –1.8 V. Within these exploratory experiments, voltammograms were recorded in both scanning directions. Of the four antibiotics, AMX was the only one that was inactive. At pH 7.0 the oxidation peaks of CFX and OFX were better defined at lower scan rates. This agrees with results for similar cephalosporins previously reported on glassy carbon electrodes [18]. There were no distinguishing features from the oxidation of TC, but it showed a single reduction peak in the negative potential region. This means that Randles–Sevčik plots can only be extracted for CFX, OFX, and the reduction of TC.

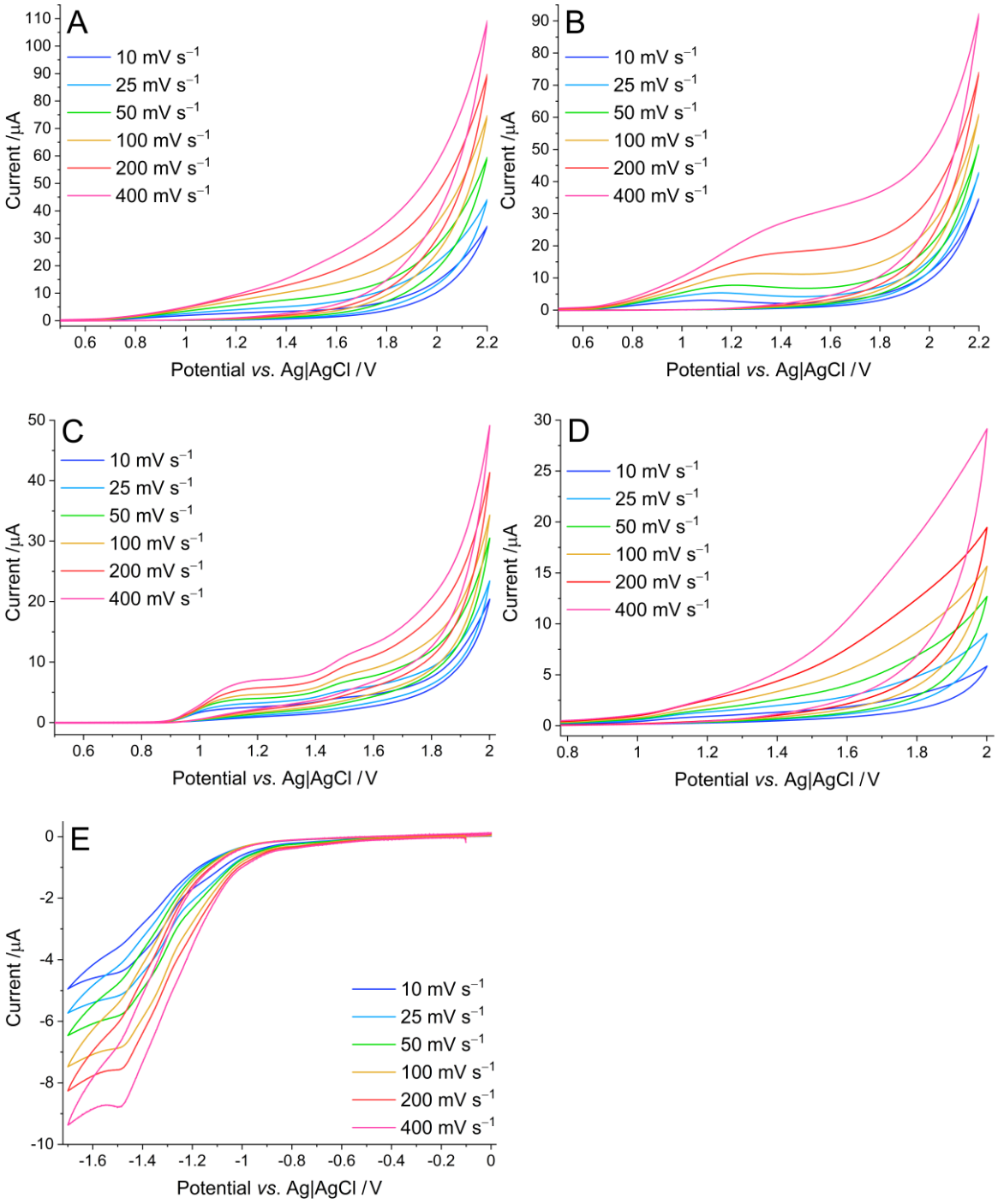


Figure 6.3 Voltammograms recorded in (A) 1 mM AMX, (B) 1mM CFX, (C) 200 µM OFX, and (D,E) 200 µM TC dissolved in 0.2 M Carmody buffer at pH 7.0. The scan rates ranged from 10 to 400 mV s^{-1}.

Plots of the peak current versus the square root of the scan rate show linear dependence (Figure 6.4). This indicates that the initial oxidation (of CFX and OFX) and reduction (of TC) occur through diffusion of the electroactive species from solution to the electrode

surface [41]. From reviewing the literature (Section 6.1), a sizeable proportion of the studies on the electrochemistry of these antibiotics at most electrode surfaces occur via oxidation of adsorbed species. Due to the chemical inertness of the diamond surface, it is relatively resistant to adsorption, evidenced by this major mechanistic difference.

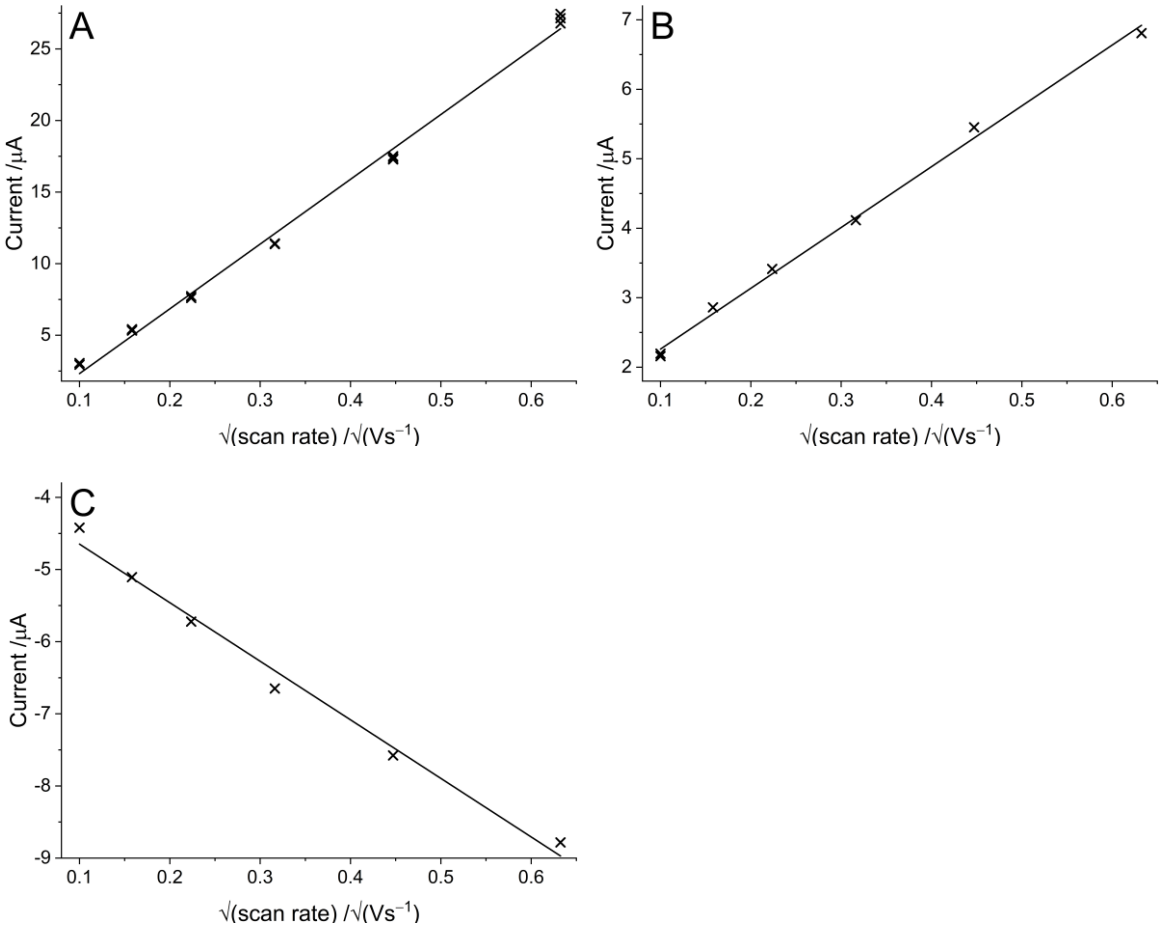


Figure 6.4 The peak currents of (A) 1mM CFX, (B) 200 µM OFX, and (C) 200 µM TC are plotted against the square root of the scan rates. The buffer pH was 7.0.

No reduction wave was observed for CFX and OFX, and no oxidation wave was observed for TC, suggesting irreversibility. From a single scan in CFX, OFX, and TC, the electrode surface loses reactivity, and substantial changes can be observed on the next voltammogram recorded. This could be because, during oxidation, extensive irreversible chemical changes result, which are often associated with strongly bound species at the electrode surface. The resulting deposits formed from these pathways cannot be simply

rinsed off with water and are non-electroactive, reducing peak currents from further experiments. To check the validity of this statement, the solution was stirred between several measurements to confirm that the electrode had become passivated, and that the current changes are not due to depletion in the analyte concentration at the electrode surface. For all experiments with CFX, OFX, and CF, 20 bipolar pulses were applied prior to measurement in a blank buffer, which returned the original activity of the electrode.

6.3.2 pH dependence

Cyclic voltammograms were recorded in solutions of 1 mM CFX, from pH 2.0 to 10.0, at a scan rate of 10 mV s^{-1}. Figure 6.5 shows the raw and baseline-subtracted forward scans.

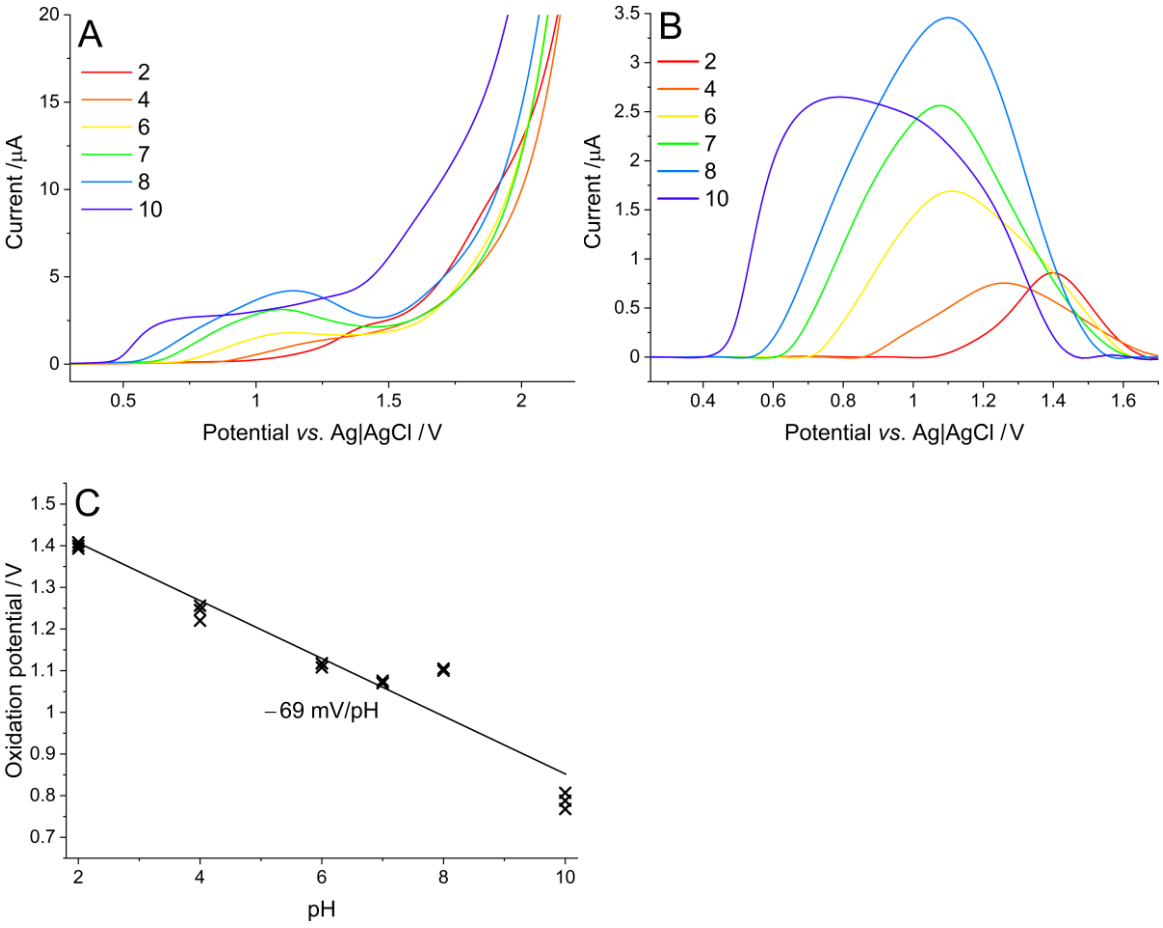


Figure 6.5 Forward CV scans of (A) 1mM CFX at pH values from 2.0 to 12.0. The backward scans show no peaks. (B) The baseline-subtracted waves from chart A. (C) The CFX peak potentials plotted against solution pH.

Figure 6.5 shows the wide pH conditions under which CFX remain electroactive. The peak current increases steadily from pH 2.0 to a maximum at 8.0, indicating that the protonated forms of CFX exhibit worse electron-transfer characteristics at the diamond electrode. When the peak potentials are plotted against pH, the slope obtained for CFX is – 69 mV per pH unit. Although the slope is 10% higher than the theoretical value, it is closer to an oxidation event where the number of protons and electrons involved are equal, than one where they are not. Due to the structural similarity between CFX and penicillin (the first β-lactam antibiotic), it is likely that they oxidise in the same way [18]. Figure 6.6 shows the scheme of oxidation.

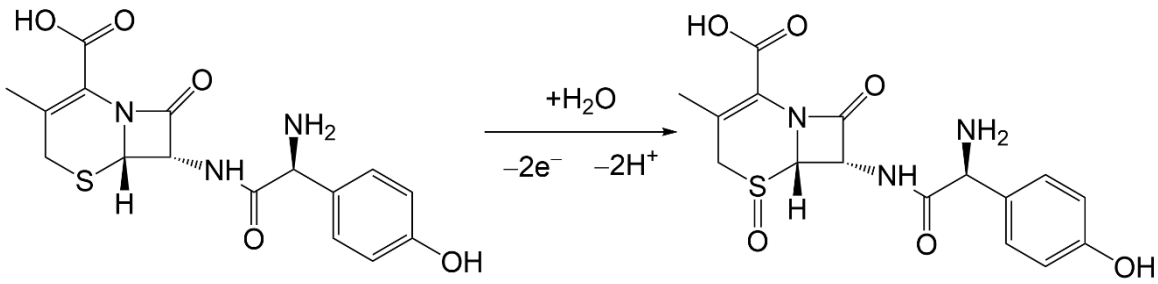


Figure 6.6 Electrochemical oxidation mechanism of cefadroxil, on the sulfide [42].

Sulfides can be electrochemically oxidised in aqueous and organic media to sulfoxides and sulfones [42,43]. Thus, the electrochemical oxidation of cephalosporins can be expected to occur at the sulfur atom on the cephalosporin nucleus, as happens in the case of their chemical oxidation [44,45,46]—in this case, most likely forming a sulfoxide, as the sulfone is preferentially produced in the presence of methanol [44].

As OFX displayed good peak definition in the scan-rate experiments, it was possible to reduce the analyte concentration to 200 μM in these pH measurements and still produce reasonable clarity at a scan rate of 10 mV s^{-1}. The raw and baseline-subtracted forward scans are shown in Figure 6.7.

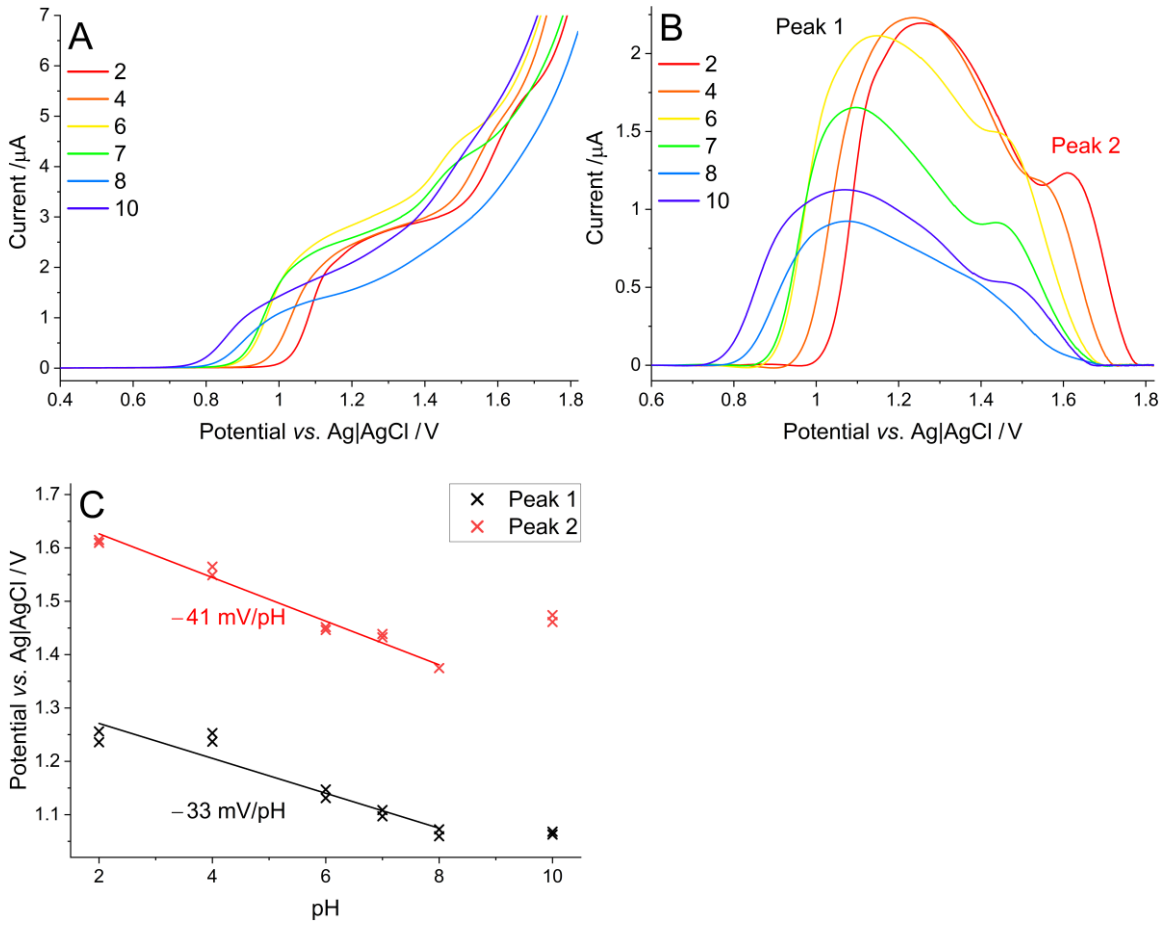


Figure 6.7 (A) Forward scan CVs of 200 µM OFX at pH values from 2.0 to 12.0. The scan rate was 10 mV s^{-1}. (B) Baseline-subtracted versions of the traces in chart A. (C) The potentials of peaks 1 and 2 plotted against solution pH.

Figure 6.7B shows that acidic conditions favour greater oxidation of OFX. generating the highest peak currents at pH 4.0. Liu et al, in 2019, using voltammetry alongside analysis with density-functional theory, have shown that, under alkaline conditions, the amino group deprotonates and OFX is primarily negatively charged [29]. This leads to greater electrostatic repulsion between the molecules and the carbon surface which overcomes the strength of hydrogen bonding between the two [29]. Consequently, as pH increases, the number of OFX molecules available to the electrode surface decreases, causing the decrease in current. The two peaks of OFX oxidation move in synchrony with each other (Figure 6.7C), at approximately the same rate against pH (– 33 mV and – 41 mV per pH

unit). This may be attributed to the two-electron–one-proton oxidation of the amino group in the piperazine ring, which can be stabilised by its delocalised π-system, possibly leading to the formation of polymers (which may explain the electrode passivation) [47]. Above pH 8.0, the oxidation potential becomes independent of the pH since according to the pKa of OFX (7.9 [48]), the piperazine group will exist mainly in its anionic form in this pH range, so no protons are transferred in the oxidation step.

The clearest change in TC occurs in the negative potential region. The measurements started at – 0.1 V and scanned to – 1.7 V. Figure 6.8A shows the raw data from the forward part of the CV, where the concentration was 200 µM. With baseline subtraction (Figure 6.8B), the actual peak potentials (Figure 6.8C) become easier to see.

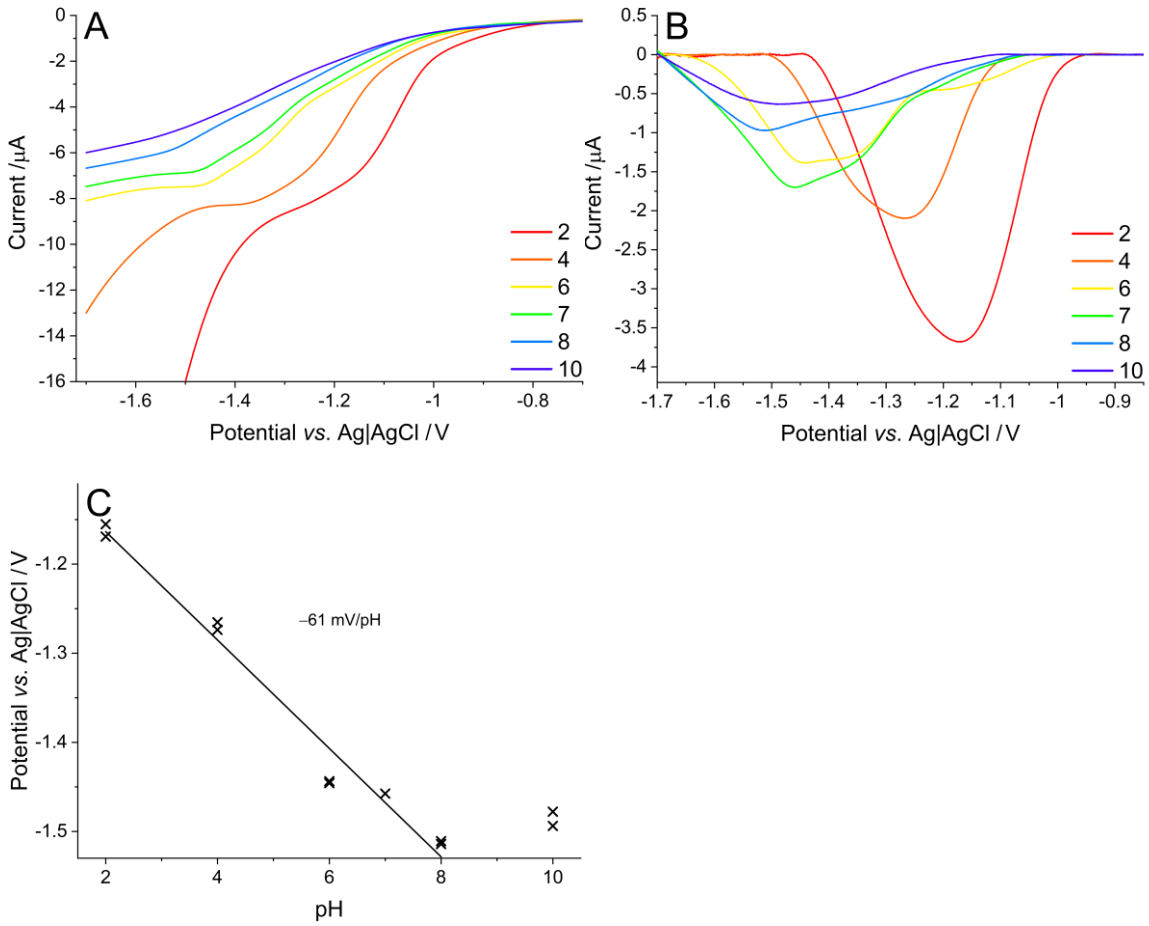


Figure 6.8 (A) Forward scan CVs of 200 µM TC at pH values from 2.0 to 12.0. The scan rate was 100 mV s^{-1}. (B) Baseline-subtracted versions of the traces in chart A. (C) The peak potentials plotted against solution pH.

There are many carbonyl, carboxyl, and amine groups on TC that are responsible for its wide variety of ionic forms [33]. The peak potential decreases linearly with respect to pH from 2.0 to 8.0, at – 61 mV/pH (close to the theoretical –59 mV), in the linear region, indicating the likelihood of TC undergoing reduction where equal numbers of protons and electrons are involved.

Overall, it can be concluded from the cyclic voltammetry data, including the scan rate and pH dependence, that the electrochemistry of the electroactive antibiotics studied undergo irreversible electron-transfer kinetics coupled to diffusional mass-transport characteristics. In particular, because of the inertness of the diamond surface, adsorption which dominates the electrochemistry on non-diamond electrodes does not take place.

6.3.3 Square-wave voltammetry

Square-wave voltammetry (SWV) as a pulsed voltammetric technique is more sensitive than CV. It was used to examine the electrode response as a function of analyte concentration. Optimisation of the parameters of SWV—step potential (Step), frequency (Freq), and pulse amplitude (Mod)—is an important stage in realising the excellent sensitivity of this method. Attempts to elicit some credible response from AMX by fine-tuning the experimental parameters were unsuccessful, see in Figure 6.9.

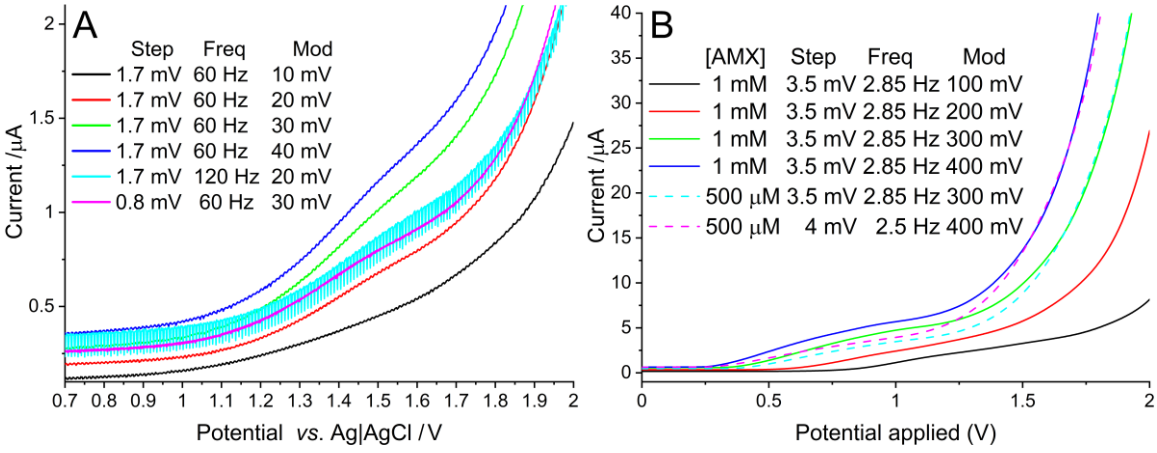


Figure 6.9 SWVs recorded with various step sizes, frequencies, and modulation amplitudes in pH7 solutions. (A) 100 μM of AMX, (B) 500 μM and 1 mM of AMX.

The trace from the blank buffer constantly rises in the regions where a peak might be expected from both analytes, thus making peak differentiation difficult. As the signal quality is below the level expected at these relatively high concentrations (1 mM, 500 µM, and 100 µM of AMX), extensive data manipulation would be needed to obtain a trustworthy calibration curve, and then not in the concentration range of interest. Therefore, the remaining time and effort was spent on the other three analytes, for which the peak definitions were clearer.

For CFX, the best peak definition was recorded with the following parameters: 0.5 mV step potential, 50 mV modulation amplitude, and a frequency of 22 Hz, which was equivalent to a scan rate of 10 mV s^{-1}. For OFX, the scan rate could be higher yet retain good peak clarity. Its SWV parameters were 3.5 mV step potential, 10 mV modulation amplitude, and a frequency of 28.5 Hz, which was equivalent to a scan rate of 100 mV s^{-1}.

At higher CFX concentrations (Figures 6.10A), the voltammograms show a two-humped wave. As the concentration drops below 80 µM, only one peak remains. Figure 6.10B shows how that the peak at 1.3 V increases in step with concentration, showing a piecewise linear relationship for the whole concentration range. If the whole range is split at the 80 µM mark, there is good linearity among the two parts. However, there is no theoretical justification for this kind of analysis, so the usefulness of this figure is limited. The detection limit is 500 nM, as it was the lowest concentration in which a peak was still distinguishable. However, it did not deviate significantly from that of the 1 µM wave, meaning that only solution concentrations including and above 5 µM should be quantified using SWV.

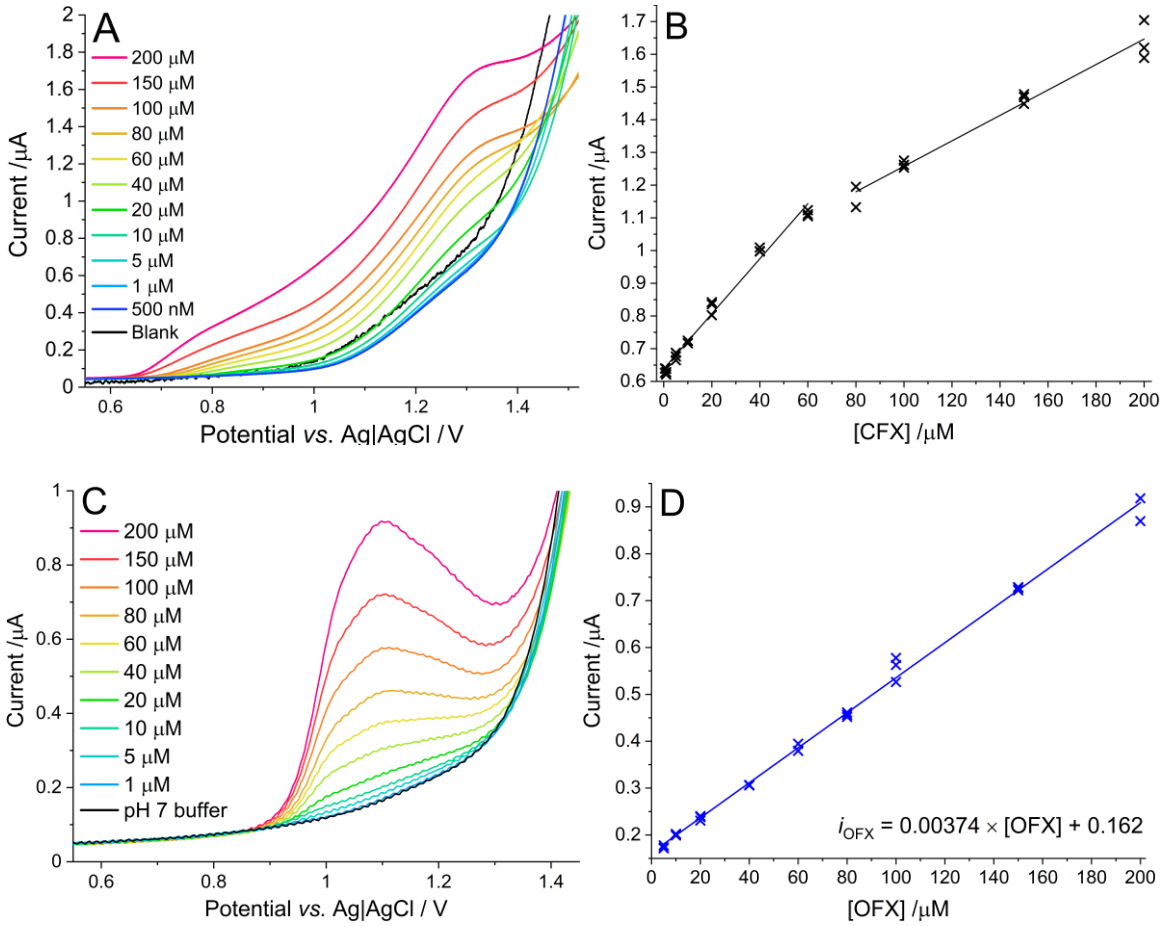


Figure 6.10 SWVs at pH 7.0 of (A) CFX at an equivalent scan rate of 10 mV s^{-1}, and (B) OFX at an equivalent scan rate of 100 mV s^{-1}. Charts C and D show the peak currents plotted against the concentrations of CFX and OFX extracted from charts A and B respectively.

For OFX, the waves show a slight two-hump outline, which was maintained as the concentration changed (Figure 6.10C). The lowest concentration that was able to be differentiated from the blank buffer was 1 µM. The peak currents at 1.1 V were used to construct Figure 6.10D, to obtain a linear calibration line with an R^2 of 0.996. This linear region is wide: up to 200 µM.

For TC, only the negative potential region produced well-defined peaks that changed with concentration. To the SWV parameters were optimised to be: 3.5 mV step potential, 50 mV modulation amplitude, and a frequency of 28.5 Hz, which was equivalent to a scan

rate of 100 mV s^{-1}. The recordings started at 0 V and scanned towards –1.8 V. The solution pH was 4.0, to compromise between signal quality and smaller deviation from neutral.

Figure 6.11A shows how the background varied as the concentration changed, making it somewhat difficult to distinguish how the peak magnitudes change without manipulating the data. Repeating the measurements at 1 nM showed some overlap with those from the 5 nM solution, thus making 5 nM the reliable detection limit. This is orders of magnitudes lower than previously reported limits for TC detection with any electrode material.

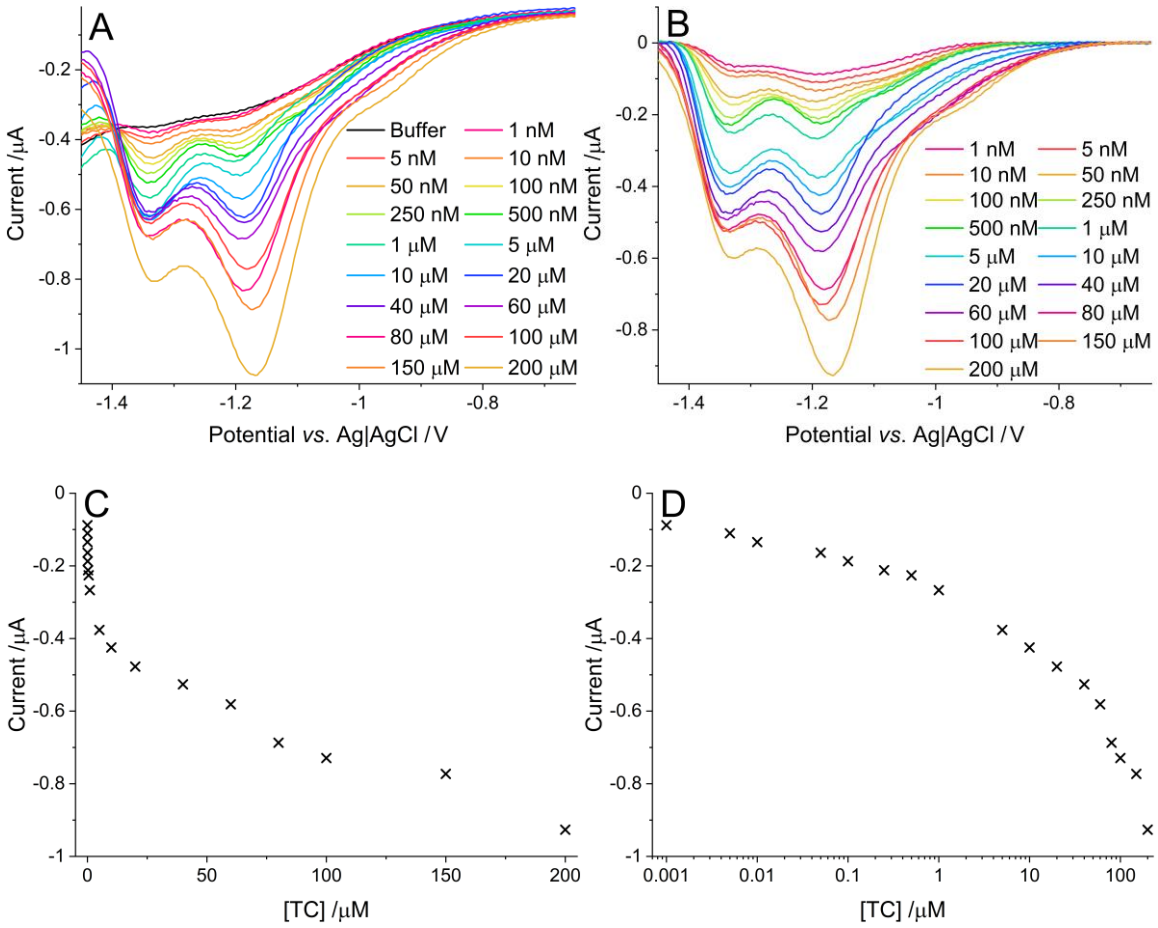


Figure 6.11 (A) SWVs of TC at an equivalent scan rate of 100 mV s^{-1}, recorded at pH 4.0. (B) The baseline-subtracted waves from chart A. The peak currents extracted from chart B are then plotted against TC concentration, displayed on a linear axis in chart C, and on a logarithmic axis in chart D.

Figure 6.11B show the baseline-subtracted waves that decrease roughly in step with

decreasing concentration. Figure 6.11C and D show the same extracted currents plotted against TC concentration, they are displayed against linear and logarithmic axes to reduce the crowding at the lower concentration regions. The relationship between the peak currents and concentration is nonlinear, where a linear relationship is theorised; so, these graphs are only qualitatively useful.

To summarise, SWV is an efficient method for the quantitative analysis of OFX and qualitative analysis of CFX and TC. Competitive detection limits were obtained for OFX and CFX, and a record low limit was obtained for TC. For fast quantitative analysis of AMX in aqueous solutions, bare BDD electrodes are not ideal.

6.4 Conclusions

The electrochemical behaviour of amoxicillin, cefadroxil, ofloxacin, and tetracycline have been studied on a base BDD electrode. On the clean hydrophilic oxidised diamond surface, diffusional electrochemistry was observed for CFX, OFX, and TC, and no electroactivity was recorded for AMX. Due to the chemical inertness of diamond surfaces, adsorption of the target analytes did not occur.

For OFX, a linear dynamic range of 1–100 μM was recorded, with a competitive detection limit of 1 μM. For CFX and TC, the peak currents changed in non-linear relationships with the concentration, from their detection limit up to the maximum concentration tested: 200 μM. The detection limit for CFX is 500 nM, which is good for an undecorated planar electrode. The limit achieved for TC is 1 nM, which is excellent, and an order of magnitude lower than previously reported.

Although the target analytes do not adsorb on the electrode surface, the products of electrochemical oxidation do even on this inert diamond electrode. Reproducible electroanalysis for CFX, OFX, and TC was performed with the aid of 20 current pulses of 10 mA cm^{-2} in blank buffer before each measurement.

The experiments showed that TC is reduced in the negative potential region, far away from the oxidation activities of CFX and OFX. This feature may enable the identification of TC in combination with either of the other two. Overall, it can be concluded that the oxidised diamond electrode is an excellent electrode material for electroanalysis in a wide concentration range of these compounds.

References

[1] M. Majdinasab, R. K. Mishra, X. Tang, and J. L. Marty, "Detection of antibiotics in food: New achievements in the development of biosensors," *TrAC - Trends in Analytical Chemistry*, vol. 127, p. 115883, 2020, doi: 10.1016/j.trac.2020.115883.

[2] A. Fleming, "On the antibacterial action of cultures of a penicillium, with special reference to their use in the isolation of *B. Influenzae*," *British Journal of Experimental Pathology*, vol. 10, no. 3, pp. 226–236, 1945.

[3] C. Walsh, *Antibiotics: Actions, Origins, Resistance*. Washington, DC: ASM Press, 2003.

[4] S. R. Palumbi, "Humans as the world's greatest evolutionary force," *Science*, vol. 293, no. 5536, pp. 1786–1790, 2001, doi: 10.1126/science.293.5536.1786.

[5] M. E. Török, F. J. Cooke, and E. Moran, "Basics of antimicrobials," in *Oxford Handbook of Infectious Diseases and Microbiology*, 2nd edn, Oxford: OUP, 2016, Chapter 1. doi: 10.1093/med/9780199671328.001.0001.

[6] M. E. Török, F. J. Cooke, and E. Moran, "Antibiotics," in *Oxford Handbook of Infectious Diseases and Microbiology*, 2nd edn, Oxford: OUP, 2016, Chapter 2. doi: 10.1093/med/9780198569251.001.0001.

[7] J. H. Powers, "Antimicrobial drug development - The past, the present, and the future," *Clinical Microbiology and Infection, Supplement*, vol. 10, no. 4, pp. 23–31, 2004, doi: 10.1111/j.1465-0691.2004.1007.x.

[8] L. L. Silver, "Challenges of antibacterial discovery," *Clinical Microbiology Reviews*, vol. 24, no. 1, pp. 71–109, Jan. 2011, doi: 10.1128/CMR.00030-10.

[9] Eric Lofgren, "Chapter 3 Getting Started with Chicks," in *The Backyard Chicken Bible: The Complete Guide to Raising Chickens*, EBook., Krause Publishers, 2014.

[10] RSPCA, "The Life of a Typical Meat Chicken," 2021. [Online]. Available: https://www.rspca.org.uk/webContent/staticImages/BroilerCampaign/EatSitSufferRepeat.pdf

[11] M. M. Swann *et al.*, "Report to the joint committee on the use of antibiotics in animal husbandry and veterinary medicine," London, 1969.

[12] J. Harvey and L. Mason, "*The Use and Misuse of Antibiotics in UK Agriculture, Part 1: Current Usage*," Bristol, 1998. doi: 10.1016/b978-1-4160-5316-3.00043-5.

[13] "*Real Farming Solutions to Antibiotic Misuse —What Farmers and Supermarkets Must Do*," 2017. http://www.saveourantibiotics.org/media/1777/asoa-report-real-farming-solutions-to-antibiotic-misues-what-farmers-and-supermarkets-must-do.pdf

[14] J. Bower, "The farm drugs scandal," *The Ecologist*, vol. 1, no. 2, pp. 10–15, 1970.

[15] "'Swann song' for routine antibiotic use, 50 years on?," 2019. http://www.saveourantibiotics.org/media/1803/swann-song-for-routine-antibiotic-use.pdf

[16] J. O'Neill, "Antimicrobial resistance: tackling a crisis for the health and wealth of

nations." *The Review on Antimicrobial Resistance* chaired by Jim O'Neill. Wellcome Collection. London, 2014.

[17] D. J. Waxman and J. L. Strominger, "Penicillin-binding proteins and the mechanism of action of beta-lactam antibiotics," *Annual Review of Biochemistry*, vol. 52, no. 1, pp. 825–869, 1983, doi: 10.1146/annurev.bi.52.070183.004141.

[18] C. G. Sanz, S. H. P. Serrano, and C. M. A. Brett, "Electrochemical characterization of cefadroxil β-lactam antibiotic and Cu(II) complex formation," *Journal of Electroanalytical Chemistry*, vol. 844, January, pp. 124–131, 2019, doi: 10.1016/j.jelechem.2019.04.077.

[19] N. Abo El-Maali, A. H. Osman, A. A. M. Aly, and G. A. A. Al-Hazmi, "Voltammetric analysis of Cu (II), Cd (II) and Zn (II) complexes and their cyclic voltammetry with several cephalosporin antibiotics," *Bioelectrochemistry*, vol. 65, no. 2, pp. 95–104, 2005, doi: 10.1016/j.bioelechem.2004.09.002.

[20] S. A. Khan, A. M. Asiri, K. Al-Amry, and M. A. Malik, "Synthesis, characterization, electrochemical studies, and in vitro antibacterial activity of novel thiosemicarbazone and its Cu(II), Ni(II), and Co(II) complexes," *The Scientific World Journal*, vol. 2014, pp. 1–9, 2014, doi: 10.1155/2014/592375.

[21] B. Feier *et al.*, "Highly selective electrochemical detection of copper (II) using N, N'-bis(acetylacetone)ethylenediimine as a receptor," *International Journal of Electrochemical Science*, vol. 10, no. 1, pp. 121–139, 2015, doi: 10.1016/j.foodchem.2010.10.080.

[22] A. G. Dalecki, C. L. Crawford, and F. Wolschendorf, "Copper and antibiotics: discovery, modes of action, and opportunities for medicinal applications," in *Advances in Microbial Physiology*, vol. 70, Academic Press, 2017, pp. 193–260. doi: 10.1016/bs.ampbs.2017.01.007.

[23] J. R. Anacona, K. Mago, and J. Camus, "Antibacterial activity of transition metal complexes with a tridentate NNO amoxicillin derived Schiff base. Synthesis and characterization," *Applied Organometallic Chemistry*, vol. 32, no. 7, pp. 1–9, 2018, doi: 10.1002/aoc.4374.

[24] T. H. Y. Pham, T. T. Mai, H. A. Nguyen, T. T. H. Chu, T. T. H. Vu, and Q. H. Le, "Voltammetric determination of amoxicillin using a reduced graphite oxide nanosheet electrode," *Journal of Analytical Methods in Chemistry*, vol. 2021, 2021, doi: 10.1155/2021/8823452.

[25] S. C. Lewin and J. T. Smith, "Bactericidal mechanisms of ofloxacin," *Journal of Antimicrobial Chemotherapy*, vol. 22, Supplement C, pp. 1–8, 1988, doi: 10.1093/jac/22.supplement_c.1.

[26] K. Rudnicki, K. Sipa, M. Brycht, P. Borgul, S. Skrzypek, and L. Poltorak, "Electrochemical sensing of fluoroquinolone antibiotics," *TrAC - Trends in Analytical Chemistry*, vol. 128, 2020, doi: 10.1016/j.trac.2020.115907.

[27] S. Pilehvar *et al.*, "A joint action of aptamers and gold nanoparticles chemically

trapped on a glassy carbon support for the electrochemical sensing of ofloxacin," *Sensors and Actuators B: Chemical*, vol. 240, no. 2017, pp. 1024–1035, 2017, doi: 10.1016/j.snb.2016.09.075.

[28] G. Zhou and J. Pan, "Polarographic and voltammetric behaviour of ofloxacin and its analytical application," *Analytica Chimica Acta*, vol. 307, no. 1, pp. 49–53, 1995, doi: 10.1016/0003-2670(95)00028-X.

[29] T. Liu *et al.*, "New insights into the effect of pH on the mechanism of ofloxacin electrochemical detection in aqueous solution," *Physical Chemistry Chemical Physics*, vol. 21, no. 29, pp. 16282–16287, 2019, doi: 10.1039/c9cp03486b.

[30] K. J. Huang, X. Liu, W. Z. Xie, and H. X. Yuan, "Voltammetric behavior of ofloxacin and its determination using a multi-walled carbon nanotubes-Nafion film coated electrode," *Microchimica Acta*, vol. 162, no. 1–2, pp. 227–233, 2008, doi: 10.1007/s00604-008-0943-z.

[31] S. R. Connell, D. M. Tracz, K. H. Nierhaus, and D. E. Taylor, "Ribosomal protection proteins and their mechanism of tetracycline resistance," *Antimicrobial Agents and Chemotherapy*, vol. 47, no. 12, pp. 3675–3681, 2003, doi: 10.1128/AAC.47.12.3675-3681.2003.

[32] C. I. Brinzila, M. J. Pacheco, L. Ciríaco, R. C. Ciobanu, and A. Lopes, "Electrodegradation of tetracycline on BDD anode," *Chemical Engineering Journal*, vol. 209, pp. 54–61, 2012, doi: 10.1016/j.cej.2012.07.112.

[33] H. Wang, H. Yao, P. Sun, J. Pei, D. Li, and C. H. Huang, "Oxidation of tetracycline antibiotics induced by Fe(III) ions without light irradiation," *Chemosphere*, vol. 119, pp. 1255–1261, 2015, doi: 10.1016/j.chemosphere.2014.09.098.

[34] J. Jeong, W. Song, W. J. Cooper, J. Jung, and J. Greaves, "Degradation of tetracycline antibiotics: Mechanisms and kinetic studies for advanced oxidation/reduction processes," *Chemosphere*, vol. 78, no. 5, pp. 533–540, 2010, doi: 10.1016/j.chemosphere.2009.11.024.

[35] D. Vega, L. Agüí, A. González-Cortés, P. Yáñez-Sedeño, and J. M. Pingarrón, "Voltammetry and amperometric detection of tetracyclines at multi-wall carbon nanotube modified electrodes," *Analytical and Bioanalytical Chemistry*, vol. 389, no. 3, pp. 951–958, 2007, doi: 10.1007/s00216-007-1505-7.

[36] Y. A. Akeneev, G. B. Slepchenko, V. I. Deryabina, T. M. Gindullina, I. O. Maximchuk, and T. I. Shchukina, "Determination of tetracycline in honey by voltammetry," *Procedia Chemistry*, vol. 15, pp. 355–359, 2015, doi: 10.1016/j.proche.2015.10.056.

[37] G. Guo, F. Zhao, F. Xiao, and B. Zeng, "Voltammetric determination of tetracycline by using multi-wall carbon nanotube-ionic liquid film coated glassy carbon electrode," 2009. www.electrochemsci.org

[38] M. Turbale, A. Moges, M. Dawit, and M. Amare, "Adsorptive stripping voltammetric determination of Tetracycline in pharmaceutical capsule formulation using

Poly(Malachite green) modified glassy carbon electrode," *Heliyon*, vol. 6, no. 12, Dec. 2020, doi: 10.1016/j.heliyon.2020.e05782.

[39] H. Wang, H. Zhao, and X. Quan, "Gold modified microelectrode for direct tetracycline detection," *Frontiers of Environmental Science and Engineering in China*, vol. 6, no. 3, pp. 313–319, Jun. 2012, doi: 10.1007/s11783-011-0323-5.

[40] Y. Ni, S. Li, and S. Kokot, "Simultaneous voltammetric analysis of tetracycline antibiotics in foods," *Food Chemistry*, vol. 124, no. 3, pp. 1157–1163, Feb. 2011, doi: 10.1016/j.foodchem.2010.07.028.

[41] R. G. Compton and C. E. Banks, "Chapter 4 Cyclic voltammetry at macroelectrodes," in *Understanding Voltammetry*, 2nd edn, London: Imperial College Press, 2011, pp. 107–155.

[42] B. Feier, A. Gui, C. Cristea, and R. Săndulescu, "Electrochemical determination of cephalosporins using a bare boron-doped diamond electrode," *Analytica Chimica Acta*, vol. 976, pp. 25–34, 2017, doi: 10.1016/j.aca.2017.04.050.

[43] V. Jouikov and J. Simonet, "Electrochemical reactions of sulfur organic compounds," *Encyclopedia of electrochemistry*, vol. 8e. Wiley-VCH, Weinheim, Germany, 2004.

[44] J. K. Park and S. Lee, "Sulfoxide and sulfone synthesis via electrochemical oxidation of Sulfides," *Journal of Organic Chemistry*, 2021, doi: 10.1021/acs.joc.1c01657.

[45] M. C. Dodd, D. Rentsch, H. P. Singer, H. P. E. Kohler, and U. von Gunten, "Transformation of β-lactam antibacterial agents during aqueous ozonation: Reaction pathways and quantitative bioassay of biologically-active oxidation products," *Environmental Science and Technology*, vol. 44, no. 15, pp. 5940–5948, Aug. 2010, doi: 10.1021/es101061w.

[46] A. Karlesa, G. A. D. de Vera, M. C. Dodd, J. Park, M. P. B. Espino, and Y. Lee, "Ferrate(VI) oxidation of β-lactam antibiotics: Reaction kinetics, antibacterial activity changes, and transformation products," *Environmental Science and Technology*, vol. 48, no. 17, pp. 10380–10389, Sep. 2014, doi: 10.1021/es5028426.

[47] M. S. Borisenko and M. V. Solovskiy, "Stability of ofloxacin and cyprofloxacin polymer salts in aqueous solutions," *Russian Journal of Physical Chemistry A*, vol. 95, no. 6, pp. 1156–1159, Jun. 2021, doi: 10.1134/S0036024421060042.

[48] C. Yang, S. Zhang, Y. Liu, and W. Huang, "Electrochemical behaviors of ofloxacin and its voltammetric determination at carbon nanotubes film modified electrode," *Frontiers of Chemistry in China*, vol. 3, no. 3, pp. 353–358, 2008, doi: 10.1007/s11458-008-0055-7.

[49] X. Si, C. Bai, X. Gong, J. Han, Z. Chen, and Y. Ding, "Detection of ofloxacin by differential pulse voltammetry in drugs based on a novel P-aminobenzene sulfonic acid/graphene electrochemical sensor," *International Journal of Electrochemical Science*, vol. 15, no. 9, pp. 8883–8891, Sep. 2020, doi: 10.20964/2020.07.46.

Chapter 7

Summary and outlook

This thesis investigated the range of applications of boron-doped diamond (BDD) in the electrochemical detection of molecules relevant to human and environmental health. The investigation of the analytes chosen may be divided into four areas: (1) dopamine and DNA, both biological molecules that are increasingly studied via electrochemistry; (2) 2-amino-fluorenone, a polluting waste product from oil and gas refineries; (3) pesticides, the detection of which current technology is yet to miniaturise; (4) antibiotics, the surveillance of which may slow their obsoletion. Overall, the oxygen-terminated BDD showed versatile applicability for the detection of these compounds; the activation of the electrode surface can be enhanced by electrochemical means; and previously unreported limits of detection were obtained by parameter adjustments. The main results and conclusions from each chapter are summarised in the following four paragraphs. The thesis ends with a brief discussion of future work.

7.1 Summary

Chapter 3 described the investigation of the application and mechanisms of electrochemical activation in the context of dopamine sensing. Anodic and cathodic pulsed polarisations were optimised to oxidise and reduce the polymeric layers responsible for electrode fouling and to reactivate the BDD surface. These pulses, used in the presence of organic species, can produce more-active electrode states than those present in pristine electrodes. This cleaning method requires the electrode material to be chemically inert, be able to withstand large currents, and to be without surface additions. We believe that this approach can

readily be applied to the development of reusable and robust electrochemical sensors for dopamine.

Chapter 4 investigated the voltammetric behaviour of 2-amino-9-fluorenone (2-AFN), an electroactive pollutant frequently used as a model chemical carcinogen, and its interaction with genetic material. Cyclic voltammetry was used to investigate the redox behaviour of 2-AFN in buffered solutions of pH 2.0–12.0. Differential pulse and square-wave voltammetry, with electro-reactivation of the surface *in situ* were used to obtain the detection limit of 2-AFN. Calibration curves of spiked buffers were measured in the concentration range from 1 nM to 100 μM, with the limit of 10 nM achieved under optimised conditions. After incubation with DNA, 2-AFN-DNA adducts were identified, and the degree of intercalation was compared between single- and double- stranded DNA. At the same time, the specificity of BDD to nucleotides was tested, and its ability to quantify the amount of genetic damage was checked.

The research in *Chapter 5* focused on synthetic chemicals which cause systematic pathology. Non-enzymatic detection of carbamate and organophosphate pesticides was performed on oxidised BDD electrodes. Cyclic voltammetry of the carbamates showed distinctive waveforms that allowed for simultaneous detection, and their mechanisms explored. Electrochemical interaction with malathion semi-permanently altered the BDD's surface, which was then probed by electrochemistry and spectroscopy. Pulsed voltammetry parameters were optimised to obtain better sensing performance for the carbamate pesticides.

Chapter 6 covered the use of the unmodified BDD to investigate the electrochemical behaviour of four antibiotics widely used in industrial farming and seldom studied with electrochemistry. Here, BDD electrodes were applied to the analysis of ofloxacin for the first time. Square-wave voltammetry was used to achieve competitive detection limits of 1

μM for OFX, 500 nM for CFX. A detection limit of 1 nM was also found for TC, which is an order of magnitude lower than previously reported. All three exhibited a wide dynamic range, up to 200 μM. A major advantage of using a BDD electrode was realised for this project.

The conclusion for the research in these experiments is that oxygen-terminated BDD provides good performance for a wide range of detection applications. In general, better results are obtainable with electrochemical pre-treatments which removes adsorbates and reactivates the surface.

7.2 Outlook

In future studies, sensitivity may be improved if the BDD electrode surface were to be modified with metallic or carbon nanostructures, and perhaps the addition of enzymes like acetylcholinesterase, DNA gyrase, or β-lactamase could increase the specificity for pesticides and antibiotics. However, compared with a bare, oxidised BDD electrode, doing either would reduce the robustness and longevity of the set-up. Not only is the present set-up effective for the qualitative and quantitative analysis of some of the compounds discussed, but also the unique material properties of BDD would be suitable for applications in electro-oxidation degradation where the destruction and removal of these compounds is desired.

The work presented in this thesis opens several avenues for further study. Firstly, there are engineering challenges to develop electrode holders for these BDD plates in inverted, rotating-disk, flow-injection, or photoelectrochemical configurations. By changing the physical structure of the electrodes and their modes of interaction, the potential for application is broadened. Secondly, due to the non-enzymatic nature of detection, there are open questions about the redox mechanisms and specificity. Possible ways to shine light on that area is to couple electrochemistry with UV-vis, mass-spectrometric, or

chromatographic techniques, in order to get the best quantitative and qualitative data. Finally, a weatherproof portable electrochemical workstation could be developed, which would enable remote long-term data collection and thus fuller utilise the robustness and the longevity of BDD plates in the real world.